Circuit Quantum Electrodynamics with Flux Qubits

by

Jean-Luc Orgiazzi

A thesis
presented to the University of Waterloo
in fulfillment of the
thesis requirement for the degree of
Doctor of Philosophy
in
Electrical and Computer Engineering - Quantum Information

Waterloo, Ontario, Canada, 2019

© Jean-Luc Orgiazzi 2019

Examining Committee Membership

The following served on the Examining Committee for this thesis. The decision of the Examining Committee is by majority vote.

External Examiner: Dr. William A. Coish
Associate Professor, Dept. of Physics,
McGill University

Supervisors: Dr. Adrian Lupaşcu
Associate Professor, Dept. of Physics & Astronomy,
University of Waterloo

Dr. Michal Bajcsy
Assistant Professor, Dept. of Electrical & Computer Engineering,
University of Waterloo

Internal Member: Dr. Christopher Wilson
Professor, Dept. of Electrical & Computer Engineering,
University of Waterloo

Internal Member: Dr. Raafat Mansour
Professor, Dept. of Electrical & Computer Engineering,
University of Waterloo

Internal-External Member: Dr. Matteo Mariantoni
Assistant Professor, Dept. of Physics & Astronomy,
University of Waterloo

Author's Declaration

This thesis consists of material all of which I authored or co-authored: see Statement of Contributions included in the thesis. This is a true copy of the thesis, including any required final revisions, as accepted by my examiners.

I understand that my thesis may be made electronically available to the public.

Statement of Contributions

The material in Chapter 4 is published in the following with the permission of AIP Publishing:

Reference: Florian R. Ong, Jean-Luc Orgiazzi, Arlette de Waard, Giorgio Frossati, and Adrian Lupaşcu. Insertable system for fast turnaround time microwave experiments in a dilution refrigerator. *Rev. Sci. Instrum.*, 83(9):093904, sep 2012. doi: 10.1063/1.4754634. URL `https://aip.scitation.org/doi/10.1063/1.4754634`

Contributions: A.W. and G.F. provided the cold-insertable probe along with the dilution refrigerator. F. R. O., J. -L. O. and A. L. conceived and designed the microwave sample connection system presented in this work. F. R. O., J. -L. O. and A. L. wrote and edited the paper. All authors discussed the results and commented on the manuscript at all stages. We acknowledge Harmen Vander Heide, Andrew Dube and Michael Lang from Science Technical Services at University of Waterloo for help with design and realization of the mechanical assembly. We also acknowledge Mustafa Bal and Chunqing Deng for acquiring the preliminary data on qubit measurements using this setup.

The material in Chapter 7 is published in the following with the permission of APS:

Reference: J.-L. Orgiazzi, C. Deng, D. Layden, R. Marchildon, F. Kitapli, F. Shen, M. Bal, F. R. Ong, and A. Lupaşcu. Flux qubits in a planar circuit quantum electrodynamics architecture: Quantum control and decoherence. *Phys. Rev. B*, 93(10):104518, March 2016. doi: 10.1103/PhysRevB.93.104518. URL `https://link.aps.org/doi/10.1103/PhysRevB.93.104518`

Contributions: I designed and fabricated the device. J. -L. O., C. D. , F. R. O. and A. L. designed the experimental setup. I conducted the experiments with the help of C. D., R. M., and D. L.. A. L. and I worked on analyzing the data and numerical simulations with the help of F. K., F. S. and C. D.. A. L. supervised the theoretical and experimental work. We acknowledge useful discussions with Patrice Bertet, Pol Forn-Díaz, and Ali Yurtalan.

Abstract

This thesis presents circuit quantum electrodynamic (cQED) experiments done with artificial atoms coupled to a high quality factor superconducting microwave resonator. This work discusses the theoretical framework, design, fabrication, implementation and characterization of a multi-qubit system using superconducting persistent current qubits, often referred as flux qubits.

We developed a new type of cryogenic aid for fast turnaround microwave experiments. The minimum turnaround time to perform microwave experiments in dilution refrigerators is typically a few days, as required by cooling down and warming up the entire refrigerator. The cryogenic microwave payload and wiring needed for each qubit and resonator add a significant heat load to the system which typically only has a few µWs of cooling power at millikelvin temperatures. We present a new experimental approach we developed in which a suitable sample holder is attached to a cold-insertable probe and brought in contact with transmission lines permanently mounted inside the cryostat. The total turnaround time is reduced to 8 hours if the target temperature is 80 mK. This new measurement method increased our ability to successfully identify good devices with fast design-characterization iterations, while allowing months-long measurements at 30 mK.

Our device architecture uses several qubits, each of which is controlled via on-chip fast flux bias lines. Readout of the qubit's quantum state is performed by homodyne detection of the resonator field at large driving power. We observe long coherence times at the optimal bias point of the flux qubits and present decoherence measurements around this optimal point, where the flux qubits couple mostly to magnetic flux noise. Dynamical decoupling techniques employing fast microwave pulses are used to protect the qubit's coherence and allow calculating the magnetic flux noise power spectral density of the qubit's environment. Photon-mediated interaction between distant qubits in the resonator allows the implementation of a two-qubit controlled-NOT gate using the selective darkening technique.

This multi-qubit superconducting design is an interesting platform to study the decoherence properties of flux qubits, the properties of strong interaction of electromagnetic radiation with macroscopic quantum systems. These results demonstrate the potential of cQED as a platform for fundamental investigations of decoherence and quantum dynamics of flux qubits.

Acknowledgments

I would first like to thank my supervisors, Dr. Adrian Lupaşcu, Dr. Michal Bajcsy, and Dr. Hamed Majedi (who co-supervised me until mid-2015), for the opportunity, the supervision and support through my PhD candidacy.

I am grateful to the members of my advisory committee, Dr. Christopher Wilson, Dr. Raafat Mansour, Dr. Matteo Mariantoni, and my external PhD examiner, Dr. William A. Coish, for their time, feedback, great questions during the defense examination, and their valuable advices for improving the thesis manuscript.

I am extremely grateful to have had the opportunity to work with and learn from the postdoctoral researchers in the Superconducting Quantum Devices (SQD) group of Adrian Lupaşcu. Thank you: Jay Gambetta, Mohammad H. Ansari, Mustafa Bal, and Florian Ong for sharing your knowledge and precious experience, ranging from theory and fabrication to measurements and data analysis.

Much of the work discussed in this thesis was only made possible through the cooperative efforts of all of the members of the SQD Laboratory. I am extremely grateful to Chunqing Deng who spent all those years with me in the lab or cleanroom. Many thanks in particular for their help in the lab or cleanroom to Ryan Marchildon, David Layden, Ali Yurtalan, Feyruz Kitapli, Martin Otto, Feiro Shen, Zheng Cui and Jason Soo Hoo.

My special thanks goes to the Quantum NanoFab team of the Institute for Quantum Computing (IQC): Brian Goddard, Rodello Salandanan, Nathan Nelson-Fitzpatrick, lead by Vito Logiudice.

I am grateful to the IQC management & administration team, and the University of Waterloo's technical staffs who provided support to various aspects of our experiments throughout my PhD: Roberto Romero from IQC, Zhenwen Wang from Science Technical Services (STS) for his helps with electronics, John Potzold from the engineering student machine shop who taught me everything about milling machines and lathes operation, the members of the machine shop of STS, in particular Andrew Dube and Michael Lang, lead by Harmen Vander Heide for their help with the design and realization of the mechanical assembly.

I am thankful for my friends and colleagues through the years: Haig, Agnes, Hamid, Audrey, Erika, Jonathan, Marta, Peter, Razieh, Kaveh, Mike, Andrew, Anita, Jeremy, Carolyn, John, Thomas, Meghan, Kim, Martin, Vadiraj, Sandbo, to name only a few.

I am also grateful to Patrick Smutek† of Plassys-Bestek SAS, Dr. Arlette de Waard and Dr. Giorgio Frossati from Leiden Cryogenics B.V. for their great advices, and help over the phone with our cleanroom equipment or dilution fridge.

Many thanks to Dr. Sahel Ashhab from the Qatar Foundation, Dr. Eyal Buks from the Technion Israel Institute of Technology, and Dr. Roman Lutchyn from Microsoft Research for providing us help in understanding the data in experiments.

Lastly, I would like to express my appreciation to Ali Yurtalan and Denis Melanson for their useful comments on this thesis.

Dedication

This thesis is dedicated to Canadian taxpayers and visionary benefactors that made this work possible.

Table of Contents

List of Figures **xxi**

List of Tables **xxv**

1 Introduction **1**

1.1 Quantum information and quantum computing 1

1.2 Superconducting qubits 3

1.3 Cavity quantum electrodynamics with superconducting electrical circuits 4

1.4 Statement of research and summary of key results 5

1.5 Thesis overview 6

2 Circuit quantum electrodynamics with flux qubits **9**

2.1 Josephson junctions based qubits 10

2.1.1 Making artificial atoms with electrical circuits 10

2.1.2 The Josephson effect 11

2.1.3 From Josephson junctions to qubits 14

2.2 The persistent current qubit 14

2.2.1 Quantum mechanical model of a flux qubit 15

2.2.2 Simplified two-level model 18

2.2.3 State preparation and coherent manipulation 20
2.3 Superconducting microwave resonators 22
2.3.1 Transmission line resonator theory 23
2.4 Coupling of a flux qubit to a resonator 29
2.4.1 Jaynes-Cummings Hamiltonian: resonant and dispersive regimes 31
2.5 Qubit state readout 35
2.6 Qubit-qubit coupling using a cavity bus 36
2.7 Decoherence of flux qubits 37
2.7.1 The formal description of decoherence 37
2.7.2 Circuit quantum electrodynamics sources of decoherence 42
2.8 Chapter summary 42

3 Experimental setup 45

3.1 I-V measurements 46
3.2 Magnetic field biasing and shielding 46
3.2.1 Magnetic flux biasing of superconducting flux qubits 47
3.2.2 Shielding 51
3.3 Microwave setup 55
3.3.1 Room-temperature equipment 55
3.3.2 Low-temperature equipment 57
3.3.3 PCB and sample holder 58
3.4 Insertable probe 59
3.5 Chapter summary 60

4 Insertable system for fast turnaround time 63

4.1 Introduction 64

4.2 Experimental setup 65

4.2.1 Dilution refrigerator with cold-insertable probe 65

4.2.2 Fixture for guided insertion of sample holder and coupling to microwave lines 66

4.3 Operation 70

4.4 Examples of measurements 71

4.4.1 Measurement of transmission using a through transmission line 72

4.4.2 Measurement of a coplanar waveguide resonator 73

4.4.3 Measurement of a circuit-QED device using a superconducting flux qubit . 75

4.5 Conclusion 77

5 Design and fabrication of a multi-qubit device 79

5.1 Flux qubit design and fabrication 80

5.1.1 Simulation and parameters optimization 80

5.1.2 Fabrication of Josephson junctions and flux qubits 81

5.1.3 Josephson Junctions characterization 84

5.2 Design & fabrication of superconducting resonators with qubits 88

5.2.1 Superconducting coplanar waveguide design 88

5.2.2 Numerical simulations 89

5.2.3 Fabrication of CPW resonators and qubit integration 95

5.3 Chapter summary 96

6 Control and measurement of flux qubits in cQED 99

6.1 Identifying the qubits symmetry points: resonator transmission Vs applied magnetic flux 100

6.2 Vacuum Rabi splittings . . . 102

6.3 Spectroscopy measurements . . . 105

6.3.1 Continuous wave spectroscopy . . . 105

6.3.2 Pulsed spectroscopy . . . 107

6.4 Readout characterization . . . 110

6.4.1 Case 1: one qubit at its symmetry point . . . 111

6.4.2 Case 2: both qubits at their symmetry points . . . 113

6.5 Ground state initialization . . . 116

6.6 Qubit manipulation . . . 117

6.6.1 Rabi oscillations . . . 117

6.6.2 Pulses calibration . . . 119

6.7 Pulse scheme for qubit energy relaxation and dephasing measurements . . . 120

6.7.1 Qubit energy relaxation T_1 . . . 120

6.7.2 Ramsey fringes experiment: T_2^* . . . 123

6.7.3 Spin echo experiments: $T_{2\text{echo}}$ . . . 125

6.7.4 Dynamical decoupling pulse sequence experiments . . . 128

6.8 Qubit-qubit coupling strength measurement . . . 131

6.9 Chapter summary . . . 131

7 Decoherence measurements of flux qubits **135**

7.1 Introduction . . . 136

7.2 Device architecture, cQED model, and preliminary device characterization . . . 137

7.3 Decoherence measurements results, analysis, and discussion . . . 139

7.4 Qubit-qubit interaction . . . 143

7.5 Chapter summary . . . 144

8 Implementation of a Controlled-NOT gate 145

8.1 Theory overview of the selective darkening technique 146

8.2 Microwave setup for a CNOT gate implementation 149

8.3 Experimental protocol 150

8.3.1 Finding compensation conditions 150

8.3.2 CNOT pulse scheme 154

8.4 Results 154

8.4.1 CNOT gate at various speeds 154

8.4.2 2D scans 156

8.4.3 Improving the CNOT gate fidelity 157

8.5 Chapter summary 159

9 Conclusions and outlook 161

References 165

APPENDICES 187

A Appendix A 189

A.1 Pd/Au markers on Si fabrication using PMGI SF7 / Shipley 1811 190

A.2 Aluminium resonator fabrication using negative photoresist ma-N 1410 191

A.3 Josephson junctions and Flux qubits fabrication using PMGI SF7 / PMMA 950K A3192

List of Figures

2.1 Quantum harmonic and anharmonic electrical oscillators. 10
2.2 Josephson tunnel junction. 11
2.3 Schematic model of a flux qubit. 15
2.4 Potential energy of a 3-junction qubit as a function of phases. 17
2.5 Calculated eigenenergies of the flux qubit circuit versus the applied magnetic flux Φ_{ext}. 19
2.6 Calculated eigenenergy difference between the first excited state and ground state of the full quantum mechanical model and pseudo spin-$\frac{1}{2}$ model. 19
2.7 The Bloch sphere. 21
2.8 Electrical harmonic oscillators. 24
2.9 S_{21} of transmission line resonator: amplitude, phase and IQ-plane circle. 28
2.10 Cavity QED representation. 31
2.11 Measurement in the resonant regime. 34
2.12 Measurement in the dispersive regime. 35
2.13 Schematic view of a coplanar waveguide layout with two flux qubits. 36

3.1 Superconducting coils configuration cutout. 49
3.2 Magnetic field compensation model. 53
3.3 Detailed schematic of the experimental setup. 56

3.4 Microwave board for the packaging of the 3 mm x 7 mm diced samples. 58
3.5 Sample holder with additional copper cover. 59
3.6 Insertable probe with sample holder. 60
3.7 Experimental setup. 61

4.1 Section view of the CF-650 refrigerator and its insertable probe. 66
4.2 Drawings of the mechanical assemblies. 67
4.3 Interfacing between insertable devices and the microwave setup. 68
4.4 Microwave characterization of the probe and sample holder assembly. 72
4.5 Transmission measurement of a CPW resonator. 74
4.6 Example measurement for a circuit-QED experiment. 76

5.1 Qubit frequency calculations 81
5.2 Josephson junctions based device design, fabrication and testing process flow. . . . 83
5.3 SEM image at 45° of a Josephson junction. 84
5.4 Flux qubit fabrication process. 85
5.5 Room temperature characterization of Josephson junctions. 87
5.6 Resonator capacitor simulation. 90
5.7 Qubit drive line inductive coupling. 91
5.8 Microwave resonator with qubit drive line simulation model. 93
5.9 Energy leakage through the fastlines. 94
5.10 Mask pattern for a typical device with web ground. 96

6.1 Resonator S_{21} and magnetic field sweep. 101
6.2 Vacuum Rabi splitting for qubit 1. 103
6.3 Vacuum Rabi splitting for qubit 2. 104

6.4 Numerical simulation of qubit 2 vacuum Rabi splitting. 104
6.5 Observations of photon-number splitting. 106
6.6 Qubit spectroscopy pulse diagram. 108
6.7 Qubit 2 spectrum. 108
6.8 Qubits spectroscopy over time. 109
6.9 Qubit 1 readout contrast map. 112
6.10 Qubit 1 readout contrast map near the resonator bare frequency. 114
6.11 Two qubits joint readout versus readout amplitude and frequency. 115
6.12 Two qubits joint readout: matrix condition number map. 115
6.13 Average photon-number versus frequency at different temperatures. 116
6.14 Pulse diagram for Rabi measurements. 117
6.15 Rabi oscillations versus drive amplitude. 118
6.16 Qubit 1 Rabi oscillations. 119
6.17 Qubit 1 $R_{x\frac{\pi}{2}}$ pulse calibration. 120
6.18 Pulse diagram for T_1 measurements. 121
6.19 T_1 measurement for qubit 2 at its symmetry point. 121
6.20 First three current mode in a $\lambda/2$ resonator. 122
6.21 Multimode Purcell effect. 123
6.22 Fit of qubit 1 T_1 to the multimode Purcell effect model with an intrinsic qubit T_1. 124
6.23 Pulse diagram for T_2^* measurements. 124
6.24 Ramsey fringes measurements for qubit 2 at its symmetry point. 126
6.25 Pulse diagram for Spin echo measurements. 127
6.26 Spin echo measurement for qubit 2 at its symmetry point. 127
6.27 Diagram for a CPMG pulse sequence. 128
6.28 Filter function for various number of π pulses. 129

6.29 Qubit 1 coherence decay with a CPMG pulse sequence and calculated frequency noise PSD. 130

6.30 Qubit-qubit avoided crossing: peak spectroscopy analysis. 132

7.1 Flux qubit device summary. 137

7.2 Energy relaxation rate versus transition frequency for qubit 1. 140

7.3 Decoherence and frequency noise PSD. 142

7.4 Qubit-qubit anticrossing. 143

8.1 Energy-level diagram of the two coupled qubits. 147

8.2 Dressed qubit frequencies due to qubit-qubit coupling. 148

8.3 Energy-level diagram for a CNOT gate and preparation pulse. 149

8.4 CNOT gate experimental setup schematic. 151

8.5 CNOT gate microwave experimental setup board. 152

8.6 Rabi frequencies of both qubits controlled through each qubit lines. 152

8.7 Microwave pulse sequence to find the compensation conditions for the SD technique. 153

8.8 CNOT gate microwave pulses sequence with qubit 2 as the control qubit. 154

8.9 Table of parameters for cancellation condition of the $|00\rangle \leftrightarrow |10\rangle$ and CNOT rotations on the $|01\rangle \leftrightarrow |11\rangle$ transition, with obtained CNOT Rabi speeds and envelope decay constant. 155

8.10 CNOT Rabi oscillations measured at various speeds. 156

8.11 CNOT oscillations 2D map. 157

8.12 CNOT gate with control qubit preparation in ground, superposition or excited state. 158

8.13 CNOT rotations on qubit 1 obtained at two different speeds. 159

List of Tables

6.1 W37_c2d device resonator parameters. 133

6.2 W37_c2d device qubits parameters measured at their respective symmetry points. 133

Chapter 1

Introduction

1.1 Quantum information and quantum computing

Quantum mechanics describes the interplay of energy and matter at the microscopic level. Its name derives from the observation that some physical quantities do not vary continuously but can only be changed by discrete amounts: for example any kinetic momentum is an integer multiple of the Planck constant. This branch of physics was born with the idea that energy has to be quantized, which was first proposed by Max Planck in 1900 while trying to derive a model for the spectrum of black body radiation. Quantum mechanics has been tremendously successful at modeling and predicting many of the aspects of nature, from the properties of microscopic systems such as isolated atoms in its early years, to the coherent behaviour of macroscopic systems containing billions of atoms in the last decades. In 1982, Richard Feynman provided an abstract model for a quantum system that could be used to perform computation and showed how such a machine could act as a simulator for quantum physics [3]. Following on the ideas seeded by Feynman, David Deutsch presented in 1985 a seminal paper [4] introducing a processor that would exploit the laws of quantum mechanics. The proposed quantum processor could perform some computational tasks more efficiently than could be achieved by classical processors. In 1994, Peter Shor discovered a quantum algorithm that could factorize large numbers into their prime numbers with an exponential speedup over its classical counterpart [5]. Two years later Lov Grover presented a new quantum search algorithm with a polynomial speedup [6]. Such discoveries initiated the field of quantum computing.

Quantum information is concerned with the processing and transmission of information using quantum systems. It is anticipated that these concepts will allow for much faster computation [7] and in fact quantum information technologies are already on the market such as quantum cryptography which enables sending information in an absolute secure way. In conventional computing, the basic unit of information is the bit - a physical system with two possible states, 0 and 1. Its quantum analog, the qubit, can be prepared in states $|0\rangle$ or $|1\rangle$, but also in any arbitrary quantum superposition of these two states. However, superpositions are easily destroyed due to interactions with the environment of the qubit and can only survive for a short time. For instance, this coherence time can be as long as a few seconds for real atoms which are well isolated from the external world due to their small size. On the contrary, when dealing with condensed matter based artificial atoms, whose macroscopic size makes them very sensitive to any fluctuation of the electromagnetic environment, the coherence time is typically of the order of nano- to tens of microseconds only. Improving the coherence time in such mesoscopic systems is a major challenge of experimental and scalable quantum computing.

One could describe a quantum computer by an ensemble of qubits that can be coupled to each other. In order to perform quantum algorithms, the controlled evolution of the quantum state of the whole system has to be achieved. Then by measuring the qubits states at the end of the computation, a partial answer to the initial problem can be provided. Indeed a quantum state being a statistical concept, it cannot be obtained from a single system realization but can instead be reconstructed from an ensemble of copies through measurements on different realizations.

Several requirements for the implementation of a physical quantum computer were enumerated by DiVincenzo [8]:

- scalability: a large number of reliable qubits is needed,
- efficient initialization of the qubit state (reset),
- availability of a universal set of quantum gates,
- quantum coherence: long coherence time compared to gate operation time,
- high-fidelity readout of individual qubits.

Different physical systems have been investigated to explore their potential for making quantum processors, including trapped ions, liquid or solid state nuclear magnetic resonance, and quantum dots. Among them, semiconductors structures enabling the manipulation of individual spins in quantum dots or superconducting circuits using Josephson junctions have attracted a lot of attention because they can be implemented in a scalable fashion using well-established micro- and nanofabrication techniques. However, due to their large size, superconducting structures are strongly coupled to their environment which leads to a short coherence time.

1.2 Superconducting qubits

Superconducting qubits use Josephson junctions as building blocks, which are nanostructures made of two superconductors separated by a thin insulating layer [9]. In addition to Josephson junctions, they may also be formed by a combination of superconducting wires, inductors, and capacitors. Superconducting qubits, the system investigated in this work, present unique prospects for scalability, for two reasons: many qubits can be fabricated on the same chip as well as basic components needed to couple them efficiently to each other, and multiple-qubit control can be achieved using available high-speed electronics developed in the areas of computing and telecommunications.

The quantum behaviour of a superconducting qubit takes advantage of the non-dissipative superconducting state and of the intrinsic nonlinearity of the current-phase relation of the Josephson junction. The application of electrical signals either to a single qubit or two coupled qubits allows for the implementation of one- and two-qubit gates, respectively, as required for the operation of a quantum computer.

The best recorded gate fidelity for a single superconducting qubit, a measure of how well the ideal operation is performed, was about 98 % in 2008 [10] but nowadays exceeds 99.98 % [11]. The best fidelities achieved for two-qubit gates are lower (>99 % at the end of 2018). However, since 2006, this has been sufficient for the demonstration of a fundamental controlled-NOT (C-NOT or CNOT) gate [12] (a universal gate in quantum computing), and for the preparation and measurement of entangled states [13]. These fidelities are below the threshold for fault tolerance required for large-scale quantum computing [14]. However, ten years ago, various experiments [15] showed early on that there was a significant potential for further improvement. Indeed, lots of progress to improve the quantum coherence of superconducting qubits has been made in recent years [16]. Maintaining long coherence times with efficient qubits state readout remains a very active field of research, and is critical to allow scaling a quantum computation architecture.

1.3 Cavity quantum electrodynamics with superconducting electrical circuits

Cavity quantum electrodynamics (QED) explores the interaction of a single atom with light at the single photon level [17]. An electromagnetic field (optical or microwave range) is confined inside a 3D resonator with a high-quality factor Q (Fabry-Pérot cavity) [18]. Atoms are prepared in a controlled quantum state and sent one by one in the cavity where they interact with the quantized electromagnetic field during a finite transit time, unless atom trapping techniques are used. Measuring the properties of the outcoming radiation allows for the study of this interaction. Such experiments have not only demonstrated basic quantum computation operations using Rydberg atoms as qubits [17]; they also have enabled the generation and detection of non-classical states of light [19], and provided a powerful platform to study fundamental quantum mechanics in open systems [20] and decoherence mechanisms. Cavity QED is thus an interesting candidate for use in quantum information processing and transmission [17, 18, 21]. However, its implementation requires gigantic and ambitious experimental setups that make any scalable multi-qubit architecture very difficult (if not impossible) to build outside a dedicated physics lab.

Cavity QED using superconducting electrical circuits has been proposed as an architecture for quantum computation. The 3D cavity is replaced by a one-dimensional transmission line resonator and real atoms are replaced with superconducting qubits behaving as artificially engineered atoms [22]. As in the 3D case, the atom can be coupled to the light through its electrical dipole but in the 1D case one can design the system such that this coupling can also use the electric or magnetic moment of the (artificial) atom. As in cavity QED, this system is well described by the Jaynes-Cummings model [23]. In this model, the interaction between the atom and the photon is described by a coupling strength g which expresses the rate at which the electromagnetic field and the atom exchange their quantum of energy when brought to resonance. However, for such a coherent process to be observed, the decay rates of the cavity and of the atom have to be much smaller than g, a regime called strong coupling. The 1D implementation of cavity QED, referred to as circuit QED [24], enables to reach these criteria more efficiently than in the 3D case because:

- at any time the artificial atom is placed at the optimal position maximizing the dipolar interaction (antinode of electric field $\vec{E}$) and thus g
- the confinement of the electromagnetic field leads to a small mode volume also yielding a high $|\vec{E}|$.

The advantages of this platform for quantum computing are reinforced by the fact that placing the qubits in resonators poorly coupled to the environment can provide strong inhibition of spontaneous emission (Purcell effect), potentially leading to greatly enhanced qubit lifetime and coherence time as well as allowing high-fidelity measurements of the state of multiple qubits. The design used allows for qubits to be placed up to centimeters apart while still enabling qubit-qubit interaction and entanglement [22]. Circuit QED can also be used to generate single microwave photons on demand [25, 26] and even create highly non-classical states of the electromagnetic field such as arbitrary superpositions of Fock states [27]. In the past few years, the field of circuit QED has evolved and matured from theory to successful experiments that have explored the foundations of quantum physics [28] and have tested devices that are good candidates for realizing a scalable quantum processor [24, 27, 29, 30, 31, 32, 33, 34, 35, 36].

1.4 Statement of research and summary of key results

In this work, techniques adopted from atomic cavity quantum electrodynamics are applied to superconducting nanoscale circuits to realize qubits. Amazingly, a micron-sized structure containing billions of atoms can be accurately described as a single "artificial" atom. Such qubits can be embedded in a one-dimensional transmission line resonator and used to study the interaction between radiation and matter in new ways and to explore a wider range of parameters. Superconducting qubits of the so-called flux type can be engineered to couple strongly to such resonators. The coupling to the resonator is implemented using the inductance of a shared line.

We will use a system with flux qubits with different transition energies coupled to a high Q-factor microwave resonator as a platform for studying the coherent interaction of quantized electromagnetic radiation and artificial atoms, with the underlying goal of realizing the prototype of a scalable multi-qubit quantum processor.

This dissertation discusses the theoretical framework, design, implementation and characterization of a multi-qubit system using flux qubits. Macro and nanolithography techniques are used to fabricate high-quality aluminium resonators with embedded flux qubits. A custom cold-insertable cryogenic system is devised to allow fast turnaround operation at millikelvin temperatures. The design developed in this dissertation allows the manipulation of the quantum state of each qubits using short microwave pulses applied via on-chip fast flux bias lines. Readout of the qubit's quantum state is performed by homodyne detection of the resonator field. High power resonator drive allows readout contrast exceeding 70 % on some devices.

Measured device characteristics and performance are presented. We observe long coherence times at the optimal bias point of the flux qubits and present decoherence measurements around this optimal point, where the flux qubits couple mostly to magnetic flux noise. Away from the symmetry point, decoherence is due to $1/f$ flux noise, with a measured density of 2.6×10^{-6} Φ_0 $/\sqrt{\mathrm{Hz}}$ at 1 Hz. Dynamical decoupling techniques employing fast microwave pulses are used to protect the qubit's coherence and allow calculating the magnetic flux noise power spectral density of the qubit's environment. Measurements of low-frequency noise based on Ramsey interferometry confirms the flux noise has a $1/f^{\alpha}$ dependence, with alpha close to 1, over a large frequency range. Results on the realization of an entangling gate between two qubits, toward the realization of a universal set of quantum gates, are presented. Photon-mediated interaction between distant qubits in the resonator, which act as quantum bus, allows the implementation and characterization of a fast C-NOT gate using the selective darkening technique [37].

This multi-qubit superconducting quantum processor is an interesting platform to study the decoherence properties of flux qubits, the properties of strong interaction of electromagnetic radiation with macroscopic quantum systems and test the scalability of such architecture.

1.5 Thesis overview

The core of this thesis is structured in the following way. **Chapter 2** discusses the theoretical concepts which this experimental work is based on. The properties of superconducting Josephson junctions are reviewed leading to the theory of operation of a persistent current (flux) qubit circuit. When placed in a superconducting microwave resonator, this two level system can interact with the microwave resonator in similar ways as a natural atom placed in a 3D cavity, as in cavity quantum electrodynamics experiments. The Jaynes-Cummings Hamiltonian is therefore discussed and explored under its relevant resonant and dispersive regimes, the later being used to measure the state of a qubit in the cavity. We also explain how the resonator can act as a quantum bus enabling qubit to qubit coupling. The experimental setup used to characterize the fabricated devices is introduced in **Chapter 3**. The devices are characterized at about 30 mK in an environment which needs to have low RF and MW noise, low external magnetic field fluctuations while at the same time brings close to the device multiple coaxial cables and magnetic field coils, enabling the tuning and control of the qubits and measurements of the resonator transmission.

A cold insertable probe system allowing fast device exchange is described in **Chapter 4**. This easily swappable sample connection system greatly reduced the overhead associated with warming up, opening and replacing a sample before cooling everything again. We present some early results that helped validating this setup. Next, in **Chapter 5**, the design strategies of the qubits and resonators are presented. We use various numerical simulation tools to study and validate the different subsystems of the global design. Fabrication techniques for both the qubits and resonators are presented, emphasizing the fabrication and testing workflow to keep the critical parameters within tolerance. In **Chapter 6**, we look at the various experimental schemes used to characterize flux qubits in cQED. We verify that the qubits are operated in the dispersive limit, strongly coupled to the resonator. We are able to tune two distant qubits in a quantum superposition of states. In **Chapter 7**, we present experimental results on the decoherence of flux qubits around their optimal bias point using Ramsey interferometry, spin echo, and dynamical decoupling pulse techniques. **Chapter 8** then studies the implementation of a fast two-qubit C-NOT gate, where two flux qubits are coupled through the same resonator. Finally **Chapter 9** concludes with the work of this thesis and some of its experimental achievements in the domain of ultra fast driving of a flux qubit, ultra strong coupling, and a practical application like an AC magnetometer scheme implemented with this cQED platform.

Chapter 2

Circuit quantum electrodynamics with flux qubits

In this chapter, we build step by step the model of circuit quantum electrodynamics (cQED) combining an artificial atom and a resonator, focusing on the implementation using flux qubits. The artificial atoms are the two-level systems that will act as controllable qubits, and the resonator is the cavity used to protect the qubits from the environment and used to readout the state of the qubits. Starting from the description of a superconducting Josephson junction, we describe how we can build superconducting qubits that behave as controllable two-level systems. Superconducting microwave resonators theoretical description based on 1D transmission lines is then presented. A quantum mechanics model -the Jaynes-Cummings model- of this artificial atom coupled to the resonator is introduced as the fundamental basis of operation of the devices of this work. In particular, the dispersive regime, in which the qubit state shifts the resonator frequency, is fundamental to the qubit readout scheme presented. Three additional aspects of this system relevant to our study are then introduced: qubit state readout in the dispersive regime, qubit-qubit interaction mediated by the resonator, and decoherence of flux qubits in cQED.

2.1 Josephson junctions based qubits

2.1.1 Making artificial atoms with electrical circuits

In order to obtain an artificial atom, or qubit, we need a system with discrete energy levels that can be populated in a controlled manner by applying electromagnetic radiation. Using electrical circuits, the basic idea is to start from a simple LC oscillator (see Fig. 2.1 (a)): quantum mechanically the charge q on the capacitor and the flux ϕ through the inductor can be treated as conjugate variables and the energy spectrum of this harmonic oscillator is given by $E_n = h\nu_r(n + 1/2)$, where $\nu_r = 1/2\pi\sqrt{LC}$ is the frequency of the oscillator.

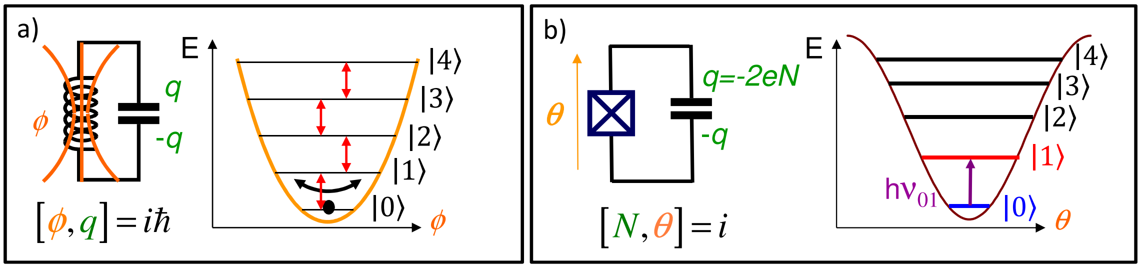

Figure 2.1: Two types of quantum oscillators. Quantum harmonic **a)** and anharmonic **b)** electrical oscillators represented in both cases by their equivalent electrical circuit and the plot of their potential energy E as the phase across the inductor varies. The ground state and the first 4 energy levels are labeled and represented by horizontal lines in both potential energy wells of **a)** and **b)**.

To have control on the population of the energy levels (and especially to be able to prepare the system by allowing it to relax to the ground state) the thermal population of any excited level should be vanishingly small. This is realized by cooling down the system to a temperature T such as $k_B T \ll h\nu_r$. This condition is not satisfied for microwave resonators at 300 K. By using a dilution refrigerator, temperatures of $T \approx 10$ mK can be attained. Resonators in the microwave range cooled at these temperatures are thermalized very effectively. For example, $h \times 2\,\text{GHz} = 10 \times k_B \times 10\,\text{mK}$.

Then, since quantum effects are suppressed by dissipation, the oscillator must be composed of reactive impedances. Using a superconducting circuit maintained at a temperature well below its critical temperature T_c will satisfy this criterium.

However, a harmonic oscillator cannot enable one to selectively address transitions between given levels since all the neighboring energy spacings are degenerate. Thus we need to add some nonlinearity in the system to lift this degeneracy. For instance, if we could engineer a nonlinear inductor as represented in Fig. 2.1 (b), we would obtain an anharmonic potential in which the two lowest energy levels can be addressed separately from all the other levels, defining a qubit. The Josephson junction described in the next subsection behaves as a nonlinear inductor while adding no dissipation to the circuit.

2.1.2 The Josephson effect

Electronic circuits based on superconductor-insulator-superconductor (SIS) Josephson junctions (JJs) play an important role in technology with applications like superconducting quantum interference devices (SQUIDs) which are the most sensitive magnetic field sensing devices, allowing for the study of the neural activity of the brain. JJs arrays have also been used to fabricate a very precise and stable voltage-standard reference.

Josephson junctions are formed by two superconducting electrodes separated by a very thin insulating barrier through which quantum tunneling of Cooper pairs can occur. JJs are characterized by imposing a difference in the quantum phases θ_i that define the superconducting wave functions Ψ_i on both sides (Fig. 2.2).

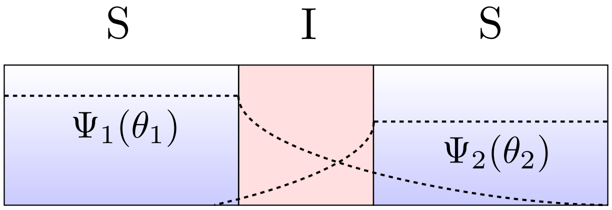

Figure 2.2: Josephson tunnel junction. The superconducting wave functions Ψ_i inside the two superconductors S have a certain quantum phase θ_i. When the barrier I separating the two electrodes is thin enough for the wave functions to overlap, Cooper pairs can pass the barrier by non-dissipative quantum tunneling, resulting in a current.

Josephson junctions fulfill both prerequisites of being non-dissipative and non-linear. Indeed two equations describe the JJ behaviour by relating the superconducting phase difference $\varphi = \theta_2 - \theta_1$

across the junction to measurable electrical quantities such as the supercurrent I_{s} through the JJ and the voltage V across it [38]:

- the DC Josephson equation:

$$I_{\mathrm{s}} = I_c \sin\left(\theta_2 - \theta_1\right) = I_c \sin\varphi, \tag{2.1}$$

where I_c is the critical current of the junction, dependent on the barrier geometry and on insulator properties.

- the AC Josephson equation:

$$V = \frac{\Phi_0}{2\pi}\frac{d\varphi}{dt}, \tag{2.2}$$

where the flux quantum constant is defined as:

$$\Phi_0 = \frac{h}{2e} \approx 2.067 \times 10^{-15}\ \mathrm{T.m}^2. \tag{2.3}$$

Defining the generalized flux Φ through the Josephson junction as $\Phi(t) = \int_{-\infty}^{t} V(t')dt'$, we can rewrite Eq. (2.2) as:

$$\varphi = 2\pi\frac{\Phi}{\Phi_0}, \tag{2.4}$$

which when combined with Eq. (2.1) leads to:

$$I_{\mathrm{s}} = I_c \sin 2\pi\frac{\Phi}{\Phi_0}. \tag{2.5}$$

A new parameter, the *Josephson inductance* is introduced and defined as:

$$L_{\mathrm{J}} = \frac{\Phi_0}{2\pi I_c}, \tag{2.6}$$

and can be combined with (2.5) to give:

$$I_{\mathrm{s}} = \frac{\Phi_0}{2\pi L_{\mathrm{J}}} \sin 2\pi\frac{\Phi}{\Phi_0}. \tag{2.7}$$

In general a relation of the type $I = I(\Phi)$ corresponds to an inductor and, therefore, the Josephson junction behaves like one. Moreover for arbitrary values of Φ the inductance defined as $d\Phi/dI_{\mathrm{s}}$ depends on I_{s} and so is non-linear.

A first energy scale characterizing the Josephson junction is given by the typical magnetic energy stored in the corresponding inductor L_J. This defines the Josephson energy E_J as:

$$E_\mathrm{J} = \frac{\Phi_0 I_c}{2\pi}. \tag{2.8}$$

Now due to the accumulation of charges when current flows, a capacitance C is associated with the junction barrier which yields a second characteristic energy for the Josephson junction, the charging energy E_c:

$$E_\mathrm{c} = \frac{(e)^2}{2C}. \tag{2.9}$$

A Josephson junction can, therefore, be viewed as a parallel combination of a capacitor and of a nonlinear inductor, yielding an anharmonic oscillator. The splitting between the first two energy levels is given by $h\nu_\mathrm{p}$ where $\nu_\mathrm{p} \approx 1/2\pi\sqrt{L_\mathrm{J}C}$ is called the plasma frequency of the JJ (in the limit of $E_\mathrm{J} \gg E_\mathrm{c}$).

The materials choice, the dimension of the junctions, the thickness of the barrier and the purity of the films defines its energy parameters as defined above. The charging energy depends on the geometry of the junction, the area of the overlap as well as the thickness and relative permittivity of the dielectric separating the two electrodes. The Josephson energy depends also on the area of the junction and on the thickness of the insulating layer. It is therefore of prime importance to have the best control possible over the fabrications techniques in order to build devices with measured parameters as close as possible to the design values. One way to verify the performance of the JJs and evaluate its energy parameters is to perform a room temperature measurements of the normal state resistance R_n of the junctions from which the critical current at zero temperature can be found using the Ambegaokar-Baratoff relation [39]:

$$I_c = \frac{\pi\Delta(0)}{2eR_\mathrm{n}}, \tag{2.10}$$

where e is the electron charge and $\Delta(0)$ is the superconducting energy gap at $T = 0\,\mathrm{K}$.

Finally, if we replace the single JJ by two JJs in a SQUID geometry, the ensemble behaves as a single JJ whose critical current can be modulated by applying an external magnetic flux. Thus, L_J is tunable and so is the frequency of our artificial atom, which enables a great versatility in the design parameters compared to the situation with real atoms.

2.1.3 From Josephson junctions to qubits

An isolated Josephson junction would in principle be sufficient to make a qubit. However the plasma frequency $\nu_\mathrm{p} = 1/2\pi\sqrt{L_\mathrm{J}C}$ (valid in the limit of $E_\mathrm{J} \gg E_\mathrm{c}$) at which the device should be operated is fixed by the materials used to build the junction (both L_J and C depend on the precise area of the junction but for their product these dependencies cancel each other). For typical Al/$\mathrm{Al_2O_3}$/Al junctions, $\nu_\mathrm{p} \approx 26\,\mathrm{GHz}$, which is a too high value to allow for affordable and reliable microwave equipment in the lab (sources, low noise amplifiers, circulators, mixers...). Inserting the JJ in a circuit which adds capacitance and/or inductance enables to reduce this operation frequency in the range 2-18 GHz where electronics is more easily available. Furthermore, an isolated JJ cannot conveniently be manipulated by free external RF fields; local antennas have to be added to enable efficient capacitive or inductive couplings with the microwave sources.

Various implementations of superconducting qubits based on Josephson junctions have been realized. Circuits can have different topologies (superconducting island capacitively coupled to gates, current biased JJ, JJ inserted in a superconducting loop) and JJ with different ratio $E_\mathrm{J}/E_\mathrm{c}$. The most appropriate quantum variable describing these quantum systems is either the phase through the JJ (phase qubit [40, 41] and transmon [42, 43] with $E_\mathrm{J} \gg E_\mathrm{c}$), the charge on the electrodes of the JJ (charge qubit [44] with $E_\mathrm{J} \ll E_\mathrm{c}$), or the flux threading a superconducting loop interrupted by one or several JJs (flux qubit [45, 29] with $E_\mathrm{J}/E_\mathrm{c} \approx 10$), or even a combination of these variables [46].

In this research project, I will use the flux qubit. Its topology, theory of operation, and the way we can prepare and read out its quantum state are presented in the following sections.

2.2 The persistent current qubit

The Josephson persistent current qubit, more commonly known as the flux qubit [45, 47], is composed of a superconducting loop with three or more Josephson tunnel junctions. The size of the loop is usually only a few micrometers and the Josephson junctions areas well below one micrometer squared, realizable using fabrication techniques such as electron beam lithography and shadow mask metal evaporation presented in chapter 3. When cooled down to appropriate temperatures and when biased with an external magnetic flux close to half a flux quantum Φ_0, this electrical circuit behaves as a quantum mechanical two-level system, where the corresponding states consists of clockwise and counter-clockwise persistent currents in the loop. These currents I_p produce magnetic fields of opposite directions and are usually in the range of hundreds of nanoamperes. The following subsection 2.2.1 presents the model describing the dynamics of this system. A simplified two-level model for the two lowest energy states is derived next in subsection 2.2.2. Lastly, subsection 2.2.3 present the basis for state preparation and coherent manipulation of these quantum objects.

2.2.1 Quantum mechanical model of a flux qubit

A typical flux qubit is composed of a superconducting loop interrupted by three or more (four in our design) Josephson junctions. Fig. 2.3 is a schematic of such a qubit with three junctions represented by a cross symbol. Their intrinsic capacitance C_i is explicitly drawn. The junctions are characterized by their associated critical current $I_{\mathrm{c},i}$. φ_i represents the superconducting phase difference as introduced in section 2.1.2. The loop is threaded with a magnetic flux Φ_ext and we neglect its self inductance.

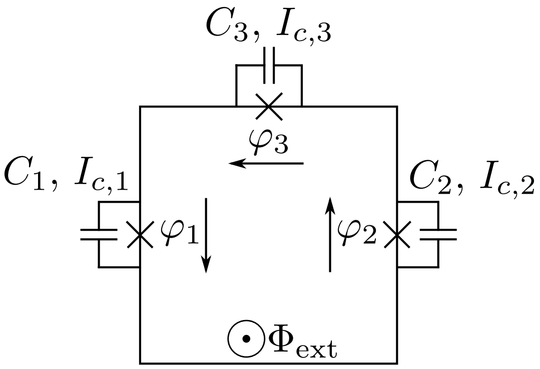

Figure 2.3: Schematic model of a flux qubit. The qubit consists of a superconducting loop with three Josephson tunnel junctions. The junctions are characterized by their critical current $I_{c,i}$ and intrinsic capacitance C_i. The externally applied magnetic flux Φ_ext can be used as external control parameters.

In order to derive a quantum mechanical description of a flux qubit, the Lagrangian and classical Hamiltonian of this electrical system are first obtained. The capacitive energy associated with a junction i is $\frac{1}{2}C_iV_i^2$, where V_i is the voltage across C_i. Using the AC Josephson equation (2.2), this energy term can be transformed and rewritten as a kinetic energy:

$$T(\dot{\vec{\varphi}}) = \sum_{i=1}^{3} \frac{1}{2} C_i \left(\frac{\Phi_0}{2\pi}\right)^2 \dot{\varphi_i}^2 = \sum_{i=1}^{3} \frac{e^2}{E_{\mathrm{c},i}} \left(\frac{\Phi_0}{2\pi}\right)^2 \dot{\varphi_i}^2, \tag{2.11}$$

where $E_{\mathrm{c},i} = (2e)^2/(C_i)$ is the charging energy associated with the displacement of a single charge carrier, a cooper pair, which is $2e$ for superconductors.

Then the potential energy is simply the sum of the phase dependent Josephson energies of the junctions:

$$U(\vec{\varphi}) = \sum_{i=1}^{3} E_{\mathrm{J},i}[1 - cos(\varphi_i)], \tag{2.12}$$

where $E_{\mathrm{J},i} = \Phi_0 I_{c,i}/(2\pi)$. The Lagrangian of the system (the Euler-Lagrange equations are the Kirchoff law for the circuit) is thus:

$$\begin{aligned} L(\vec{\varphi}, \dot{\vec{\varphi}}) =& T(\dot{\vec{\varphi}}) - U(\vec{\varphi}) \\ L(\vec{\varphi}, \dot{\vec{\varphi}}) =& \sum_{i=1}^{3} \frac{e^2}{E_{\mathrm{c},i}} \left(\frac{\Phi_0}{2\pi}\right)^2 \dot{\varphi_i}^2 - \sum_{i=1}^{3} E_{\mathrm{J},i}[1 - cos(\varphi_i)]. \end{aligned} \tag{2.13}$$

The loop geometry of the flux qubit imposes quantization of the total flux (sum of applied magnetic flux and generalized fluxes through each JJ):

$$\sum_{i=1}^{3} \varphi_i + 2\pi \frac{\Phi_{\mathrm{ext}}}{\Phi_0} = 2\pi m, \tag{2.14}$$

where the integer m is the number of full phase cycles. This constraint reduces the number of degrees of freedom to two instead of three. Now if we consider two junctions having the same area and the third one being smaller by a scaling factor α we can rewrite the Lagrangian as:

$$\begin{aligned} L(\vec{\varphi}, \dot{\vec{\varphi}}) =& \frac{e^2}{E_\mathrm{c}} \left(\frac{\Phi_0}{2\pi}\right)^2 [\dot{\varphi_1}^2 + \dot{\varphi_2}^2 + \alpha(-\dot{\varphi_1} - \dot{\varphi_2})^2] + \\ & E_\mathrm{J} \left[\cos(\varphi_1) + \cos(\varphi_2) + \alpha \cos\left(-\varphi_1 - \varphi_2 - 2\pi \frac{\Phi_{\mathrm{ext}}}{\Phi_0}\right)\right], \end{aligned} \tag{2.15}$$

where the constant energy term $-E_\mathrm{J}(2 + \alpha)$ was dropped. Figure 2.4 plots the classical potential energy landscape versus the two degrees of freedom (φ_1 and φ_2) for three different external magnetic flux biases. The potential has two minima, whose depth depends on the ratio of the external magnetic flux to flux quantum, and which are separated by a distance $2 \arccos\left(\frac{1}{2\alpha}\right)$ in the (φ_1, φ_2) plane.

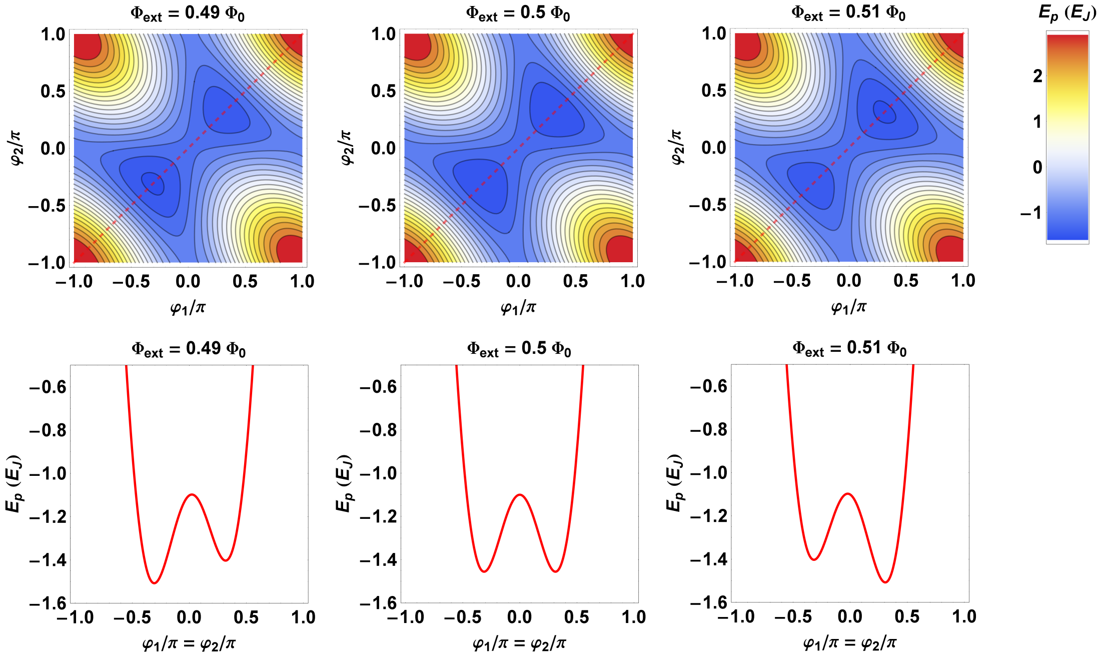

Figure 2.4: Potential energy of a 3-junction qubit as a function of phases. Potential energy of a 3-junction qubit as a function of phases φ_1 and φ_2 and for three externally applied magnetic fields Φ_{ext}. For magnetic fields close to Φ_{ext} and relative sizes of $\alpha = 0.5$ to 1, the system has a double well potential. The calculations are performed using $E_{\text{J}} = 1$, $\Phi_0 = 1$, and $\alpha = 0.70$.

The canonical variables p_1 and p_2 can be derived from the Lagrangian:

$$p_1 = \frac{\partial L}{\partial \dot{\varphi}_1} = C\left(\frac{\Phi_0}{2\pi}\right)^2 [\dot{\varphi}_1 + \alpha(-\dot{\varphi}_1 - \dot{\varphi}_2)], \tag{2.16}$$

$$p_2 = \frac{\partial L}{\partial \dot{\varphi}_2} = C\left(\frac{\Phi_0}{2\pi}\right)^2 [\dot{\varphi}_2 + \alpha(-\dot{\varphi}_1 - \dot{\varphi}_2)], \tag{2.17}$$

and the Hamiltonian of the system can be obtained by a Legendre transformation. The Hamiltonian can be quantized by transforming the system using the charge basis ($\varphi \to -i\hbar\frac{\partial}{\partial q}$). The integer charge states n_i, representing the charges on the superconducting islands, are expressed as:

$$p_1 = \hbar n_1, \tag{2.18}$$

$$p_2 = \hbar n_2. \tag{2.19}$$

Quantum mechanically $\hat{\varphi}$ and $\hat{n}$ are conjugate variables which means:

$$[\hat{\varphi}, \hat{n}] = i. \tag{2.20}$$

The quantized Hamiltonian can then be written as:

$$\begin{aligned} H(\vec{\varphi}, \vec{n}) =& E_\mathrm{c}\left[\frac{1+\alpha}{1+2\alpha}n_1^2 - \frac{2\alpha}{1+2\alpha}n_1 n_2 + \frac{1+\alpha}{1+2\alpha}n_2^2\right] - \\ & E_\mathrm{J}\left[\cos(\varphi_1) + \cos(\varphi_2) + \alpha\cos\left(-\varphi_1 - \varphi_2 - 2\pi\frac{\Phi_\mathrm{ext}}{\Phi_0}\right)\right]. \end{aligned} \tag{2.21}$$

Figure 2.5 plots the three lowest energy levels of a flux qubit as a function of the applied magnetic flux for typical parameters. When Φ_ext is close to half a flux quantum, we observe that the two lowest energy states are well separated from the others. This subsystem can be used as a two-level system (TLS) defining a qubit. The minimum level separation is denoted as Δ. The three junctions model derived above can be extended to a larger number of junctions. The qualitative behaviour remains the same, but the additional junctions and their relative sizes contribute to tune the persistent currents and Δ. In this project the flux qubits fabricated will have four junctions. Indeed, the fourth junction restores the symmetry of the coupling of the qubit with its control line coupled through mutual inductance [48].

2.2.2 Simplified two-level model

In the region where $\Phi_\mathrm{ext} = 0.5\ \Phi_0$ the energy splitting between the lowest (ground) and first excited state is smaller than the splitting between the first excited state and the higher excited states. We can restrict the Hilbert space to the two lowest energy states and describe the system as a spin$-\frac{1}{2}$ in a magnetic field. The Hamiltonian of this simplified system is expressed in the flux basis as:

$$H = -\frac{\varepsilon}{2}\hat{\sigma_\mathrm{z}} - \frac{\Delta}{2}\hat{\sigma_\mathrm{x}}, \tag{2.22}$$

where $\varepsilon = 2I_\mathrm{p}(\Phi_\mathrm{ext} - \frac{1}{2}\Phi_0)$, with I_p the persistent current flowing in the loop; Δ is the energy gap at the avoided crossing and $\hat{\sigma_i}$ are the Pauli spin matrices. Figure 2.6 presents the calculation of the ground and first excited states energies for the non-truncated Hilbert space (circles) and for the two levels model (line), showing that the TLS approximation is reasonable.

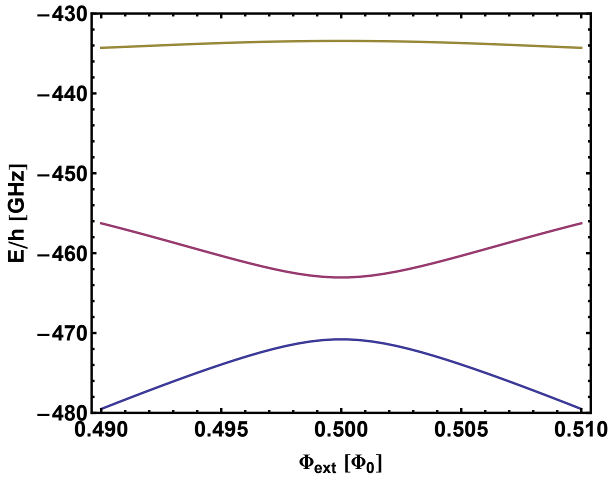

Figure 2.5: Calculated eigenenergies of the flux qubit circuit versus the applied magnetic flux Φ_{ext}. Close to $\Phi_0/2$, the two lowest levels are well separated from the higher levels, forming an effective two-level system. This two-level system can be used as a logical qubit. The calculations are performed using $E_{\text{J}} = h \times 375.5\,\text{GHz}$, $E_{\text{c}} = h \times 3.61\,\text{GHz}$, and $\alpha = 0.63$.

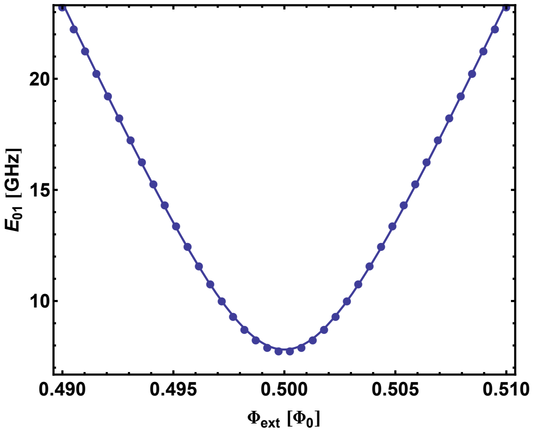

Figure 2.6: Calculated eigenenergy difference between the first excited state and ground state of the full quantum mechanical model (circles) and pseudo spin-$\frac{1}{2}$ model (solid lines). The energy separation at $\Phi_{\text{ext}} = 0.5 \times \Phi_0$ is equal to Δ, and the slopes away from this point are proportional to the persistent currents of the states. The calculations are performed using the same parameters as in Fig. 2.5.

2.2.3 State preparation and coherent manipulation

The operation of a quantum computer requires qubits to be initialized in a known pure state. In the case of superconducting qubits, initialization is typically performed simply by thermalization with the environment. In its steady state a qubit is in the ground state with a probability P_g given by the Boltzmann factor relation:

$$P_\mathrm{g} = 1/(1 + e^{-\hbar\omega_{01}/k_B T}), \tag{2.23}$$

with ω_{01} the transition frequency and T the temperature. Given the temperature attainable with a dilution refrigerator, of typically 1-20 mK, and the transition frequencies in the few GHz range, the fidelity of preparation of the ground state is in the 90 % to 95 % range. In many superconducting qubit experiments it has been observed that the probability of preparing the ground state is lower than the calculation based on the temperature of the cryostat, possibly due to hot excitations. A different approach to state preparation is based on using a projective quantum measurement, as implemented in [49], which leads to preparation fidelities exceeding 98.8 %.

Following preparation, the controlled unitary evolution of the qubit can be used to prepare any desired state. Before discussing quantum controlled evolution, we first present a convenient way to visualize the state of a qubit - the Bloch representation. Any pure state of a qubit can be written as the superposition:

$$|\psi\rangle = \alpha|0\rangle + \beta|1\rangle, \tag{2.24}$$

with $|0\rangle$ ($|1\rangle$) the ground (excited) state and α and β complex numbers satisfying the normalization condition $|\alpha|^2 + |\beta|^2 = 1$. This state can be also expressed, up to a global phase factor, as:

$$|\psi\rangle = \cos\left(\frac{\theta}{2}\right)|0\rangle + e^{i\varphi}\sin\left(\frac{\theta}{2}\right)|1\rangle, \tag{2.25}$$

where $0 \leqslant \theta \leqslant \pi$ and $0 \leqslant \phi \leqslant 2\pi$. Therefore the quantum state is in a unique correspondence with a point on a unit radius sphere with polar angle θ and azimuthal angle ϕ (see Fig. 2.7). Besides serving to represent the state, the Bloch sphere picture is also very useful in visualizing the dynamics of the qubit. Indeed, the most generic Hamiltonian H of a qubit can be written as:

$$H = -\frac{\hbar}{2}\boldsymbol{\omega}(t)\boldsymbol{\sigma}, \tag{2.26}$$

with $\boldsymbol{\sigma}$ a vector formed of the three Pauli matrices, σ_x, σ_y, and σ_z, and $\boldsymbol{\omega}(t)$ a time dependent vector. It can be shown that the time dynamics of the polarization vector $\boldsymbol{p}$ (with $\boldsymbol{p} \equiv \langle\boldsymbol{\sigma}\rangle$)

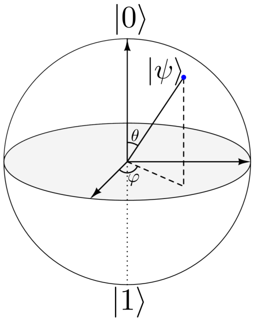

Figure 2.7: The Bloch sphere. The quantum mechanical state of a qubit $|\psi\rangle = \cos(\theta/2)|0\rangle + e^{i\varphi}\sin(\theta/2)|1\rangle$, up to a global phase factor, represented on a Bloch sphere.

describing the state of the qubit on the Bloch sphere is given by:

$$\frac{d\boldsymbol{p}}{dt} = \boldsymbol{p} \times \boldsymbol{\omega}(t), \tag{2.27}$$

which is a precession around the vector $\boldsymbol{\omega}$.

The evolution of a flux qubit is controlled by changing the magnetic flux, which is the only controllable parameter in the Hamiltonian. The most common way to implement control of the qubit is by modulating a magnetic flux at a frequency ω which is resonant or near-resonant with the transition frequency of the qubit $\omega_{01} = \sqrt{\Delta^2 + \epsilon_0^2}$, with ϵ_0 determined by the static part of the magnetic flux applied to the qubit. We have:

$$\epsilon(t) = \epsilon_0 + \widetilde{\epsilon}(t), \tag{2.28}$$

$\widetilde{\epsilon}(t)$ the time dependent part. The Hamiltonian of the qubit:

$$H = -\frac{\varepsilon_0 + \widetilde{\epsilon}(t)}{2}\hat{\sigma_{\mathrm{z}}} - \frac{\Delta}{2}\hat{\sigma_{\mathrm{x}}}, \tag{2.29}$$

becomes, after an unitary transformation which diagonalizes the static part:

$$H = -\frac{\hbar\omega_{01}}{2}\sigma_z - \widetilde{\epsilon}(t)\left(\frac{\Delta}{\omega_{01}}\sigma_x + \frac{\epsilon}{\omega_{01}}\sigma_z\right). \tag{2.30}$$

In the time dependent part of the Hamiltonian, the part proportional to σ_z vanishes when the qubit is operated at the symmetry point ($\epsilon_0 = 0$). In general, when driving the qubit near resonance with a driving amplitude much smaller than the transition frequency, the role of the time dependent term proportional to σ_z in (2.30) can be neglected [50, 51]; we will disregard this term in the following.

We consider driving with a single tone at frequency ω and time-dependent amplitude and phase. Neglecting the σ_z term as discussed above, we write the Hamiltonian (2.30) as:

$$H = -\frac{\hbar\omega_{01}}{2}\sigma_z - \hbar A(t)\cos\left(\omega t + \phi(t)\right)\sigma_x, \tag{2.31}$$

with the amplitude $A(t)$ and phase $\phi(t)$ varying slowly in time on the time scale of the inverse of the transition frequency $2\pi/\omega_{01}$. Without driving, the dynamics of the qubit consists of fast precession of the pseudovector at frequency ω_{01}. It is convenient to analyze the dynamics in a rotating frame, by performing the unitary transformation $U_{\mathrm{rf}} = e^{-i\omega t/2\sigma_z}$. The evolution of the qubit in this new frame is governed by the Hamiltonian:

$$\widetilde{H}(t) = -\frac{\hbar(\omega_{01}-\omega)}{2}\sigma_z - \left(A(t)\cos\phi(t)\cos(\omega t) + A(t)\sin\phi(t)\sin(\omega t)\right)\left(\cos(\omega t)\sigma_x + \sin(\omega t)\sigma_y\right). \tag{2.32}$$

This Hamiltonian can be simplified by performing the rotating wave approximation (RWA): the terms corresponding to frequency 2ω are disregarded. With the RWA the Hamiltonian becomes:

$$\widetilde{H}_{RWA}(t) = -\frac{\hbar(\omega_{01}-\omega)}{2}\sigma_z - \frac{A(t)\cos\phi(t)}{2}\sigma_x - \frac{A(t)\sin\phi(t)}{2}\sigma_y. \tag{2.33}$$

Qubit evolution is implemented using controlled rotations. In general, we define rotations of angle θ around axis $\boldsymbol{n}$ by the operator $R(\boldsymbol{n},\theta) = e^{-i\frac{\theta}{2}\boldsymbol{n\sigma}}$. The ability to perform rotations of arbitrary angle around two perpendicular axes allows the implementation of any unitary operation [7]. This is achievable using Hamiltonian (2.33) by taking on resonance driving and control of driving amplitude and phase.

2.3 Superconducting microwave resonators

In the on-chip implementation of cavity quantum electrodynamics, the 3D cavity is replaced by a one-dimensional transmission line resonator made out of a superconducting material, as introduced in Ch. 1. The qubits are embedded in this microwave resonator. This resonator is used for the control and the readout of the qubits' state, as well as for intermediating interactions between qubits. Embedding a qubit in a resonator has the advantage of partially protecting it from spontaneous emission owing to the Purcell effect, improving its coherence times. The quality factor (or equivalently the coupling to the external world) can be engineered in order to either perform fast measurement or to increase the time of interaction of the microwave photons with the qubits.

At or near resonance, the superconducting coplanar waveguide resonator can be approximated as an LC resonator weakly coupled to the external transmission lines by capacitors C_c. This model allows for an intuitive understanding of the device, but higher harmonic modes of the CPW resonator should be included in a more rigorous description.

The fundamental mode of the uncoupled resonator corresponds to a $\lambda/2$ resonance with frequency:

$$f_r = \frac{c}{\sqrt{\epsilon_\mathrm{eff}}}\frac{1}{2\Lambda}. \tag{2.34}$$

where $c/\sqrt{\epsilon_\mathrm{eff}}$ is the phase velocity denoted by v_ph, with c the speed of light in vacuum, ϵ_eff the effective permittivity of the CPW line, and Λl the length of the resonator. ϵ_eff depends on the geometry of the waveguide and the relative permittivities of the different materials used to build it (substrate covered by a possible oxide layer). When the conductor layer of the CPW is a thin layer of superconducting material, the additional kinetic inductance of the cooper pairs affects the propagation of the wave.

As the resonator is operated at tens of mK, which is well below the critical temperature of the superconductor, it is expected that the resistive losses are negligible. The substrate should be highly resistive with a small dielectric loss tangent to minimize further dissipation.

2.3.1 Transmission line resonator theory

The simplest model describing an electrical oscillator consists of an inductance L in parallel with a capacitor C (Fig. 2.8 a). Although it is useful to analyze the dynamics of the circuit in terms of current $i(t)$ and voltage $V(t)$ it is convenient to use instead the charge q on the capacitor plates and the generalized flux $\phi = \int_0^t V(\tau)d\tau$. For an inductor, ϕ is nothing else than the magnetic flux but this definition allows to define a flux for any two port component. Since $V(t) = q(t)/C = \partial_t\phi/C$, ϕ can be viewed as a position variable and q its conjugate momentum.

The (classical) energy H_c of the circuit is:

$$H_\mathrm{c} = \frac{q^2}{2C} + \frac{\phi^2}{2L}, \tag{2.35}$$

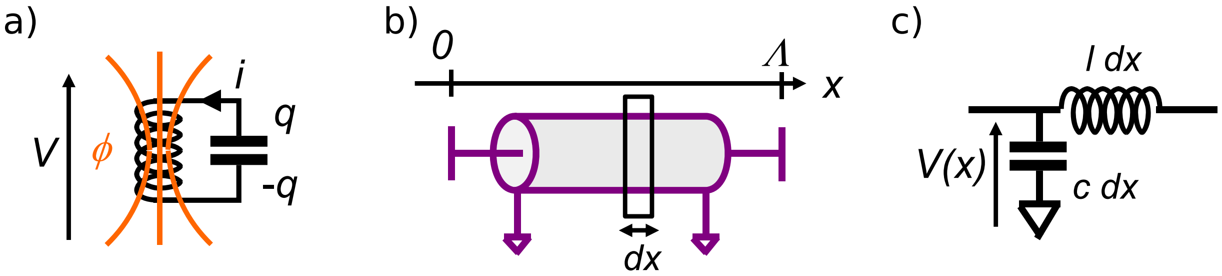

Figure 2.8: Electrical harmonic oscillators. a): lumped element circuit. **b)**: distributed version (section of transmission line). **c)**: model for a infinitesimal section dx of the transmission line.

and the Hamilton's equation of motion read:

$$\dot{\phi} = -\frac{\partial H}{\partial q} = -\frac{q}{C} \text{ and } \dot{q} = \frac{\partial H}{\partial \phi} = \frac{\phi}{L}, \tag{2.36}$$

which yields for both q and ϕ the sinusoidal time dependence with characteristic frequency $\omega_0 = 1/\sqrt{LC}$.

To move from the classical to the quantum picture, we use the correspondence principle. Noting that the Poisson bracket $\{\phi, q\} = 1$, where:

$$\{A, B\} = \frac{\partial A}{\partial \phi}\frac{\partial B}{\partial q} - \frac{\partial A}{\partial q}\frac{\partial B}{\partial \phi}, \tag{2.37}$$

we transform the ϕ into a position operator $\hat{\phi}$ whereas q becomes its conjugate momentum $\hat{q}$, with the requirement that these operators satisfy the commutation relation $\left[\hat{\phi}, \hat{q}\right] = i\hbar$ [52].

Defining the dimensionless annihilation and creation operators $\hat{a}$ and $\hat{a}^\dagger$ as:

$$\hat{a} = \frac{\phi}{\phi_r} + i\frac{q}{q_r} \text{ and } \hat{a}^\dagger = \frac{\phi}{\phi_r} - i\frac{q}{q_r}, \tag{2.38}$$

with $\phi_r = \sqrt{2\hbar\omega_0 L}$ and $q_r = \sqrt{2\hbar\omega_0 C}$, we can write the (quantum) Hamiltonian of the circuit as:

$$\hat{H} = \hbar\omega_0(\hat{a}^\dagger\hat{a} + 1/2), \tag{2.39}$$

which is the well known Hamiltonian of a harmonic oscillator.

In the microwave regime, reactances packaged as regular components for circuit boards do not behave ideally. For instance, a wound inductor is likely to be shunted by a parasitic capacitance. Also, because their size is comparable to the wavelength of the signal, it is not possible to assign just a local voltage value. A strategy to overcome this problem is to pattern these components directly on-chip out of metallic thin films. An electrical resonator can be made of lumped elements (for instance an interdigitated capacitor in parallel with a meander line inductor), in which case the model described above applies directly. However, it is also convenient use as a resonator a segment of a transmission line (or equivalently of a coplanar waveguide when implemented on chip). In this case the inductance and capacitance are not localized but rather distributed all along the resonator (see Fig. 2.8 b) : c and l are the capacitance and inductance per unit length). From here on we discuss the case of a distributed resonator.

We define a local phase:

$$\phi(x,t) = \int_0^t V(x,\tau)d\tau, \tag{2.40}$$

and its conjugate variable the local density of charge:

$$\rho(x,t) = cV(x,t) = c\partial_t\phi. \tag{2.41}$$

Kirchoff's circuit laws applied to the element dx of the transmission line yield the wave equation:

$$\partial_t^2\phi - lc\partial_x^2\phi = 0. \tag{2.42}$$

The open ends at $x = 0$ and $x = \Lambda$ impose:

$$\partial_t\rho(0,t) = \partial_t\rho(\Lambda,t) = 0 \text{ which leads to} \tag{2.43}$$

$$\partial_x\phi(0,t) = \partial_x\phi(\Lambda,t) = 0, \tag{2.44}$$

which allows to write the general solution for the dynamical variable as discrete sums over an infinity of spatial modes labeled by an integer k:

$$\phi(x,t) = \sqrt{\frac{2}{\pi k}}\sum^{k}\phi_k(t)\cos\left(\frac{k\pi x}{\Lambda}\right), \tag{2.45}$$

$$\rho(x,t) = \sqrt{\frac{2\pi k}{\Lambda}}\sum^{k}q_k(t)\cos\left(\frac{k\pi x}{\Lambda}\right). \tag{2.46}$$

ϕ_k and q_k represent the conjugate phase and charge of an equivalent LC resonator with $C_k = c\Lambda/(\pi k)$, $L_k = l\Lambda/(\pi k)$, and resonance frequency $\omega_k = 1/\sqrt{L_k C_k}$. Each of these modes can then be quantized as we described above.

Up to now we did not introduce any energy loss in our description of circuits. This is a fairly good assumption provided we are dealing with pure reactances connected to each other with superconducting wires. However at microwave frequencies energy-loss channels open, such as radiation and loss in the dielectrics or in the substrate. For each mode k these internal losses can be characterized by an internal energy decay rate:

$$\kappa_{\mathrm{int},k} = \frac{P_{\mathrm{loss},k}}{E_{\mathrm{stored},k}} = \frac{\omega_k}{Q_{\mathrm{int},k}}, \tag{2.47}$$

where $E_{\mathrm{stored,k}}$ is the energy stored in the mode k, $P_{\mathrm{loss,k}}$ is the power leaking out of the mode, and $Q_{\mathrm{int},k}$ is defined as the *internal* quality factor of the resonator. When $Q_{\mathrm{int},k} \gg 1$ the dynamics of the resonator around ω_k is to a very good approximation the same as if it were a single mode resonator, a property which we will use extensively in our work: indeed our qubit readout scheme consists in driving the resonator near the resonance frequency of its first mode. Note, however, that from the qubits point of view this is not as simple because in most regimes of interest the qubits need to be detuned from the resonator. In this situation, the qubits "see" many modes that need to be considered to quantitatively account for their relaxation time (see section 6.7).

To characterize a resonator (e.g. to measure the frequency and quality factor of its resonant modes) or to probe its internal electromagnetic field (which in cavity or circuit-QED allows to infer the state of the qubits), it is necessary to couple it to some measurement setup. In our case, this is done by capacitively coupling the input and output ports of the resonator to transmission lines. A microwave field $\underline{A}_{\mathrm{in}}(t)$ feeds the input via C_{in} and a field $\underline{A}_{\mathrm{out}}(t)$ is emitted at the output via C_{out}. Here $\underline{A}_{\mathrm{in/out}}$ is the amplitude of the propagating field at the resonator boundaries: $\underline{A}_{\mathrm{in}}$ (resp. $\underline{A}_{\mathrm{out}}$) is C-number proportional to the $V^+(0,t)$ (resp. $V^-(\Lambda,t)$). $\underline{A}_{\mathrm{in/out}}$ is expressed in $\mathrm{Hz}^{-1/2}$, such as $|\underline{A}_{\mathrm{in/out}}|^2$ can be interpreted as the number of photons impinging/exiting the resonator [53, 54]. [1]

This coupling is a path for the energy stored in the resonator to relax at a rate $\kappa_{\mathrm{in/out}}$, which affects the quality factor of the resonator. We thus define the *external* quality factor as:

---

[1] Transmission lines typically have a characteristic impedance $Z_0 = 50\,\Omega$, and they are matched to $50\,\Omega$ components or instruments. This means that the resonator is now capacitively coupled both at its input and output to an environment which can be modeled as a $50\,\Omega$ resistance.

$$Q_{\text{ext}} = \frac{\omega_r}{\kappa_{\text{ext}}}, \text{ with} \tag{2.48}$$

$$\kappa_{\text{ext}} = \kappa_{\text{in}} + \kappa_{\text{out}}. \tag{2.49}$$

The *total* quality factor Q_{tot} of the resonator is then expressed as:

$$\frac{1}{Q_{\text{tot}}} = \frac{1}{Q_{\text{int}}} + \frac{1}{Q_{\text{ext}}}. \tag{2.50}$$

Note that Q_{ext} can be engineered by changing the value of the capacitors $C_{\text{in/out}}$, and can be finely tuned geometrically. On the other hand Q_{int} is upper bounded by microscopic processes (of the order of 10^6) in the case of coplanar waveguide resonators. A considerable effort is currently made by the superconducting qubits field together with the material science community to understand and overcome these losses [55, 56, 57].

Now let's look at the response of a transmission line resonator. As we will see in the next subsection, we can experimentally access the scattering matrix (or S_{ij} parameters with i and $j =$ 1 or 2) of the resonator [58], and in particular its transmission $S_{21} = \underline{A}_{\text{out}}/\underline{A}_{\text{in}}$ (see Fig. 2.9). To calculate S_{21} we consider a drive at frequency ω close to the frequency ω_r of the first resonant mode of the transmission line (note that ω_r is the *coupled* resonance frequency, that is the frequency ω_1 described above plus a shift due to the coupling capacitors). The dynamics of the field in the resonator is described by creation and annihilation operators $\underline{\alpha}^\dagger(t)$ and $\underline{\alpha}(t)$ such as:

$$[\underline{\alpha}(t), \underline{\alpha}^\dagger(t)] = 1 \text{ and } H_{\text{r}} = \hbar\omega_r(\underline{\alpha}^\dagger(t)\underline{\alpha} + 1/2). \tag{2.51}$$

The time evolution of $\underline{\alpha}(t)$ includes the Hamiltonian evolution, a loss term, and a drive term. It can be written as follows:

$$\frac{d\underline{\alpha}}{dt} = \frac{i}{\hbar}[H_{\text{r}}, \underline{\alpha}(t)] - \frac{\kappa_{\text{tot}}}{2}\underline{\alpha}(t) + \sqrt{\kappa_{\text{in}}}\underline{A}_{\text{in}}(t). \tag{2.52}$$

The factor 1/2 in front of κ_{tot} stands for the fact that κ_{tot} is the decay rate of the energy, whereas $\underline{\alpha}$ is an amplitude. The last term describes the coupling of the input field to the internal field via the input-output theory [53]. The same theory allows to write $\underline{A}_{\text{out}}(t) = \sqrt{\kappa_{\text{out}}}\ \underline{\alpha}(t)$.

Now assuming a sinusoidal drive $\underline{A}_{\text{in}}(t) = A_{\text{in}}e^{-i\omega t}$ and focusing on the response at ω ($\underline{\alpha}(t) = \alpha e^{i\omega t}$ and $\underline{A}_{\text{out}}(t) = A_{\text{out}}e^{i\omega t}$), we have:

$$\alpha = \frac{2\sqrt{\kappa_{\text{in}}}}{\kappa_{\text{tot}} - 2i(\omega - \omega_r)} A_{\text{in}}, \tag{2.53}$$

and

$$S_{21} = \frac{A_{\text{out}}}{A_{\text{in}}} = \frac{2\sqrt{\kappa_{\text{in}}\kappa_{\text{out}}}}{\kappa_{\text{tot}} - 2i(\omega - \omega_r)}. \tag{2.54}$$

The square modulus of α is the average number of photons stored in the resonator. $|A_{\text{in}}|^2$ is related to the incident power P_{in} expressed in watts through:

$$P_{\text{in}} = \hbar\omega_r |A_{\text{in}}|^2. \tag{2.55}$$

At resonance:

$$\bar{n} = \frac{4\kappa_{\text{in}}}{\kappa_{\text{tot}}^2}|A_{\text{in}}|^2 = \frac{4\kappa_{\text{in}}}{\hbar\omega_r\kappa_{\text{tot}}^2}P_{\text{in}}. \tag{2.56}$$

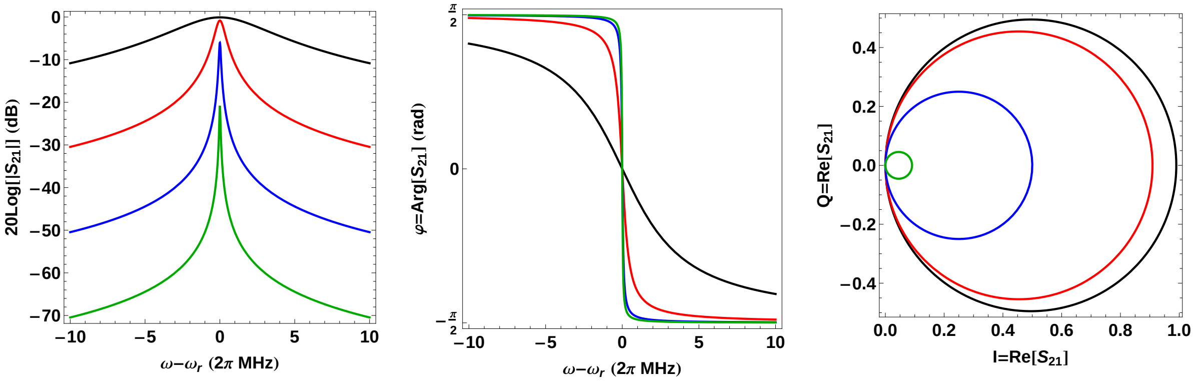

Figure 2.9: S_{21} of transmission line resonator: amplitude, phase and IQ-plane circle. S_{21} of transmission line resonator around its first mode. $\omega_r = 2\pi$ 6 GHz, $Q_{\text{int}} = 10^5$ and $Q_{\text{ext}} =$ 1000 (black), 10^4 (red), 10^5 (blue) and 10^6 (green). Coupling capacitors are chosen symmetric. **(left)** Amplitude of S_{21} expressed in dB. **(middle)** Phase of S_{21}. **(right)** Response in IQ plane for ω spanning the resonance.

Figure 2.9 shows the complex transmission of a resonator around its first mode for several quality factors. $|S_{21}|$ is a Lorentzian centered on ω_r and with half-width at half-height κ_{tot}. The phase $\varphi =$Arg$[S_{21}]$ experiences a π shift at the resonance. Several ratios between internal and external losses κ_{int} and κ_{ext} are relevant to consider:

- For $\kappa_{\text{int}} \gg \kappa_{\text{ext}}$ the resonator is undercoupled, which means that most of the energy entering the resonator is lost through irreversible internal processes before exiting. The output field amplitude is thus much smaller than that of the input field even at resonance which is a situation to avoid. Indeed the level of the output field would be in the order of or lower than the noise level (low signal-to-noise ratio). Such regime is not desirable for qubit measurements, where the state of the qubit interacting with the resonator is inferred from the resonator's measured state.

- For $\kappa_{\text{int}} \ll \kappa_{\text{ext}}$ the resonator is overcoupled. All the energy entering the resonator is reemitted in the $50\,\Omega$ environment either at the input or the output. Note that we can engineer the coupling capacitors such as $C_{\text{in}} < C_{\text{out}}$ to favor the output port path. For a given number of photons stored in the resonator (and, as we will see, a given measurement induced dephasing rate onto the qubits), this increases the readout signal.

- For $\kappa_{\text{int}} = \kappa_{\text{ext}}$ the resonator is critically coupled: half of the energy is absorbed by microscopic processes and half of it exits through the coupling capacitors.

In circuit-QED the choice of the quality factor is important and depends on what role is played by the resonator. Concerning Q_{int}, the larger the better since any energy lost internally cannot be exploited by the experimentalist. On the other hand Q_{ext} can serve different purposes: resonators with very high Q_{ext} $(10^5 - 10^7)$ could be used as quantum memories (also with very high Q_{int}) or bus mediating interactions between qubits. Resonators with lower Q_{ext} $(10^2 - 10^4)$ are adapted for qubit readout (too high a Q_{ext} would need a too long time to energize the resonator, during which the qubit may relax). However, too low a Q_{ext} increases the relaxation rate of the qubit due to the Purcell effect. The choice of Q_{ext} is thus the result of a trade-off, especially in the simple architecture we implement, where only one resonator plays several antagonistic roles (readout and coupling bus).

2.4 Coupling of a flux qubit to a resonator

In this section, we evaluate the coupling strength of a flux qubit placed in a coplanar waveguide resonator. Contrary to Rydberg atoms in cavity QED or transmon qubits in circuit QED, where the coupling of the qubit to the EM field is achieved through its electrical dipole, the flux qubit is more likely to interact with the magnetic field in the cavity through its magnetic dipole. So it should be placed in a region where the intra-cavity magnetic field is maximum. Thus we calculate here the coupling of a flux qubit placed at a current antinode. The coupling strength g is therefore given by:

$$g = \mu \frac{B_{0\ \mathrm{rms}}}{\hbar}, \tag{2.57}$$

where $B_{0\ \mathrm{rms}}$ is the zero-point root mean square magnetic field generated by the current quantum fluctuations at the antinode of the resonator [59] and where:

$$\mu = I_{\mathrm{p}} A \tag{2.58}$$

is the dipole moment of the flux qubit; I_{p} is the persistent current flowing in the loop of area A. In order to estimate $B_{0\ \mathrm{rms}}$, we consider the zero-point energy of the resonator and obtain:

$$\frac{1}{2} L I_{\mathrm{rms}}^2 = \frac{1}{4} \hbar \omega_{\mathrm{r}} \tag{2.59}$$

$$I_{\mathrm{rms}} = \sqrt{\frac{\hbar \omega_{\mathrm{r}}}{2L}}, \tag{2.60}$$

where L is the total equivalent inductance of the resonator near resonance. The field at the antinode of the fundamental mode can be approximated as:

$$B_{0\mathrm{rms}} \approx \frac{\mu_0 I_{\mathrm{rms}}}{\pi r}, \tag{2.61}$$

where μ_0 is the vacuum permeability and r is half the width of the gap between the center conductor and the ground plane if we assume the qubit is placed at the center of the gap. With the above approximation, the coupling strength between a flux qubit and the resonator is approximately:

$$g \approx \frac{I_p A \mu_0}{\hbar \pi r} \sqrt{\frac{\hbar \omega_{\mathrm{r}}}{2L}}. \tag{2.62}$$

Bourassa *et al.* introduced the theory of operation of a circuit QED architecture where the loop of the flux qubit is directly coupled to the center conductor of a coplanar waveguide [60]. This is related to older work by Chiorescu *et al.* [29] where galvanic coupling was used for coupling the qubit to harmonic oscillators. Directly coupling the qubit loop to the center conductor has the advantage of increasing the coupling strength of the qubit to the resonator without having to increase the loop area of the flux qubit, making it less prone to magnetic flux noise and decoherence. Our work will make use of this approach.

2.4.1 Jaynes-Cummings Hamiltonian: resonant and dispersive regimes

The key parameters describing a cavity QED system are the cavity resonance frequency ω_r, the atomic transition frequency ω_q, and the strength of the atom-photon coupling g. The atom decays at a rate γ and transits in the cavity for a time t_{transit}. The photon in the cavity decays at a rate κ as represented in Fig. 2.10.

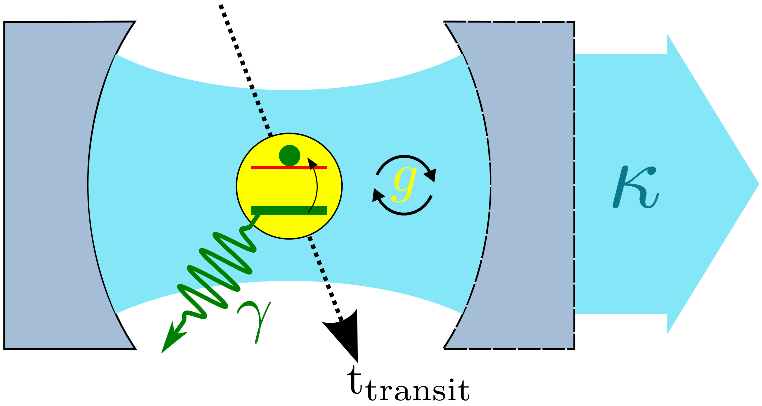

Figure 2.10: Cavity QED representation. A cavity QED system formed by two concave mirrors (the dashed delineated mirror on the right is leaky), which supports a single mode electromagnetic field resonance. This mode has a decay rate κ and is coupled with a coupling strength g to a two-level system with spontaneous decay rate γ. This two-level is typically not static and has a cavity transit time t_{transit} [22].

This representation remains valid in the case of circuit QED. However, since the artificial atoms are solid state devices built within the microwave resonator, there is no analogy between the transit time as modeled in cavity QED experiments where atoms falls in vacuum in the cavity and interact with the mode supported by the two mirrors for a short time only. For our experiments, we can therefore consider $t_{\text{transit}} = \infty$.

Jaynes-Cummings Hamiltonian model

Considering a flux qubit placed in a microwave resonator that can be excited with microwave signal, the Hamiltonian of the complete system is given by:

$$H = H_{\text{q}} + H_{\text{r}} + H_{\text{int}} + H_{\text{d}}, \tag{2.63}$$

where H_q is the qubit Hamiltonian, H_r describes the resonator and H_int the interaction between the qubit and the electromagnetic field in the resonator. H_d models the driving of the qubit by an external microwave tone. The qubit Hamiltonian given by Eq. (2.26) can be further simplified if the qubit is operated at or near the degeneracy point. If we consider the basis in which the ground state $|\uparrow\rangle$ and the excited state $|\downarrow\rangle$ correspond to symmetric and antisymmetric superpositions of clockwise and anti-clockwise persistent current, H_q can be expressed as:

$$H_\mathrm{q} = \frac{\hbar\omega_q}{2}\left(|\uparrow\rangle\langle\uparrow| - |\downarrow\rangle\langle\downarrow|\right) = \frac{\hbar\omega_q}{2}\sigma_\mathrm{z}, \tag{2.64}$$

where $\hbar\omega_q$ is the energy levels separation and ω_q is the qubit Larmor frequency (see also section 2.2) given by:

$$\sqrt{\varepsilon^2 + \Delta^2}. \tag{2.65}$$

If it is assumed that the coplanar resonator supports only one mode, its Hamiltonian H_r is expressed as:

$$H_\mathrm{r} = \hbar\omega_\mathrm{r}\left(a^\dagger a + \frac{1}{2}\right), \tag{2.66}$$

where $a^\dagger$ is the creation operator and a the annihilation operator which respectively creates and destroy a single photon at frequency $\omega_\mathrm{r}/2\pi$ in the resonator. In this single-mode limit, the resonator can be viewed as a harmonic oscillator with energy levels given by $\hbar\omega_\mathrm{r}(n+1/2)$ where n represents the number of photons.

The interaction between the qubit and the radiation is given in the rotating wave approximation by the Hamiltonian:

$$H_\mathrm{int} = \hbar g(a^\dagger\sigma^- + \sigma^+ a), \tag{2.67}$$

where $\sigma^+ = \sigma_\mathrm{x} + i\sigma_\mathrm{y}$ and $\sigma^- = \sigma_\mathrm{x} - i\sigma_\mathrm{y}$ are the raising and lowering operators for the qubit. The terms $a^\dagger\sigma^-$ models the process by which the qubit emits a photon at the expense of going from its excited state to its ground state, and the term $\sigma^+ a$ describes the excitation of the qubit by absorbing a photon.

When the system is interacting with a classical drive field at frequency $\omega/2\pi$, photons are exchanged between the resonator and this driving field. This process is modeled by:

$$H_\mathrm{d} = \xi\left(e^{-i\omega t}a^\dagger + e^{i\omega t}a\right), \tag{2.68}$$

where ξ is the drive amplitude.

Summing terms 2.34 to 2.37 we obtain the expression of the driven Jaynes-Cummings Hamiltonian [61]:

$$H = \frac{\hbar\omega_q}{2}\sigma_\mathrm{z} + \hbar\omega_\mathrm{r}\left(a^\dagger a + \frac{1}{2}\right) + \hbar g(a^\dagger\sigma^- + a\sigma^+) + \xi\left(e^{-i\omega t}a^\dagger + e^{i\omega t}a\right). \tag{2.69}$$

In addition to these Hamiltonian terms, the system is subject to dissipation. The interaction of the resonator-qubit system with its environment includes various mechanisms leading to the loss of coherence:

- The microwave photons leak out of the cavity at a rate $\kappa = \omega_\mathrm{r}/Q$, with Q the quality factor of the resonator.
- The qubit decays at a rate $\gamma = 1/T_1$, where T_1 is the energy relaxation time of the qubit.
- The qubit encounters pure dephasing at a rate $\gamma_\phi = \frac{1}{T_\phi} = \frac{1}{T_2} - \frac{1}{2T_1}$, where $T_2 = \frac{1}{\gamma_2}$, with γ_2 the total dephasing rate.

Depending on the magnitude of the detuning $\delta = \omega_q - \omega_\mathrm{r}$ compared to g, we can distinguish two major modes of operation of the coupled system: the resonant and dispersive regimes.

Resonant regime

When $|\delta| \ll g$, the system is in the so-called resonant regime. In the strong coupling regime, *ie* when the coupling strength is greater than both the rate κ at which photons are lost from the resonator and the relaxation rate γ of the qubit ($g > \kappa, \gamma$), the system undergoes a coherent exchange at a rate $2g$ between a photon and an excitation of the qubit, a process called vacuum Rabi oscillations. Approximately $2g/(\kappa+\gamma)$ of such cycles are expected to occur before the system loses its coherence. With a loaded quality factor $Q = 10^5$, commonly achievable with a low-loss superconducting microwave coplanar waveguide resonator, $\kappa/2\pi \approx 0.1\,\mathrm{MHz}$. With a qubit of relaxation time $T_1 \approx 1\,\mu\mathrm{s}$, we obtain a relaxation rate $\gamma/2\pi \approx 1\,\mathrm{MHz}$. Thus with $g \approx 50\,\mathrm{MHz}$, the coherence is lost after ≈ 1000 vacuum Rabi oscillations.

When performing spectroscopy of the cavity while changing the frequency of the qubit (with an external magnetic flux), we observe an anti-crossing when $\omega_q \approx \omega_r$, which is the signature of the strong coupling (Fig. 2.11). The maximum splitting at resonance between both spectroscopy lines is given by $2g$.

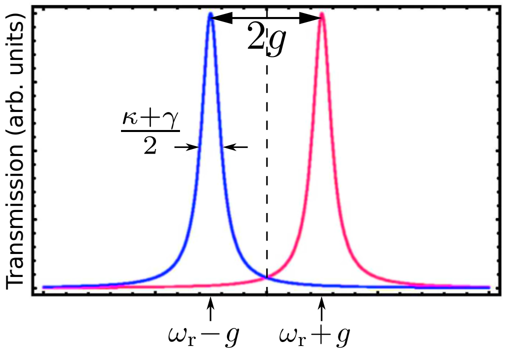

Figure 2.11: Measurement in the resonant regime. In the absence of qubit (with $\omega_q = \omega_r$) or with a coupling $g = 0$, the resonator transmission spectrum would be centered on the dashed line. We observe an anti-crossing when $\omega_q \approx \omega_r$ [22].

Dispersive regime

In contrast, when the detuning $|\delta| = |\omega_q - \omega_r|$ is large compared to g (dispersive regime), one can perform a unitary transformation of the Hamiltonian H and if we keep g/δ terms up to the second order only, we can write an effective Hamiltonian:

$$H_{\text{disp}} = \hbar \left[\omega_r + \frac{g^2}{\delta} \sigma_z \right] a^\dagger a + \frac{\hbar}{2} \omega_q \sigma_z. \tag{2.70}$$

From this Hamiltonian we note that the cavity frequency becomes qubit-state dependent and is given by $\omega_r \pm g^2/\delta$. The frequency shift of the cavity when the qubit state is changed from $|\Downarrow\rangle$ to $|\Uparrow\rangle$ is given by $2g^2/\delta$, a quantity called the *cavity pull*. This property can be used to read out the qubit state as will be described below.

Moreover, in the dispersive regime, the Hamiltonian describing the interaction between the field and the qubit has the form:

$$H_{\text{int}} = \frac{g^2}{\delta} \sigma_z a^\dagger a, \tag{2.71}$$

which commutes with the isolated qubit Hamiltonian ($[H_{\text{int}}, H_{\text{q}}] = 0$), thus enabling a quantum non-demolition measurement (QND) of the qubit state [22]. After a QND measurement, the qubit is projected onto the state which was measured implying that successive readouts yield the same result. This property is important in quantum information when an algorithm needs to leave the qubit in a controlled state after it is measured.

2.5 Qubit state readout

In the dispersive regime, the readout of the qubit state can be realized by sending microwave radiation into the cavity and probing either the transmitted or reflected signal. Indeed the amplitude and phase of the outcoming microwave signal carries information on the qubit state. This dispersive readout has the advantage of having low back-action on the qubit.

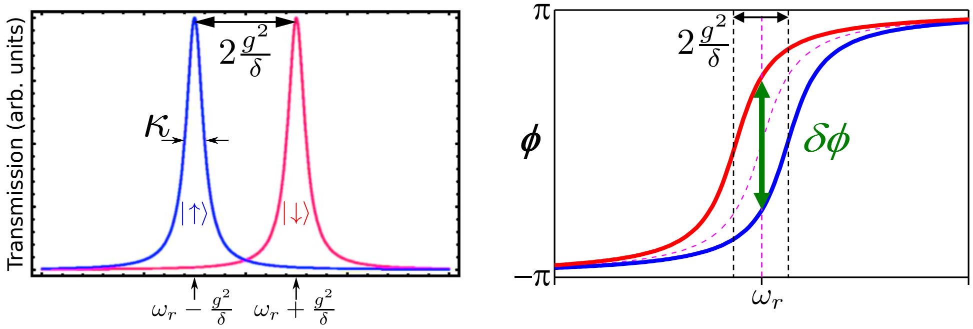

Figure 2.12: Measurement in the dispersive regime. (left) Qubit state dependent cavity transmission spectrum. The resonance is pulled by an amount $\pm g^2/\delta$, shown as red for when the qubit is in the excited state and blue for when the qubit has relaxed to the ground state. **(right)** Both qubits states yield transmitted phases ϕ that are measured with a homodyne scheme [22]. We define the readout contrast (in % of 2π) as the difference between the two S-curve at ω_r.

An example of transmission spectrum (amplitude and phase) in the dispersive regime is shown in Fig. 2.12. Sending a microwave pulse at frequency $\omega_r/2\pi$, the phases of the outcoming pulses when the qubit is in $|\downarrow\rangle$ or $|\uparrow\rangle$ will differ by an amount $\delta\phi$ proportional to $\frac{g^2}{\kappa\delta}$. The outcoming phases can be monitored by performing homodyne measurements. The larger $\delta\phi$ the better the discrimination between both phases encoding the qubit states and thus the larger the fidelity of the readout. A small detuning δ improves $\delta\phi$ but we should take care of remaining in the dispersive regime. A low cavity decay rate (or equivalently a large quality factor Q) should also improve the fidelity of the readout, however a large Q resonator requires a longer measurement time, time during which the qubit can relax, leading to a loss of fidelity. There is, therefore, an optimum value of Q that maximizes the fidelity of the dispersive readout.

Moreover, the dispersive measurement scheme can be used to read out simultaneously the states of several qubits coupled to the same resonator. In that case there as many cavity pulls as there are combinations of qubits states (2^m for m qubits). Such multi-qubit dispersive readout has been successfully demonstrated with 3 transmon qubits [62].

2.6 Qubit-qubit coupling using a cavity bus

Coupling of qubits using a cavity bus

The dispersive measurement scheme presented in section 2.5 can also be used to couple distant qubits placed along the same resonator, since the photons of the microwave probing signal can get entangled with the qubit state and mediate this interaction to other qubits. Figure 2.13 shows the layout of a resonator with two flux qubits where the effective qubit-qubit interaction Hamiltonian is expressed as:

$$H_{\text{int}} = \frac{g_1 g_2 (\delta_1 + \delta_2)}{2(\delta_1 \delta_2)} (\sigma_1^+ \sigma_2^- + \sigma_1^- \sigma_2^+), \tag{2.72}$$

where g_i is the coupling strength of qubit i to the cavity, and where $\delta_i = \omega_i - \omega_r$, with ω_i the frequency of qubit i.

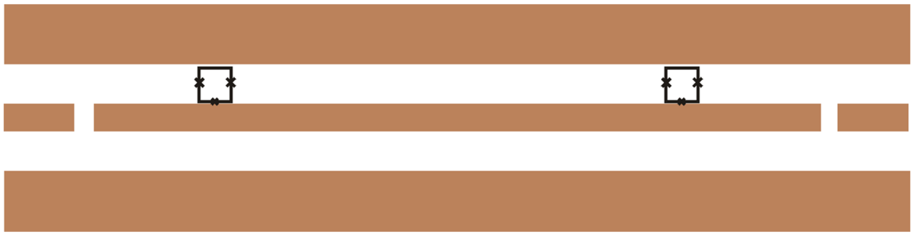

Figure 2.13: Schematic view of a coplanar waveguide layout with two flux qubits. The resonator acts as a quantum bus, enabling qubit-qubit coupling.

Two qubit gates using selective darkening of degenerate transitions

De Groot *et al.* [37] have recently introduced a method to selectively suppress one transition of a degenerate pair while coherently exciting the other, effectively creating artificial selection rules. It requires driving two qubits simultaneously with the same frequency and specified relative amplitude and phase. Although their experimental results were based on a system of two flux qubits coupled through mutual inductance [63], placed next to each other, their technique can directly be applied to other superconducting flux qubit.

The driving required can be described by the following Hamiltonian:

$$H_{\text{drive}} = a_1 \cos(\omega t + \varphi_1)\sigma_x^{(1)} + a_2 \cos(\omega t + \varphi_2)\sigma_x^{(2)}, \tag{2.73}$$

where ω is the driving frequency and a_i and φ_i are the driving amplitude and phase for qubit i [37]. This pulse scheme will be used with two distant flux qubits embedded in a CPW resonator. This Selective Darkening (SD) technique will be discussed in more details in Ch. 8 and experimental results from one device will be presented.

2.7 Decoherence of flux qubits

2.7.1 The formal description of decoherence

In this subsection we discuss the theoretical framework used to describe decoherence of a two-level system interacting with its environment. In the subsection 2.7.1.1 we present and briefly discuss the decoherence of a qubit interacting with a Markovian environment, a situation which is applicable to many relevant sources of decoherence in superconducting qubits. In subsection 2.7.1.2 we discuss decoherence due to low frequency noise, a situation highly relevant in the case of superconducting circuits for noise sources such as flux and charge noise.

2.7.1.1 Lindblad form

We consider a qubit interacting with its environment. Let us start with the system-bath model Hamiltonian:

$$\mathcal{H} = \mathcal{H}_{\text{qb}} + \mathcal{H}_{\text{qb-bath}} + \mathcal{H}_{\text{bath}}, \tag{2.74}$$

with $\mathcal{H}_{\text{qb}} = -\frac{\hbar\omega_{10}}{2}\sigma_z$ the qubit Hamiltonian, expressed in the energy eigenbasis with ω_{10} the transition frequency, $\mathcal{H}_{\text{bath}}$ the bath Hamiltonian, and $\mathcal{H}_{\text{qb-bath}}$ the qubit-bath interaction. The interaction Hamiltonian is assumed to take the form:

$$\mathcal{H}_{\text{qb-bath}} = Af, \tag{2.75}$$

with A a qubit operator and f a bath operator. We are interested in the evolution of the density operator ρ of the qubit, which is obtained from the density matrix of the combined qubit-bath system by partial tracing over the bath degrees of freedom. The evolution of the combined qubit-bath system is generally complex. An approximate solution can be obtained when the Markov approximation holds. Specifically it is assumed that the correlation time of the environment is short compared to the time scales of the qubit evolution induced by the bath. In the following we will state the main results without presenting a detailed derivation. A detailed discussion can be found in many quantum optics textbooks, see for example [64].

The evolution of the density matrix of the qubit is described the following *master equation*:

$$\dot{\rho}(t) = \Gamma_{1\to 0}\mathcal{D}[\sigma_-]\rho(t) + \Gamma_{0\to 1}\mathcal{D}[\sigma_+]\rho(t) + \frac{1}{2}\Gamma_\varphi\mathcal{D}[\sigma_z]\rho(t). \tag{2.76}$$

In the equation above the quantities $\Gamma_{1\to 0}$, $\Gamma_{0\to 1}$, and Γ_φ are decoherence rates the significance of which will be discussed in detail below. The symbols $\mathcal{D}[\hat{\sigma}_-]$, $\mathcal{D}[\hat{\sigma}_+]$, and $\mathcal{D}[\hat{\sigma}_z]$ denote superoperators, which change an operator (the density matrix in this case) into another operator. Specifically, these operators are written in the Lindblad form: given an operator σ, the superoperator $\mathcal{D}[\sigma]$ is defined by its action on the operator ρ in the following way:

$$\mathcal{D}[\sigma]\rho \to \sigma\rho\sigma^\dagger - \frac{1}{2}\sigma^\dagger\sigma\rho - \frac{1}{2}\rho\sigma^\dagger\sigma. \tag{2.77}$$

We discuss the evolution of the density matrix elements as induced by the master equation (2.76). The diagonal elements of the density matrix ρ_{00} and ρ_{11} are the probabilities to find the qubit in state 0 and 1 respectively. We will denote these elements by P_0 and P_1 respectively. The diagonal elements of the density matrix, ρ_{01} and $\rho_{10} = \rho_{01}^*$ are a measure of the coherence of a superposition of the ground and excited states.

The time evolution of the probabilities P_0 and P_1 is given by:

$$\frac{dP_0}{dt} = -\Gamma_{0\to 1}P_0 + \Gamma_{1\to 0}P_1 \tag{2.78}$$

$$\frac{dP_1}{dt} = -\Gamma_{1\to 0}P_1 + \Gamma_{0\to 1}P_0. \tag{2.79}$$

These equations indicate that $\Gamma_{0\to 1}$ ($\Gamma_{1\to 0}$) is the transition rate from the ground (excited) to the excited (ground) state. These rates are given by the following expressions:

$$\Gamma_{1\to 0} = \frac{1}{\hbar^2}|A_{10}|^2 S_f(\omega_{10}) \tag{2.80}$$

$$\Gamma_{0\to 1} = \frac{1}{\hbar^2}|A_{10}|^2 S_f(\omega_{01}). \tag{2.81}$$

Here $A_{10} = \langle 1|A|0\rangle$ is the matrix element of the qubit operator in the coupling Hamiltonian (2.75) and $S_f(\omega)$ is the spectral density of the environmental fluctuations at frequency ω. The frequency $\omega_{01} = -\omega_{10}$. The latter is defined as:

$$S(\omega) = \int_{-\infty}^{\infty} d\tau e^{i\omega\tau} \langle \hat{f}(\tau)\hat{f}(0)\rangle, \tag{2.82}$$

where $\langle ..\rangle$ denotes a quantum statistical expectation value over the thermal state of the bath.

The expressions (2.80) and (2.81) show that the transition rates of the qubit are connected with quantum fluctuations of the environment at the transition frequency of the qubit ω_{10} [2] and at its negative. The qubit relaxation/excitation is associated with absorption/emission of the energy by the environment. The relaxation and excitation rates are related by the detailed balance condition:

$$\frac{\Gamma_{0\to1}}{\Gamma_{1\to0}} = \frac{S_f(\omega_{01})}{S_f(\omega_{10})} = e^{-\frac{\hbar\omega_{10}}{k_B T}}, \tag{2.83}$$

with the last equality following from the properties of the spectral density function. This relation determines the following ratio between the steady state populations $P_{0,ss}$ and $P_{1,ss}$ in the steady state:

$$\frac{P_{1,ss}}{P_{0,ss}} = e^{-\frac{\hbar\omega_{10}}{k_B T}}, \tag{2.84}$$

which shows that the interaction with the environment results in a steady state distribution of the qubit given by the Boltzmann factors with the temperature T of the bath.

The steady state of the qubit, with probabilities given by (2.84), is reached with a rate $\Gamma_1 = \Gamma_{1\to0} + \Gamma_{0\to1}$. This rates determines the energy relaxation time $T_1 = \Gamma_1^{-1}$. At low temperatures the energy relaxation rate is determined primarily by the decay rate: $\Gamma_1 \approx \Gamma_{1\to0}$.

We next discuss the evolution of the coherences of the density matrix. Starting with (2.76), we find:

$$\dot{\rho}_{01} = -\left(\frac{\Gamma_1}{2} + \Gamma_\phi\right)\rho_{01}. \tag{2.85}$$

Here the pure dephasing rate Γ_ϕ is defined as:

$$\Gamma_\varphi = \frac{1}{\hbar^2}(|A_{11} - A_{00}|^2)S(0). \tag{2.86}$$

---

[2] In our type of devices, the qubit transition frequency ω_{01} is actually renormalized due to its dispersive interaction with the resonator, the Lamb shift it experiences due to its interaction with vacuum fluctuations and other environmental effect as well. Because this Lamb shift is small at the operating point of our devices, we can neglect it our treatment of decoherence.

The decay of the qubit coherence has a rate $\Gamma_2 = \Gamma_1/2 + \Gamma_\phi$, arising both from energy decay/excitation processes (Γ_1) and from processes occurring without exchange of energy with the environment (Γ_ϕ). The pure dephasing rate contains a factor, $A_{11} - A_{00}$, which describes the sensitivity of the qubit energy level difference to fluctuations of the operator f of the environment. The rate is proportional to the spectral density of fluctuations at zero frequency, indicating that no energy exchange takes place in pure dephasing.

2.7.1.2 Low frequency noise

In superconducting qubits we are often concerned with a situation in which the Hamiltonian of the qubit can be written in the following way:

$$H_{\mathrm{qb}} = -\hbar \frac{\omega_{10} + \xi(t)}{2} \sigma_z, \tag{2.87}$$

where ω_{10} is a fixed component of the energy level splitting and $\xi(t)$ is a random component. The latter is a classical stochastic process, which may result from a quantum environment, however, it has statistical properties which do not require a quantum mechanical description. If the noise process $\xi(t)$ has a short correlation time, the tools used in subsection 2.7.1.1 may be used to describe it. However, there are relevant situations when the noise process has a long correlation time, with flicker noise being a very well known example.

When dealing with classical noise, the effect on the qubit coherence can be dealt with in the following way. Assume that a superposition of energy eigenstates $\alpha|0\rangle + \beta|1\rangle$ is prepared. After a time τ this superposition evolves into $\alpha|0\rangle + e^{i\phi(\tau)}\beta|1\rangle$. The acquired phase $\phi(\tau) = \bar{\phi}(t) + \Delta\phi(\tau)$ contains a deterministic part $\bar{\phi} = -\omega_{10}\tau$ and a part due to the noise $\Delta\phi(\tau) = -\int_0^\tau \xi(t)dt$.

We describe the effect of the noise on the phase of a superposition using the coherence function $C(\tau) = \langle e^{i\Delta\phi(\tau)}\rangle$. Here the average $\langle..\rangle$ is taken over realizations of the noise process. The coherence function is a measure of the coherence of an ensemble. The ensemble can be formed from multiple quantum systems exposed to different realizations of the noise, or from a single qubit exposed to different realizations of noise a large number of times. The latter is the situation typically applicable to superconducting qubits. We note that the coherence function is connected to the off-diagonal element of the density matrix $\rho_{01}(\tau)$ of the ensemble. It can be shown that when the qubit is coupled both to an environment which induces the Markovian type decoherence as discussed in the previous section, with relaxation rate $\Gamma_{1,\mathrm{M}}$ and dephasing rate $\Gamma_{\phi,\mathrm{M}}$, the decay of the off-diagonal elements of the density matrix is given by:

$$\rho_{01}(t) = \rho_{01}(0)C(t)e^{-\left(\frac{\Gamma_{1,\mathrm{M}}}{2}+\Gamma_{\phi,\mathrm{M}}\right)}. \tag{2.88}$$

With independent knowledge of the Markovian relaxation and dephasing rates, the decay of the density matrix off-diagonal elements allows for determining the coherence function, which provides information on the noise process.

More generally, the application of a quantum control sequence to the qubit results decoherence described by the coherence function:

$$C_{\xi,s}(\tau) = \langle e^{i\int_0^\tau s(t)\xi(t)dt}\rangle. \tag{2.89}$$

Here $s(t)$ is a function related to the control sequence. Various control sequences are commonly used to characterized the decoherence of qubits, of which the two most common one are the Ramsey and the spin echo sequences (see also section 6.7.2 and section 6.7.3 of Ch. 6). For a Ramsey sequence (free induction decay) $s(t) = 1$. For a spin echo sequence, the function s is given by:

$$s(t) = \begin{cases} 1 & \text{if } 0 < t < \tau \\ 0 & \text{if } \tau < t < \tau + t_\pi \\ -1 & \text{if } \tau + t_\pi < t < 2\tau + t_\pi, \end{cases} \tag{2.90}$$

where t_π is the duration of the π pulse and τ is the duration of the free evolution periods before and after the π pulse (see Section 6.7.4 for more details).

An important type of noise process is the Gaussian noise. This type of noise process has the property that all the sampled distributions at defined time intervals are described by a multi-variate Gaussian distribution. For Gaussian noise, the coherence function can be expressed by:

$$C_{\xi,s}(\tau) = e^{-\frac{1}{2}\int_0^\tau dt_1 \int_0^\tau dt_2 s(t_1)s(t_2)\langle\xi(t_1)\xi(t_2)\rangle}. \tag{2.91}$$

By expressing the correlation function $\langle\xi(t_1)\xi(t_2)\rangle$ in terms of its Fourier transform $S_\xi(\omega)$, the coherence function can be expressed as:

$$C_{\xi,s}(\tau) = e^{-\int_{-\infty}^{\infty} d\omega S_\xi(\omega)F_{s,\tau}(\omega)}, \tag{2.92}$$

where the filter function is defined as:

$$F_{s,\tau}(\omega) = \frac{1}{4\pi}\left|\int_0^\tau dt s(t)e^{-i\omega t}\right|^2. \tag{2.93}$$

The filter function can be "designed" by changing the control function $s(t)$ which allows the study the spectral density of the noise, an aspect discussed in more detail when discussing the CPMG experiments (see Section 6.7.4 and Ch. 6).

2.7.2 Circuit quantum electrodynamics sources of decoherence

In this subsection we discuss the decoherence of a superconducting qubit coupled to a cavity. This source of decoherence is much better understood than other sources of noise, due to microscopic mechanisms. However, it is important to consider it due to the fact that it may have a significant or even dominant role in decoherence. Moreover, the ability to understand this source in quantitative detail is important in order to separate its effect against other sources.

Energy relaxation due to Purcell effect

Consider the dispersive regime of cQED. The ground state of the system is $|g0\rangle$, with g the qubit ground state and 0 the ground state of the resonator. The qubit-like first excited state of the system is given, in the rotating wave approximation, by $|e0\rangle - \frac{g}{\omega_{10}-\omega_r}|g1\rangle$. The resonator is in interaction with an environment which induces energy relaxation with a rate κ. A resonator energy relaxation process, which takes state $|1\rangle$ to state $|0\rangle$, will induce a transition between the qubit-like excited state and the system ground state, due to the hybridized nature of the excited state. Therefore, the qubit relaxes with a rate $\Gamma_1 = \left(\frac{g}{\omega_{10}-\omega_r}\right)^2 \kappa$, where the factor $\left(\frac{g}{\omega_{10}-\omega_r}\right)^2$ accounts for the admixture of resonator-like excitation in the combined system excited state.

The role of the Purcell effect has been verified in detail in numerous cQED experiments; a first detailed report of this effect is given in [15]. A distributed resonator may have multiple modes coupled to the qubit in a non-negligible manner. The total energy relaxation rate can be simply calculated by addition of energy relaxation rates induced by each mode. To ensure convergence of the total rate, the role of the mode-independent decay rate has to be taken into account [65].

2.8 Chapter summary

This chapter introduced different mathematical models and formulations for: Josephson junctions, persistent current flux qubit, coherent manipulation of qubits, superconducting transmission line resonators and coupling to qubits, dispersive readout of qubit in cQED, qubit-qubit coupling, and decoherence models of quantum systems. Designing a superconducting qubit device and interpreting the measured data accurately requires a good understanding of those models including their limitations.

Chapter 3

Experimental setup

In this chapter, the main aspects of the experimental setup are presented. Experiments are performed in a Leiden Cryogenics dilution refrigerator, model CF-650, in which the superconducting devices are cooled down to temperatures ranging between 20 and 40 mK. The qubits and the resonator are controlled with DC and microwave equipment at room temperature without appropriate filtering and amplification at both room and cryogenic temperatures. One of the difficulties in realizing experiments involving superconducting quantum devices, is to find the right balance between contradictory processes such as: protecting the device from electromagnetic (EM) sources and thermal noise while bringing microwave antennas a few microns away from the qubits, applying precise magnetic field to the device while isolating it from ambient magnetic field fluctuations and noise from the biasing setup, or cooling down the device close to absolute zero while bringing multiple semi-rigid coax cables and DC leads in its proximity.

Thanks to careful device and apparatus design, good electromagnetic interference (EMI) shielding and filtering, thermal leakage budget estimation, and cryogenic filtering, most of the adverse effects that would prevent the quantum devices from operating properly can be reduced to acceptable levels. What defines an acceptable level depends on the parameters of the device under test, such as, *e.g.*, the qubit and resonator operating frequencies. The following sections address the key elements of the design of the experimental setup, grouped in three main categories: the setup used for Josephson junctions (JJs) I-V measurements during the design and fabrication characterization phase of this work, the magnetic flux bias of the qubits and the shielding requirements for proper operation, and finally the microwave setup and sample holder which can be inserted while the dilution fridge is maintained at cryogenic temperatures.

3.1 I-V measurements

Before making full devices, the fabrication process of aluminium JJs was fine-tuned by measuring I-V characteristics of test devices at low temperatures. A simple sample box that can be mounted on the dilution fridge insertion probe was fabricated out of Oxygen-Free High-Conductivity (OFHC) copper. Silver varnish is used to thermally anchor the device to the copper sample box, and the device is wire bonded to a gold-plated printed circuit board (PCB), allowing 2 or 4-wire measurements. The cryogenic DC lines are filtered with 2-pole RC filters anchored at the mixing chamber plate. The mounting of this sample holder on the insertion probe allowed for relatively easy change and testing without warming up the whole fridge.

A custom battery powered low-noise voltage-controlled current source with a low-pass filter cutoff frequency below 10 Hz is used with a computer-controlled Yokogawa 7651 to bias the junctions. The voltage is measured using a battery operated low-noise voltage preamplifier SR560 and an Agilent 34401A 6.5 digit multimeter. In addition, a custom 24-channel breakout box with filtering was built to allow interfacing the apparatus to the probe's 24-pin connector. Great care was put into insuring the EMI shielding between the measuring equipment and the device, using a hermetically sealed box, π-filters and shielded twisted pair cables, minimizing possible ground loops and leakage.

3.2 Magnetic field biasing and shielding

This section discusses the magnetic flux biasing setup to control the qubits operating point as well as the strategies used for magnetic field shielding to protect the devices from lab environment AC field and slow background earth magnetic field drifts.

Any unwanted local magnetic field coupling to the qubit loop can affect negatively the dephasing of the qubits and the ability to operate the qubits at the desired operating point during long measurements. Due to their extreme sensitivity to ambient magnetic field, flux qubits need to be shielded from the ambient fluctuation of the magnetic field by the use of superconducting shields, higher permeability metal shields or a combination of both. In addition to passive shielding, active compensation techniques for the magnetic field fluctuations can also be implemented.

The following subsections present the requirements and implementation of the magnetic flux bias for a multi-qubit device as well as the passive and active shielding used in all the experiments of this work.

3.2.1 Magnetic flux biasing of superconducting flux qubits

As presented in Ch. 2, a flux qubit loop needs to be threaded by an applied magnetic flux in order to operate. When this applied flux is close to $\frac{\Phi_0}{2}$, the qubit is working near its degeneracy point, where the splitting Δ is usually tuned to be in the GHz range.

The device design we developed can accommodate up to four flux qubits on the same chip. Therefore, we implemented a magnetic field flux bias scheme based on one large coil and four small coils (see Fig. 3.1). With this arrangement, the qubits could be brought close to their symmetry point using the large coil, and furthermore, they could independently be controlled using the four additional small coils. The superconducting coil implementation and operation with a low-noise voltage-to-current bias source is described in the two following subsections.

Coil setup and assembly

Bias scheme and model. Given the unavoidable cross coupling between the various coils which are closely packed next to each other, we have to consider the full linear coupling model described for a single qubit and three coils, by:

$$\varepsilon_{\mathrm{qb}} = \mathrm{M}_0 V_0 + \mathrm{M}_1 V_1 + \mathrm{M}_2 V_2 + \varepsilon_{\mathrm{offset}} \tag{3.1}$$

where $\varepsilon_{\mathrm{qb}}$ is the magnetic energy of a flux qubit, $\varepsilon_{\mathrm{offset}}$ is due to the background magnetic field when no current bias is applied on any coil, V_i for $i \in \{0, 1, 2\}$ are the voltages set to control the current buffers biasing the superconducting coils, and M_i for $i \in \{0, 1, 2\}$ are the mutual coupling terms, which values are obtained with biasing one coil at a time and measuring each qubit's frequency. If we know the voltages and the resulting $\varepsilon_{\mathrm{qb}}$ for $n \geq 4$, *i.e.*

$$\left\{\varepsilon_{\mathrm{qb}}^{(i)}, (V_0^{(i)}), (V_1^{(i)}), (V_2^{(i)})\right\}_{i=1}^{n} \tag{3.2}$$

we can find the optimal values of the unknowns by evaluating:

$$\begin{bmatrix} \mathrm{M}_0 & \mathrm{M}_1 & \mathrm{M}_2 & \varepsilon_{\text{offset}} \end{bmatrix} = \begin{bmatrix} \varepsilon_{\text{qb}}^{(1)} & ... & \varepsilon_{\text{qb}}^{(n)} \end{bmatrix} \times \begin{bmatrix} V_0^{(1)} & ... & V_0^{(n)} \\ V_1^{(1)} & ... & V_1^{(n)} \\ V_2^{(1)} & ... & V_2^{(n)} \\ 1 & ... & 1 \end{bmatrix}^+ . \tag{3.3}$$

For the case of two qubits ($n = 2$) and three coils, as presented in this work, we find the M_{ij} and offset values by evaluating:

$$\begin{bmatrix} \mathrm{M}_{10} & \mathrm{M}_{11} & \mathrm{M}_{12} & \varepsilon_{\text{offset1}} \\ \mathrm{M}_{20} & \mathrm{M}_{21} & \mathrm{M}_{22} & \varepsilon_{\text{offset2}} \end{bmatrix} = \begin{bmatrix} \varepsilon_{\text{qb1}}^{(1)} & ... & \varepsilon_{\text{qb1}}^{(n)} \\ \varepsilon_{\text{qb2}}^{(1)} & ... & \varepsilon_{\text{qb2}}^{(n)} \end{bmatrix} \times \begin{bmatrix} V_0^{(1)} & ... & V_0^{(n)} \\ V_1^{(1)} & ... & V_1^{(n)} \\ V_2^{(1)} & ... & V_2^{(n)} \\ 1 & ... & 1 \end{bmatrix}^+ . \tag{3.4}$$

After this calibration procedure, all the parameters of this model are entered in the custom control software, which allows easy manipulation of the qubits operating point automatically.

Design and implementation of biasing coils The flux biasing was achieved using coils made of superconducting wires wound on an OFHC copper core. The superconducting wire used to wind the coils is a single filament NbTi wire (T48B-M wire family from Supercon Inc.) of 31 µm diameter in a copper matrix with a 1.5:1 copper to NbTi ratio forming a 50 µm wire, insulated with polyvinyl-enamel (Formvar) for an overall diameter of 66 µm. The copper cores' surfaces were finely deburred and polished to avoid any potential scratching of the insulation that could then lead to an electrical short. One possible counter measure to avoid such a problem is to apply a thin coat of epoxy on the copper core and cure it, before winding the wire.

Given the great number of turns necessary for winding the large coil, a custom winding machine was designed and built. Since the Formvar enamel can be removed by the solvents contained in the popular cryogenic varnish GE 7031, we used Stycast 1266 epoxy as a safer alternative. Due to its short pot life, some small amount of epoxy was carefully applied with a fine brush every couple layers of windings. Thanks to its low viscosity, it could permeate these layers, chasing the air that would have otherwise been trapped. This manual winding was done under a binocular to aid the guiding of the fine wire, avoid overlap, and permit a tight packing of the turns.

An additional length of the coil wire was kept to act as the superconducting leads, that could then run from the mixing chamber up to the 4 K plate where they would be electrically connected to the cryogenic leads coming from room temperature. However, since the single filament T48B-M wire is coated by a thin layer of copper, it was found to be a non negligible source of heating of the mixing chamber (a few mK).

A better approach was implemented for the set of coils mounted on the insertable probe that will be introduced later in this chapter in Sec. 3.4 and in more details in the next chapter. We made use of NbTi multifilament wire leads with copper matrix for the leads, but etched the copper at various locations to reduce thermal leakage to the mixing chamber stage. Indeed, the thermal conductivity of the superconducting wire core is negligible. Another set of leads was also implemented between the 4 K stage and the mixing chamber stage using a single core NbTi filament of 125 µm diameter with no copper matrix, and which was plated with rhodium at both ends to allow the soldering to the copper matrix fine superconducting wire of the coils, at the mixing chamber level. The superconducting leads are coiled with a few turns around a copper rod at each thermal stage and secured with Stycast 2850 epoxy.

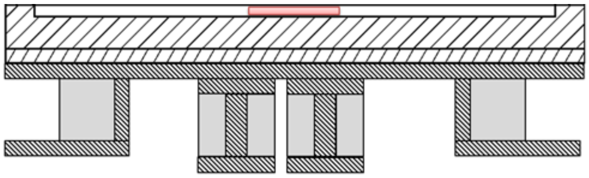

Figure 3.1: Bottom of sample holder and superconducting coils configuration cutout. The device location is represented in red. The coil windings are shaded in light grey. The dashed areas are copper parts.

Testing and possible improvements. After the epoxy curing, each coil were thermally cycled in liquid nitrogen a couple times and tested against electrical short circuits. The large coil was tested at about 25 mK for a few hours with a current bias of 70 mA, a current way above what was actually needed for the flux qubit area used in this work. No observable temperature increase was observed at this high current, confirming that the solder joint resistance was negligible.

To protect the dilution mixture from suddenly boiling off during a potential quench event of the coils, we soldered 50 Ω resistors in parallel with the coils at the solder joints of the 4 K plate. However the coil operations over 5 years proved to be reliable and a quench never occurred.

Fast current bias changes can lead to eddy currents in the copper sample holder and the coil copper core, leading to heat dissipation. For experiments requiring fast magnetic bias changes, it would therefore be advantageous to replace the copper core of the coils with one made of a good non-metal thermal conductor. Some coils core were cast with Stycast 1266 epoxy and further machined on a lath, maintaining good structural integrity and ability to be finely polished. Although no coils were effectively wound with it, we partially verified the feasibility of this approach.

Another strategy is to use a large coil for biasing globally the multiple-qubit device and use on chip local fast bias lines to fine tune the local DC field. To prevent any heating of the thermal plates of the dilution fridge and consequently the device, one would need to use a cryogenic bias tee so that the DC current would not dissipate too much energy if it had to pass through all the microwave attenuators and resistive coax cables of the microwave lines used to excite the qubits through this same flux bias line. Moreover, the printed circuit board and all metal interconnects may need to be superconducting to prevent large heat dissipation.

Current buffer for low-noise operation

Despite the low mutual inductance coupling between the coil and the qubit loops of our devices (0.65 pH between the large coil and the qubits loop and about 55 fH between the small coils and the qubits loop) it is important not to introduce spurious magnetic field noise due to a noisy current source that would be biasing these coils. To achieve this, while keeping the flexibility to perform computer-controlled current sweeps and have long term stable operation at a given bias point, the first approach would be to use a low-noise commercial current source like the Yokogawa 7651. It provides excellent accuracy, high resolution and stability. However, in he current mode, the low-frequency AC noise was found to contain an unacceptable level of 60 Hz noise and harmonics.

One could possibly implement a multiple pole filter to try to reduce these low-frequency components, but it was found to be more efficient to operate this DC source as a voltage source (with lower noise specifications) controlling a battery-operated voltage-controlled current source (that we'll call current buffer). This active circuit made of two low-noise operational amplifiers and a few passive components effectively acts as an active filter.

The circuit was realized by Zhenwen Wang from the Science Technical Service electronic group at the University of Waterloo. It consists of an OP27, a low-noise/offset/drift operational amplifier and an OPA602, a precision field-effect transistors (FET) operational amplifier with an extremely low input bias current (1 pA maximum). We choose Vishay precision wire-wound resistor MR100 family with 0.01 % tolerance and 10 ppm/°C temperature coefficient. The circuit works with 12 V lead-acid batteries[1] with enough capacity for a few weeks of operations between recharges.

The voltage control signals are fed to a hermetically shielded box with differential signals using BNC connectors and cables and the current signal is fed in a custom interconnection box with multiple differential channels which also contain pi-filters and ferrite beads. The signals are then fed to the dilution fridge 24-pin vacuum feedthrough with doubly shielded twisted pairs cables. The cryogenic resistive DC leads between the room-temperature stage and the 4 K plate, in series with the inductance of the superconducting leads and coils provide another level of intrinsic filtering.

3.2.2 Shielding

EMI shielding is inherently provided by the various layers of aluminium and copper thermal shields of the cryostat itself. The sample holder made of copper is also providing shielding against RF interference. However, low-frequency radiations and DC field fluctuation are not effectively absorbed or reflected by materials with a relative permeability close to 1. At 60 Hz the skin depth in aluminium is about 2 cm. Recalling that the skin depth is the depth at which the induced AC current density has fallen to $1/e$, from its maximum on the surface, we can conclude that it is preferable to have the induced AC currents fallen to a negligible amount (1 % or less) to prevent affecting the device in the sample space. For the previous example with (normal state) aluminium shields, this would require a 5 to 6 cm wall to protect the device, which is impractical.

The laboratory being in proximity to other dilution fridges and ESR experiments with high Tesla magnets, it is therefore necessary to also devise a way to be immune to the field sweeps that occur during our measurements. The magnetic field of the earth also fluctuates throughout the day and night, up to a few hundreds nT in the z-axis of interest (given the orthogonal orientation of the flux qubit loop).

---

[1] For this type of sensitive apparatus, it's always desirable to choose the battery technology with the lowest internal resistance for the required capacity (a few mΩ at nominal operating conditions), that results in the lowest associated voltage noise.

In this work, we use multi-layer high permeability cryogenic circular shields as well as an active compensation system to maintain a stable DC background field.

Passive shielding

The cryogenic shield is composed of three stacked cylindrical shells made from 1 mm thick sheets of low-temperature Cryoperm® 10. It consists of a nickel iron alloy heat treated in hydrogen to obtain optimal shielding characteristics at low cryogenic temperatures. The relative permeability μ_r at DC is about 30000 at 4 K, and about 70000 at 50 Hz for a 1 mm thick sheet. The useful sample space bounded by the most inner layer is of about 75 mm diameter for an effective height of 280 mm. The overall diameter of the structure is 136 mm with an overall height of 310 mm. The multi layer shield is open at the top to allow the insertion of the sample probe described in more details in the next chapter. An additional device can be placed at the bottom of the shield.

Due to this open design, the shielding factor is reduced since the magnetic field can re-enter from the top. The shielding factor profile due to an ambient vertical z-component magnetic field (set to 50 µT) was computed with the finite element (FEM) numerical solver COMSOL Multiphysics$^{®}$ for this structure. At the partial depth inside the shield where the sample holder inserted with the probe, the shielding factor in the axial direction is about 50. At the depth inside the shield where the fixed sample holder is located (a few inches below the probe one) the shielding factor is about 1500.

This design could be greatly improved in the future by designing an insertion probe sample holder that would contain a cryogenic high mu metal top “hat” to result in a somewhat closed shield design. Indeed, with sufficient metal to metal overlap, a box with cover shield design can perform almost as well as a fully closed box.

Active shielding

Model. Figure. 3.2 presents the model considered in the design of a simple magnetic field compensation system using only one sensor placed in proximity of the qubit device while remaining outside the fridge and at room temperature, and a compensation coil on the outside of the fridge. The figure does not show the superconducting coils placed just below the device which provide flux bias at the desired operating point from which we do not want to deviate over time scale of

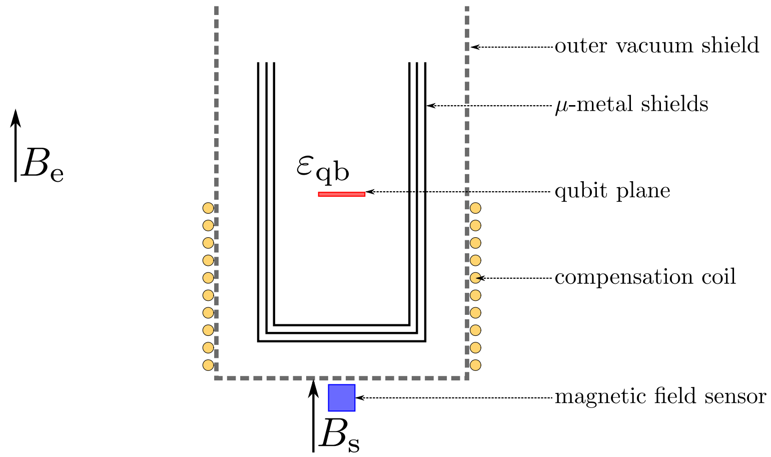

Figure 3.2: Magnetic field compensation model. B_e is the z-component of the ambient magnetic field of the lab and B_s the field measured by the sensor, the linear superposition of B_e and the field generated by the compensation coil (as well as the local disturbance of of the ambient field due to the proximity of the high μ-metal shields).

many hours preferably. Let B_e be the external magnetic field present in the vertical direction. We assume B_e to be uniform in the lab environment and its fluctuations are due to sources that are far away from the qubit. In the absence of current in the compensation coil, the sensor placed below the outer vacuum shield of the cryostat measures $B_s = B_e$. We neglect the possible deformation of the magnetic field at the sensor due to the proximity of the cryogenic high mu-metal shields or other ferromagnetic objects outside the dilution fridge. B_s also measures the magnetic field created by the coil when biased by a current I_{coil} and is linearly related to it by a constant β_{sc}. We neglect the potential field generated by the small superconducting coils placed below the flux qubits device leaking through the shields. Let the magnetic bias of the qubit $\varepsilon_{qb} = \sqrt{\nu_{qb}^2 - \Delta^2}$, be linearly related to a change in the remnant external magnetic field not attenuated by the cryogenic shields by a constant α_{qe}, as well as dependent upon the compensation current through the coil by a constant β_{qc}. We can therefore write the above relation in the following matrix form:

$$\begin{bmatrix} B_s \\ \varepsilon_{qb} \end{bmatrix} = \begin{bmatrix} 1 & \beta_{sc} \\ \alpha_{qe} & \beta_{qc} \end{bmatrix} \times \begin{bmatrix} B_e \\ I_{coil} \end{bmatrix} \tag{3.5}$$

and proceed with the extraction of the unknown coefficients with some simple measurements.

- β_{sc}: while B_e is stable, *i.e.* over a short time scale, sweep the current in the coil from 0 to

$\pm 100\,\mathrm{mA}$ and record B_s. Extract the slope β_sc.

- α_qe: with no current in the coil, record the qubit frequency ν_qb with spectroscopy measurements and B_s while B_e changes during a superconducting magnet sweep up to $6\,\mathrm{T}$ located in an adjacent lab about fifteen meters away (measured as a change of $\sim 250\,\mathrm{nT}$ at the sensor). Extract the slope α_qe.
- β_qc: while B_e is stable, sweep the current in the coil and record the qubit frequency ν_qb with spectroscopy measurements. Extract the slope β_qc.

Implementation. The compensation system is implemented using a computer-controlled low-noise 24-bit ADC/DAC with a simple PID algorithm, which acquires the voltage output of the magnetic field sensor and generates a compensation voltage output which controls a current buffer biasing the coil. The sensor used is a 3-axis Bartington MAG-03MSES500 with internal noise of 7-10 $\mathrm{pT_{rms}}\ /\sqrt{\mathrm{Hz}}$ at $1\,\mathrm{Hz}$, of which only the z-axis is used. The current buffer module and the sensor are both battery operated to minimize spurious noise. The batteries only need to be recharged about once every two weeks at a time when the sample is not being measured. The output of the magnetic field sensor is averaged over ten $60\,\mathrm{Hz}$ cycles, which limits the overall speed of the compensation system but improves the noise level. This system is well suited for slow fluctuations in the ambient field.

For a true AC compensation system capable a mitigating $60\,\mathrm{Hz}$ and higher harmonics, a higher bandwidth analog implementation of a PID controller would be preferred. Using a larger coil, or a Helmholtz or Maxwell coils configuration would be preferred to improve the field uniformity. The current system performance was, however, deemed satisfactory and allowed many hours measurement runs without needing to readjust the local flux biasing of the two qubits when operated close to their symmetry point.

A future improvement on this implementation could make use of an in situ SQUID-based magnetic sensor placed inside the sample space instead of the external magnetic field sensor. The magnetic coil feedback could be applied directly to the superconducting coil rather than an external coil like shown in Fig. 3.2.

3.3 Microwave setup

This section discusses on the equipment needed for the microwave control and readout of the resonator and qubits system as well as on how the sample was interfaced with the cryogenic microwave lines. We can simply classify the microwave signals in two categories: inputs and outputs of the device. The input lines are heavily attenuated and filtered to minimize the noise from the room temperature equipment and cables. The output line contains both cryogenic and room temperature amplifiers to increase the signal, carrying information about the qubit and resonator.

3.3.1 Room-temperature equipment

Figure. 3.3 shows a detailed schematic of the experimental setup. The chip containing two flux qubits and a coplanar waveguide resonator is enclosed in a copper box, which is placed inside a three-layer high permeability metal shield (Sec. 3.2.2). An active magnetic field compensation system placed outside the cryostat is used to further reduce slow drifts of the ambient magnetic field (Sec. 3.2.2). A set of superconducting coils is attached to the device copper box, and used to provide independent magnetic flux biases to the two qubits. The coils are supplied by custom-designed ultra-stable voltage-to-current converters, each controlled by a Yokogawa 7651 voltage source (Sec. 3.2.1).

Each qubit is individually controlled using shaped microwave pulses that are generated using a microwave synthesizer Agilent PSG E8257D, an arbitrary waveform generator Tektronix AWG5014, and a Marki IQ-0318 (IQ-1545) mixer for qubit 1 (2). To further reduce microwave leakage to the qubit during coherent state evolution or qubit ground state initialization, each microwave synthesizer is isolated from the corresponding mixer by a Hittite HMC-C058 switch which provides an isolation $\geq$65 dB up to 6 GHz, and $\geq$50 dB up to 18 GHz. Agilent 8495H programmable step attenuators are used to adjust the pulse amplitude over a wide range. A band pass filter (BPF) in each control line is used to suppress low-frequency noise and spurious harmonics, which are detrimental to qubit coherence, and to prevent cavity excitation.

Qubit state measurement is done using dispersive readout [66], by measuring the transmission of microwave pulses through the resonator, using a custom built setup.

The readout pulses are generated in a similar fashion to the qubit control pulses, using a Phase Matrix QuickSyn FSW-0010 microwave synthesizer, a LeCroy AWG-1104 arbitrary waveform

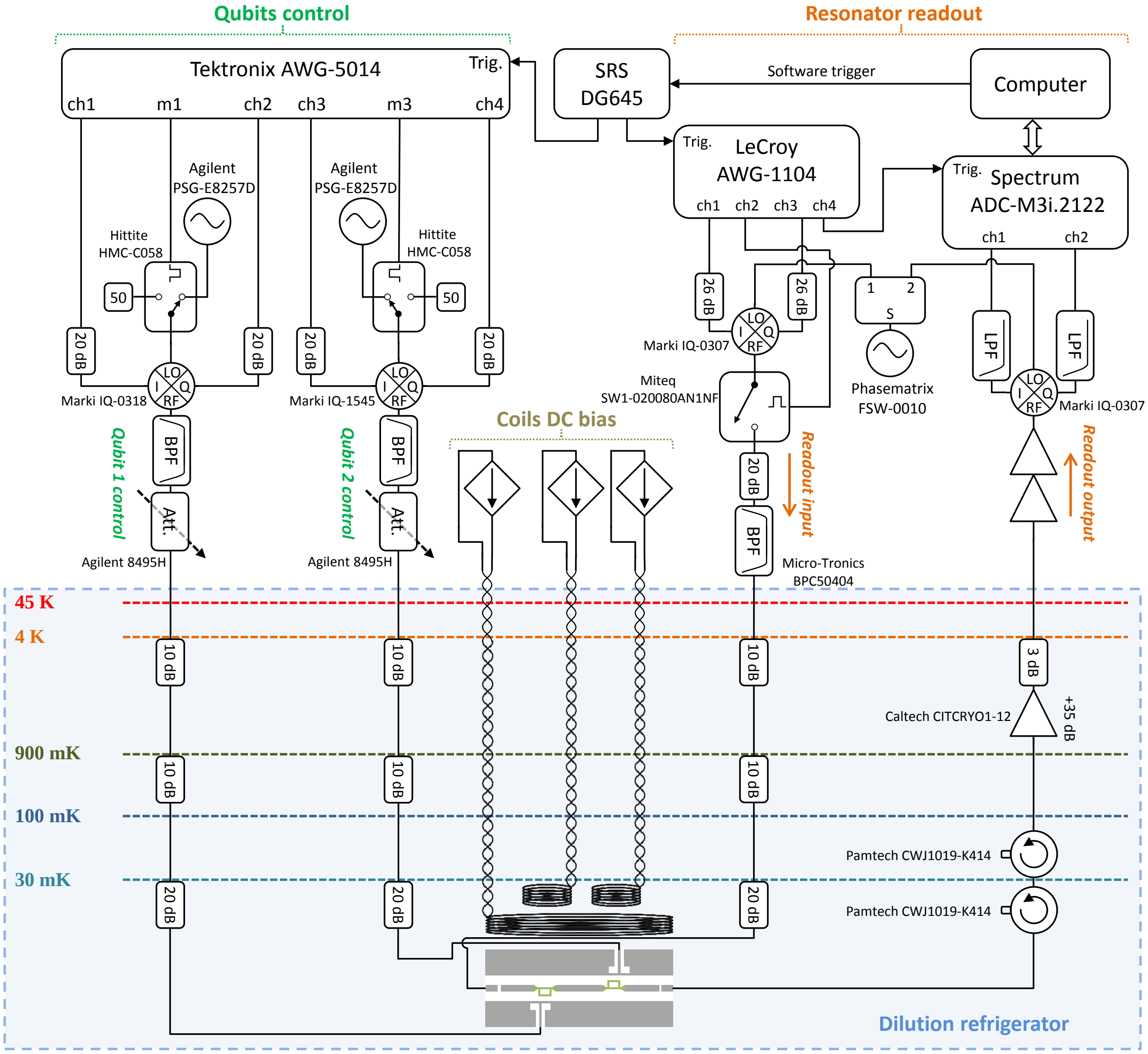
Qubits control
Resonator readout
Tektronix AWG-5014
Trig.
ch1
m1
ch2
ch3
m3
ch4
SRS
DG645
Software trigger
Computer
Trig.
LeCroy
AWG-1104
ch1
ch2
ch3
ch4
Trig.
Spectrum
ADC-M3i.2122
ch1
ch2
Agilent
PSG-E8257D
Agilent
PSG-E8257D
Hittite
HMC-C058
Hittite
HMC-C058
50
50
20 dB
20 dB
20 dB
20 dB
LO
I
Q
RF
Marki IQ-0318
Marki IQ-1545
26 dB
26 dB
Marki IQ-0307
1
2
S
Phasematrix
FSW-0010
LPF
LPF
Marki IQ-0307
Miteq
SW1-020080AN1NF
Coils DC bias
Qubit 1 control
Qubit 2 control
BPF
BPF
Att.
Att.
Agilent 8495H
Agilent 8495H
20 dB
BPF
Readout input
Readout output
Micro-Tronics
BPC50404
45 K
4 K
900 mK
100 mK
30 mK
10 dB
10 dB
20 dB
3 dB
Caltech CITCRYO1-12
+35 dB
Pamtech CWJ1019-K414
Pamtech CWJ1019-K414
Dilution refrigerator

Figure 3.3: Detailed schematic of the experimental setup. The description is given in the text.

generator, a Marki IQ-0307 mixer, and a Miteq switch model SW1-020080AN1NF. The readout input line is filtered by a 6-10 GHz band pass filter from Micro-Tronics, model BPC50404. The readout output signal is amplified using cryogenic (see next Sec. 3.3.2) and room-temperature amplifiers. After demodulation [58], done with another Marki IQ-0307 mixer, the quadratures of the readout output pulse are sampled using a Spectrum M3i.frm-e122 digitizer. A Stanford Research Systems digital delay generator DG645 controls the synchronization of the arbitrary waveform generators and digitizers.

3.3.2 Low-temperature equipment

All the transmission lines inside the cryostat are coaxial lines made of either beryllium copper or stainless steel between room temperature and the 4 K plate, stainless steel between the 4 K plate and the mixing chamber plate (for the input lines), copper for all the lines coupling the various modules anchored to the mixing chamber plate, or superconducting niobium titanium for the output of the resonator between the mixing chamber and the 4 K plate where the low noise cryogenic amplifier is located.

The appropriate choice of cable material and dimensions depends on the heat leakage and microwave attenuation properties that the user needs to achieve considering the number of signals that need to interface with the coldest stage, and the relatively limited cooling power of a typical dilution refrigerator (a few µW at about 10 mK). Calculations and estimations are done with the help of good cryostat design and low-temperature books such as the ones by Ekin [67] and Pobell [68].

Custom copper thermal clamps bypass the heat flow to the respective plate of the dilution refrigerator to which it is attached. Microwave attenuators compatible with cryogenic operation from XMA are inserted in the microwave lines at the various thermal stages. They provide a fixed attenuation of the signal which reduces the amount of noise. In addition, they provide a heat conduction path between the center and outer conductor of the coaxial cable. The center conductor of the coaxial lines would otherwise only be cooled down through imperfect thermal interfaces with the Teflon dielectric and coaxial conductors. Microwave components, connectors and cable are chosen in their non magnetic version whenever possible.

The output line of the resonator contains two Pamtech CWJ1019-K414 isolators thermally anchored at the mixing chamber plate to minimize the noise coming from the cryogenic amplifier input located at the 4 K stage. The low-noise high electron mobility transistor amplifier used is a Caltech CITCRYO1-12 with a relatively flat gain of 35 dB between 1 and 12 GHz with an equivalent noise temperature of only 4.5 K around 6 GHz.

3.3.3 PCB and sample holder

The measured device is interfaced with the microwave coaxial lines described in the previous sections with a microwave compatible PCB, housed in the copper sample holder. The microwave ceramic substrate is made of Rogers laminate TMM10i (about 500 µm thick) with an ϵ_r of about 9.9, close to the value of silicon. The microwave CPW traces and ground planes are defined on both sides of the substrate, and vias connects both top and bottom ground planes to minimize spurious parallel plate and strip line modes. The PCB and sample holder round shape and dimensions are chosen so that it could fit in the 50 mm opening of the insertion probe system introduced in the next section.

The metal traces of the PCB are also gold-plated with a non-magnetic high-purity soft gold to prevent oxidation of the copper trace over time, and allow a reliable wire bonding of the device to the microwave lines. A wedge bonder is used to connect the device to the PCB using 1.2 mils diameter aluminium (with 1 % Silicon) wire. A pocket is machined in the center of the PCB to

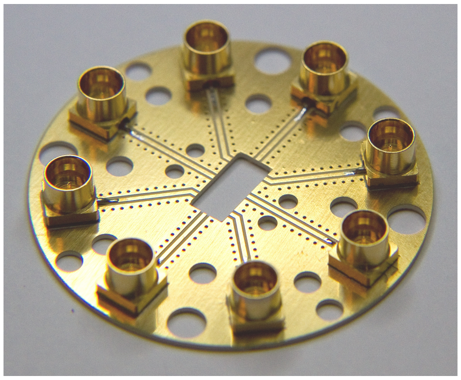

Figure 3.4: Connectorized PCB. Microwave board with a 35 mm diameter used for the packaging of the 3 mm x 7 mm diced samples. It is made from a microwave Rogers TMM10i substrate, with 500 µm thickness, and is metalized on both side with 1 oz. electroplated copper which was then gold plated. 8 SMP connectors are soldered to the 50 Ω coplanar waveguides.

allow the device to be glued with silver varnish or a small amount of PMMA A2 resist to the copper sample holder on which the PCB is screwed on. The eight 50 Ω coplanar waveguide lines of the PCB are connectorized with right-angle SMP connectors from Rosenberger as shown in Fig. 3.4. The sample holder cover design is presented in more details in the next chapter.

An additional copper cover was affixed above the sample space in order to suppress box resonance modes in the frequency range of operation of the device. Figure 3.5 shows the assembly of the PCB, the bottom part of the sample holder and the added copper part before attaching the top cover. The addition of this copper part also helped in removing an artifact observed in the transmission curve around the resonance of a high-quality factor resonator which expressed itself as an asymmetric resonance peak instead of the expected Lorentzian shape.

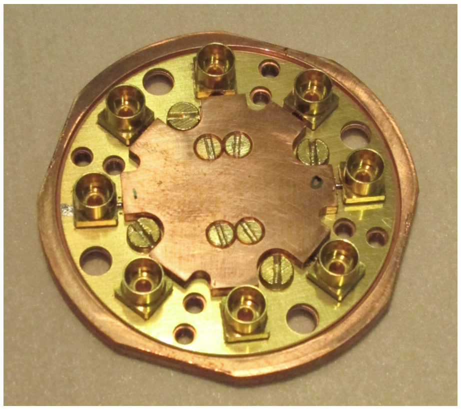

Figure 3.5: Bottom of sample holder with additional copper cover. The additional copper cover mounted on top of the PCB and wire-bonded device is used to suppress box resonances. ('I' and 'O' indicate the input and output of the resonator device).

3.4 Insertable probe

The majority of the work reported in this thesis was performed using an insertable probe. It allowed rapid device swap by bypassing the need to warm-up and cool down the entire cryostat. The insertable probe also proved to be very useful when needing to thermal cycle a device between 30 mK and 4 K, for example, or find a good working device with multiple qubits with frequencies in the desired range from a single fabrication batch. Figure. 3.6 shows the probe on the workbench ready to be inserted into the dilution refrigerator. This system, its design and structure, as well as its operation are described in greater details in the next chapter, Chap. 4.

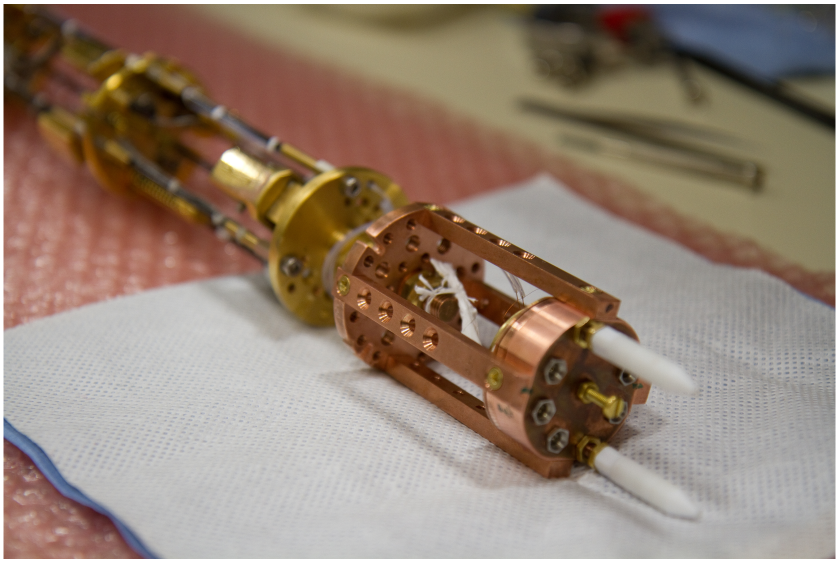

Figure 3.6: Insertable probe with sample holder. View of the insertable probe with the sample holder and coils on the workbench.

3.5 Chapter summary

In this chapter we presented the main elements of the experimental setup used to study superconducting devices comprised of a planar resonator and flux qubits. To give a better feeling to the reader of what such an experimental setup, as presented schematically in Fig. 3.3 with its sub-components introduced in this chapter, looks like, Fig. 3.7 shows a picture of the laboratory with the top-loading probe inserted and with all the necessary equipments mounted on racks. On the left, the DC rack, and on the right the two microwave racks, with the instruments required to control up to two qubits (with one extra AWG unused in the picture).

All this equipment can support the operation of a chip with two qubits (up to four supported in the layout). Moving forward, with the goal of integrating more qubits on a single chip, it becomes obvious that such experimental efforts will require significant work in optimizing the

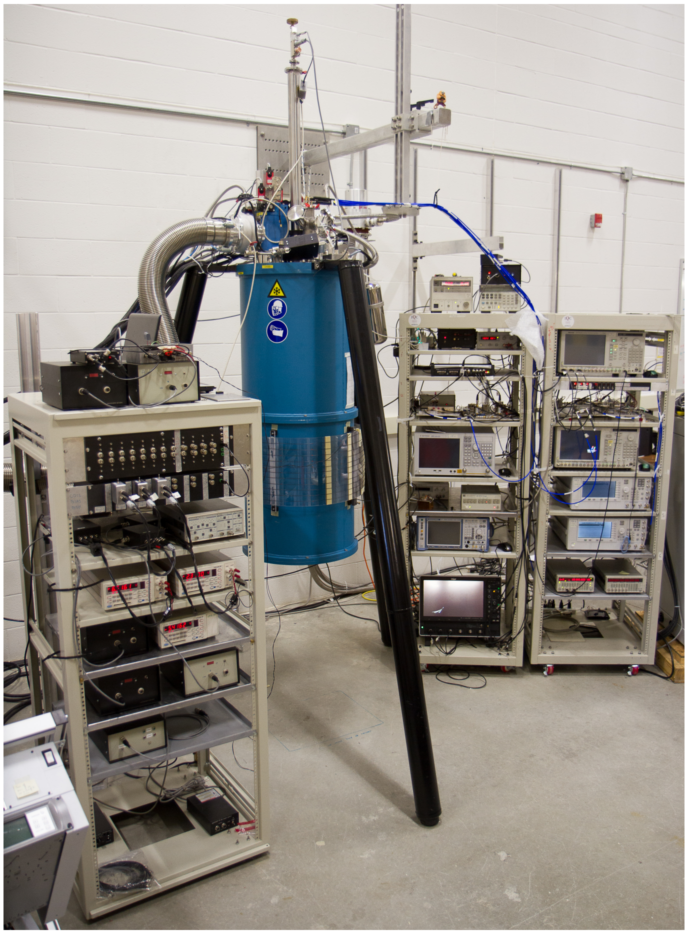

Figure 3.7: Experimental setup. General view of the experimental setup developed in this work with the DC rack on the left of the fridge and two microwave racks on its right. The probe is inserted in the dilution fridge with a device, and the magnetic field compensation system's coil can be seen warped around the blue outer vacuum shield of the unit.

room temperature and cryogenic apparatus, which, for now, represents a large fraction of the cost involved in such an experiment. This can be achieved by creating custom microwave hardware with a smaller footprint, covering only the necessary frequency range needed for the quantum processor being operated, and sharing identical resources rather than duplicating it in each individual piece of equipment (stable clock generation for example).

Chapter 4

Insertable system for fast turnaround time microwave experiments in a dilution refrigerator[1]

This chapter presents some preliminary results on resonator and flux qubit measurements that were used to verify the validity of the setup and its proper operation for further characterizing flux qubit devices.

We acknowledge Harmen Vander Heide, Andrew Dube and Michael Lang from Science Technical Services at University of Waterloo for help with design and realization of the mechanical assembly. We also acknowledge Mustafa Bal and Chunqing Deng for acquiring the preliminary data on qubit measurements using this setup.

---

[1] The content of this chapter, after this preamble, is reproduced from: Florian R. Ong, Jean-Luc Orgiazzi, Arlette de Waard, Giorgio Frossati, and Adrian Lupaşcu. Insertable system for fast turnaround time microwave experiments in a dilution refrigerator. *Rev. Sci. Instrum.*, 83(9):093904, sep 2012. doi: 10.1063/1.4754634. URL `https://aip.scitation.org/doi/10.1063/1.4754634`. Copyright 2012, AIP Publishing LLC, with the permission of AIP Publishing.

4.1 Introduction

A growing variety of experiments requires the combination of ultra-low temperatures (below 100 mK) and the application and detection of electrical signals with bandwidth as large as tens of GHz. These experiments cover a wide area of research, including quantum computing with solid-state devices [9, 69], quantum optics on chip [70], development of quantum limited amplifiers [71, 72, 73, 74], nanoelectromechanical resonators [75, 76, 77], fundamental transport phenomena in mesoscopic devices [78, 79, 80], and broadband microwave spectroscopy in Corbino geometry [81]. The combination of millikelvin temperatures and microwave frequencies arises naturally when studying mesoscopic physics in solid-state systems. On the one hand quantum effects typically become relevant at low temperatures. Examples include collective behaviour in superconductors [82], or the increase of the electronic coherence length beyond system size in mesoscopic systems [83]. On the other hand microwaves are needed to probe relevant energy scales, such as the plasma frequency in Josephson junctions [9], or the charging energy and Zeeman splitting in semiconducting nanostructures [78, 84]. Furthermore, lowering the temperature T down to a regime where $k_{\mathrm{B}}T \ll h\nu$, where k_B is the Boltzmann constant, h is the Planck constant and $h\nu$ is the energy gap from the ground to the first excited state of the quantum system, enables preparation of the ground state and results in optimal coherence [61].

The research areas enumerated above require that a mesoscopic device is placed in a dilution refrigerator. Preparation of the cryostat for cooldown (installation of vacuum cans and radiation shields, pumping of large volumes) and the actual cooldown to millikelvin temperature take, depending on the configuration of the system, a time varying between half a day and three days. To warm up the system and then replace the device, an additional time of a few hours to a day is needed. Combining a cold insertable probe developed by Leiden Cryogenics [85] and a new type of sample connection system we were able to reduce these overhead times dramatically. The turnaround time, defined here as the minimum time needed to measure two successive devices at 80 mK, is reduced to 8 hours. This method has a significant impact on experiments which require multiple device testing.

4.2 Experimental setup

In this section we present the experimental setup, which builds on a cryogen-free dilution refrigerator type CF-650 and a cold-insertable probe, both available from Leiden Cryogenics [85].

4.2.1 Dilution refrigerator with cold-insertable probe

The dilution refrigerator CF-650 has the following basic characteristics. The cooling power is 650 µW for an operation temperature of 120 mK. The base temperature, without experimental wiring installed, is 12 mK. After the installation of wiring for our experiments, the lowest temperature reached at the mixing chamber is 20 mK. Three line-of-sight access ports with a 50 mm diameter run through the inner vacuum can (IVC) from the top plate down to below the mixing chamber. One of them can be used to fit a 2 meter long cold insertable probe (see Fig. 4.1). The thermalization of the probe is achieved by a mechanism in which anchoring clamps attached to the successive probe stages are brought into contact with the fixed plates of the refrigerator at different temperatures. To establish contact, the anchoring clamps are moved sideways using a knob at the top of the probe.

The Leiden Cryogenics insertable probe comes with a loadlock chamber that can be clamped on any of the three IVC access ports (Fig. 4.1.a). Apart from thermometry related wires, the probe is fitted in its standard configuration with a set of twelve twisted pair wires which can be used for low-frequency electrical measurements. It is possible to add more wires. However, the addition of transmission lines is only possible to a limited extent. The reason is that a coaxial cable has a diameter of the order of millimeters for reasonably low attenuation at high frequencies. Coaxial connectors, filters and attenuators occupy an even larger space. An even more severe problem occurs for experiments involving low-noise microwave measurements, which require the installation of circulators/isolators and amplifiers. These packaged components have a bulky profile which could not fit in the space allowed by the probe. While a larger probe diameter is possible, such a design would make manipulation more difficult and also would lead to increased heat leakage. An additional problem is the fact that microwave amplifiers dissipate a significant amount of heat (typically 1-100 mW), and therefore are less efficiently thermalized when mounted on the insertable probe than when thermally anchored to one of the cold plates in the refrigerator.

Motivated by the difficulties enumerated above with adding transmission lines on the cold insertable probe we introduce a method for sample insertion explained in the next subsection.

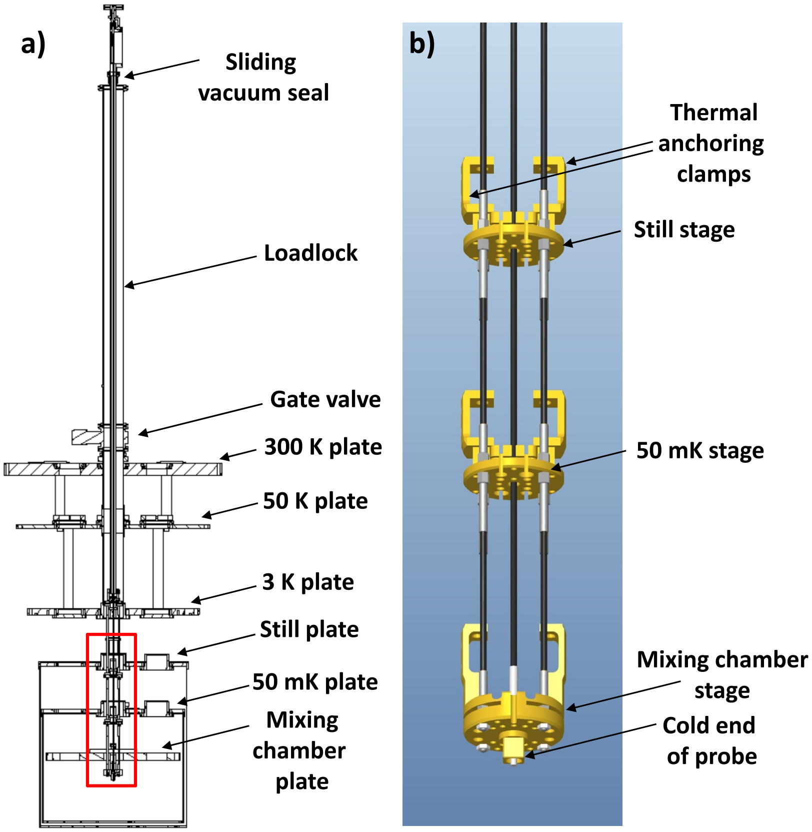
a)
Sliding vacuum seal
Loadlock
Gate valve
300 K plate
50 K plate
3 K plate
Still plate
50 mK plate
Mixing chamber plate
b)
Thermal anchoring clamps
Still stage
50 mK stage
Mixing chamber stage
Cold end of probe

Figure 4.1: Section view of the CF-650 refrigerator and its insertable probe. a) General view of the system. **b)** Close-up view of the low-temperature parts of the probe, corresponding to the red rectangle in panel a).

4.2.2 Fixture for guided insertion of sample holder and coupling to microwave lines

Figure. 4.2 shows a drawing of the insertion system, consisting of two mechanical assemblies. The top assembly is attached to the cold end of the insertable probe (Fig. 4.1.b) and thus is mobile. It holds the sample holder to be cooled down. The bottom assembly is attached to the mixing chamber of the refrigerator. The top and bottom assemblies are electrically interconnected by an arrangement of SMP adapters [86] (cf Fig. 4.3.a) including spring connectors (so-called bullets). The latter allow for slight misalignment without impairing microwave properties. All the

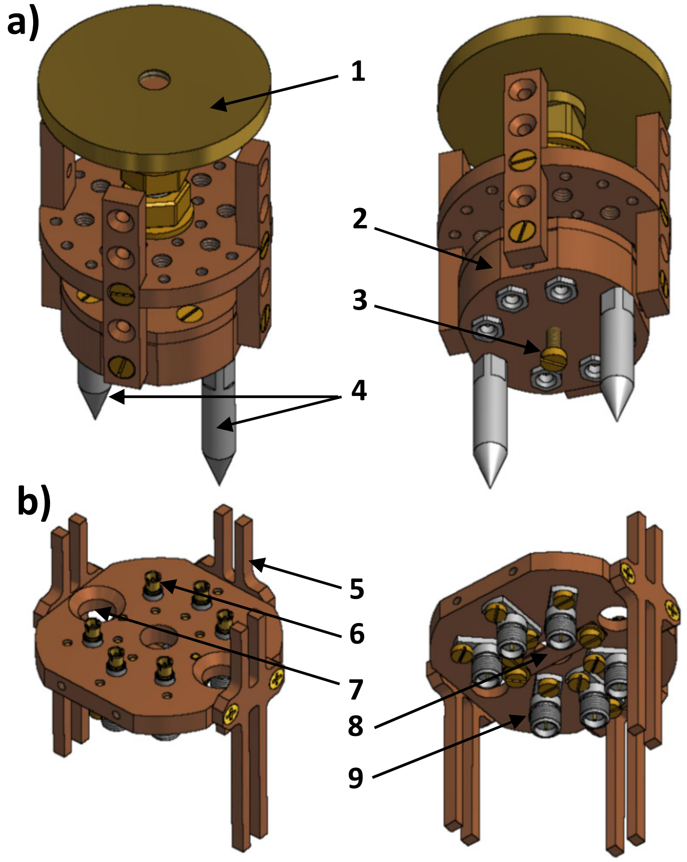

Figure 4.2: Drawings of the mechanical assemblies, seen from two point of views. The top assembly **a)** is attached to the end of the insertable probe, while the bottom assembly **b)** is permanently fixed to the mixing chamber of the refrigerator. 1: cold end of probe. 2: sample holder. 3: stopper. 4: Teflon guiding rods. 5: rails, height adjustable with respect to the mixing chamber. 6: SMP-SMP adapter ("bullet"). 7: guiding hole. 8: beryllium copper strip. 9: SMP-SMA adapter.

metallic parts are machined from OFHC copper for optimal thermalization. The temperature of the inserted device is measured using a calibrated 100 Ohm SPEER carbon resistor thermometer thermally anchored to the cold end of the probe. The sample holder and its fixture to the cold end are machined out of OFHC copper, ensuring good thermalization.

The transmission lines used in the experiments run from the top plate of the refrigerator (where they are fed into the IVC using vacuum feedthroughs) down to the mixing chamber plate. They are mechanically attached to all the refrigerator plates for proper thermal anchoring. The lines are terminated by SMA microwave connectors plugged to the bottom mechanical assembly.

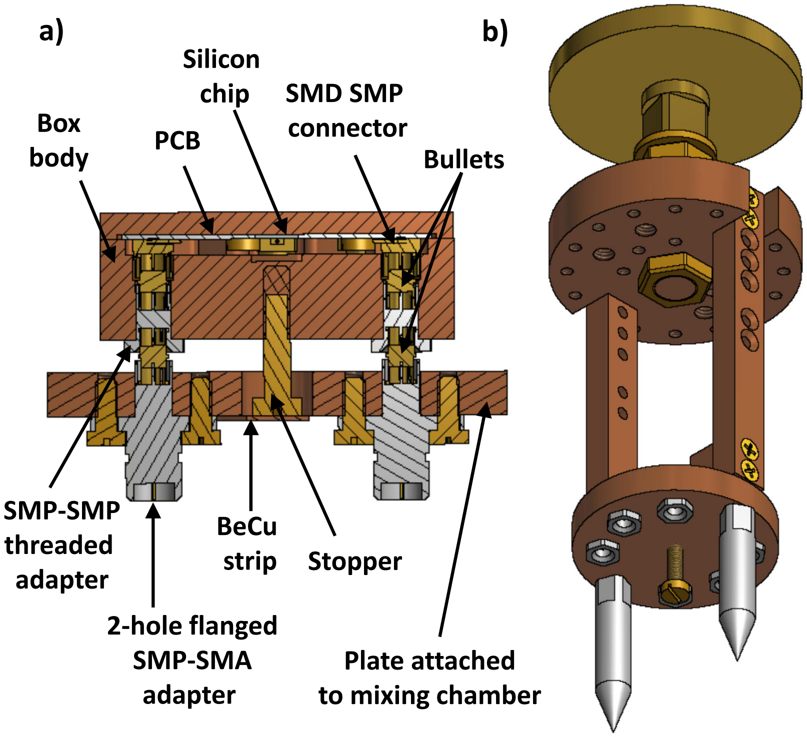
a)
b)
Silicon chip
SMD SMP connector
Box body
PCB
Bullets
SMP-SMP threaded adapter
BeCu strip
Stopper
2-hole flanged SMP-SMA adapter
Plate attached to mixing chamber

Figure 4.3: Interfacing between insertable devices and the microwave setup. a) Close-up section of the interconnected part of the setup presented on Fig. 4.2, in the situation where top and bottom assemblies mate. **b)** Alternative to assembly used to connect sample holders not specifically designed to be mated directly onto the bottom assembly.

The top mechanical assembly is attached to the lowest stage of the cold-insertable plate, which is thermally clamped to the mixing chamber after the probe is fully inserted. This assembly carries the sample holder. The substrate (typically a silicon chip) which contains the device to be measured is connected by wire bondings to a printed circuit board (PCB) (Fig. 4.3.a). Both the chip and the PCB are enclosed in the sample holder. The free volume inside the sample holder is kept as small as possible to move any parasitic resonance above our measurement bandwidth (typically 20 GHz). Launching SMP connectors are soldered on the PCB. Microwave connections to the outside of the sample holder are realized with threaded SMP-SMP adapters which prevent RF leakage in and out the device's space.

The threaded SMP adapters directly mate with bullet adapters on the bottom assembly. The bullets are designed to accommodate relatively large axial and longitudinal misalignments without a significant degradation of the microwave transmission up to 40 GHz. This is important for this system where significant misalignment may occur during insertion and cooldown.

The alignment of the two assemblies prior to connector mating is done using two Teflon rods (diameter 7 mm) in the top assembly sliding through guiding holes (diameter 8 mm) in the bottom assembly. The holes are tapered and the Teflon rods are terminated in a conical profile to enable easy reach. Coarse angular alignment is done simply using visual marks on the room temperature parts of the probe. A stopper system is designed with a screw protruding from the top assembly, whose head lies on a beryllium copper strip attached to the bottom assembly. This arrangement prevents all the weight of the probe from being entirely supported by the RF connectors when the probe is in the fully inserted position.

Magnetic shielding of the experiment, which is very critical *e.g.* for work with superconducting flux qubits or squid devices, is done in the following way. A magnetic shielding system, formed of three concentric cylindrical high-magnetic permeability layers, is permanently attached to the mixing chamber plate of the dilution refrigerator. This shield surrounds the bottom mechanical assembly and enables reaching shielding factors between typically 100 and 1000, depending on the insertion depth. This configuration allows for good magnetic shielding without requiring the shielding element to be part of the sample holder, which simplifies the setup.

We note that the connection between the fixed RF lines and the sample can be made in a more indirect but more versatile way than presented above, where the sample holder had to be specifically designed to mate the bottom assembly. Figure 4.3.b shows the top assembly of this alternative arrangement (the bottom assembly is the same as above). The sample holder of Fig. 4.2 and Fig. 4.3.a is replaced here by a simple plate hosting threaded SMP-SMP adapters mating the bottom assembly. In contrast with the previous arrangement the upper side of these adapters is now free to be connected via coaxial cables to any sample holder that fits in the experimental space. This configuration adds more flexibility to the setup, and allows for wiring sample holders whose design prevents direct connector mating. In the following we will focus our discussion on the direct configuration (Figs. 4.2 and 4.3.a), but the results hold for the alternative configuration as well.

4.3 Operation

We describe in this section the experimental procedure to cooldown and connect a device with the insertable probe, indicating the duration of each step.

We start in a state where the IVC contains exchange gas and all the plates of the refrigerator have a temperature of approximately 4 K. This temperature is maintained by running the pulse tube cooler. The dilution circuit is under vacuum and the ^{3}He-^{4}He mixture is stored at room temperature. The IVC port used for probe insertion (in this case the central 50 mm line of sight port) is isolated by a manual gate valve.

Once the device is wire-bonded to the PCB and enclosed in the sample holder, we attach the top assembly to the end plate of the probe using a threaded rod. The probe is attached to the IVC port and its loadlock is pumped for typically 30 min to reach a few 10^{-2} mBar. Then the gate valve to the IVC is opened, the sliding seal is loosened, and the probe is inserted in the IVC. Visual markers on the load lock are used to roughly align the Teflon guides of the top assembly with the guiding holes of the bottom assembly, before inserting the probe all the way down and mating the RF connectors. Finally the sliding seal is tightened and the probe is brought in thermal contact with the refrigerator plates. Note that since room temperature parts are brought in contact with the plates at ≈ 4 K, the insertion procedure has to be done slowly and carefully, which takes approximately 15 min.

Due to the considerable heat transferred to the refrigerator the temperatures of the cold plates increase up to approximately 50 K. This heat is extracted by the pulse tube cooler. After 3 hours all the IVC volume is thermalized at ≈ 3.8 K. Once the exchange gas in the IVC has been adsorbed by charcoals (≈ 10 min) the mixture can be condensed. After an additional 2h30 the coldest stage of the probe reaches 80 mK. 2h30 are further needed to reach a temperature of 40 mK. In stationary regime, the probe temperature settles typically to 10 mK above the dilution refrigerator base temperature [87].

Removing the probe proceeds as follows. First the ^{3}He-^{4}He mixture is recovered. This step is optional, however it has the following advantages: the risk of sudden pressure increase in the dilution unit is removed and it leaves the system in a state compatible with the next use of the insertable probe. After the thermal clamps are released and the sliding seal slightly loosened, the probe is retracted in the loadlock, the IVC is isolated, and exchange gas is introduced to speed up thermalization to room temperature. The overall time to remove the probe and bring it to room temperature is 1h to 1h30.

In summary it takes less than 6h30 between sample mounting and performing measurements at 80 mK, which is a temperature low enough to characterize superconducting devices involving aluminium Josephson junctions in a regime where quasiparticle poisoning is negligible [82]. The critical time is the thermalization to 4 K after insertion from room temperature, since all the cooling power is provided by a pulse tube rather than Helium vapors as in a regular dip-stick configuration.

At the time we write this manuscript this operating mode has been repeated over 40 times in 8 months and the design has proven extremely robust. Actually not a single mechanical part or RF connector has needed replacement yet. As discussed in detail in the next section, the RF properties have also proven reliable and stable over time.

We note that it is possible to insert/remove the probe without extracting the mixture. Maintaining the circulation has the advantage that the temperature increase during probe insertion/removal is significantly lower, which is advantageous if other experiments are being done on devices attached to the refrigerator mixing chamber plate. The disadvantage of this alternative method is the fact that probe insertion requires a more controlled thermalization procedure, by successively clamping to all the plates during insertion, which requires significantly more care. In addition, there is a more significant risk of uncontrolled pressure increase in the dilution circuit.

4.4 Examples of measurements

In this section we present examples of microwave measurements performed with the insertable system. We focus here on experiments related to the field of superconducting quantum devices, however we emphasize that this approach can be applied to any experiment requiring microwave frequencies and dilution temperatures. All the RF components used to build the mobile connections are rated up to at least 40 GHz. However the fixed parts of the measurement lines (SMA connectors) are specified to 18 GHz, and our microwave setup contains circulators whose maximum working frequency is 12 GHz. So in this work the tested bandwidth is DC to 12 GHz, but we expect the performances of the design to be similar up to at least 18 GHz.

We first present the characterization of the assembly by measuring the transmission using a wideband through connection. Then we present transmission measurements of a coplanar waveguide (CPW) resonator. Finally we show measurements performed on a superconducting qubit coupled to a microwave resonator.

4.4.1 Measurement of transmission using a through transmission line

A first characterization of the setup consists in measuring the microwave transmission of the RF interconnections, to ensure that the stacking up of RF connectors described in Section 4.2 does not introduce unacceptable insertion loss or spurious resonances. For that purpose a PCB which contains a coplanar wave guide (CPW) is mounted in the sample holder.

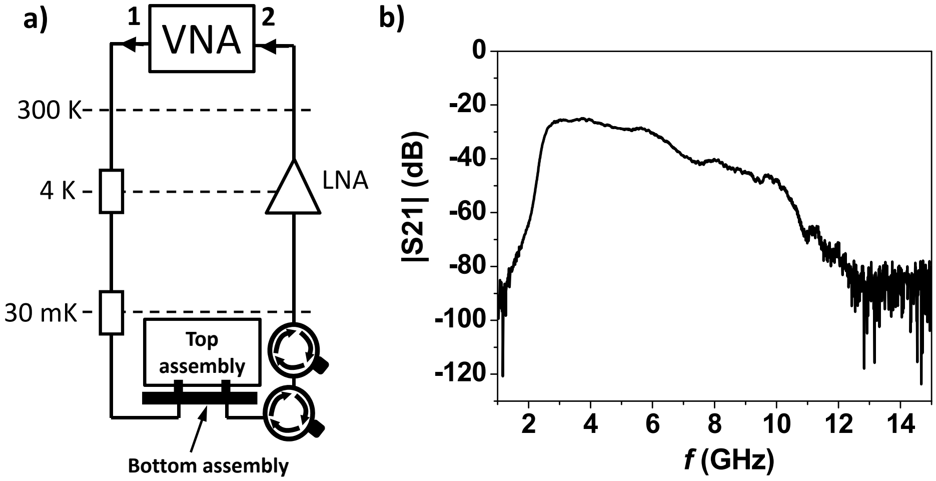

Figure 4.4: Characterization of the assembly. a) Setup used to measure the microwave transmission of a device. The rectangles are attenuators, the circles with arrows are isolators. LNA = Low Noise Amplifier. **b)** Modulus of the transmission through a coplanar waveguide PCB at $T = 50\,\mathrm{mK}$.

The measurement setup is sketched on Fig. 4.4.a. A vector network analyzer (VNA) sends a microwave tone of frequency f from its Port 1. The signal travels through coaxial lines and attenuators down to the bottom assembly where it is connected to the sample holder. The output signal passes through two isolators, is amplified by a cryogenic Low Noise Amplifier (LNA), and reaches Port 2 of the VNA. The VNA measures the complex transmission S_{21} from Port 1 to Port 2 as a function of f.

In a preliminary characterization at room temperature, with access to the mixing chamber, we measured the transmission as sketched on Fig. 4.4.a and compared it to a reference measurement where the whole assembly was replaced with a coaxial cable (data not shown). In the former case $|S_{21}(f)|$ lies 0.1 to 1 dB below the reference and does not exhibit sudden variations or modulations. This shows that the interconnecting scheme of the assembly does not act as a significant source of loss or reflection at room temperature.

Figure 4.4.b shows the amplitude of S_{21} measured at $T = 50\,\mathrm{mK}$ after the insertion procedure described in Section 4.3. S_{21} is a smooth function of f, which is remarkable given the multiple interconnections involved in the setup. By calculating the attenuation and gain of the measurement line at a few frequencies spanning our measurement bandwidth (2-10 GHz), we estimate the losses added by the insertable assembly to lie within the uncertainty range (± 2 dB) of the overall expected transmission.

The connecting of the microwave connectors is very reproducible and was tested by applying the following protocol: connect the coplanar wave guide at low temperature, measure transmission, release, warm up, cool down, reconnect, remeasure. Within the uncertainty of the VNA (0.2 dB) we observe no difference on the transmission between two successive measurements of the same device.

4.4.2 Measurement of a coplanar waveguide resonator

We now turn to the characterization of a superconducting microwave resonator, a model system in microwave engineering [58] as well as a building block for various areas of physics, including photon detection devices for astronomy [88], circuit quantum electrodynamics (circuit QED) [22, 24], or quantum limited amplifiers [71, 73, 74]. The device presented here is a distributed element resonator made of a CPW whose central line is interrupted by two gaps forming capacitors and defining a cavity [58], as sketched in the insert of Fig. 4.5.a. The device is made from aluminium (thickness 200 nm) on a silicon substrate, using a liftoff process.

The measurement setup is identical to the one used in 4.4.1 and sketched on Fig. 4.4.a. The

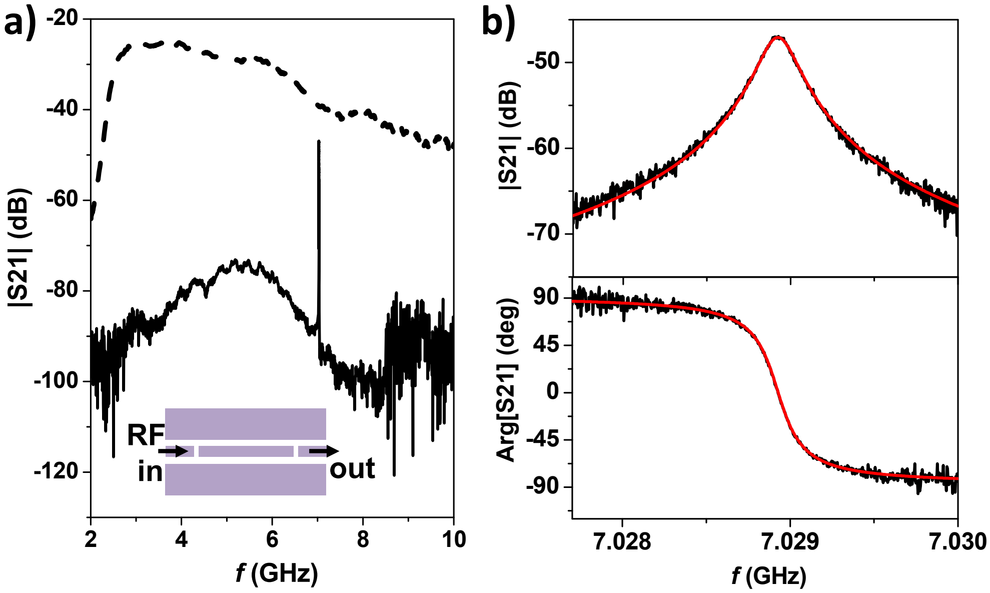

Figure 4.5: Transmission measurement of a CPW resonator. a) Full line: amplitude of S_{21} over the full measurement bandwidth. Dashed line: reference transmission measured with a through PCB. Inset: sketch of the device. **b)** Close-up view of the complex transmission on the resonance probed at the single photon level. The red thick lines show Eq. 4.1 for the best fitted values of circuit parameters.

complex transmission S_{21} for this device is shown in Fig. 4.5.a over the full measurement bandwidth (full line). We observe a transmission peak around 7 GHz corresponding to the first mode of the resonator. Apart from this peak, $|S_{21}|$ lies well below the transmission measured previously with a through PCB and reproduced in Fig. 4.5.a as the dashed line. In particular $|S_{21}|$ does not exhibit parasitic features like box resonances or spurious capacitive coupling between ports. The absence of parasitic transmission combined to the insertion loss below 2 dB stated previously can be seen as a proof of the robustness of the design from the microwave point of view.

We show on Fig. 4.5.b a close-up view of the first mode probed at the level of one photon populating the cavity on average when the drive is resonant. To separate the external and internal quality factors (respectively Q_e and Q_i, yielding a total quality factor $Q_\mathrm{t} = (1/Q_\mathrm{e} + 1/Q_\mathrm{i})^{-1}$) we fit the complex transmission $S_{21}(f)$ with the transfer function:

$$\tau(f) = \frac{A}{Q_\mathrm{e}} \frac{1}{\frac{1}{Q_\mathrm{t}} + 2j\frac{f-f_0}{f_0}} e^{j\varphi_0}, \tag{4.1}$$

where $A = 1/|S_{21}^\mathrm{ref}|$ is a normalization factor obtained directly from the through measurement (dotted line), f_0 is the loaded resonance frequency, and φ_0 is a global phase factor. We obtain $f_0 = 7.029\,\mathrm{GHz}$, $Q_\mathrm{e} = 53{,}000$ and $Q_\mathrm{i} = 77{,}000$. f_0 and Q_e are in good agreement with the designed values, and the internal quality factor Q_i reaches a state of the art value for non epitaxial aluminium on silicon resonators at the single photon level [57].

In this subsection we only presented measurements of a CPW type resonator measured in a transmission configuration. However, the versatility of the setup allows for other types of resonators (*e.g.* lumped elements circuits, multiplexed notch resonators) measured in either reflexion or transmission configuration.

4.4.3 Measurement of a circuit-QED device using a superconducting flux qubit

We conclude this section with results obtained on a circuit-QED experiment [22, 24] with a flux qubit. The device is sketched on Fig. 4.6.a and consists of a flux qubit [45] inductively coupled to a coplanar waveguide resonator [35]. A superconducting coil attached to the sample holder enables biasing of the qubit with a DC flux Φ_ext, and a local wideband flux line placed close to the qubit is used for fast bias and drive with RF signals.

We only present here the main results and focus on typical figures of merit evaluating the quality of the electromagnetic environment that couples to the device in our setup. For the details we refer the reader to the literature covering the topic [89, 22, 24]. Circuit-QED focuses on the coherent interaction between light and matter at the single excitation level. Coherence is extremely sensitive to electromagnetic noise coupling to the device, which can significantly enhance the relaxation and pure dephasing rates of the qubit. Probing the coherence of a qubit is thus a way to measure the electromagnetic isolation of the whole device.

First, qubit spectroscopy is performed as a function of the flux bias applied to the qubit ring. The qubit state is readout using a dispersive measurement scheme [22]: the resonator is driven at its resonance frequency and the qubit-state-dependent phase ϕ of the transmitted signal is

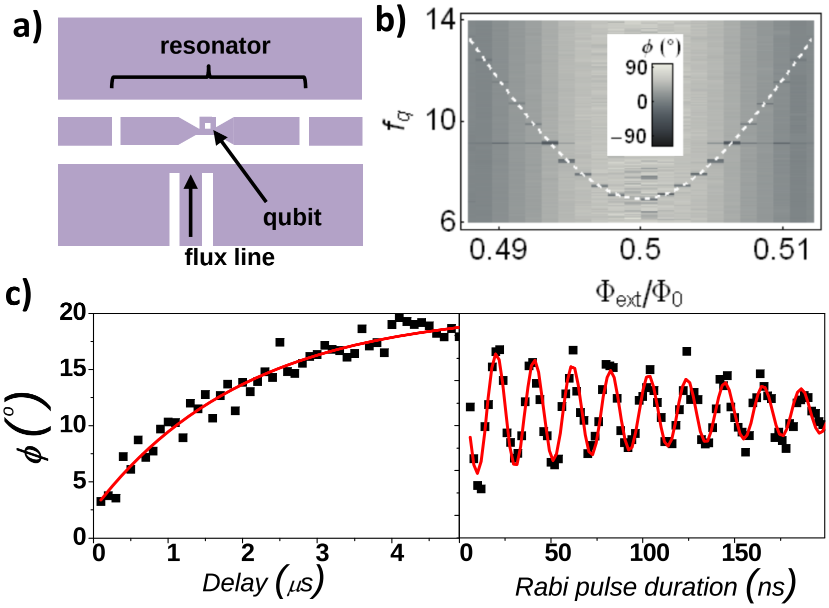

Figure 4.6: Circuit-QED experiment. a) Sketch of the device. **b)** Spectroscopy of the qubit. The dashed line is a fit of the qubit transition frequency. **c)** Relaxation (left) and Rabi oscillations (right) measurements. Dots are data, red lines are fits.

measured by homodyne detection (Fig. 4.6.b). The spectroscopic data can be used to extract the parameters describing the flux qubit-resonator coupled system. The dashed line on Fig. 4.6.b is plotted for a tunneling energy $\Delta = \hbar\times$ 6.90 GHz, a persistent current $I_\mathrm{p} = 150\,\mathrm{nA}$ and a qubit-resonator coupling $g = \hbar\times$ 95 MHz.

Next the coherence of the flux qubit is probed. In superconducting qubits, decoherence has two components of comparable importance: relaxation and pure dephasing. Figure 4.6.c shows two kinds of time domain experiments allowing to estimate the coherence of a qubit: energy relaxation (left panel), and Rabi oscillations (right panel). Both experiments are performed at $\Phi/\Phi_0 = 0.507$. The relaxation is exponential with a time constant $T_1 = (2.0 \pm 0.2)$ μs, whereas the characteristic damping time of the Rabi oscillations is $T_\mathrm{R} = (180 \pm 25)$ ns. These values of T_1 and T_R are consistent with state of the art experiments involving flux qubits away from the symmetry point [90]. We thus conclude that our insertable system can be used for sensitive experiments where preserving coherence is challenging.

4.5 Conclusion

We designed and tested a mechanical system for connection of devices to high-frequency transmission lines into a running dilution refrigerator. This system is used in combination with a cold insertable probe to perform fast turnaround experiments using low noise large bandwidth electrical measurements at temperatures below 100 mK. The total time to cool a device down to 80 mK and warm it up to room temperature using this system is 8 hours, which is a major improvement over the regular mode of operation used so far in similar experiments. This system is robust: it was used over 40 times over a time period of 8 months. We showed two examples of measurements enabled by this method. The first example is a transmission measurement of a superconducting cavity. The second experiment is a study of a persistent current qubit, in which the qubit has coherence time comparable with state of the art at this time in the field. This method will be highly relevant to various experiments in the field of low-temperature physics, in particular for quantum coherence studies.

Chapter 5

Design and fabrication of a multi-qubit device

This chapter presents the main aspects of the design and fabrication of persistent current flux qubits used in planar microwave resonators. Variations of design parameters effectively lead to changes in the geometry or changes in the material properties of the metals and dielectrics used to build the devices. While some parameters can be independently chosen, under the constraints of the global design goals, at the system level, others are interdependent. For example, qubit and resonator frequencies, qubit coupling strength to the resonator, mutual inductance between the qubit and the drive line, are some of the parameters that one needs to select appropriately to maintain sufficient qubit coherence while optimizing qubit-qubit coupling. Mathematical modeling of the many variables of the global design is necessary to find a set of realizable optimal parameters for a set of specific goals.

We address in this chapter the most relevant steps of the fabrication. The devices are fabricated on a high-resistivity silicon wafer, in a two-step process. In the first step, we use optical lithography, electron-beam metal evaporation and lift-off to define a 190 nm to 200 nm thick aluminium layer containing the CPW resonator and magnetic flux control lines. In the second step, the flux qubit devices are realized using electron-beam lithography followed by in situ argon milling, standard shadow evaporation of aluminium, and lift-off. The superconducting flux qubits are formed by two aluminium layers with thickness 40 nm and 65 nm respectively, with an in situ grown aluminium oxide layer formed by exposing the first layer to a pure oxygen flow in partial vacuum (dynamic oxidation).

Each of the various fabrication techniques and pieces of equipment used bring inherent variability of the realized devices due to fabrication parameters fluctuations. It is thus critical to test the range of parameters that can be reached reliably, uniformly, and repeatedly, to allow optimizing a subset of the experimental parameters. Test Josephson junctions, Niobium and Aluminium CPW resonators were independently fabricated and thoroughly tested at mK temperatures prior to integrating the flux qubits in the resonator.

5.1 Flux qubit design and fabrication

To achieve the main goal of this project, which is to study persistent current flux qubits in a cQED setup, and to do so efficiently, we want a device design that can support up to four qubits embedded in the resonator at the same time, while having full control of the design parameters such as qubit frequency, qubit coupling to the resonator, and independent qubit drive. It is desired that the qubits operate at different frequencies in order to control and address them individually. We target, in our original designs, qubit energy gaps spaced by about 1 GHz. An additional goal is to study the flux noise performance of the qubit with its environment, with which the coupling is proportional to the magnitude of the persistent current threading the qubit loop. A large superconducting persistent current and specific loop size is therefore targeted by adjusting the critical current density of the junctions and the overall geometry of the qubit which shares a line with the centerline of the resonator to which it couples inductively. The next subsections present some of the steps of such a design procedure as well describe the steps to fabricate aluminium Josephson junctions and flux qubits reliably.

5.1.1 Simulation and parameters optimization

Using the theoretical framework introduced in Ch. 2, Subsection 2.2.1, we can extend the derivation of the Hamiltonian for the three junctions to four junctions, to compute the eigenenergies versus the applied magnetic flux Φ_{ext}. We define the parameter β as the ratio of the area of the large (fourth) junction over the area of the two identical junctions of the flux qubit. For typical junction critical current densities ($\approx 12\,\mu\text{A}/\mu\text{m}^2$) and junction capacitance per area ($\approx 80\,\mu\text{F}/\mu\text{m}^2$) used in this work, we find the four junctions model tends toward the three-junction (3-JJ) model when this fourth junction is large ($\beta \gg 15$). The SEM images of Fig. 5.2 and of Fig. 5.4 (c) depict a typical 4-JJ flux qubit as used in this work. The energy gap of the qubit Δ is plotted in Fig. 5.1a as a function of the JJ size ratio α for different β. The 3-JJ model, using the same E_J, E_c and junctions sizes, is included for comparison. Given the geometry of our flux qubit loop design and fabrication constraints that will be explained in Subsection 5.1.2, we choose values for β ranging between 2 and 3.

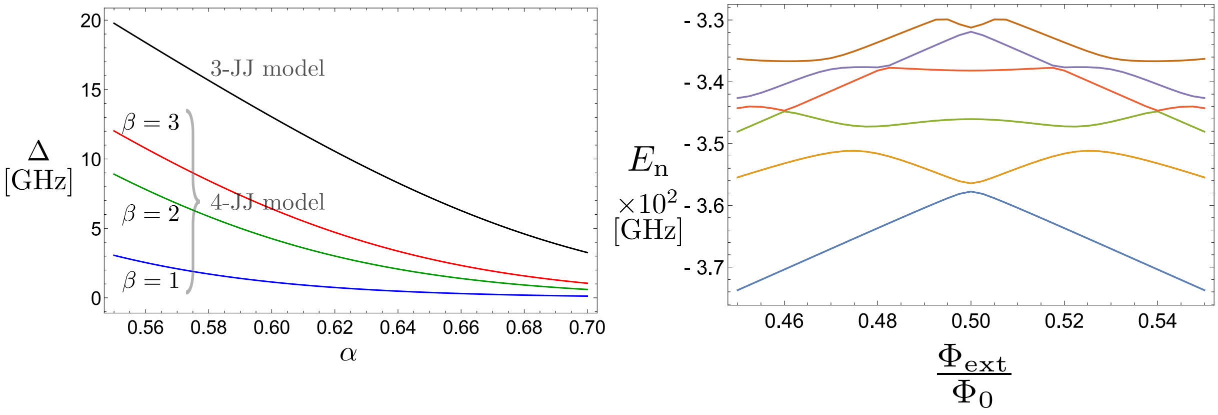

(a) **(b)**

Figure 5.1: Qubit frequency calculations. **(a)** Qubit energy gap Δ: computed Δ versus α for the 3- and 4-JJ models, for different β, $E_\mathrm{J} = 361.87\,\mathrm{GHz}$, $E_\mathrm{c} = 3.987\,\mathrm{GHz}$. **(b)** Qubit eigenenergies: the first six eigenenergies plotted versus the qubit external flux frustration for the case of $\beta = 2.4$ and $\alpha = 0.61$, same E_J and E_c as in a).

In this figure we can see that as α increases, the slope of the qubit's Δ frequency starts to decrease before flattening as α tends to 1. A fabrication error of only a few nanometers on the length of the α junction can lead to a shift of Δ of a few GHz. Therefore the choice of α and its precise realization greatly affect the resulting devices operating point and dependent parameters. Figure 5.1b plots the first six eigenenergies for the case where $\beta = 2.4$ and $\alpha = 0.61$, a value used for the devices for which experimental results are presented in the subsequent chapters.

5.1.2 Fabrication of Josephson junctions and flux qubits

In this work, we use the shadow evaporation technique to fabricate Josephson junctions where the metal layers are deposited though a hanging resist system [91, 92]. A segment of a resist mask can be suspended at a known distance from the substrate. With this masks offset, deposition at normal incidence angle is not necessary as commonly used for standard lift-off. The deposition angle can be varied in order to vary the size of the mask's image on the substrate. Using two depositions at different angles allows creating section of metal that overlaps, where the feature size can be smaller than the openings in the overlying resist layer which carries the electron-beam defined pattern information.

To achieve high resolution the top resist should be chosen accordingly. PMMA on top of a copolymer methacrylate and methacrylic acid (P(MMA-MAA)) is often used. In this work however, we selected polydimethylglutarimide (PMGI) as the first (under-) layer to benefit from solvent selectivity during the developing process. It is negligibly sensitive to e-beam irradiation and the size of the obtained undercut is dependent on parameters for which we have a good control, namely: the temperature and duration of the baking step, the duration of the chemical development, and temperature of the chemistry (in our case the relatively stable temperature of the cleanroom).

An aluminium Josephson junction design, fabrication, validation, and testing process was developed, whose main steps are summarized in the process flow diagram of Fig. 5.2. At every step of the fabrication optical inspection (O.I.) was used to catch early any flaws and stop-and-restart the fabrication of a given batch of silicon dies as needed. SEM imaging allows measuring the main critical dimensions of the design accurately which, once corroborated with the resists thickness measurements, metal shadow offsets and JJs resistance measurements, allows for fine adjustments of the e-beam dose or geometry of the GDS files for example.

Figure 5.3 shows an SEM image at 45° of a test structure made of two tapered wires which tips overlap and define a Josephson junction. The total 'geometric' area of the JJ also takes into account the bottom electrode sidewall over which the top electrodes climb on. The total 'real' area of the JJ which depends on the surface roughness of the bottom and top metal layers and number and size of aluminium grains is unknown. However, what matters is to have a good control on the geometry of the junction and the oxidation process, while maintaining constant the metal surface roughness and grainy structure. The level of wafer surface cleanliness, the background vacuum level of the evaporation chamber, and the metal evaporation rate to form the junctions were kept constant throughout this project to obtain repeatable textured films.

The major steps of a flux qubit fabrication process are presented in Fig. 5.4 from the point where the pattern of the qubit has been defined by e-beam lithography and the PMMA/PMGI

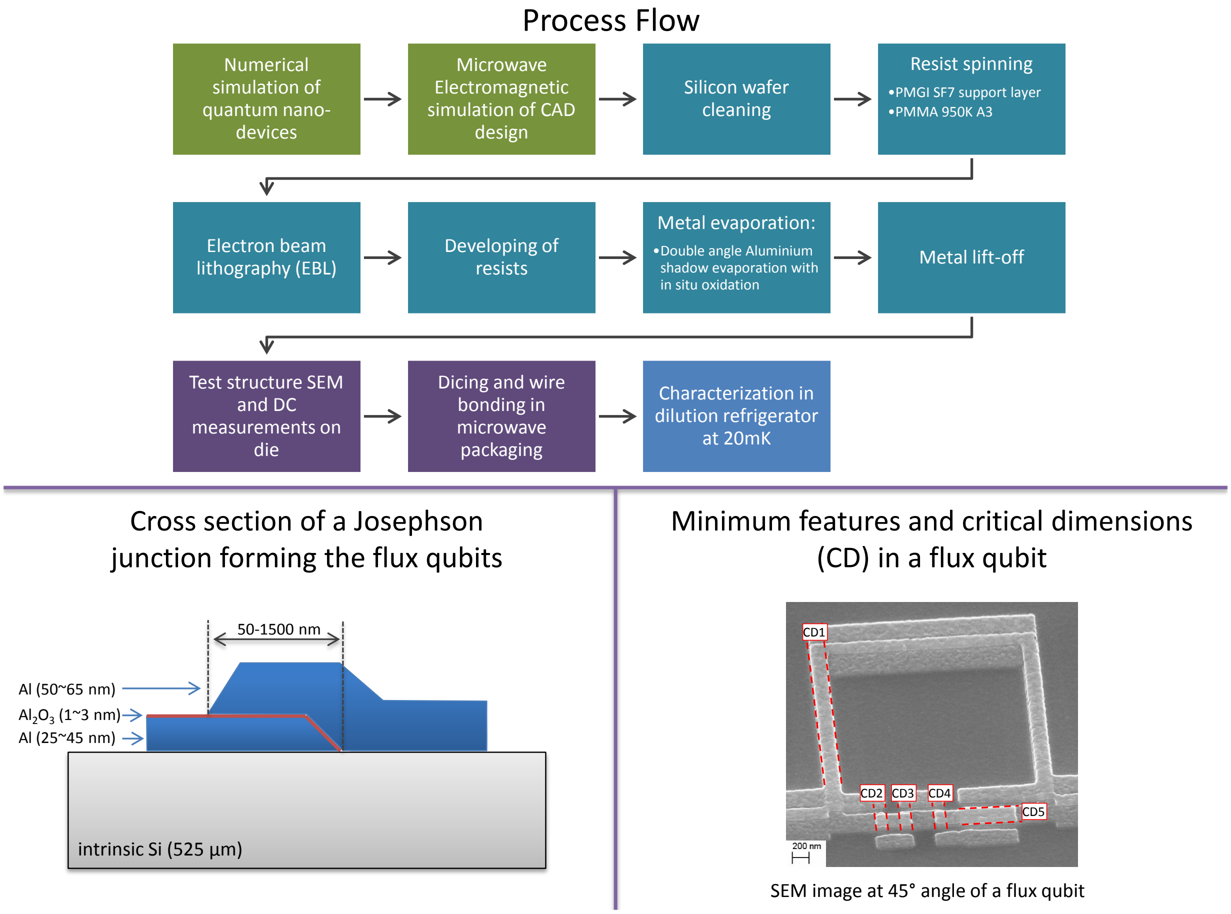
Process Flow
Numerical simulation of quantum nano-devices
Microwave Electromagnetic simulation of CAD design
Silicon wafer cleaning
Resist spinning
•PMGI SF7 support layer
•PMMA 950K A3
Electron beam lithography (EBL)
Developing of resists
Metal evaporation:
•Double angle Aluminium shadow evaporation with in situ oxidation
Metal lift-off
Test structure SEM and DC measurements on die
Dicing and wire bonding in microwave packaging
Characterization in dilution refrigerator at 20mK
Cross section of a Josephson junction forming the flux qubits
50-1500 nm
Al (50~65 nm)
Al_2O_3 (1~3 nm)
Al (25~45 nm)
intrinsic Si (525 µm)
Minimum features and critical dimensions (CD) in a flux qubit
CD1
CD2
CD3
CD4
CD5
200 nm
SEM image at 45° angle of a flux qubit

Figure 5.2: Josephson junctions based device design, fabrication and testing process flow. **(Top)** Typical Josephson junction based device fabrication process flow implemented in this work. Details about the various steps are explained in the main text. **(Bottom left)** Cross section representation of a typical Josephson junction defined by the overlap of two aluminium layers separated by a thin layer of dielectric material. **(Bottom right)** SEM image of a flux qubit indicating the main critical dimensions (CD) of the design. For example reducing the width CD1 increased the mutual coupling of the qubit to the coplanar resonator with which it is sharing this line. For a given width CD5, the JJ length CD4 defines the size of the alpha junction in relation with the two other identical sized ones defined by CD2 and CD3.

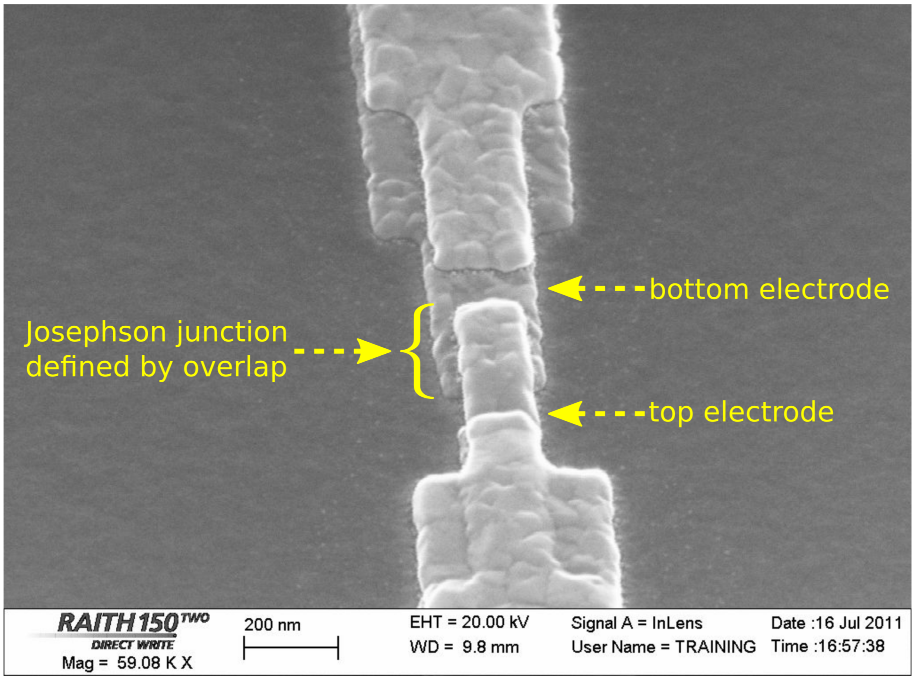
Josephson junction
defined by overlap
bottom electrode
top electrode
RAITH 150 TWO
DIRECT WRITE
Mag = 59.08 K X
200 nm
EHT = 20.00 kV
WD = 9.8 mm
Signal A = InLens
User Name = TRAINING
Date :16 Jul 2011
Time :16:57:38

Figure 5.3: SEM image at 45° of a Josephson junction. A 40 nm thick bottom electrode is evaporated at +20°, followed by an oxidation step and the evaporation of 65 nm thick top electrode at the opposite angle. The overlap of the two electrodes, as indicated in yellow in the image, defines the Josephson junction.

resist stack has been developed (see figure legend for more details and Appendix A.3 for the fabrication recipe).

5.1.3 Josephson Junctions characterization

Prior to making actual flux qubit devices, arrays of test JJ on silicon dies, on which resist were spun and baked at the same time as the flux qubit devices, are typically written at various e-beam doses around the nominal one, to account for slight variations or drifts in the processing or apparatus parameters. The DC resistance characterization at room temperature as well as a careful SEM dimensional inspection allows adjusting slightly the geometry of the flux qubit junctions to be written, the e-beam dose if needed, and in some cases the oxidation step variables.

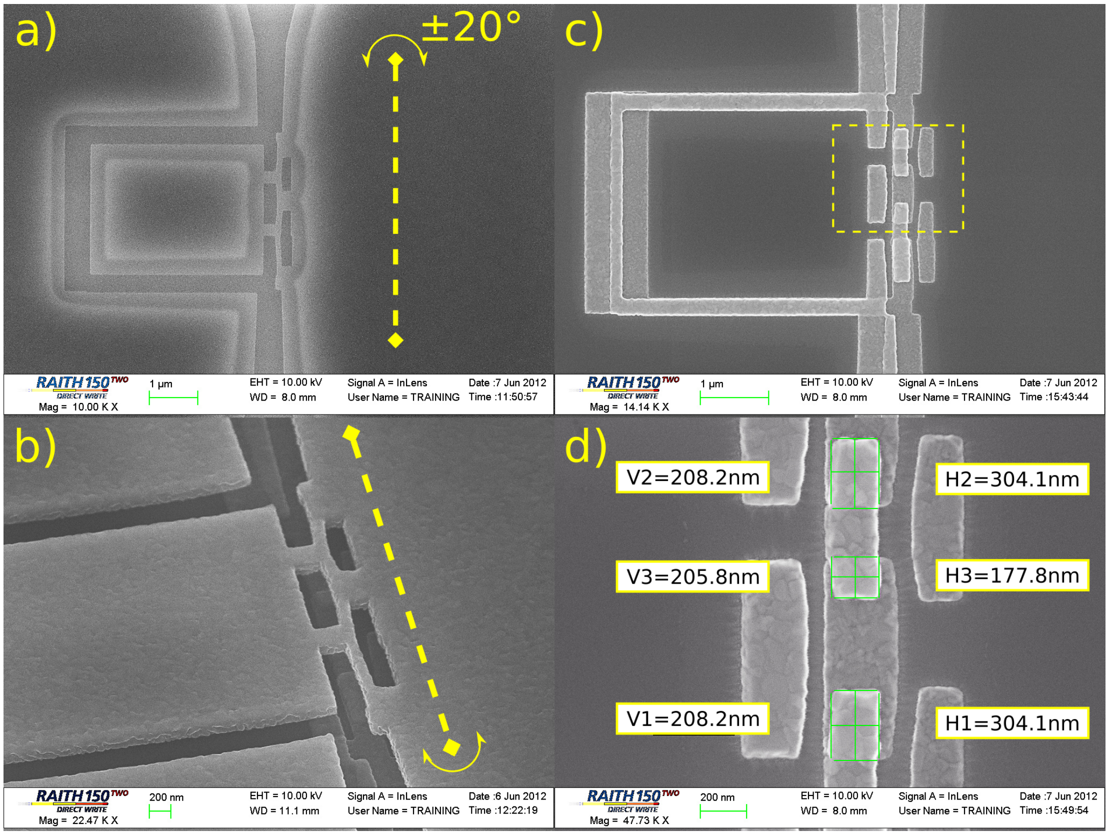
a)
±20°
c)
b)
d)
V2=208.2nm
H2=304.1nm
V3=205.8nm
H3=177.8nm
V1=208.2nm
H1=304.1nm
RAITH150 TWO DIRECT WRITE
Mag = 10.00 K X
1 µm
EHT = 10.00 kV
WD = 8.0 mm
Signal A = InLens
User Name = TRAINING
Date :7 Jun 2012
Time :11:50:57
Mag = 14.14 K X
1 µm
EHT = 10.00 kV
WD = 8.0 mm
Signal A = InLens
User Name = TRAINING
Date :7 Jun 2012
Time :15:43:44
Mag = 22.47 K X
200 nm
EHT = 10.00 kV
WD = 11.1 mm
Signal A = InLens
User Name = TRAINING
Date :6 Jun 2012
Time :12:22:19
Mag = 47.73 K X
200 nm
EHT = 10.00 kV
WD = 8.0 mm
Signal A = InLens
User Name = TRAINING
Date :7 Jun 2012
Time :15:49:54

Figure 5.4: Flux qubit fabrication process. (a) SEM top view of a developed flux qubit PMMA/PMGI resist mask after e-beam exposure. The incoming electron flux for imaging is enough to heat up the 110 nm suspended PMMA mask which gets deformed in the narrow section that defines the junctions. This SEM observation is not part of the regular process and is solely for the sake of documenting this work. The axis of rotation used during the two metal evaporations is shown in dashed yellow. **(b)** A $-45°$ SEM image of the same zone as in a) after the metal evaporations and oxidation steps. In the front plate, the metalized PMMA mask is observed. About 430 nm below, on the silicon substrate, parts of the defined qubits can be noticed. **(c)** SEM top view of the finished qubit after a lift-off step to remove unwanted metalized mask. **(d)** SEM magnification with distance measurements of the section of c) highlighted by a dashed yellow box. The measured JJ sizes (CDs) are compared with the desired design parameters. Based on the measurements, the α junction is found to be 0.578 smaller than the two identical junctions.

Unlike transmon qubit designs where the critical current density is typically in the order of $1\,\mu\mathrm{A}\,\mu\mathrm{m}^{-2}$, our flux qubits, designed to explore the strong coupling regime, uses junctions with critical current densities in the range of 10 to $20\,\mu\mathrm{A}\,\mu\mathrm{m}^{-2}$. The thickness and composition of the JJ oxide barrier for such current densities make the junction relatively sensitive to dielectric breakdown. For this reason, we use an LCR meter (model NF ZM2372 [93]), in conjunction with a properly grounded 4-point probe station, with an excitation voltage that goes as low as 10 mV.

In Fig. 5.5, we show an example of the processing done for test JJ oxidized with an oxygen flow of $25.7\,\mathrm{cm}^3/\,\mathrm{min}$ (see Fig. 5.5 b) for typical flow stability over ≈ 7 min). Figure 5.5 a) shows the SEM images of multiple JJs next to their manually processed version using the open source image tool Fiji [94] (based on ImageJ [95]) to estimate their area. Following the contour of the aluminium grains on the perimeter of the top layer with a contour drawing tool, we can measure the area in pixel unit. Using the SEM dimension bar of each image as a reference, this area is then scaled to metric units, using the fact that the image of the SEM is made of square pixels. Note that the artist's hand is free to choose the best path to take on the edge of the junction where the top layer climbs the bottom layer (on the far right in each of the presented images), which precise shape is obstructed from the SEM top view. A straight line or following slightly the well-defined visible aluminium grains of the top layer seems a reasonable approach. This measured area is further adjusted to take into account the area on the vertical sidewall of the climbed edge, which we call 'corrected area' in the plot's horizontal axis of Fig. 5.5 c), which allows extracting the slope $R_\mathbf{n}$ of the linear fit of JJ resistance data points. Note that the intercept is left unconstrained and represent the resistance (about $60\,\Omega$) of the evaporated aluminium traces between the large probe pads and the junctions. All junctions' patterns share the same wire geometry template.

During the resistance measurements, great care was taken to minimize the influence of stray light from ambient sources or the ring light of the binocular of the probe station. We observed that photo-induced charges and photo dependent conductivity of the high resistance FZ silicon wafer could significantly affect the value of the measured resistances.

Fabricating test JJs, at least monthly, is a good recommended practice to maintain a working and predictable process, in a multi-user shared environment, that involves wet chemistry, sensitive e-beam lithographic equipment, argon milling, metal evaporation and gas oxidation.

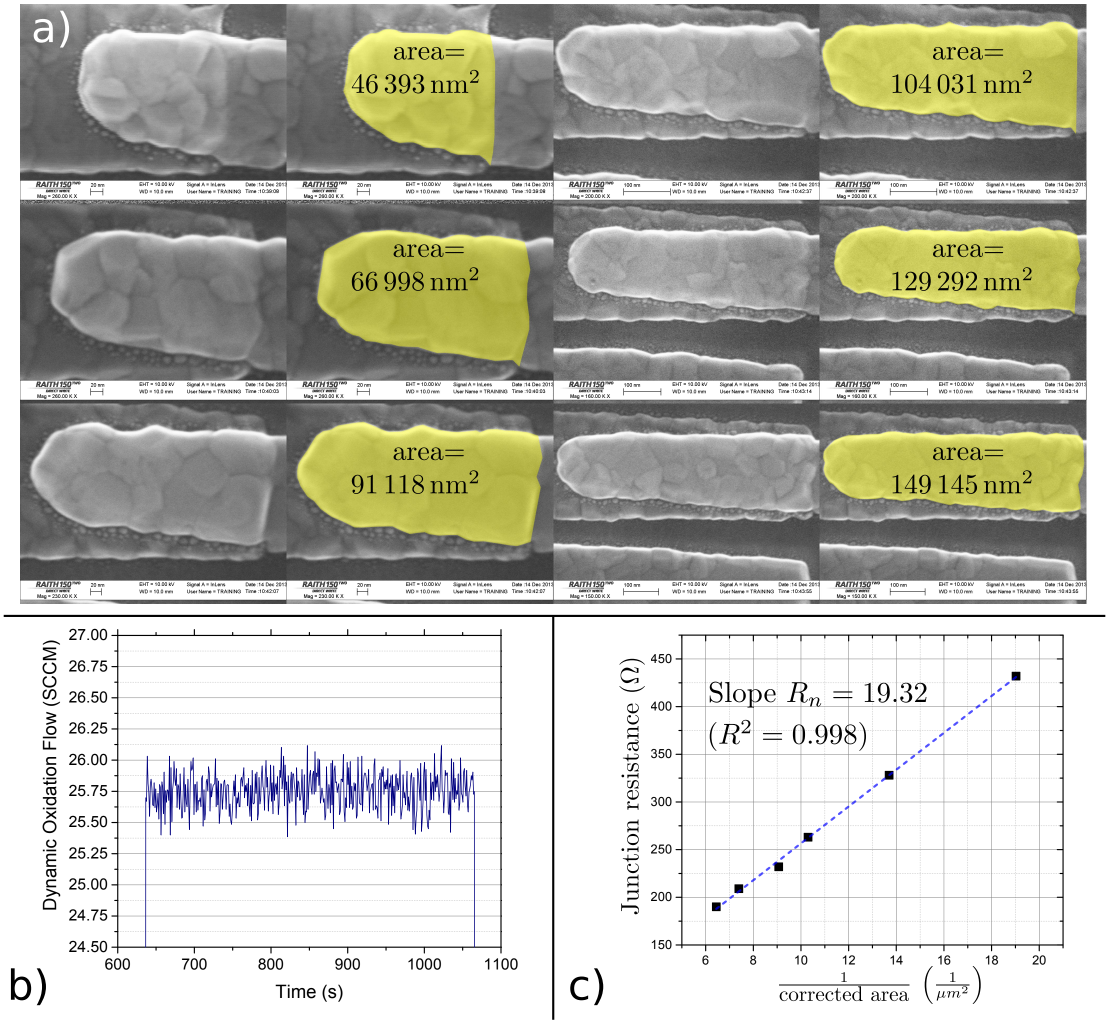

Figure 5.5: Room temperature characterization of Josephson junctions. **(a)** SEM images of six junctions with their processed images to estimate the area. In this example, the e-beam defined patterns of the JJs was rounded. This SEM imaging, which can been destructive for the JJ, is only done after careful resistance measurements of devices that are not meant to be tested cold. **(b)** Plot of the measured flow of oxygen during the 7 min long oxidation process, were the flow set point was 25.7 cm^3/min. **(c)** Junctions resistance plotted versus one over the corrected area previously estimated from the procedure of a).

5.2 Design and fabrication of superconducting resonators with integrated flux qubits

The design of the CPW resonators is relatively straightforward. Some requirements with respect to its frequency, internal and external quality factors needs to be fulfilled to allow qubit state preparations and measurements. The resonator frequency needs to satisfy the following quantum condition $hf \gg k_B T$ for the lowest attainable temperature of our probe system of $T = 30\,\mathrm{mK}$. The external quality factor controlled by the coupling capacitors controls the photons leakage rate out of the resonator, which needs to be faster than the qubits decay rates. Naturally, the choice of dielectric substrate, superconducting metal films and geometry needs to lead to a low dissipative and radiative loss design at the resonance frequency. In this section we address some of the design and fabrication choices made in order to successfully operate magnetic flux biased superconducting qubits in a planar superconducting resonator.

5.2.1 Superconducting coplanar waveguide design

The design of a superconducting CPW $\frac{\lambda}{2}$ resonator follows a similar procedure as presented in previous works in this field [96, 97, 98]. The choice of resonance frequency is also selected considering the cryogenic components of the experimental setup available commercially, namely the cryogenic amplifiers and circulators that operate optimally in the range of 5 to 8 GHz. Choosing a resonance frequency above the qubits energy splitting Δ allows the observation of anti-crossings as the qubit energy is magnetically tuned, thus facilitating the extraction of the device key parameters. With these constraints in mind, we chose a design target frequency range of 6.5 to 7 GHz. We choose to design and fabricate the devices using high purity float zone (FZ) silicon wafer with low amount of dopants and contamination, with resistivity typically exceeding $10\,000\,\Omega$-cm. The resonance frequency ω_c of the fundamental mode is defined by the total length l of the centerline and the effective dielectric constant ϵ_{eff}: $\omega_c = \frac{c\pi}{l\sqrt{\epsilon_{\mathrm{eff}}}}$. We used numerical solvers such as ANSYS ® HFSS ™, Sonnet ®, and FastHenry to assist the design and validation while also fabricating test resonators to converge to a set of desirable parameters.

5.2.2 Numerical simulations

We first find by simulating some simple parametrized CPW structures the necessary gap distances, for centerline width of 6 and 8 µm, to approach a characteristic impedance $Z_0 = 50\,\Omega$, and which can be reliably microfabricated with optical lithography. Next, we simulate various input and output capacitor geometries, where capacitors finger length and spacing are swept. This allows designing the resonator layout with appropriate tapered launching pads and meanders to fit in the Si chip size we selected.The qubit drive line mutual coupling to a qubit loop is simulated with FastHenry and the distance of the qubit to its antenna is adjusted accordingly. The four qubit drive lines are added to the resonator design and the final device is again simulated in HFSS ™ for final verification. This way, potential spurious resonances and leakage can be detected and taken into account in the iterative design flow.

Simulation of coupling capacitors:

Input and output capacitors of the coplanar waveguide resonator are simulated using Sonnet ® simulation software. Figure 5.6b shows an example of a parametrized design where the capacitance $\mathrm{Ck}_n,\ (n = 1, 2)$ is obtained as follow:

$$\mathrm{Ck}_n = \frac{1}{\omega \times \mathrm{Im}\left[\frac{1}{\mathrm{Y}_{21}}\right]},\ \text{with } n = 1, 2,\ \omega \approx \omega_c, \tag{5.1}$$

where Y_{21} is the Y-parameter obtained from the simulation.

Simulation of qubit control lines:

While the qubit frequency is tuned with a macroscopic superconducting coil placed below the silicon device, the qubit energy transitions are controlled with microwave pulses sent through a dedicated microwave line. This qubit control line couples to the qubit inductively through a microwave antenna embedded in the CPW ground plane of the resonator, in close proximity to the flux qubit loop. Although this device layout supports sending some DC current in this antenna to tune the qubit frequency operating point, the choice was made instead to separate the DC and MW biasing of the flux qubits with the coils and the MW antenna respectively. DC biasing through the patterned aluminium antenna would have required special consideration for the choice of materials for the PCB, connectors and wiring, which would have all needed

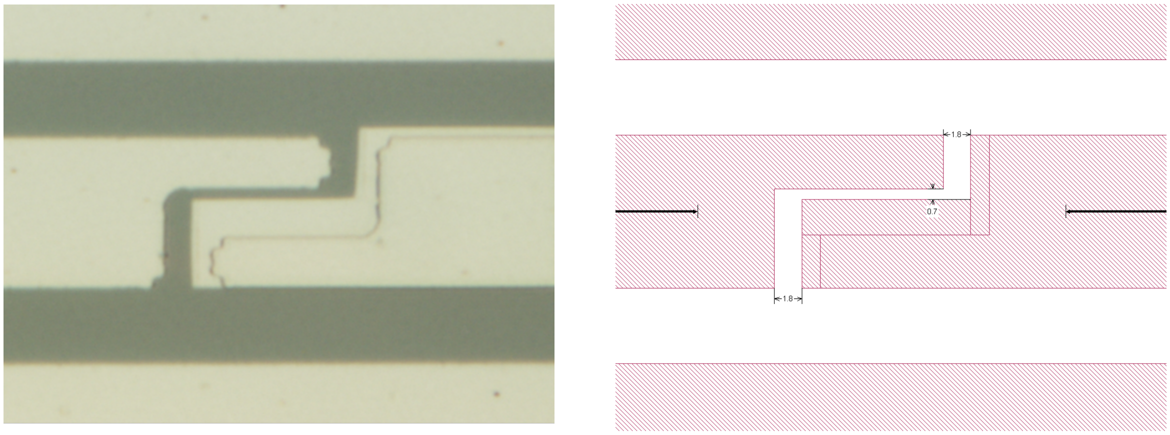

(a) (b)

Figure 5.6: Resonator capacitor simulation. (a) Optical image of the output coupling capacitor of the CPW resonator of a fully realized device. Image colors: Aluminium (light) on Silicon (dark). A patch of aluminium was added on top of the optically defined capacitor to increase its value from 0.92 fF to 1.72 fF. Proper contacting is ensured with Argon milling. Dimensions of the realized feature are measured to update the simulation model. **(b)** Layout of the model simulated in Sonnet with updated dimensions from the optically inspected device. Horizontal (vertical) separation between the fingers of the capacitor is measured to be 1.8 µm (0.7 µm). Black arrows on each side of the capacitor structure indicate the pushed reference plane used during the de-embedding of the simulated results to extract the admittance, assuming 50 Ω ports.

to be superconducting with non-dissipative contacts. Also, such approach requires a cryogenic bias-tee and appropriate filtering for the DC line at the mixing chamber, in order to independently attenuate (filter) the MW line of the qubit drive.

Figure 5.7a shows a schematic representation of the device layout with red arrows showing the path of the microwave current I that splits equally into the two branches of the antenna which are connected to the ground plane. This two-branch symmetric antenna design allows better microwave pulse signal delivery to the qubit coming from the CPW qubit control line, rather than a design that would comprise of a single stripline (with or without interrupting the ground plane along the resonator CPW). Notice that in order to have an effective inductive coupling to the qubit loop it is required that the flux qubit loop be off-centered with respect to the antenna axis of symmetry. The blue arrows and labels represent the mutual inductance between the qubit

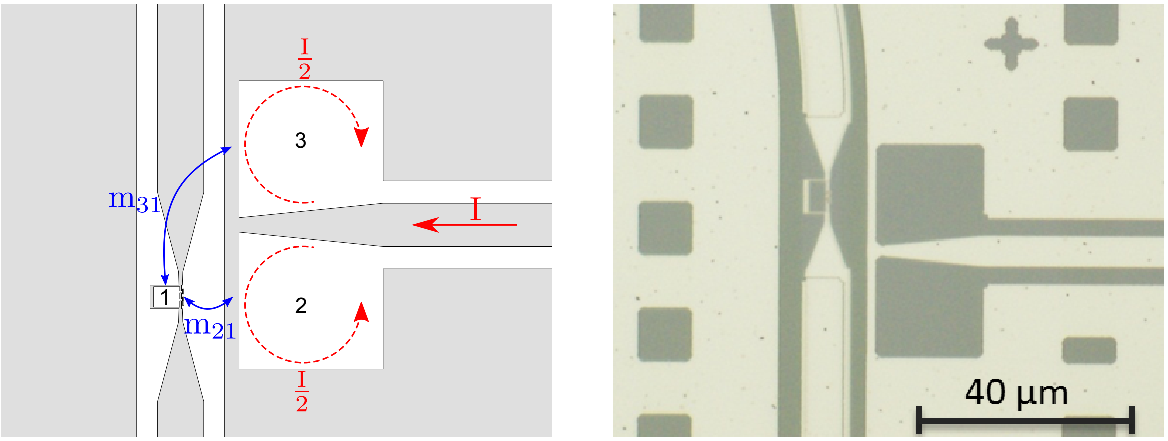

(a) **(b)**

Figure 5.7: Qubit drive line inductive coupling. **(a)** Schematic of a section of the layout of a flux qubit embedded in the centerline of a CPW with a nearby control bias line to drive the qubit through inductive coupling. **(b)** Optical image of a section of a fully realized device showing a qubit and its control bias line. Image colors: Aluminium (light) on Silicon (dark).

loop and the two antenna loops labeled 2 and 3. Figure 5.7b is an optical image of a device (at position of the qubit 3) which also shows that there was a slight misalignment to the right of the EBL patterned layer that defines the qubit and its contact pad to the centerline of the resonator. Such shift in the ideal placement of the qubit brings a larger mutual inductance coupling of the qubit to the antenna loop which means a fast qubit drive for the same microwave power of the room temperature instruments. However, the qubit energy decay and dephasing through the antenna will also get enhanced, emphasizing the need for precise alignment during fabrication and maintaining good control over the critical dimensions.

A simplified version of the schematic of Fig. 5.7a is modeled and simulated with the numerical solver FastHenry to simulate and extract the self and mutual inductances of the antenna-qubit system:

$$\begin{array}{l} \text{loop } 1(\textit{qubit}) \\ \text{loop } 2 \\ \text{loop } 3 \end{array} \begin{bmatrix} m_{11} & m_{12} & m_{13} \\ m_{21} & m_{22} & m_{23} \\ m_{31} & m_{32} & m_{33} \end{bmatrix} . \tag{5.2}$$

The effective mutual inductance M_{eff} between the qubit and the antenna is computed as follow from the matrix elements obtained from the simulation:

$$M_{\text{eff}} = \frac{m_{21} - m_{31}}{2}. \tag{5.3}$$

In our designs, M_{eff} typically ranges from 50 to 70 fF. The modeled qubit loop self-inductance is the value used to estimate the shared inductance with the resonator to compute the coupling strength g of the qubit to the cavity modes, and ranges from 10 to 15 pF in the devices of this work.

Simulation of resonator and qubit drive lines:

The full resonator layout is simulated in HFSS ™, taking into account the final silicon device size once diced and wafer thickness, as well as the height of the conductor above the device once confined in the copper cover shown in Ch. 3 Fig. 3.5. Due to restricted computer memory[1] at the time of the design phase, the modeled device uses lossless conductors and dielectrics. The patterned metal structures are modeled having no thickness and with a perfect electrical conductor (PEC) boundary condition. The waveports are configured with a renormalizing impedance of 50 Ω[2]. We are interested in verifying the potential presence of unwanted spurious resonances and leakage in the range of frequencies where we want to characterize qubits, *i.e.* 1 to 10 GHz. Figure 5.8 shows a representative 3D view of the simulated 6-port device layout where the metal layer mesh is visible (see figure caption for more details).

Running the 6-port analysis[3] of the model of Fig. 5.8 reveals the amount of signal leaking from the resonator to the four other fastline ports. Indeed, the qubit drive lines antennas defined within the ground planes of the resonator are able to channel some energy out at all frequencies and in particular at the fundamental mode of the resonator. This energy decay path effectively reduces what we had previously labeled the internal Q factor. Figure 5.9a shows the simulated transmission amplitudes S-parameters, from the input of the resonator to the five other ports of

---

[1] The matrix formulation of a system using lossy materials (or, even worse, anisotropic materials) takes significantly more memory than a lossless model and with a computer with limited RAM, this limitation could prevent solving the problem with a fine enough mesh adequately.

[2] A more precise port modeling could include the inductance (≈ 1 nH/mm) of the aluminium wirebonds that connect each tapered CPW launching pads to the 50 Ω CPW PCB traces.

[3] A 2-port model with only the resonator and no fastlines is simulated as well, which showed unwanted resonance modes of field oscillating between the two ground plane halves, which motivated the addition of wirebonds to bridge every isolated islands of ground plane in the packaged devices.

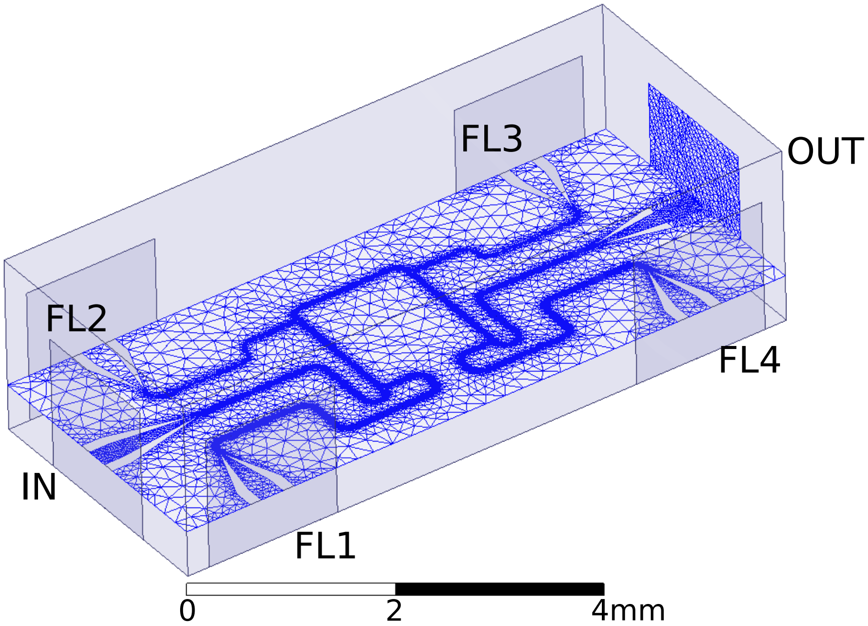

Figure 5.8: Microwave resonator with qubit drive line simulation model. 3D view of the resonator model simulated in HFSS ™, where the meshed conductors and meshed output wave port are shown. The model is comprised of 3 layers: a silicon substrate, resonator metal layer, and vacuum, bounded by perfectly conducting bottom and top outer boundaries. the four sides are set with a perfectly radiative boundary condition. FLx (qubit position index x = 1, 2, 3, 4) represent the qubit drive lines, that we commonly call *fastlines* in this work.

the device. Summing up the four amplitudes of the S(FLx, IN) parameters at resonance, we find that about 7.8 % of the power fed into the resonator input is lost through the fastlines. For this reason, we decide to evaporate a metal patch on top of the patterned qubit drive line antennas when working on devices where only two qubits are e-beam patterned, thus restoring a continuous ground plane in this area.

Summary on the use of numerical modeling:

Using numerical tools to simulate device parameters and anticipate variations in performance due to geometrical changes was very useful in reducing the number of fabrication and test iterations.

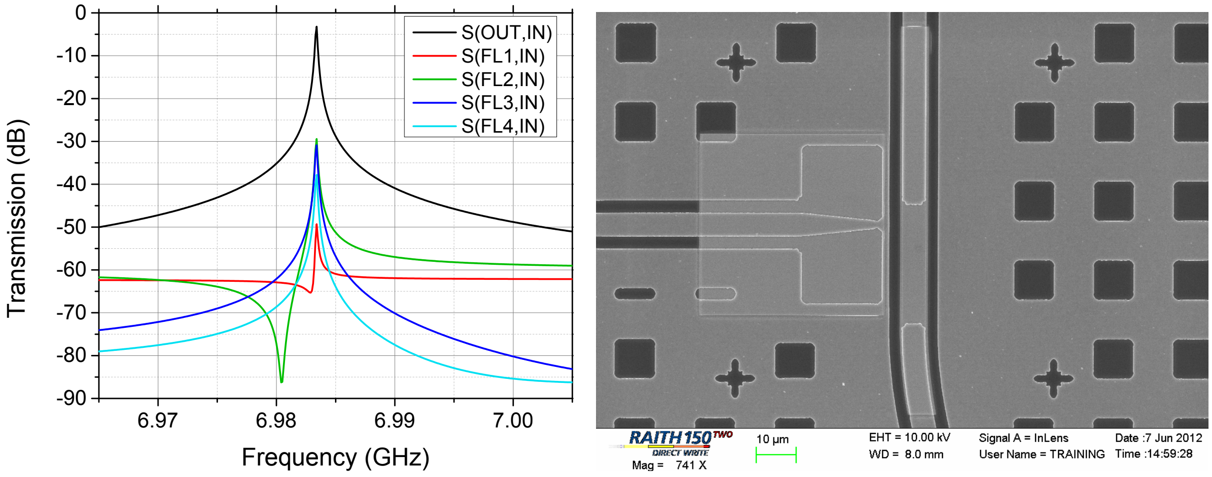

(a) **(b)**

Figure 5.9: Energy leakage through the fastlines. **(a)** Resonator energy leakage through the fastlines. Results of simulation of the transmission amplitudes (in dB) from the input of the resonator (IN) to the five other ports (see Fig. 5.8), around the fundamental mode of this simulated resonator centered at 6.9834 GHz. **(b)** SEM image of a patched fastline. Double shadow angle evaporation of aluminium on top of the unused fastline to minimize energy loss through this microwave line when no qubit is patterned next to it. A similar metal patch is shorting the resonator gap present in the layout, with two large overlap contact area to ensure a lossless superconducting contact.

With the results of the various simulations presented in this chapter, optical and e-beam masks were prepared including variations targeting specific design goals such as (ultra) strong coupling or strong driving of the qubits. To better understand the effect of the setup on the device performance in the future, a more accurate 3D modeling of the silicon chip in the microwave PCB with wirebonds and SMP connectors interconnects could further improve the predictions of energy decay channels or spurious resonances as seen by the qubits. This becomes particularly relevant as the cQED chips become bigger, integrating a larger number of qubits and control lines where cross-talk and frequency crowding become a serious challenge. Some aspects of the fabrication of the resonators including the qubits are presented in the next sections, and a more detailed fabrication recipe is found in Appendix A.

5.2.3 Fabrication of CPW resonators and qubit integration

Since the devices are to be operated in magnetic flux, niobium was first chosen as the material for the microwave resonators due to its critical temperature of 9.7 K and high critical field H_{c2} approaching 1 T. However, we encountered some issues obtaining a reliable aluminium to niobium superconducting contacts as well as issues with aluminium metal film continuity when climbing a patterned Nb structure due to steep edges stemming from the dry etching process use to define the Nb resonators. We switched to fabricating the resonators with evaporated aluminium from the Plassys evaporator used for making the junctions. An array of square holes is added to the layout of the ground plane area to help with losses associated with the dynamic of magnetic vortices and the magnetic dependence of the Q factor and frequency shifts [99, 56, 100, 101, 102, 103].

To optimize the e-beam writing procedure and improve alignment that was done manually for each device, we first pattern the bare wafer with Pd/Au alignment markers which have good contrast against the silicon background or surrounding aluminium ground planes, when scanned by the automatic alignment scripts. We use a bi-layer photoresist process which is described in Appendix A.1. The 4 inch mask containing various test structures and design variations is defined with a single layer of MaN-1410 negative photoresist which is patterned with standard optical lithography equipment (broadband UV wavelengths of an MA6 aligner). Developing the resist in Ma-D 533/S for a controlled amounts of seconds creates a negative slope profile well suited for the aluminium evaporation and lift-off process used (see Appendix A.2 for a more detailed fabrication recipe). To improve the cleanliness of the metal to dielectric interface and metal film morphology, the patterned wafer is then loaded in an oxygen plasma asher and descummed with a 10 s 50 W recipe. The wafer is further cleaned after being loaded in the Plassys evaporator with an in-situ gentle argon milling. ≈ 190 nm of aluminium are evaporated at an angle of 5° using the planetary motion of the motorized evaporator wafer holder. This creates a small slope to every metal edges to prevent having the same coverage problems experienced with the Nb straight edges. Given the presence of about a million $10 \times 10\,\mu$m aluminium flakes of the web ground (see Fig. 5.10) that needs to float away from the wafer during the lift-off step of a 4 inch wafer, we use ultrasonic agitation with acetone and PG Remover solvent baths with the wafer front surface oriented down and kept at a distance from the bottom of the glass dish.

The wafer is diced into 17×17 mm pieces which are then cleaned and prepared for fabricating the qubits as per the procedure presented in section 5.1.2. The layer of aluminium defining the resonators is first cleaned from its natural oxide with in-situ argon milling just prior to evaporating

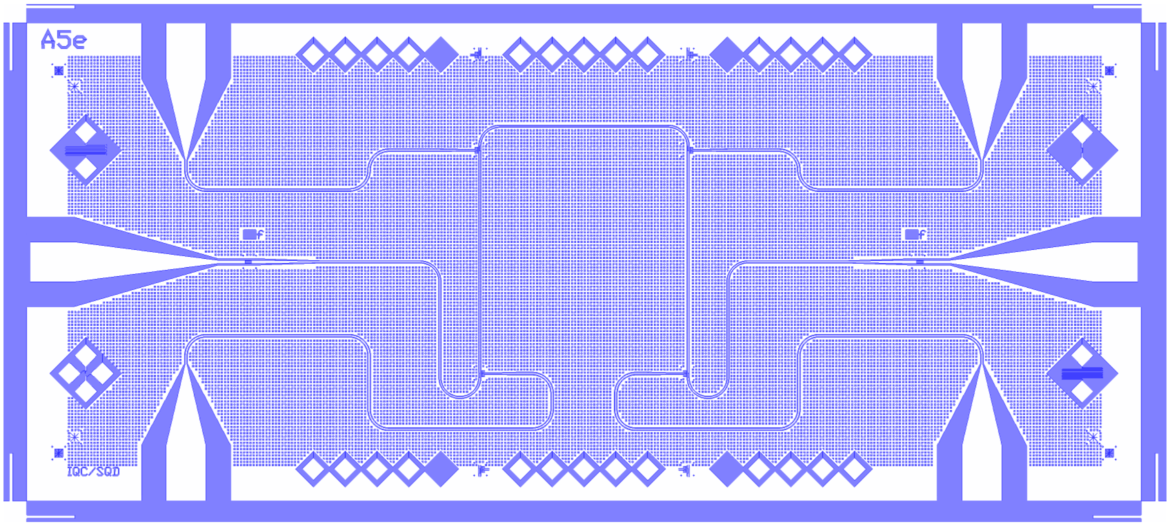

Figure 5.10: Mask pattern for a typical device with web ground. $10 \times 10\,\mu\text{m}$ squares spaced by $10\,\mu\text{m}$ from edge to edge are patterned on the ground plane keeping a minimum safe distance of $20\,\mu\text{m}$ away from the edges of the CPW traces. Various test structures are defined on the edges of the device for measuring film resistance, aluminium to aluminium contact resistance and test junctions.

the first aluminium layer of qubits and patches. This milling is done at the same two angles of the shadow evaporation process to ensure good contact where the metal will be projected below the PMMA overhangs. After this last liftoff and optical inspection and JJ characterization, the dies are coated with a temporary photoresist before being further diced into $3 \times 7\,\text{mm}$ devices ready for packaging, wirebonding and characterization.

5.3 Chapter summary

In this chapter, we have covered the main aspects of the design and fabrication of multi-qubit cQED devices with superconducting planar CPW resonators. We used a collection of mathematical modeling and EM numerical solvers to compute and predict device parameters from which we can derive experimental parameters. For example, we can, at the design stage, estimate the required microwave power of the lab equipment, needed to perform a CNOT gate with two qubits with different g coupling strength. The main challenge of the fabrication efforts was the variability in producing repeatable qubit alpha junctions due to its small size and the high transparency of the junction. In the chapter to follow, we present experimental results of the various characterization steps performed to control and measure the devices we designed.

Chapter 6

Control and measurement of flux qubits in cQED

Previous chapters introduced the model describing the interaction of flux qubits with a superconducting microwave resonator, the design of such a device, some aspects of the experimental setup, the fabrication and initial characterization of test devices. In this chapter, the various measurement techniques and parameter extraction needed for the characterization of flux qubits in a cQED setup are presented. The order follows the natural steps in which the measurements were first performed after cooling the device, with the exceptions that some are concurrent and interrelated since some metrics extracted are used for the calculation of other parameters.

All the results presented in this chapter and the upcoming ones were obtained with a two-qubit device called "W37_c2d" (W stands for wafer, other characters are device coordinates on the 4-inch mask), unless otherwise mentioned. A picture of this device indicating the locations of the two qubits within this four fastline template device is shown in the next chapter (see Fig. 7.1). It will simply be referred as the device in the text after this introduction.

This design was a refinement of the design of a device characterized just before the cool down of "W37_c2d" which showed the response of two flux qubits but which was poisoned by trapped magnetic flux vortices. The trapped magnetic flux vortices were due to the needed applied magnetic field from the coils to operate the small loop area qubits. In addition to magnetic field sweep hysteresis, another other detrimental effect was the creation of some random resonator frequency jumps. This former device had low qubit energy splitting Δ preventing the proper preparation in the ground state of the qubits due to photon thermal population and other possible noise channels. Learning from those limitations, we made the loops of the flux qubits of "W37_c2d" larger, $\sim 24\,\mu\text{m}^2$, and optimized junction sizes and critical current to yield higher Δ/h qubit frequencies. The output capacitance of the resonator was increased to lower the loaded Q factor and provide more output signal to be fed to the cryogenic amplifier at the 4 K stage.

The careful characterization of the qubits energy decay and dephasing time constants, states preparations and interaction strengths with the resonator and the other qubit are fundamental if a more complex system is to be built. Most measurements introduced in this chapter were repeated numerous times and only one or two typical curves are presented for each. A more detailed study of qubit decoherence is presented in Ch. 7.

6.1 Identifying the qubits symmetry points: resonator transmission versus applied magnetic flux bias

After the initial cool down we first verify that we measure a sharp resonance when no magnetic field is applied. Although we have a calculated estimate for the mutual inductance between the coil and the qubit, we need to sweep the current bias of the coil and record the resonator spectrum which contains the signature of the qubit, to get a more precise value. Also, depending on the cooling conditions of the device and magnetic shields used, we expect some shifts that will are taken into account in our models and analysis. For this measurement, a VNA is connected to the microwave input and output ports of the resonator lines, with some additional attenuation at its input, and the frequency is swept around the bare resonator frequency. The estimated microwave power at the input of the resonator is -143 dBm to ensure a low average number of photons in the resonator. The transmission amplitude and phase are recorded while the large superconducting coil of the device sample holder is biased with a low noise voltage controlled current source.

Figure 6.1 is a 2D map of transmission traces acquired at each magnetic flux bias. Since our setup assembly composed of high-μ metal shields, coils and the superconducting device lead to some slight hysteresis in the magnetic response during B-field sweeps, certain precautions had to be taken. For example, for this figure's measurement, the coil was first swept from 0 V bias to +2.86 V and then swept down to -2.5 V without any interruptions while recording the data. Depending on the measurements run, we sometimes observed a small horizontal offset between the up and down sweeps. Also, it's important to note that the current bias of the coils was

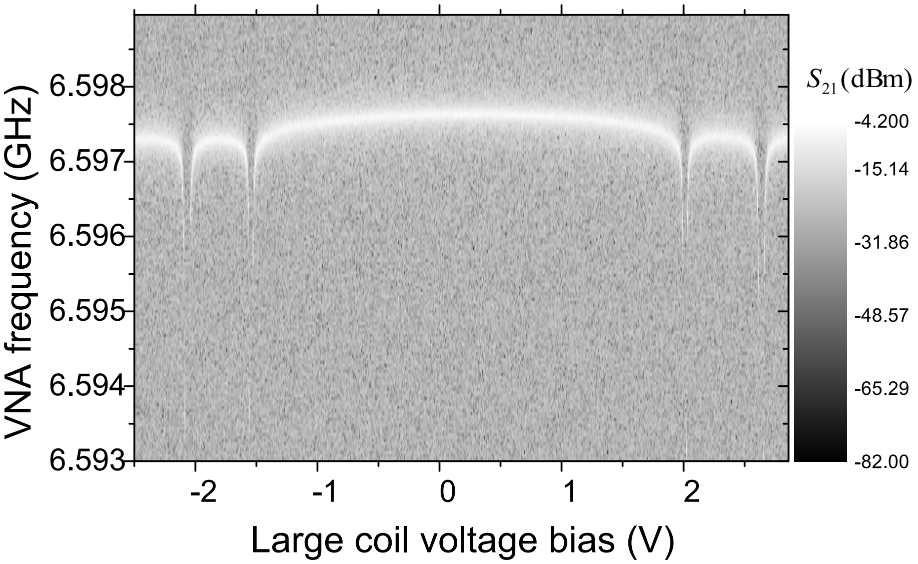

Figure 6.1: Resonator S_{21} and magnetic field sweep. Resonator S_{21} traces acquired with a VNA (along the vertical axis) while sweeping the bias of the large coil. Light intensities in the gray scale plot represent the high transmission level of the resonator when it is at resonance. Partial view of the avoided crossings between the resonator and the qubits are observed when the flux threading the qubits loops tunes the qubits frequencies in resonance with the resonator frequency.

never turned on or off suddenly in between measurements, and any desired current bias value was reached through a slow sweep so at to avoid heating in the metallic parts of the device packaging due to Eddy currents.

We observe a slight bending as the magnitude of the field is increased due to the field dependence of the kinetic inductance of the aluminium film of the resonator, however, this was not quantified in this work. As the magnitude approaches $+2\,\mathrm{V}$ we observe a sharp bend of the transmitted signal, the typical signature of a vacuum Rabi splitting due to the interaction of one qubit biased at the effective frequency of the resonator. A similar feature is observed at around $+2.6\,\mathrm{V}$. With flux qubits, we expect this pattern to repeat at every multiple of Φ_0 associated with their loop size.

We note the flux coordinates of the four observed dips and can associate them to their respective qubit since the qubit loops were made of slightly different areas. Qubit 'A' (later identified as qubit 1) with dips centered at −2.07576 V and +2.6337 V has a Φ_0 that corresponds to 4.70946 V. Qubit 'B' (later identified as qubit 2 with a larger loop area) with dips centered at −1.54453 V and +2.00001 V has a Φ_0 that corresponds to +3.54454 V. We also note a slight asymmetry (about 12 %) in the dip positions around 0 applied magnetic field, due to remnant magnetic field around the sample and the attenuated vertical component of the magnetic field of the earth still present in the sample surrounding space. The large coil bias parameter now calibrated can be used to individually control one qubit or the other. However this single large coil does not provide independent control of the qubits and for this reason we need to also repeat such calibration experiment with the small superconducting coils present in our design while maintaining the large coil at a fix bias (see Sec. 3.2.1, page 47 for details of this implementation). However, this procedure requires careful calibration and knowledge of the qubit Δ's and ε's, which are obtained with spectroscopy measurements presented in Sec. 6.3.

6.2 Vacuum Rabi splittings

The Jaynes-Cummings Hamiltonian of Eq. (2.70) can be diagonalized in the RWA and we obtain the following dressed eigenstates:

$$|+,n\rangle = \cos\theta_n|e,n\rangle + \sin\theta_n|g,n+1\rangle \tag{6.1}$$

$$|-,n\rangle = -\sin\theta_n|e,n\rangle + \cos\theta_n|g,n+1\rangle, \tag{6.2}$$

with

$$\tan 2\theta_n = \frac{2g\sqrt{n+1}}{\delta}, \tag{6.3}$$

and with the eigenenergies:

$$E_{\pm,n} = \hbar\omega_r\left(n+1\right) \pm \frac{\hbar}{2}\sqrt{4g^2\left(n+1\right)+\delta^2}, \tag{6.4}$$

which for the case of tunable energy gap flux qubits can be rewritten as:

$$E_{\pm,n} = \hbar\omega_r\left(n+1\right) \pm \frac{\hbar}{2}\sqrt{4g_{\text{eff}}^2\left(n+1\right)+\delta^2}, \tag{6.5}$$

where the effective qubit resonator coupling energy scales with the detuning:

$$\hbar g_{\text{eff}} = \hbar g\frac{\Delta}{\hbar\omega_q}. \tag{6.6}$$

When $\delta = 0$ the states $|e, n\rangle$ and $|g, n+1\rangle$ are degenerate and lead to an anti-crossing where the resonator peak splits into two, with a peak separation of $2g$, an effect known as the vacuum Rabi splitting.

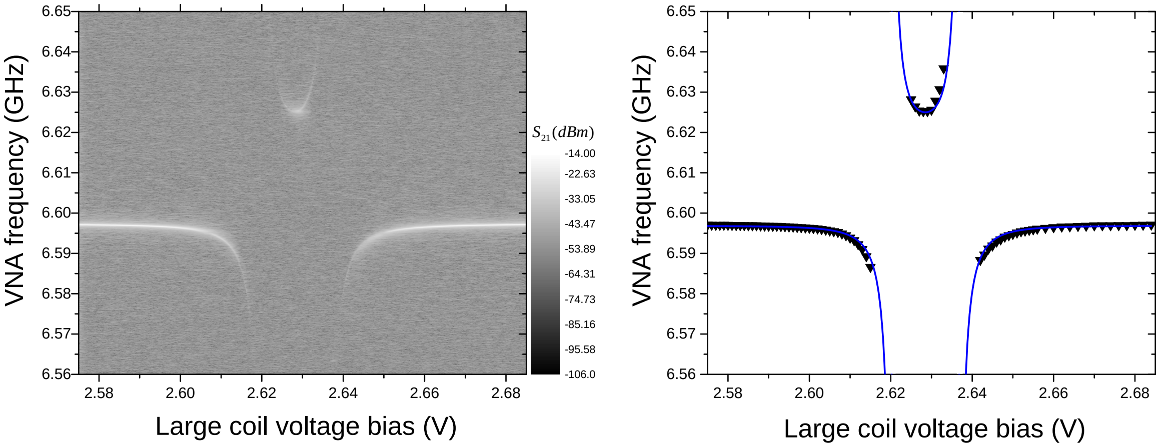

Figure 6.2: Vacuum Rabi splitting for qubit 1. (left) Resonator S_{21} traces versus magnetic coils bias showing vacuum Rabi splitting of qubit 1 with the resonator. **(right)** Extracted peaks center frequencies with fit to theoretical prediction in the RWA of the dispersive regime.

Vacuum Rabi splittings are experimentally observed when the flux threading the qubits loops tunes the qubits frequencies in resonance with the bare resonator frequency ω_r. Figure 6.2 and 6.3, which are fine zoomed scans similar to Fig. 6.1 but with a larger frequency span, show the resonator S_{21} traces acquired with a VNA (along vertical axis), while sweeping the bias of the large coil placed below the sample holder. The center frequencies of the resonance peaks of the S_{21} traces are extracted and we can fit the data to the dressed resonator frequency formula:

$$\tilde{\omega}_r = \frac{\omega_r + \omega_q}{2} \pm \sqrt{\left(\frac{g\Delta}{\hbar\omega_q}\right)^2 (n+1) + \left(\frac{\omega_q - \omega_r}{2}\right)^2}, \tag{6.7}$$

where $\hbar\omega_q = \sqrt{\varepsilon^2 + \Delta^2}$, and n is an integer number of photons in the resonator.

The model agrees overall well with the data for fit parameters that are in accordance with the design targets. However, we notice a slight disagreement between the shape of the fit and qubit 2 data points when the qubit is biased around its symmetry point (coil bias = 2.012 V). Varying the values of Δ_2 or g_2 in the fit around nominal values do not lead to a change of the

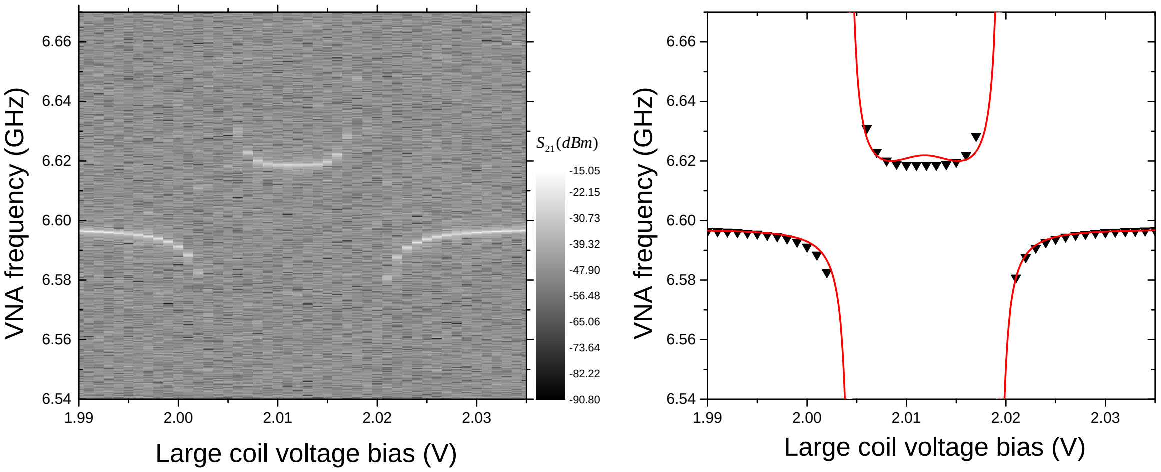

Figure 6.3: Vacuum Rabi splitting for qubit 2. (left) Resonator S_{21} traces versus magnetic coils bias showing vacuum Rabi splitting of qubit 2 with the resonator. **(right)** Extracted peaks center frequencies with fit to the theoretical prediction in the RWA of the dispersive regime.

overall shape. When fixing Δ_2 to its real value of 3.664 GHz, later found with spectroscopy as explained in the section 6.3, we obtain $g_2/2\pi \simeq 270\,\mathrm{MHz}$.

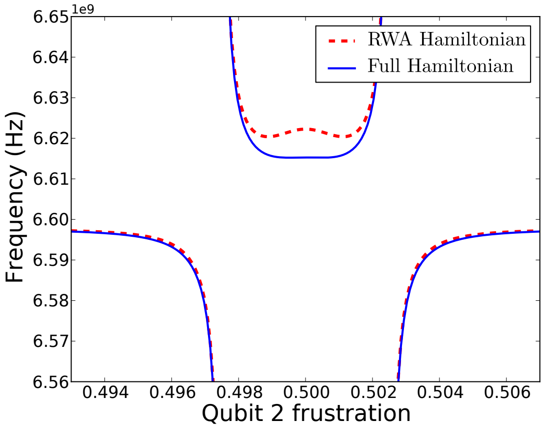

Figure 6.4: Numerical simulation of qubit 2 vacuum Rabi splitting for two cases: (dashed red lines) using the Hamiltonian in the RWA, (blue lines) using the Hamiltonian without dropping the counter rotating terms $a^{\dagger}\sigma_{+}$ and $a\sigma_{-}$.

We performed numerical simulations (*i.e.* numerical diagonalization) using the Jaynes-Cummings

Hamiltonian in both the RWA limit and in the case where the counter-rotating terms $a^\dagger\sigma_+$ and $a\sigma_-$ are not dropped. We find evidence of the limits of the RWA approximation considering the relatively large magnitude of g_2 in this system. Figure 6.4 shows the calculated cavity dressed frequency for both cases for $g_2/2\pi = 270\,\mathrm{MHz}$. The blue curve (full Hamiltonian) agrees qualitatively with the experimental data points of Fig. 6.3. Indeed, the flattening around the qubit symmetry point follows more accurately the shape of the data points. However, because we used the coarse g_2 estimate found previously for this full Hamiltonian simulation, the blue curve has a slight vertical offset with respect to the data. More precise values for the qubit frequencies are obtained with spectroscopy measurements presented in the next section. More precise values for the g coupling strengths are obtained with photon-number splitting experiments as described in section 6.3.1.

6.3 Spectroscopy measurements

Spectroscopy scans allow finding the qubit resonant frequency for a given applied magnetic flux bias. Since the qubit is sensitive to small variations of the ambient magnetic field, spectroscopy measurements were done between every measurement done in this work in order to have an accurate knowledge of the qubit frequency at a given time and apply the necessary compensations as needed before the external magnetic field would drift further and cause a noticeable change in the qubit frequency.

6.3.1 Continuous wave spectroscopy

Observation of photon-number splitting

The Jaynes-Cummings Hamiltonian in the dispersive approximation introduced in (2.70) can be rearranged in another way, so that the interaction is expressed in terms of a shift of the qubit frequency rather than a shift in the resonator frequency:

$$H_{\mathrm{disp}} = \hbar\omega_r\left(aa^\dagger + \frac{1}{2}\right) + \frac{1}{2}\hbar\left[\omega_q + \frac{2g^2}{\delta}a^\dagger a + \frac{g^2}{\delta}\right]\sigma_z. \tag{6.8}$$

The bare frequency of the qubit ω_q is shifted by the Lamb shift [104] $\frac{g^2}{\delta}$ and in addition by $2\chi = \frac{2g^2}{\delta}$ per photon in the resonator. This effect is called the AC Stark shift [105] and was observed experimentally by measuring the qubit spectroscopy in the presence of photons in the resonator. We used a VNA in a continuous wave (CW) mode to probe the resonator at its dressed state frequency when the qubit is in the ground state and swept the frequency of the signal sent through the qubit control line. The power of the VNA source was varied to results in different average photon population $\bar{n}$. Figure 6.5a shows the spectroscopy traces obtained at two VNA powers for qubit 2 at its symmetry point, effectively resulting in power estimates at the input of the device of -143.25 dBm ($P_{\text{VNA}} = -60$ dBm) and -138.25 dBm ($P_{\text{VNA}} = -55$ dBm). The calculated $\bar{n}$ are $\simeq 0.57$ and $\simeq 1.81$ respectively (neglecting photons population due to background thermal radiation). We observe multiple spectroscopy peaks AC stark shifted by 2χ from which we can calculate the g coupling. The peaks distribution reflects the Fock states of the resonator driven by a coherent drive which amplitudes are weighted by a Poisson distribution with mean photon-number $\bar{n}$ [31, 106].

Figure 6.5: Observations of photon-number splitting for both qubits. The coupling strength g between the artificial atoms and the resonator is obtained from the relation $2\chi = 2g^2/\delta$.

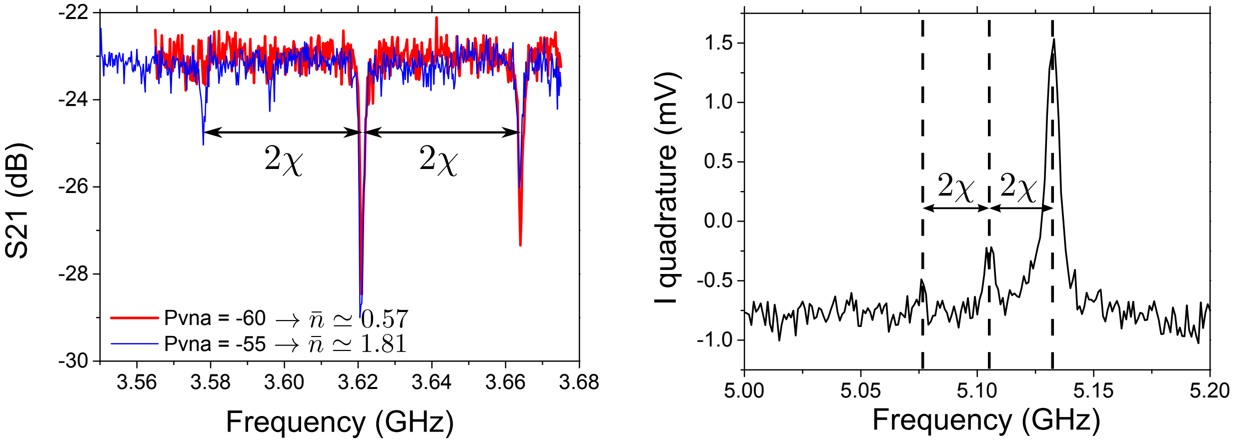

(a) Observation of photon-number splitting for qubit 2 biased at its symmetry point while probing the resonator with a VNA at a frequency $\omega_r - \chi$. The qubit dressed state is AC Stark shifted to lower frequencies. The AC Stark shift per photon in the cavity is $2\chi/2\pi = -43.5\,\text{MHz}$.

(b) Observation of photon-number splitting for qubit 1 biased at its symmetry point with a pulsed readout measurement with a $T_{\text{rep}} = 10\,\mu\text{s}$. The qubit dressed state is AC Stark shifted to lower frequencies. The AC Stark shift per photon in the cavity is $2\chi/2\pi = -29\,\text{MHz}$.

Given the width of the qubit peaks and the magnitude of 2χ, a large number of Fock states could be resolved for qubit 2 while increasing the power of the VNA. The peaks widths were only negligibly increased at a VNA power of - 45 dBm ($\bar{n} \simeq 18$) due to measurement induced dephasing.

Alternatively, photon-number splitting can be observed with a pulse measurement by reducing the repetition time of the readout pulse T_{rep} so that there are still photons left in the cavity at the frequency of the readout pulse during the qubit excitation. We reduced the T_{rep} of our regular measurements protocol from 130 µs, which is long enough for the cavity photons to decay, to 10 µs. The high Q factor of the resonator of the device and a $T_{\text{rep}} = 10\,\mu\text{s}$ allowed the observation of AC Stark shift as shown in Fig. 6.5b for qubit 1 at its symmetry point. The qubit drive amplitude was set to be large in order to distinguish the shifted peaks, which resulted in large peaks widths. We obtained with either of the two techniques a coupling $g_1/2\pi \simeq 150\,\text{MHz}$ and $g_2/2\pi \simeq 252\,\text{MHz}$ for qubit 1 and 2 respectively.

6.3.2 Pulsed spectroscopy

Qubit spectrum

The qubit pulsed spectroscopy measurement protocol is shown in Fig. 6.6 and consists in applying a long microwave pulse at a given frequency to the qubit so as to prepare the qubit in a superposition of states $|0\rangle$ and $|1\rangle$ if the applied frequency is resonant with the qubit magnetic flux dependent frequency. A readout pulse is then sent through the readout line to probe the state of the resonator. Alternatively, a weak continuous signal can be sent through the readout line instead of a pulse to slowly gain information about the system with cumulated averages.

To measure the magnetic dependency of the qubit, we perform a frequency sweep of the spectroscopy protocol explained above, at various applied magnetic flux bias points. Each frequency dependent dataset is fitted with a Lorentzian or Gaussian model to extract the center frequencies (and width of the peaks). The center frequencies of the peaks we extracted are then plotted with respect to the applied magnetic flux. Figure 6.7 shows a coarse scan that was initially done to obtain a first estimate of qubit 2 parameters. From such a spectroscopy sweep we can fit the data with Eq. (2.65) and extract its persistent current I_p and its minimum energy splitting Δ. We find for qubit 1: $\Delta_1/h = 5.1317\,\text{GHz}$ and $I_{p2} = 383\,\text{nA}$; and for qubit 2: $\Delta_2/h = 3.664\,\text{GHz}$ and $I_{p1} = 351.5\,\text{nA}$.

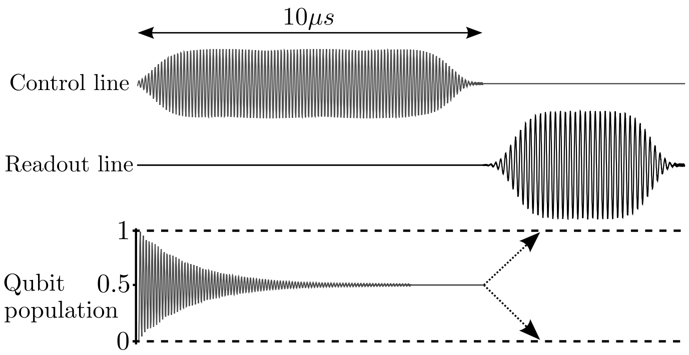

Figure 6.6: Qubit spectroscopy pulse diagram. A 10 µs pulse at a given frequency is applied to the qubit and the state of the resonator is measured with a readout pulse. The frequency is resonant with the qubit frequency, the qubit is prepared in a superposition of states and is either projected on the ground or excited state by the readout pulse. The sequence is repeated for a given pulse frequency range while the magnetic flux bias of the qubit is either kept constant or is swept to obtain a qubit spectroscopy versus qubit detuning 2D map.

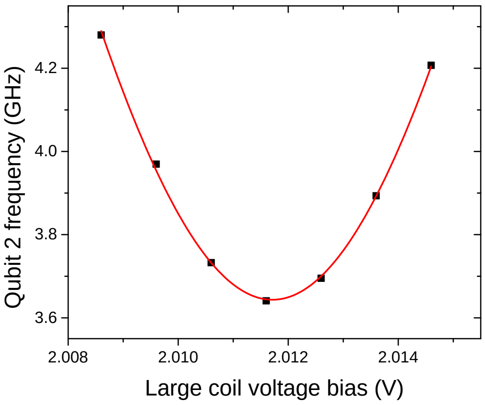

Figure 6.7: Qubit 2 spectrum. (black dots) Qubit 2 frequency versus the large coil voltage bias.(red curve) Fit to $\nu_{qb} = \sqrt{(\Delta/h)^2 + (\varepsilon/h)^2}$, where the coil voltage scale is first converted in units of Φ_0.

Spectroscopy over time

Qubit spectroscopy scans over time were done to verify the good functioning of the active magnetic field cancellation system, assuming the superconducting coil bias setup was stable itself. Indeed, without the shielding system active, measurements at anything but close to the symmetry points of the qubits were hardly stable as the qubits center frequencies were constantly drifting. Despite the passive shielding, and due to the relatively large area of the qubits and the magnetic flux focusing effect caused by the superconducting ground planes surrounding the qubits, small fluctuations of the field in the lab environment, in the order of nano Tesla, were enough to move the qubits by multiple spectral line widths. The displacement of a standard metallic lab chair a few meters away from the dilution fridge is enough to move the qubit by a couple MHz.

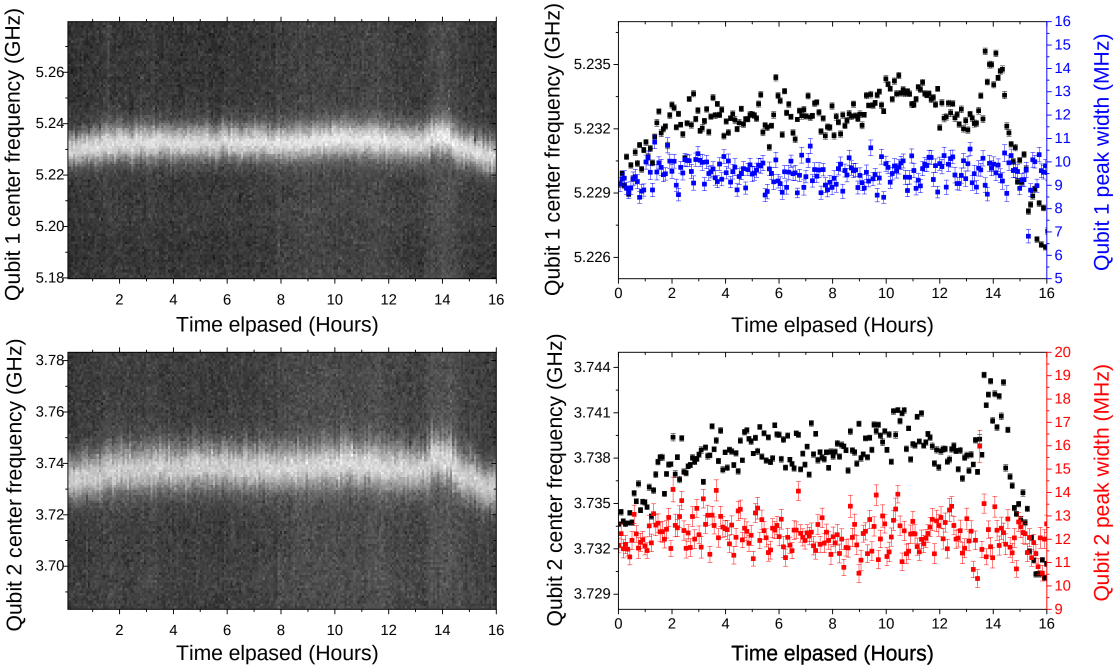

Figure 6.8: Qubits spectroscopy over time. Qubits spectroscopy over 16 hours when biased away from their symmetry points. Qubits are biased so that their coupling to the magnetic flux noise is comparable: qubit 1 at $\varepsilon_{qb1}/\nu_{qb1} = 0.18355$, and qubit 2 at $\varepsilon_{qb2}/\nu_{qb2} = 0.2$.

Figure 6.8 shows a 16 hours long scan done overnight for the two qubits biased at a coupling angle of ε/ν of about 0.2 in order for them to couple to the magnetic flux noise with a similar strength (proportional to their persistent current I_p). The 14th hour on the graph corresponds to 7:00 am of a weekday where we noticed a recurring shift of both qubits at that time. This shift correlates with a change of the ambient magnetic field measured in the lab at the position of the fridge certainly corresponding to a building DC electrical current surge.

The center frequency and width of the qubit spectroscopy peaks are extracted with a Gaussian fit and plotted on the two graphs on the right of Fig. 6.8. A linear Pearson correlation is calculated for the qubits center frequencies which measure the strength of a linear dependence between two variables. We find a normalized Pearson's r = 0.916 indicating a strong correlation between the center frequencies fluctuations of both qubits. The width of the peaks is however weakly correlated as the Pearson's r = 0.079 with a standard deviation of the width for qubit 1 of 0.5323 MHz and 0.759 MHz for qubit 2. Since the acquisition of one spectroscopy trace takes about 2.5 minutes, we can only consider the correlation numbers obtained in this time scale.

This experiment was repeated at a stronger coupling angle to the magnetic flux: $\varepsilon_{qb2}/\nu_{qb2} = 0.4$ for qubit 2 (with ν_{qb2} around 4.01 GHz) and $\varepsilon_{qb1}/\nu_1 = 0.3671$ for qubit 1 (with ν_{qb1} around 5.525 GHz). We found a center frequency correlation number r = 0.989 and peak width correlation number r = 0.022. The strong measured correlation confirms the assumptions that both qubits effectively feels the same ambient low-frequency magnetic field despite their different physical location on the chip and proximity to different size superconducting ground planes and control lines.

6.4 Readout characterization

The performance of the readout of the state of the qubits was investigated by varying three possible parameters: the duration of the readout pulse T_{readout}, the frequency of the readout signal ω_{RF}, as well as the amplitude of the readout pulse by controlling the amplitude and phase of the quadratures of the mixer. We distinguish two cases : case 1 where only one qubit is at or close to its symmetry point while the other one was flux biased to be at tens of GHz away from the other qubit frequency and resonator first mode, and case 2 where both qubits were are at their respective symmetry points. We proceeded with a rather brute force approach where a combination of parameters was swept. A zone of optimal readout contrast was found and then used for measuring the qubits. This section presents some of the typical contrast map obtained for typical values of optimal parameters we converged to for this device. The results shown below do not correct for the states preparation errors.

6.4.1 Case 1: one qubit at its symmetry point

Figure 6.9 shows the contrast map for a qubit 1 interacting with the resonator. For each point of the 2D map of Fig. 6.9a, the qubit is first prepared in the ground state and measured 10000 times. Instead of averaging on the fly the obtained homodyne voltages from the readout demodulation board, all the recorded measurements are saved. The qubit is then excited with a calibrated π pulse and similarly, 10000 measurements in the same conditions are recorded.

The data is then processed as shown in Fig. 6.9b to obtain the effective cumulative distributions for ground and excited state preparation from which we obtain the maximum contrast for an optimal voltage bin threshold. The 2D map represents on a gray scale the obtained contrast between 0 and 1. The center cone whose width increases with the drive amplitude corresponds to the bare cavity resonance driven at high power where the number of photons is large and is expected to behave non-linearly and classically. In this zone, the measured contrast is noisy, contains some apparent high contrast points, but attempts at measuring the qubit at some of these points showed only noisy signal. Due to the large power in the resonator when it is driven on resonance, it is likely that the response is no longer monostable and is very sensitive to driving amplitudes, which have slow drifts in the course of our experiments. A typical dataset like shown in Fig. 6.9b takes more than 10 hours to acquire. This noisy cone shape should, therefore, be omitted by the reader from this analysis.

The readout contrast when the probe signal ω_{RF} was set to be $\omega_r \pm \chi_{q1}$ (with $\chi_{q1} \simeq 18\,\mathrm{MHz}$) was only about $2\,\%$. By increasing the number of photon in the readout pulse, the cavity pull 2χ is effectively reduced as theoretically studied in [107] and [108], and experimentally observed in [109] for transmon devices. As the average photons population is increased, the cavity pointer states (shifted resonator frequency) reflecting the qubit states are measured with less noise and can be resolved one from the other more efficiently.

In the 2D map shown for qubit 1, we indeed observe a certain symmetry of the high contrast zones on each side of the bare cavity resonance cone. The data obtained at the red point indicated on the map is shown in the subplots below it and we obtained a readout contrast of about $65\,\%$. We observe in the ground state histogram, in black, that the qubit preparation is imperfect at this

(a) Qubit 1 readout contrast map for $T_{\text{readout}} = 4\,\mu\text{s}$. The red dots indicates the readout point for which the subplots 6.9b are shown.

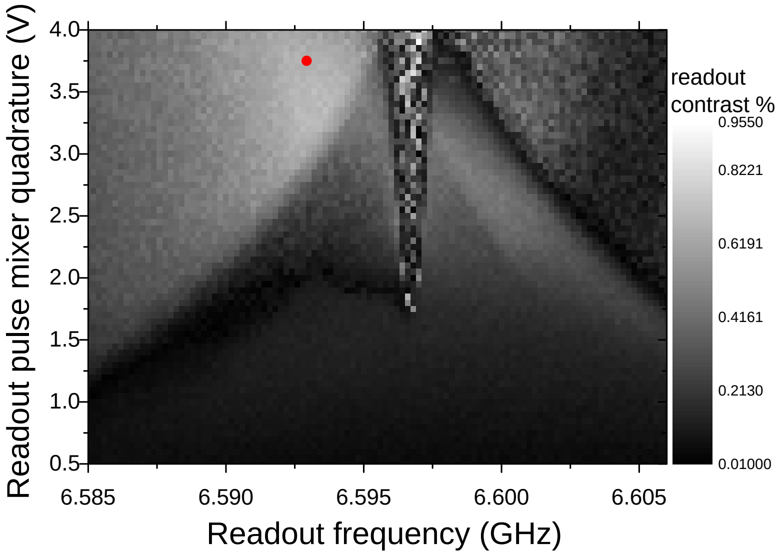

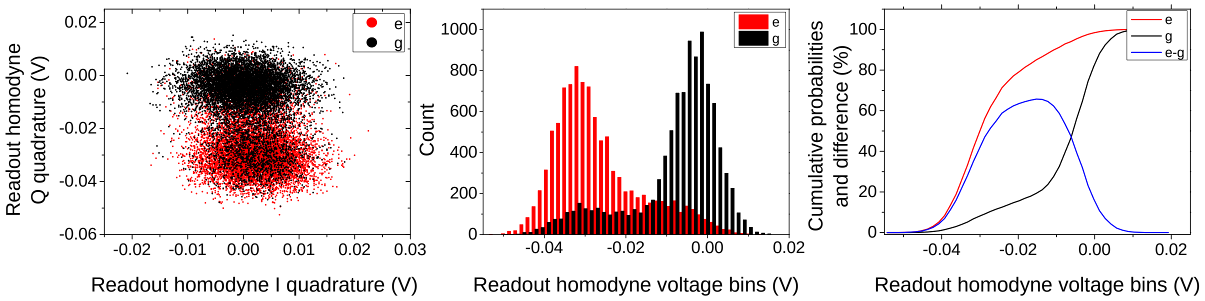

(b) Data for readout point shown in red in 6.9a: (left) 10000 individual measurements plotted on the IQ plane. (middle) Overlaid histograms for the ground and excited states measurements. (right) Cumulative probabilities and contrast (blue).

Figure 6.9: Qubit 1 readout contrast map. Qubit 1 readout contrast map as the readout frequency and pulse amplitude are swept (readout pulse duration $T_{\text{readout}} = 4\,\mu\text{s}$). Each data point is the readout contrast obtained out of 10000 consecutive measurements for both excited state and ground state preparations.

high power readout point. Reducing the drive amplitude improved the ground state preparation while maintaining readout contrasts above 60 %. For this reason, we did not operate the device as such large drive amplitude, which were indeed kept to be in the range of 1 to 2 V for most of this device study.

A finer scan around the cone described above and centered around ω_r revealed an interesting zone of high contrast at the border of its tip as shown in Fig. 6.10. The maximum contrast at the point shown in red in 6.10b exceeds 85 %. However, the histogram recorded for the excited state preparation shows an atypical distribution revealing a possibly induced decay of the qubits during the readout pulse, towards the ground state. Similar behaviour was observed for qubit 2. Further work is needed to fully understand this behaviour. This high contrast might allow single shot measurements of the qubit states with high fidelity.

6.4.2 Case 2: both qubits at their symmetry points

In order to implement and characterize the CNOT gate presented in Ch. 8, we need to be able to jointly readout the states of the two qubits for any combinations of states preparation. In this case, both qubits were operated at their symmetry points and similarly to the previous section, we varied the readout parameters to find an optimal readout point that would maximize the contrast between the four possible states $|00\rangle$, $|10\rangle$, $|01\rangle$, $|11\rangle$. The four states were prepared at each point of the readout parameters sweep and the homodyne voltages recorded.

Contrary to the previous plots for the single qubit readout case, we show in Fig. 6.11 the map of the distances on the IQ plane between the states. The states separability from the $|00\rangle$ state is relatively large but states distance like $|10\rangle \leftrightarrow |01\rangle$ are much smaller as seen on the second row.

The qubits states population for a joint readout scheme can be reconstructed with the Maximum likelihood estimation (MLE) technique which is a common approach to two-qubit quantum state tomography. Given the observed fluctuations over time of the readout parameters at a given set frequency and quadrature voltage, we need to minimize the sensitivity of the readout point to small parameters changes. Figure 6.12 shows the condition number[1] of the matrix to be inverted on the same parameters axis as the state separations. For a "good" readout point, we need to not only maximize the states separability but also minimize the matrix condition number.

---

[1] Indeed, a problem is well-conditioned if its associated condition number is small (near 1). In linear algebra, the condition number is a measure of the sensitivity of a matrix to operations.

Figure 6.10: Qubit 1 readout contrast map near the resonator bare frequency.

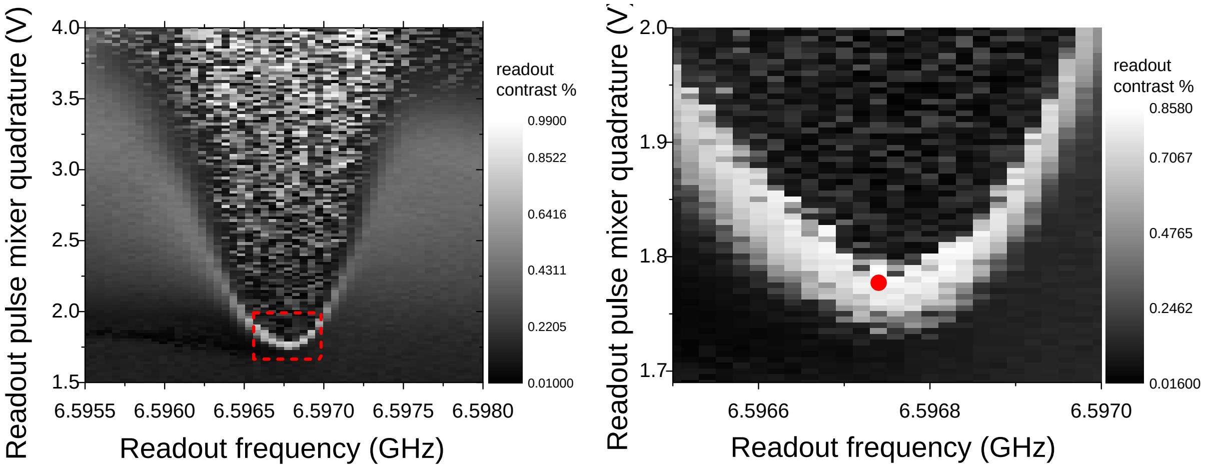

(a) Contrast map for $T_{\text{readout}} = 4\,\mu\text{s}$.

(b) Finer scan of the red box defined in **(a)**.

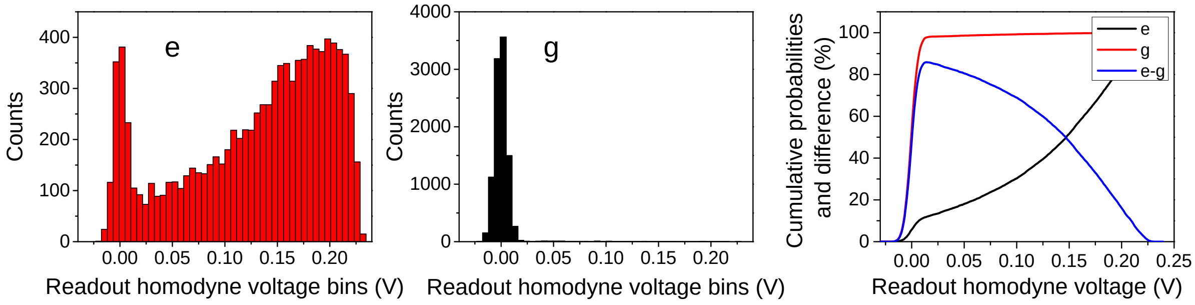

(c) Qubit 1 readout histograms for 10000 consecutive measurements when prepared in the excited state (left) and ground state (middle) for a readout pulse frequency $\nu_{\text{readout}} = 6.596\,74\,\text{GHz}$ and IQ-mixer I amplitude of 1.78 V (red dot in Fig. 6.10b). Readout pulse duration $T_{\text{readout}} = 4\,\mu\text{s}$. (right) Cumulative probabilities of histograms and their difference (blue) showing a maximum readout contrast of 85.9 %.

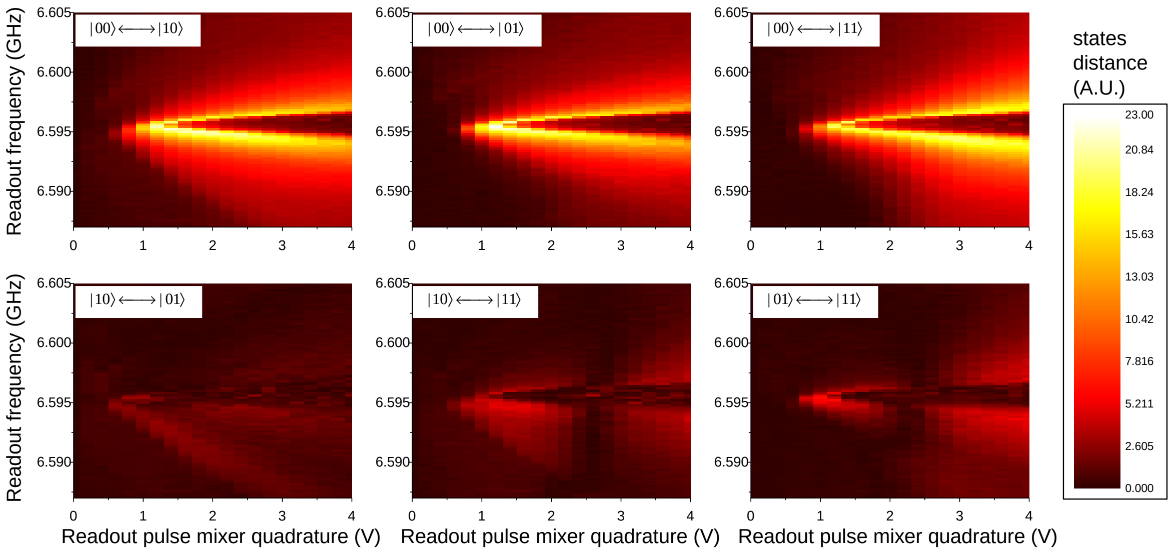

Figure 6.11: Two qubits states separation versus readout amplitude and frequency. Calculated states distance from each other on the IQ plane.

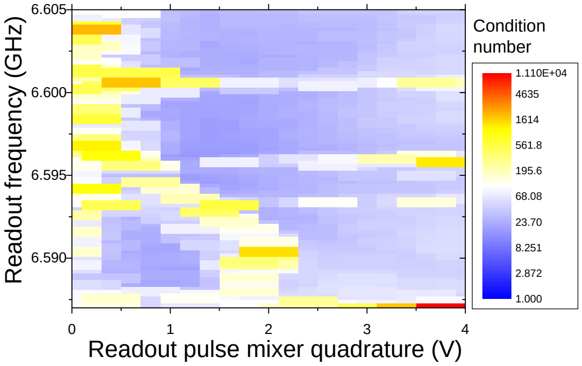

Figure 6.12: Two qubits joint readout: matrix condition number map. Calculated matrix condition number. We choose a readout point that minimizes the condition number and maximizes all the state separations.

6.5 Ground state initialization

Efficient initialization of the qubits is one of the requirements for the implementation of a physical quantum computer. With superconducting circuits, this is usually accomplished by simply waiting that the qubit relaxes to the thermal ground state which is assumed to be negligibly thermally populated at the typical temperatures reached with a dilution refrigerator. All the measurements in this work are ensemble averages of many repetitions, acquired with a repetition time T_{rep}. Given the high Q factor of the resonator and the relatively long qubits T_1, as will be presented in section 6.7.1 , a $T_{\text{rep}} = 130\,\mu\text{s}$ is chosen. The temperature of the environment coupled to the device leads to an average photon population which follows a Bose-Einstein Distribution. The probability of finding the resonator in the excited state at a temperature T and frequency ω_r is given by:

$$P_e \approx e^{-\frac{\hbar\omega_r}{k_B T}} \tag{6.9}$$

which at a reasonable upper bound of the device temperature of 50 mK leads to a $P_e \simeq 0.0017$ for the resonator (see also section 8.1.2 of Chunqing Deng's thesis [110] for more details on our measurements of thermal photons in the resonator).

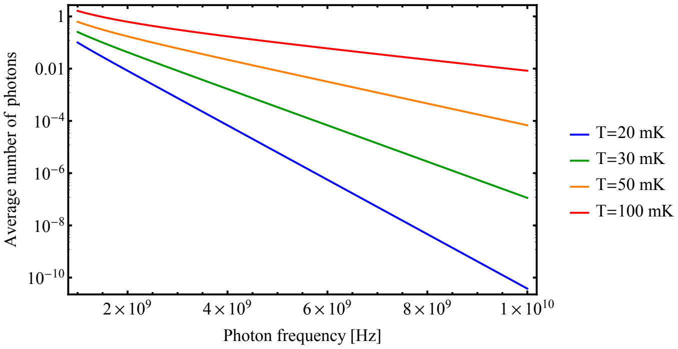

Figure 6.13: Average photon-number due to thermal population at finite temperatures versus frequency.

Qubits placed in a superconducting high Q resonator are usually isolated from the surrounding EM environment due to the resonator filtering properties. However, the fast bias lines used to control the qubits are a direct channel of thermal photons which can propagate from the higher thermal anchoring stages of the dilution fridge if improper filtering on the line is used. Figure 6.13 plots the average number of photons at various temperatures versus frequency. Qubits with low frequencies are therefore expected to have spurious thermal excitation if the effective temperature of their environment is not low enough. Microwave-induced cooling techniques [111, 112] exist, that allows reducing the effective temperature of superconducting qubits by a factor between 10 and 100.

6.6 Qubit manipulation

6.6.1 Rabi oscillations

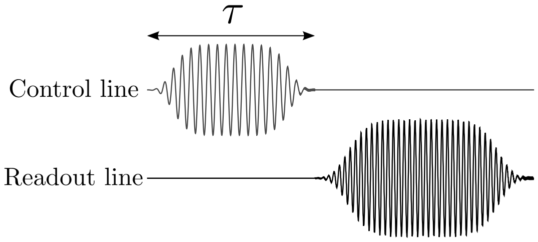

Figure 6.14: Pulse diagram for measuring Rabi oscillations between the qubit and the resonator. A pulse resonant with the qubit frequency is applied to the qubit and the state of the resonator is measured with a readout pulse. The sequence is repeated for varying pulse duration τ.

Using a coherent microwave drive, we can induce oscillatory transitions between the ground and excited state of the qubit (stimulated emission) by applying a pulse with a given amplitude and duration at the qubit frequency (see protocol in Fig. 6.14). The frequency Ω of the Rabi oscillations is proportional to the strength of the EM radiation. The Rabi frequency also depends on the detuning of the drive $\delta\omega$ from the qubit frequency and is expressed as:

$$\Omega_R = \sqrt{\Omega^2 + \delta\omega^2}. \tag{6.10}$$

Rabi oscillations measurements, where the drive frequency is swept, can, therefore be used to determine the qubit frequency when Ω_R is minimum. Figure 6.15 shows the measured linear dependence of Ω on the drive amplitude expressed in the graph as the AWG voltage applied to the mixer quadrature controlling the pulse amplitude.

Figure 6.16 shows driven Rabi oscillations measured for qubit 1. In this figure, the qubit population homodyne voltages of the vertical axis have been normalized with respect to an average

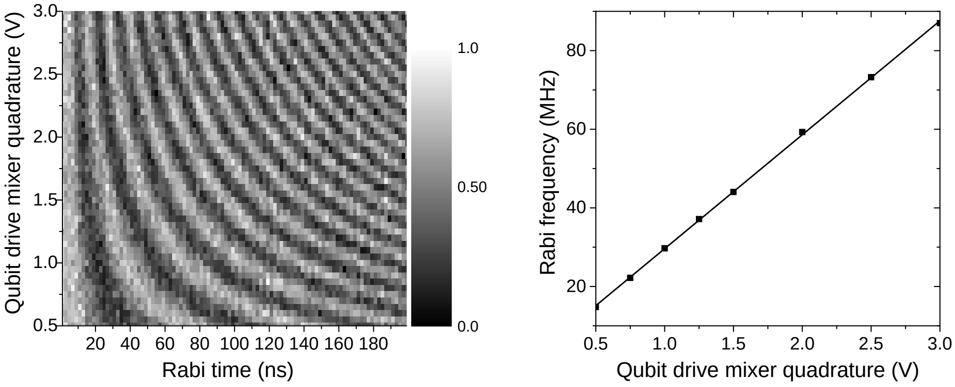

Figure 6.15: Rabi oscillations versus qubit control drive amplitude. (left) 2D map of the normalized qubit population versus Rabi time (horizontal axis) for different qubit control drive amplitude (vertical axis). Horizontal traces are decaying Rabi oscillations of the qubit at a given Rabi drive amplitude with frequency resonant with the qubit frequency. **(right)** Block dots are extracted Rabi frequency for various qubit drive voltage. The black line is a linear fit of the Rabi frequency versus the qubit drive voltage.

of 10^4 voltages measured for a ground state preparation and similarly for the π pulse preparation. This normalization does not take into account ground state preparation errors nor de-embeds the readout contrasts errors. Since each data points is an ensemble average measurement of typically 10^4 identical experiments for the same value of pulse duration τ, the observed decay of the oscillations amplitude results from noise induced variations in the Rabi frequency which leads each measurements to have different phases. This effect is amplified as the pulse duration increases.

We use Rabi oscillations measurements for the initial calibration of π and $\frac{\pi}{2}$ pulses. For a given drive amplitude, we obtain the duration of a pulse needed to have a full rotation of the qubit state on the Bloch sphere from $|0\rangle$ to $|1\rangle$ (a π rotation along the x- or y-axis). Since the time resolution of the pulses of the setup is set to one nanosecond, we then sweep the amplitude for a π pulse until a maximum homodyne average voltage is measured. More precise calibration is obtained with the procedure presented next.

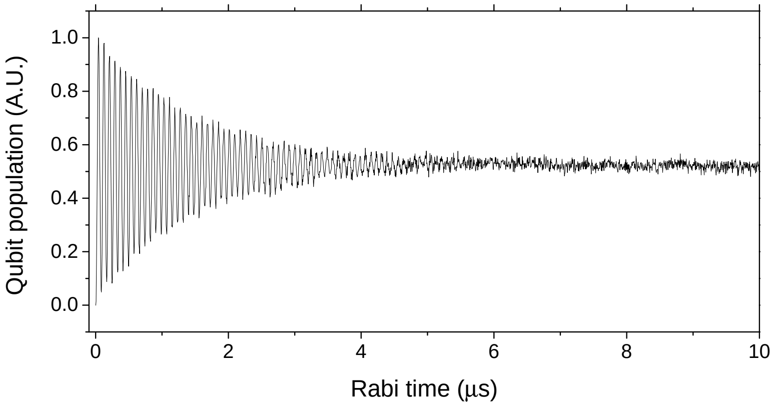

Figure 6.16: Qubit 1 Rabi oscillations. Rabi oscillations for qubit 1 showing a decay due to energy relaxation and dephasing.

6.6.2 Pulses calibration

In order to optimize single-qubit and two-qubit gates as well as prepare accurately the states of the qubits in the decoherence measurements we performed, we need to calibrate the various pulses used: $\pm R_{x\frac{\pi}{2}}$, $\pm R_{y\frac{\pi}{2}}$,$\pm R_{x\pi}$ and $\pm R_{y\pi}$ (see Sec. 2.2.3 of Ch. 2 for the definition of those pulses). A train of pulses separated by 50 ns is sent through a qubit control line and the state of the qubit is then measured.

For a perfect $\frac{\pi}{2}$ pulse we expect to find the qubit in a superposition of states corresponding to a readout homodyne voltage halfway between the ground and excited state. Since the AWG only allows time resolution in the order of the nanosecond, we tune the IQ mixer quadrature voltages with millivolts resolution for a given desired pulse duration. If the pulse results in a qubit rotation along the axis x or y slightly smaller or larger than 90 degrees, the error will accumulate and the train of n pulses (n being odd) will draw a zigzag pattern with increasing amplitude as seen in Fig. 6.17. A $\frac{\pi}{2}$ pulse is calibrated once the signal flattens optimally. π pulses are then calibrated by first sending a calibrated $\frac{\pi}{2}$ pulse followed by an odd number of π pulses. This procedure is repeated every couple hours for all the pulses used in this work, as we observed small variations over time, thought to be mostly due to temperature changes affecting the microwave setup and drifts of the DC offsets of the AWG.

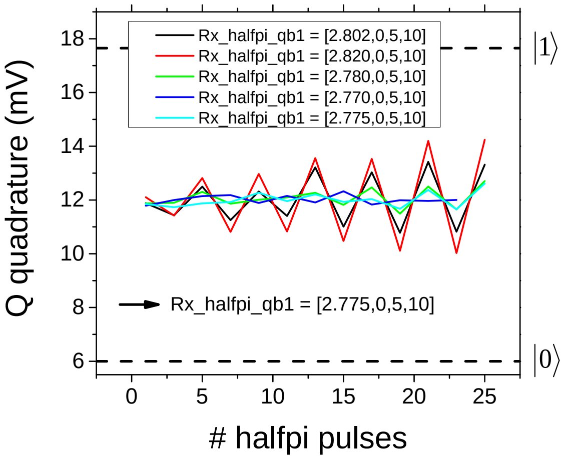

Figure 6.17: Qubit 1 $R_{x\frac{\pi}{2}}$ pulse calibration. The quadrature voltages of the qubit control IQ mixer are fine tuned to optimize the accuracy of a 5 ns $\frac{\pi}{2}$ pulse. The programming format used in the control software and shown in the labels of the legend is: [I quadrature (V), Q quadrature (V), duration (ns), variable attenuator setting (dB)]. The voltage settings that flatten optimally the measured traces of a train of pulses are kept.

6.7 Pulse scheme for qubit energy relaxation and dephasing measurements

6.7.1 Qubit energy relaxation T_1

The energy relaxation time of the qubit to its environment T_1 is extracted from an ensemble average of identical qubit preparations and measurements. The qubit, assumed to be in its ground state after waiting a sufficiently long time, is prepared in the excited state with a calibrated π pulse. After a swept time τ the qubit state is measured (see Fig. 6.18). The qubit population decays exponentially back to its ground state as τ increases.

A typical energy decay curve for qubit 2 at its symmetry point is shown in Fig. 6.19. The data points are fitted with the following formula where all parameters are kept free:

$$y = y_0 + Ae^{-\frac{\tau-\tau_0}{T_1}}. \tag{6.11}$$

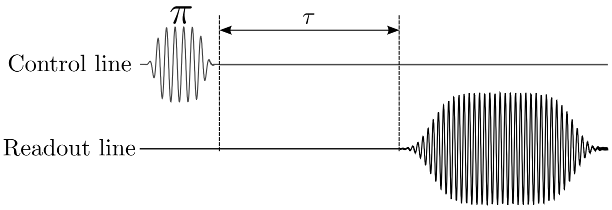

Figure 6.18: Pulse diagram for T_1 measurements. A π pulse resonant with the qubit frequency is applied and the state of the resonator is measured with a readout pulse after a time τ. The sequence is repeated for varying time τ.

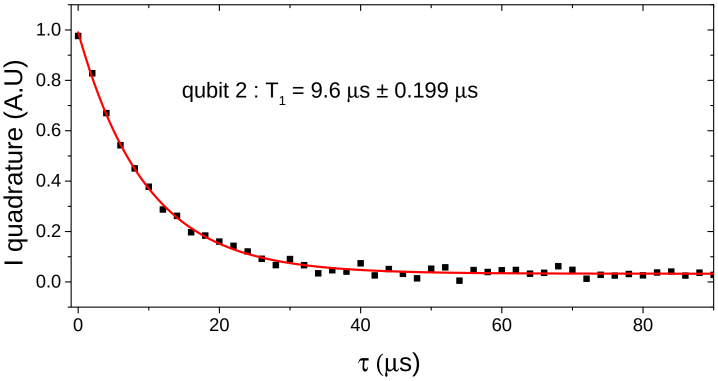

Figure 6.19: T_1 measurement for qubit 2 at its symmetry point. Measured voltage amplitude versus duration τ separating the π pulse and the readout pulse. The red curve is a fit to Eq. 6.11.

We observed for both qubits some fluctuations around nominal values from one acquisition to another in the order or ±1 µs. Typical value of T_1 for qubit 1 at its symmetry point is 5.3 µs.

In order to better understand the energy decay of the qubit due to its coupling to the resonator modes, a phenomenon called the Purcell effect, we study the T_1 decay over a wide range of frequencies. The Purcell effect of the resonator mode n has a rate given by:

$$\gamma_n = \kappa_n \left(\frac{g_n}{\delta_n}\right)^2, \tag{6.12}$$

where κ_n is the rate at which the nth mode of the resonator loses its photon, g_n the coupling of the qubit to the n$^{\text{th}}$ mode with a detuning of the qubit and resonator mode $\delta_n = \omega_q - n\omega_r$. The formulation of g_n takes into account the different profiles of the nth current mode supported by the $\lambda/2$ resonator. The shape of the first three current mode supported by the resonator of our device is shown in 6.20 where the vertical dashed line indicates the position on the device of qubit 1 (left) and qubit 2 (right) versus the length of the resonator. We can therefore calculate the corresponding g_n for the qubits and estimate the total Purcell rate, taking into account the energy decay path of the qubit due to its coupling to a 50 Ω environment through the mutual inductance coupling of its control line. Figure 6.21 shows the estimate decay time for the first three modes of the resonator and the qubit control line over a wide range of qubit frequencies.

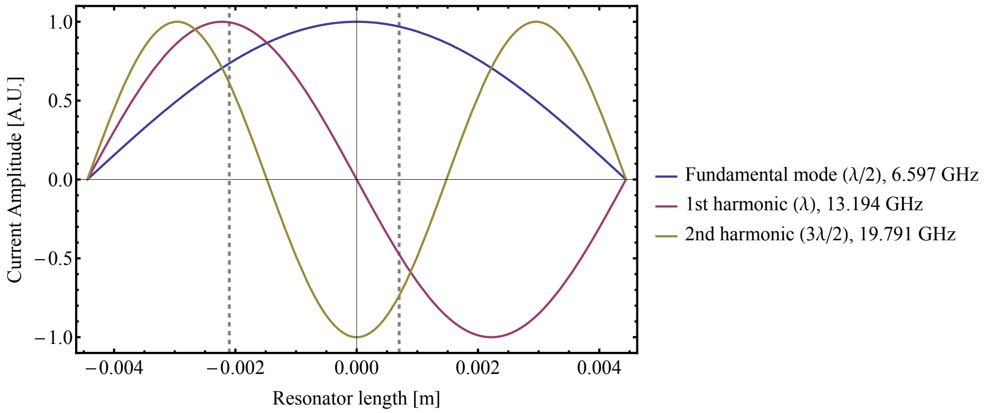

Figure 6.20: Shape of the first three current modes in the $\lambda/2$ resonator of device W37_c2d. Vertical dashed lines indicate the position of the qubits along the length of the resonator (qubit 1: left dashed line, qubit 2: right dashed line). The colored lines plot the microwave current amplitude along the length of the resonator, at $\lambda/2$ resonance and the first two harmonics.

Figure 6.22 overlays the T_1 measured for qubit 1 over a wide frequency range and the fit to the Purcell model describe above, taking into account the decay through the control line and some finite[2] intrinsic T_1 of the qubit as the only fit parameter (unconstrained). With the assumption of this model, we find for qubit 1 $T_{1,\text{int}} = 5.2\,\mu\text{s}$. Unlike transmon qubits which concentrate electric energy in between the fingers of their interdigitated capacitors and are subject to dielectric loss with a $1/f$ dependency, flux qubits are not expected to follow this trend, and therefore I did not consider an intrinsic Q factor with $1/f$ dependency. While some measurements of T_1 in between the first two cavity modes exceeded the T_1 measured close to the qubit symmetry point, others where lower. The measurements far away from the qubit symmetry point required readjusting the readout pulse and acquisition parameters. At those large detunings of the qubit and the

---

[2] We did not consider any flux dependence of the intrinsic T_1 of the qubit.

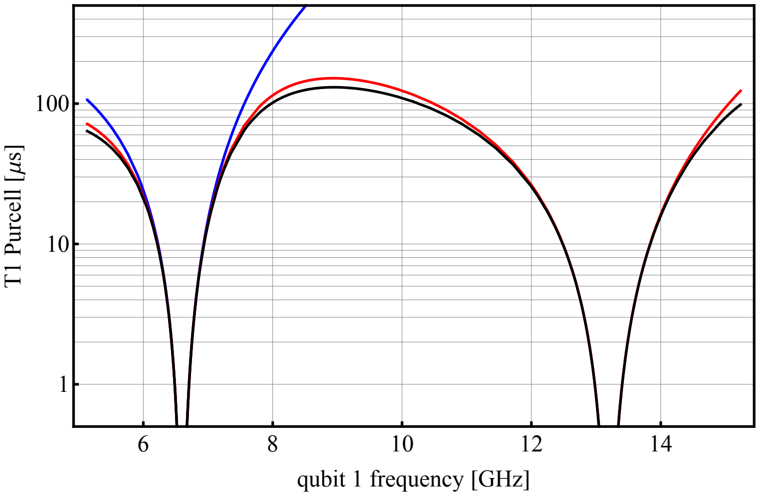

Figure 6.21: Multimode Purcell effect. Predicted T_1 versus qubit 1 frequency for the multimode Purcell effect, for the first three modes: (blue) Fundamental mode only, (red) considering the first two modes only, (black) and considering the first three modes.

resonator, the acquired readout signal was noisy. The measured qubit population decay data points were noisier than when close to the symmetry point and the resulting fitted T_1 showed large fluctuations over that range of frequencies. It is unclear if these large fluctuations are real and due to environment felt by the qubit in the 7 to 12 GHz.

6.7.2 Ramsey fringes experiment: T_2^*

The coherence time of the qubits during free evolution is obtained with Ramsey fringes experiments [113]. Two microwave pulses corresponding to a $\frac{\pi}{2}$ rotation around the x (or y) axis are sent through the qubit control lines separated by a swept time τ (see Fig. 6.23). The pulses microwave frequency is detuned from the qubit frequency by a fixed amount. The qubit, seen here as a spin, can precess freely around the z-axis during its free evolution. Decaying oscillations are measured with a frequency equal to the detuning. These oscillations reveal the effective beating of the spin precession with the off-resonant microwave excitation.

The dephasing of the qubit coherence is caused by slow variations of the effective field along its quantization axis σ_z due mostly to magnetic flux noise which causes phase randomization. Other sources of dephasing can be due to charge fluctuations in the substrate or at the interface

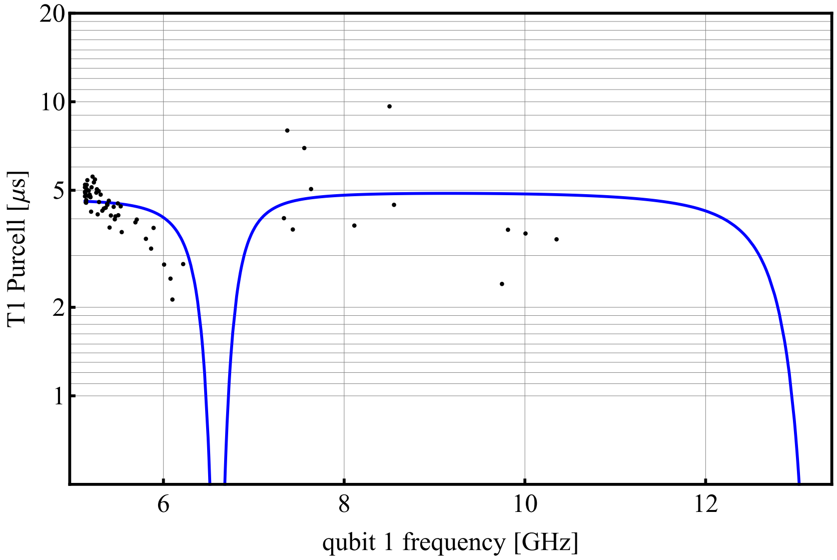

Figure 6.22: Fit of qubit 1 T_1 to the multimode Purcell effect model with an intrinsic qubit T_1. Fit of qubit 1 T_1 measured at various frequencies, to the multimode (n = 3) Purcell effect model with an intrinsic qubit $T_{1,int}$, taking into account the decay rate through the qubit control line.

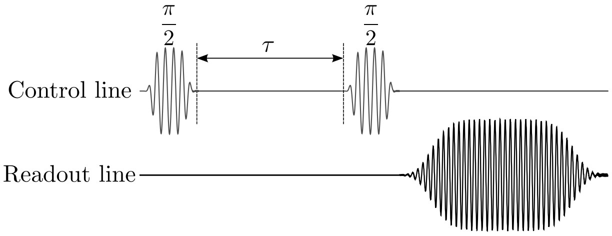

Figure 6.23: Pulse diagram for measuring the dephasing constant of the qubits T_2^*. Two $\frac{\pi}{2}$ pulses off-resonant by a few MHz with the qubit frequency are applied to the qubit, spaced by a time τ before the state of the resonator is measured with a readout pulse. The sequence is repeated for varying time τ.

with the superconducting material, trapped vortices in the superconducting film, paramagnetic or nuclear spins in proximity of the qubit, quasiparticle tunneling in the Josephson junctions of the qubit itself, coupling to phonon modes of the substrate and linked to the electrical environment to which it is connected.

From the envelope of the measured signal, we can extract the characteristic dephasing time T_2^* of the qubit at a given magnetic flux bias. In this section, only results obtained at the qubits symmetry points, where it is least sensitive to flux noise, are shown. The following chapter studies in more details the qubits decoherence mechanism. The following fitting formula is used:

$$y = y_0 + Ae^{-\left(\frac{\tau+\frac{\phi}{f}}{2T_1}\right)-\left(\frac{\tau+\frac{\phi}{f}}{T_2^*}\right)^{\alpha}}\cos(2\pi f\tau + \phi), \tag{6.13}$$

with the exponent $\alpha = 2$ for a Gaussian decay model, as typically assumed for flux qubits. Notice that the energy decay time of the qubit is previously measured and taken into account in the formula. When the qubits are at their respective symmetry points, we measured a disagreement with the assumed Gaussian decay. Figure 6.24 shows Ramsey oscillations for qubit 2 at two different microwave drive detuning. Three fitting curves are overlaid with the data points: in red for a Gaussian decay, in blue for a exponential decay fit ($\alpha = 1$) and in green for a fit where α was kept as a free parameter. For measurement shown in Fig. 6.24b we find:

- Gaussian, $\alpha = 2$: $T_2^* = 1114.17$ ns ± 30.66 ns
- Exponential, $\alpha = 1$: $T_2^* = 889.74$ ns ± 33.73 ns
- Exponential (free), $\alpha = 1.31$: $T_2^* = 1006.44$ ns ± 40.05 ns.

Although the fitting errors reported are of similar magnitude, simple observations of the graphs shows the disagreement of the Gaussian decay fit in the tails of the oscillations. In the following chapter on decoherence measurement, we study the dephasing of the qubit as the coupling to the magnetic flux noise is increased when the qubit is moved away from its symmetry point.

6.7.3 Spin echo experiments: $T_{2\mathrm{echo}}$

Spin (Hahn) echo technique [114] is a standard NMR pulse scheme [115] applicable to flux qubits which corrects slow fluctuations of the frequency of the qubit during the ensemble average measurement. For flux qubits, this technique principally cancels effects due to low-frequency

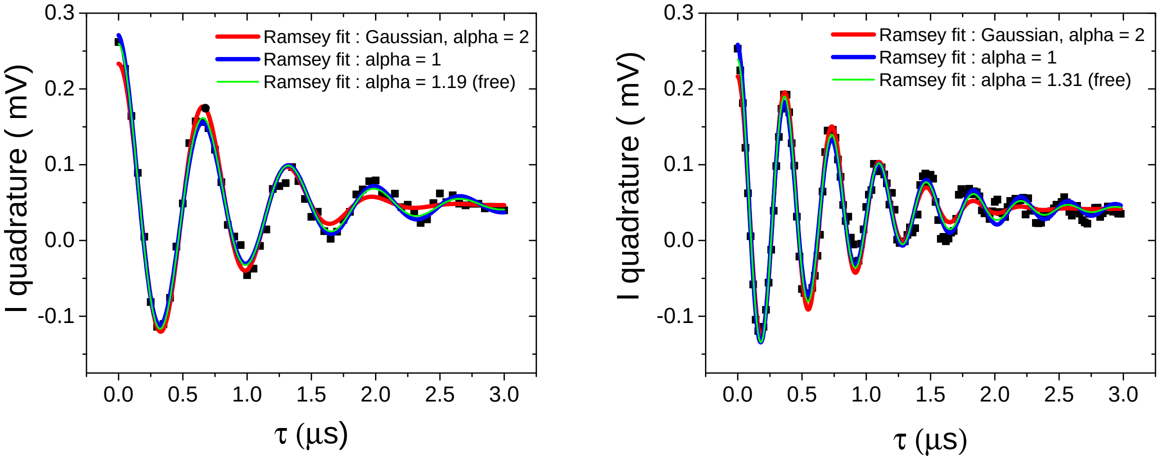

(a) Qubit 2 at its symmetry point: Ramsey sweep with a 1.5 MHz detuning with 3 different fitting procedures.

(b) Qubit 2 at its symmetry point: Ramsey sweep with a 2.7 MHz detuning with 3 different fitting procedures.

Figure 6.24: Ramsey fringes measurement for qubit 2 at its symmetry point. Measured voltage amplitude versus duration τ separating the two $\frac{\pi}{2}$ pulses (black squares). The three curves are fits to Eq. 6.13 for different α values as indicated in the legends. For the green curve, α is left as a free fit parameter, whereas it is forced to be 1 or 2 for the two others.

temporal variations of the ambient magnetic field, and, therefore one expects $T_{2\text{echo}} > T_2^*$. $T_{2\text{echo}}$ reflects better the intrinsic dephasing time of the qubit.

The spin echo pulse sequence is similar to the Ramsey one in which a π pulse is inserted in between the two $\frac{\pi}{2}$ pulses (see Fig. 6.25). If the frequency of the magnetic field perturbation during free precession do not change on the time scale of the measurement sequence, the π pulse effectively compensate for the random phase accumulated during the time $\tau/2$. In our measurements, the frequency of the microwave pulses was set to be the one of the qubit measured just before the sequence using spectroscopy and Ramsey.

A characteristic measurement for qubit 2 is shown in Fig. 6.26 with three fit curves where the choice of exponent of the following formula is varied:

$$y = y_0 + Ae^{-\left(\frac{\tau - x_0}{2T_1}\right) - \left(\frac{\tau - x_0}{T_{2\text{echo}}}\right)^{\alpha}}. \tag{6.14}$$

For this measurement with qubit 2 at its symmetry point we find:

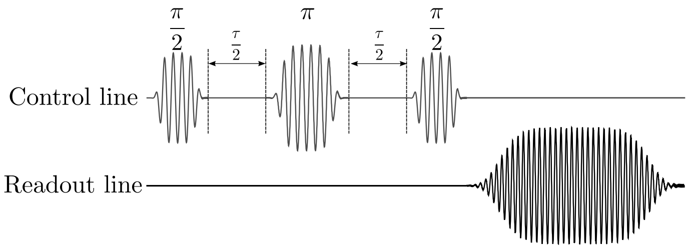

Figure 6.25: Pulse diagram for Spin echo measurements. Pulse diagram for the Spin (Hahn) echo experiment with a $T_{2\text{echo}}$ time constant. Two $\frac{\pi}{2}$ pulses and a π pulse resonant with the qubit frequency are applied to the qubit. The π pulse is applied after a time $\frac{\tau}{2}$ before the state of the resonator is measured with a readout pulse. The sequence is repeated for varying time τ.

- Gaussian, $\alpha = 2$: $T_2^* = 1255$ ns ±49.34 ns
- Exponential, $\alpha = 1$: $T_2^* = 1563.39$ ns ±61.16 ns
- Exponential (free), $\alpha = 0.94$: $T_2^* = 1608.39$ ns ±88.89 ns.

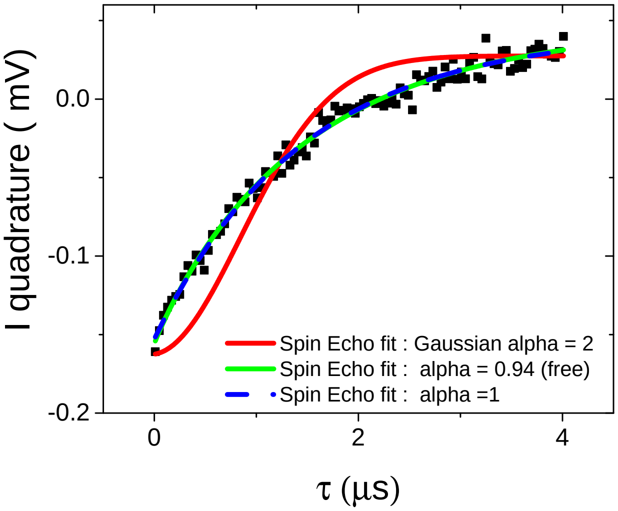

Figure 6.26: Spin echo measurement for qubit 2 at its symmetry point. Measured voltage amplitude versus duration τ separating the two $\frac{\pi}{2}$ pulses (black squares). The three curves are fits to Eq. 6.14 for different α values as indicated in the legend. For the green curve, α is left as a free fit parameter, whereas it is forced to be 1 or 2 for the two others.

The measured decay agrees well with an exponential fit. We will see in the next chapter how the decay process changes from exponential decay-like to Gaussian decay-like process as the flux qubits couple more strongly to magnetic flux fluctuations assumed to follow a Gaussian law.

6.7.4 Dynamical decoupling pulse sequence experiments

The technique of using a π pulse to cancel out the random phase accumulated during free precession, as described above in the spin echo pulse scheme, can be generalized to the use of N π pulses, resonant with the qubit. This dynamical decoupling technique is adapted from the field of NMR and often used with trapped ions [116]. A particular implementation of such dynamical decoupling pulse technique where the refocusing π pulses are uniformly spread between two $\frac{\pi}{2}$ pulses, with identical phase, is called a Carr-Purcell (CP) scheme [117]. A variant of this technique called a Carr-Purcell-Meiboom-Gill (CPMG) [118] pulse scheme contains π pulses that are 90° phase shifted with respect to the $\frac{\pi}{2}$ pulses (see Fig. 6.27). This phase offset tends to reduce the accumulating effects of π pulse calibration imperfections.

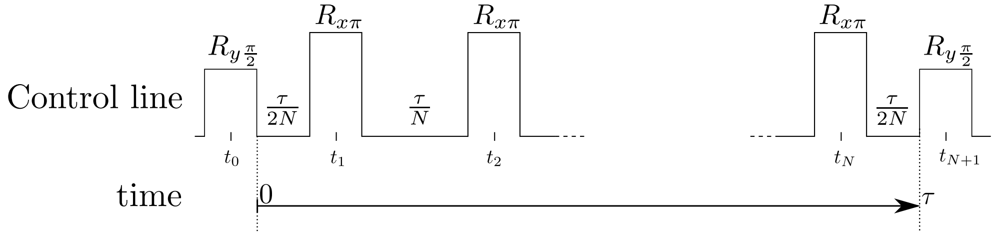

Figure 6.27: Diagram for a CPMG pulse sequence. Two $\frac{\pi}{2}$ pulses, resonant with the qubit frequency, are separated by a varying time τ. N equally spaced π pulses, which are 90° phase shifted with respect to the first $\frac{\pi}{2}$ pulse, are applied during the τ duration. The sequence is repeated for varying times τ and different numbers of π pulses.

In addition to improving the qubit pure dephasing time, we can use various CPMG pulse sequences to study the spectral composition of the noise of the qubit environment. Resolving and quantifying the spectral density of a qubit can potentially help isolating the source of the noise and help finding remedies to fight decoherence [119]. It can potentially help guiding the refinement of the design, fabrication, vacuum hygiene or electrical equipment filtering and signal conditioning. Using this dynamical decoupling noise spectroscopy technique with a flux qubits operated at a bias point where it is sensitive to flux noise is analogous to having a quantum spectrum analyzer [120]. Following similar approach as in the work of Bylander *et al.* [121] where a flux qubit with a SQUID readout was used, we present experimental results of decoherence measurements of flux qubits in cQED in Ch. 7.

The application of N refocusing π pulses in the time domain transposes to constraining the noise power spectral density (PSD) with a band-pas filter which center frequency peaks at around $\omega \approx \pi N//\tau$. Figure 6.28 shows the representation of the effective filter function $F_N(\omega, \tau)$ for $\tau = 1\,\mu\text{s}$ and a various N.

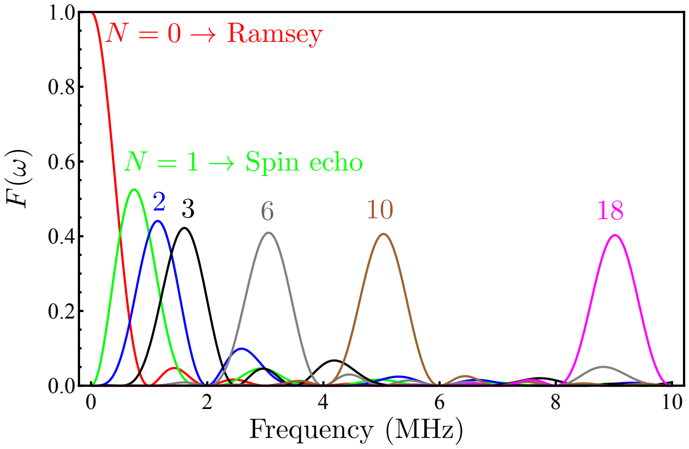

Figure 6.28: Filter function $F_N(\omega, \tau)$ of the CPMG sequence for various numbers of π pulses with $\tau = 1\,\mu\text{s}$. When N=0 the filter function is equivalent to the Ramsey type pulse sequence, and with N=1 the CPMG filtering function reduces to the one of the Spin echo sequence. The filter function peaks at around $\omega \approx \pi N//\tau$.

Assuming the noise PSD to be approximately uniform over the width of the band-pass response, we can reconstruct the PSD of the qubit flux noise over a certain range of noise frequencies. Although the derivations of the coherence function $C(\tau)$ (see Eq. 2.89), filter function, and PSD, follow the work in Bylander and Biercuk cited above (and their respective supplementary material), we redefined the filter function to take into account the decay during the N π pulses and not just the free-precession decay, in our calculation of the flux noise PSD. Another reference, the reader who would like to learn more on this topic might find useful, is Chapter A 4, Section 3 by William D. Oliver in the published lecture notes of [122].

As an example for CPMG pulses with N taking values 1, 10, and 20, the decay of coherence for qubit 1 versus the evolution time is shown in Fig. 6.29(a)-(c). Figure 6.29(d) shows the calculated qubit frequency noise PSD from those decay curves (matching symbol and color between the decay points used to compute the PSD in (a)-(c) and (d)), where qubit 1 was far from its optimal bias point, at $a = 0.2$, where the transition frequency noise is due primarily to magnetic flux fluctuations. We find a transition frequency noise PSD which is well approximated by a $1/\omega^{\alpha}$ dependence, with $\alpha = 0.71$. More extensive measurements with large N (up to $N \approx 120$) were done, which covered a wide range of frequencies.

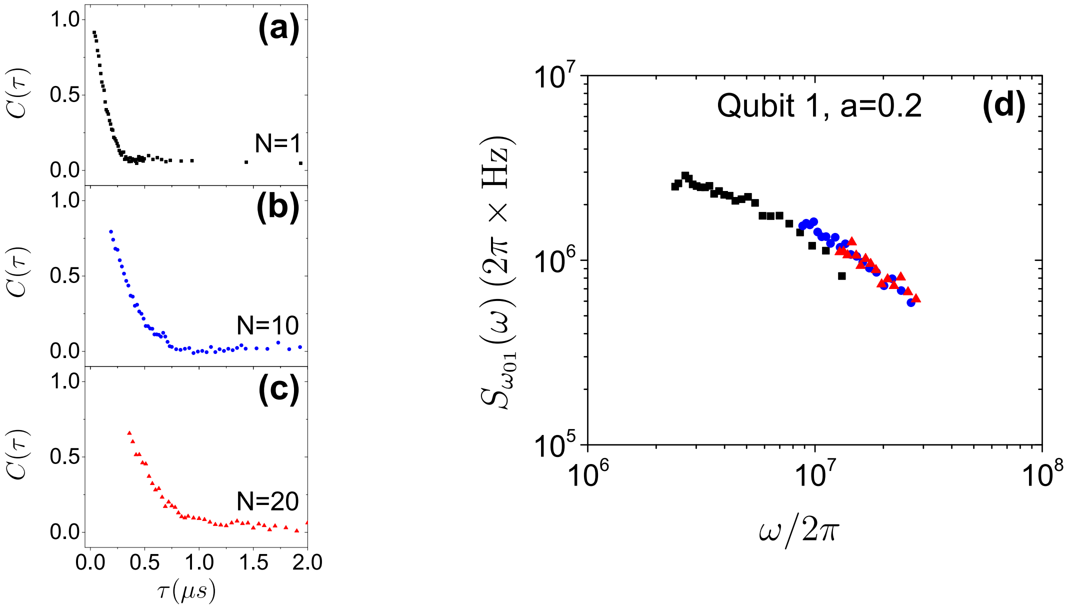

Figure 6.29: Qubit 1 coherence decay with a CPMG pulse sequence and calculated frequency noise PSD. (a-c) Qubit 1 coherence function $C(\tau)$, with τ the total time between the $\frac{\pi}{2}$ pulses, shown for three different values of N - the number of π pulses.**(d)** Qubit 1 frequency noise power spectrum density, when biased away from symmetry point (a=0.2). The black squares are calculated from the coherence function data points in (a), the blue dots from (b) and the red triangles from (c).

Dynamical decoupling techniques can also be looked at from the perspective of a filter-design problem [123], to help preserve the coherent phase of complex quantum systems. Different pulses schemes can be derived [124] which formal mathematical study can help optimize the operation of large multi-qubit systems and embedded in the drive scheme of quantum gates.

6.8 Qubit-qubit coupling strength measurement

So far, we were able to experimentally verify the ability to prepare the two qubits in the ground state, to coherently manipulate and readout the states of each qubits interacting with the resonator and measure their decoherence properties. However we have not verified that the prediction of the Hamiltonian in the dispersive regime with two qubits and a resonator of Eq. (2.72) gives rise to a qubit-qubit coupling as first demonstrated in reference [125]. The coupling strength J between the two qubits is:

$$J = \frac{g_{q1} g_{q2} (\delta_1 + \delta_2)}{2(\delta_1 \delta_2)}. \tag{6.15}$$

Given the g_{qi} coupling factors found for the two qubits with the first resonator mode and their respective detuning when biased at their respective symmetry point, we estimate $J/2\pi \simeq 19.33\,\mathrm{MHz}$.

We can experimentally measure the J parameter by tuning the qubits into resonance and measure the spectroscopy peaks separation at the avoided crossing. Indeed, similar to the vacuum Rabi splitting observed between each qubit and the resonator, when both qubits eigenstates are degenerate, there will be coherent exchange of photons between the two qubits who are effectively in a superposition of states and indistinguishable.

Figure 6.30 top left quadrant is a 2D spectroscopy sweep of qubit 2 flux biased around the frequency of qubit 1 while qubit 1 is maintained at its symmetry point. An avoided crossing is observed when $\omega_{q1} = \omega_{q2}$. Qubit 2 peak width is much broader than qubit 1 since qubit 2 is biased more than 1 GHz away from its symmetry point and its sensitivity to flux noise is increased. Center frequencies and peak width are extracted using a double peaks fitting method and the frequency difference between the peak centers of the upper minus the lower branch is plotted (see Fig. 6.30). A minimum splitting of $2J/2\pi = 37.79\,\mathrm{MHz}$ is found (or a value of $J/2\pi \simeq 18.90\,\mathrm{MHz}$) close to the calculated value. A more detailed analysis could consider additional modes of the resonator and evaluate how they might contribute to the mediated interaction between the two qubits.

6.9 Chapter summary

In this chapter, I have presented the experimental techniques needed to characterize flux qubits embedded in a superconducting microwave resonator, as well as the characteristic metrics of

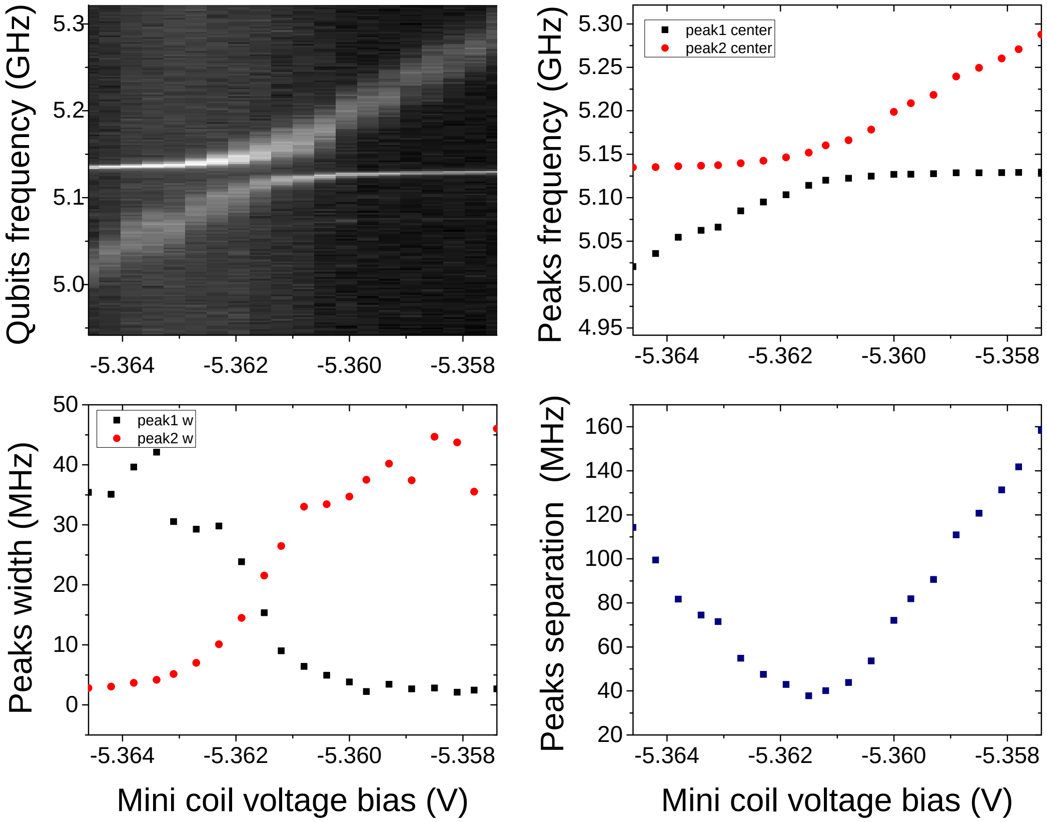

Figure 6.30: Qubit-qubit avoided crossing: peak spectroscopy analysis. (top left) Spectroscopy 2D map of qubit 1 and 2 as qubit 2 frequency is tuned by sweeping its magnetic flux bias to reach and cross qubit 1 frequency which is maintained at a fixed magnetic flux bias. An avoided crossing is observed. (top right) Extracted spectroscopy peaks center frequencies using a double Lorentzian peak fit. (bottom left) Extracted spectroscopy peaks width. (bottom right) The frequency difference between red and black peaks center frequency of top right. A minimum splitting of $2J/2\pi = 37.79\,\mathrm{MHz}$ is observed.

the system. Strong vacuum Rabi splitting was measured between the resonator and the qubits, revealing the large coupling strengths between the artificial atoms and the cavity. The preparation, control and readout of the qubit states was discussed and the techniques to measure qubit coherence times was introduced. The device showed some remarkable T_1 compared to previously reported flux qubits in cQED setups, despite the large g coupling of the qubit to the resonator and the resulting decay due to Purcell effect. Table 6.1 summarizes the characteristics of the superconducting resonator of this two-qubit device.

Resonator parameters	
Bare resonator frequency f_r	6.597 62 GHz
Single photon regime Q factor	$\sim$ 47000
3 dB resonator line width	$\sim$ 140 kHz

Table 6.1: W37_c2d device resonator parameters.

Parameters	qubit 1	qubit 2
Δ/h	5.1317 GHz	3.664 GHz
I_p	383 nA	351.5 nA
$g/2\pi$	150 MHz	252 MHz
$\delta/2\pi$	−1.4659 GHz	−2.9336 GHz
T_1	5.3 µs	9.6 µs
T_2^*	0.88 µs	1.38 µs
$T_{2\mathrm{echo}}$	1.11 µs	2.21 µs

Table 6.2: W37_c2d device qubits parameters measured at their respective symmetry points.

Table 6.2 summarizes the qubits parameters for which we found a qubit-qubit $J/2\pi$ coupling of about 18.9 MHz when both biased at their symmetry points. This coupling allowed the implementation of an entangling gate, presented in chapter 8.

Chapter 7

Decoherence measurements of flux qubits[1]

We report experiments on superconducting flux qubits in a circuit quantum electrodynamics (cQED) setup. Two qubits, independently biased and controlled, are coupled to a coplanar waveguide resonator. Dispersive qubit state readout reaches a maximum contrast of 72 %. We measure energy relaxation times at the symmetry point of 5 and 10 µs, corresponding to 7 and 20 µs when relaxation through the resonator due to Purcell effect is subtracted out, and levels of flux noise of 2.6 and $2.7\,\mu\Phi_0/\sqrt{\mathrm{Hz}}$ at 1 Hz for the two qubits. We discuss the origin of decoherence in the measured devices. The strong coupling between the qubits and the cavity leads to a large, cavity-mediated, qubit-qubit coupling. This coupling, which is characterized spectroscopically, reaches 38 MHz. These results demonstrate the potential of cQED as a platform for fundamental investigations of decoherence and quantum dynamics of flux qubits.

---

[1] The content of this chapter is reproduced and format adapted from: J.-L. Orgiazzi, C. Deng, D. Layden, R. Marchildon, F. Kitapli, F. Shen, M. Bal, F. R. Ong, and A. Lupaşcu. Flux qubits in a planar circuit quantum electrodynamics architecture: Quantum control and decoherence. *Phys. Rev. B*, 93(10):104518, March 2016. doi: 10.1103/PhysRevB.93.104518. URL https://link.aps.org/doi/10.1103/PhysRevB.93.104518. Copyright 2016, APS, with the permission of APS.

7.1 Introduction

Superconducting qubits are one of the main candidates for the implementation of quantum information processing [126] and a rich testbed for research in quantum optics, quantum measurement, and decoherence [127]. Among various types of superconducting qubits, flux-type superconducting qubits have unique features. Strong and tunable coupling to microwave fields enables fundamental investigations in quantum optics [128, 129] and relativistic quantum mechanics [130]. The large magnetic dipole moment is a key ingredient in flux noise measurements [121], sensitive magnetic field measurements [131], microwave-optical interfaces [132], and hybrid systems formed with nanomechanical resonators [133]. Finally, flux qubits have a large degree of anharmonicity which is an advantage for fast quantum control [63]. Progress on these diverse research avenues has been hampered by relatively low and irreproducible coherence times compared to other types of superconducting qubits.

In the last decade, circuit quantum electrodynamics (cQED) [134, 135] has become increasingly popular. In cQED, resonators provide a controlled electromagnetic environment protecting qubits from energy relaxation. In addition, resonators are used for qubit state measurement [136] and as quantum buses for qubit-qubit coupling [125]. In this chapter, we present an implementation of cQED with two flux qubits strongly coupled to a superconducting coplanar waveguide resonator. The qubits and the resonator are made of aluminum. The strong qubit-cavity coupling is implemented using a shared line between the qubit loops and the resonator. Local biasing and control lines provide the means to implement fast single qubit gates as well as controlled two-qubit interactions. We measure energy relaxation times of the order of 10 µs. We also characterize in detail the dephasing of the flux qubits coupled to the resonator. Based on decoherence measurements, we extract levels of flux noise of 2.6 and $2.7\,\mu\Phi_0/\sqrt{\mathrm{Hz}}$ at 1 Hz for the two qubits. We also present a spectroscopic measurement of a resonator-mediated qubit-qubit coupling, which is relevant for implementation of two-qubit gates. We note that most previous experiments on cQED with flux qubits coupled to a coplanar waveguide resonator focused on the spectroscopy of single qubits [128, 35, 137]. Jerger *et al.* [138, 139] developed a device with independent control and measurement by multiplexing of seven qubits, however the different qubits were not coupled to each other. Inomata *et al.* implemented a straddling regime readout scheme for a flux qubit capacitively coupled to a resonator [140]. The measured and intrinsic energy relaxation times are comparable and better, respectively, than the longest measured relaxation times in flux qubits coupled to dc-SQUID readout devices [121, 141], and a very significant improvement over the previous experiments with flux qubits in cQED samples, where niobium resonators were used [139, 140]. Our experimental results demonstrate the versatility of cQED with flux qubits, and its potential for further understanding and improvements of decoherence of these qubits.

7.2 Device architecture, cQED model, and preliminary device characterization

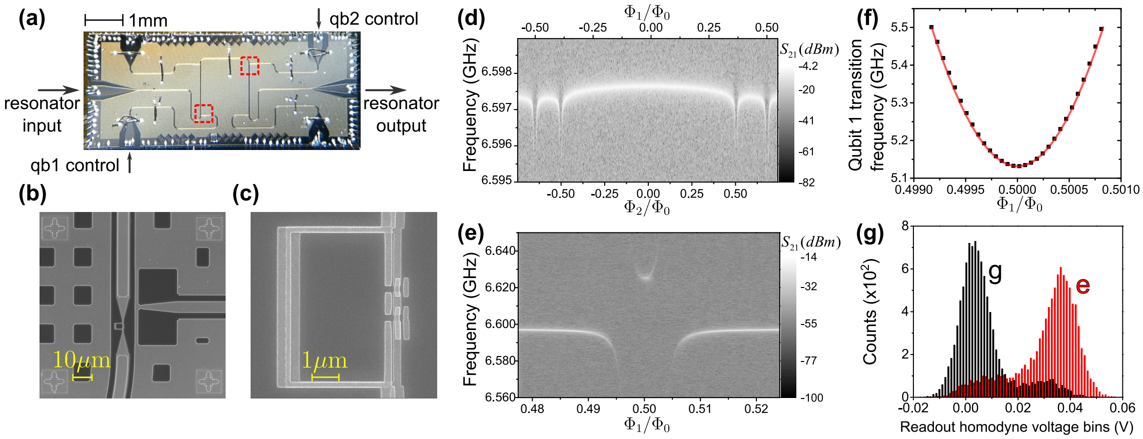

Figure 7.1: Flux qubit device summary. **(a)** Optical image of the device where the overlaid dashed rectangles indicate the position of qubit 1 (bottom left) and qubit 2 (top right). **(b)** Scanning electron microscope (SEM) image showing a qubit embedded in the CPW resonator and its local CPW control line. **(c)** SEM image of a qubit device nominally identical to that used in this work. **(d)** Resonator transmission (greyscale) versus frequency (vertical axis) and flux bias of qubit 1/2 (top/bottom axis). **(e)** Resonator transmission (greyscale) versus frequency and flux bias of qubit 1. **(f)** Qubit 1 spectroscopy measurements. The transition frequency is plotted versus the applied magnetic flux bias. The continuous line is a fit of the persistent current qubit model, yielding $I_{\mathrm{p1}} = 383\,\mathrm{nA}$ and $\Delta_1 = 5.1317\,\mathrm{GHz}$. **(g)** Readout histograms for qubit 1 resulting in a qubit state readout contrast of 72 %.

The device used in our work is shown in Fig. 7.1(a). It contains a coplanar waveguide (CPW) resonator, with two ports used for microwave transmission measurements. Two qubits are coupled to the CPW resonator, via the mutual inductance of a shared line (Fig. 7.1(b)). The qubits are persistent current type flux qubits [45], consisting of a superconducting loop interrupted by four Josephson junctions (Fig. 7.1(c)). A CPW line terminated by a low inductance shunt is coupled to each qubit and used to send microwave pulses for coherent qubit control (see Fig. 7.1(b)). The device is fabricated on an intrinsic silicon substrate, in a two step process. In the first step, optical lithography, evaporation of a 190 nm thick aluminum layer and liftoff are used to define the resonator and the control lines. In the second step, a bilayer resist (PMGI and PMMA with thicknesses 420 and 110 nm, respectively) is patterned using electron-beam lithography. Subsequently, shadow evaporation of two aluminum layers, 40 and 65 nm thick, respectively, followed by liftoff define the qubit junctions. Prior to shadow evaporation, argon milling is performed with a beam energy of 450 V for a duration of 20 s; this step is critical to ensure a high quality contact between the two aluminum layers and for the reproducibility of the Josephson junctions.

Experiments are performed in a dilution refrigerator, using a custom-designed probe for microwave transmission measurements [1]. The chip is enclosed in a copper box, which is placed inside a three-layer high permeability metal shield. An active magnetic field compensation system placed outside the cryostat is used to further reduce low-frequency magnetic field noise. A set of superconducting coils, attached to the device copper box, is used to provide independent magnetic flux biases to the two qubits. Qubit state control is done using shaped microwave pulses. Qubit state measurement is done in the dispersive regime [136], by measuring the transmission of microwave pulses through the resonator. The transmission lines for qubit control and readout are filtered using attenuators and filters placed at different temperature stages. A detailed description of the experimental setup is provided in Fig. 3.3 of Ch. 3.

We first discuss the model describing the qubits and the resonator. When the magnetic flux Φ_i $(i = 1, 2)$ applied to qubit i is close to $\overline{\Phi}_n = (n + 1/2)\Phi_0$, with n an integer and $\Phi_0 = h/2e$ the flux quantum, the qubit is described by the Hamiltonian $H_{\mathrm{qb},i} = -\varepsilon_i/2\sigma_{z,i} - h\Delta_i/2\sigma_{x,i}$. Here $\varepsilon_i = 2I_{\mathrm{pi}}(\Phi_i - \overline{\Phi}_{n_i})$, where n_i $(i = 1, 2)$ are integers, and I_{pi} and Δ_i, called the persistent current and gap [142], are determined by the qubit design parameters. The operators $\sigma_{z/x,i}$, $i = 1, 2$, are the Pauli Z and X operators for qubit i. The resonator Hamiltonian is $H_{\mathrm{res}} = \sum_{j\geq 1} \hbar\omega_{r,j} a_j^\dagger a_j$, with $\omega_{r,j}$ the resonance frequencies and $a_j^\dagger$ (a_j) the creation (annihilation) operator for mode j. The interaction between qubit i and mode j of the resonator is given by $H_{\mathrm{int},ij} = hg_{i,j}\sigma_{x,i}(a_j^\dagger + a_j)$, with $g_{i,j}$ coupling factors. Both qubits are very strongly coupled to the resonator, making it important to account for multiple resonator modes and keep counter-rotating terms.

We first present experiments on the spectroscopic characterization of the coupled qubit-resonator system. A continuous wave transmission measurement of the resonator, taken versus the applied magnetic field, is shown in Fig. 7.1(d). We observe the resonance corresponding to the first mode of the resonator at $\omega_{r,1} = 2\pi \times 6.597\,\mathrm{GHz}$. A significant change in the response occurs when the flux through each qubit is close to $-\Phi_0/2$ and $\Phi_0/2$. A narrower range scan of the transmission for qubit 1, done with a power corresponding to an average of 0.6 photons in the resonator, is shown in Fig. 7.1(e). An anticrossing is observed where the qubit and cavity are resonant. Next, qubit spectroscopy is performed by applying microwave pulses to each qubit local CPW control line. In Fig. 7.1(f) we show the spectroscopically measured transition frequency for qubit 1 versus magnetic flux. These data and similar data obtained for qubit 2 (not shown), are used to extract the qubit parameters $I_{\mathrm{p}1} = 383\,\mathrm{nA}$, $\Delta_1 = 5.1317\,\mathrm{GHz}$, $I_{\mathrm{p}2} = 352\,\mathrm{nA}$, and $\Delta_2 = 3.6634\,\mathrm{GHz}$. For each qubit, we use measurements of photon number splitting [31] for photons populating the first mode, together with a model which takes into account the first ten modes of the CPW resonator, to extract the coupling to the first resonator mode $g_{1,1} = 155.6\,\mathrm{MHz}$ and $g_{2,1} = 295.4\,\mathrm{MHz}$.

Qubit state readout is performed using homodyne detection [136]. To optimize the readout contrast, the cavity is driven strongly, in the nonlinear regime. A histogram of the homodyne voltage for qubit 1, averaged over a readout pulse duration of $4\,\mu\mathrm{s}$, is shown in Fig. 7.1(g). The readout contrast for this qubit is $72\,\%$. Similar results (not shown) are obtained for qubit 2, where the maximum readout contrast is $60\,\%$. For both qubits, readout contrast is limited primarily by the initialization procedure which is based on thermalization.

7.3 Decoherence measurements results, analysis, and discussion

We next present energy relaxation measurements. The energy relaxation times are $T_1 = 5.3\,\mu\mathrm{s}$ and $9.6\,\mu\mathrm{s}$ for qubits 1 and 2 respectively at their symmetry points. A measurement of energy relaxation rates versus magnetic flux around the symmetry point is shown in Figs. 7.3(a) and (b). Over the explored frequency range, of $35.6\,\mathrm{MHz}$ and $24.9\,\mathrm{MHz}$ for qubits 1 and 2 respectively, we observe only minor variations of the energy relaxation rate, of less than $15\,\%$ between extreme values. In Fig. 7.2 we show the energy relaxation rate Γ_1 for qubits 1 and 2 over a broad range, together with a plot of the calculated rate induced by the electromagnetic environment. The latter takes into account relaxation through Purcell effect [15] due to the first 10 modes of the resonator and relaxation due to the control line. If the relaxation due to these sources is excluded, we calculate intrinsic relaxation times of $7\,(20)\,\mu\mathrm{s}$ for qubit $1\,(2)$. In a related work we considered the role of quasiparticles in persistent current qubits [143]. The measured intrinsic energy relaxation times can be attributed to a non-equilibrium quasiparticle density of 0.12 µm^{-3} and 0.04 µm^{-3} respectively, in line with other measurements on similar devices (see [143] and references therein). While quasiparticles are the main candidate for energy relaxation, we do not exclude other potential sources, in particular loss due to amorphous interfaces and surfaces [144]. We note that lower energy relaxation times, in the $0.5 - 1$ µs range, were obtained in previous experiments with aluminum flux qubits coupled to superconducting resonators made of niobium [140, 139]. Possible reasons for the longer relaxation times in our experiment include a reduction of quasiparticle induced relaxation, due to using an all aluminum circuit, and a reduction of surface/interface loss arising due to the different processing prior to deposition of the qubit layer.

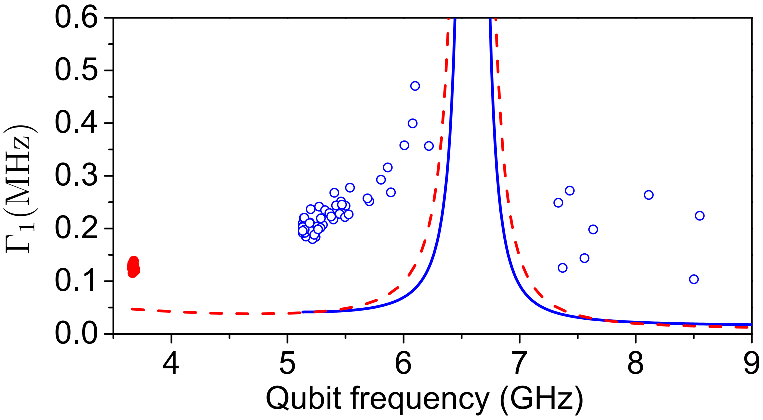

Figure 7.2: Energy relaxation rate versus transition frequency for qubit 1 (open dots) and 2 (closed dots). The combined energy relaxation rate due to the resonator and the CPW control line is shown by the continuous (dashed) line for qubit 1 (2).

We now turn to a discussion of dephasing. In Figs. 7.3(a) and (b) we present detailed measurements of dephasing performed using Ramsey and spin-echo pulse sequences [145]. Away from the symmetry point, the increased sensitivity to magnetic flux renders flux noise the dominant contribution to decoherence. We fit the coherence decay over the time τ using the expression $e^{-\Gamma_1\tau/2}e^{-(\Gamma_\phi\tau)^2}$ [145], with Γ_1 the energy relaxation rate and Γ_ϕ the pure dephasing rate. The latter depends on the type of experiment; for Ramsey (spin-echo) measurements, we denote this rate by $\Gamma_{\phi,R}$ ($\Gamma_{\phi,E}$). Gaussian decay is predicted when decoherence is dominated by noise with a power spectral density (PSD) proportional to $|\omega|^{-1}$ [145, 146, 147], with ω the angular frequency.

Assuming flux noise with a PSD given by $A/|\omega|$, the slope of $\Gamma_{\phi,E}(a)$, with $a = \varepsilon/\hbar\omega_{01}$, where ω_{01} is the angular transition frequency can be used to determine A [147]. We find $\sqrt{A} = 2.6\,(2.7)\,\mu\Phi_0$ for qubit 1 (2). These levels of flux noise are slightly larger than for the smaller aluminum flux qubits in Refs. [147, 121], in qualitative agreement with size scaling [148].

Next we discuss the dephasing of the qubits close to the symmetry point. At the symmetry point, decay is exponential, with rates $\overline{\Gamma}_{\phi,R}^{-1} = 0.77\,(0.90)\,\mathrm{\mu s}$ for Ramsey and $\overline{\Gamma}_{\phi,E}^{-1} = 1.03\,(1.85)\,\mathrm{\mu s}$ for spin-echo measurements for qubit 1 (2). We observe that both Ramsey and spin-echo curves change shape from exponential at the symmetry point to Gaussian away from this point (see Figs. 7.3(c)-(e) for spin-echo measurements of qubit 1). This suggests that dephasing can be explained by the combination of an exponential decay process and a Gaussian decay process. The latter is due to magnetic flux noise and has a rate $\Gamma_{\phi,R/E} = \gamma_{R/E}a$, for Ramsey/spin-echo, with $\gamma_{R/E}$ dependent on qubit parameters and flux noise amplitude [147]. Indeed, we find that all the coherence decay curves for each qubit can be fit by the expression $C(\tau) = e^{-\Gamma_1\tau/2}e^{-\overline{\Gamma}_{\phi R/E}\tau}e^{-(\gamma_{R/E}a\tau)^2}$, for Ramsey/spin-echo, with $\gamma_{R/E}$ as a single fit parameter (see Figs. 7.3(c)-(e)). We also performed noise measurements based on dynamical decoupling [121], shown in Figs. 7.3(f) and (g) for qubit 1 biased at $a = 0$ (the symmetry point) and at $a = 0.2$ respectively. This additional experiment confirms that a nearly frequency independent white noise source dominates dephasing at the symmetry point.

We discuss next the origin of the decoherence at the symmetry point. We first consider quadratically coupled flux noise. As discussed in Ref. [149], the decay is expected to be significantly non-exponential at short time, with a time scale estimated to be 33 (42) µs for qubit 1 (2). We have also performed numerical simulations that confirm this source is negligible. A second potential source is photon noise induced dephasing [105, 150]. We performed spectroscopy experiments (not shown) and numerical simulations which allow us find an upper bound for the thermal photon number $n_{\mathrm{th}} < 0.02$. In the strong dispersive regime [151, 152] the dephasing rate, given by κn_{th}, with $\kappa = 882\,\mathrm{kHz}$ the resonator decay rate for the first mode, is smaller than 18 kHz, thus a negligible contribution to dephasing.

We next consider dephasing due to charge noise, arising either from offset charges or quasiparticles on the qubit islands, as a potential source of dephasing at the symmetry point. The modulation of the persistent qubit transition frequency by charges, denoted by $\delta\Delta_{\mathrm{c}}$, decreases exponentially with the ratio of the Josephson (E_{J}) to charging (E_{c}) energy [142]. We numerically calculate E_{J} and E_{c} assuming proportional and inversely proportional respectively scaling with

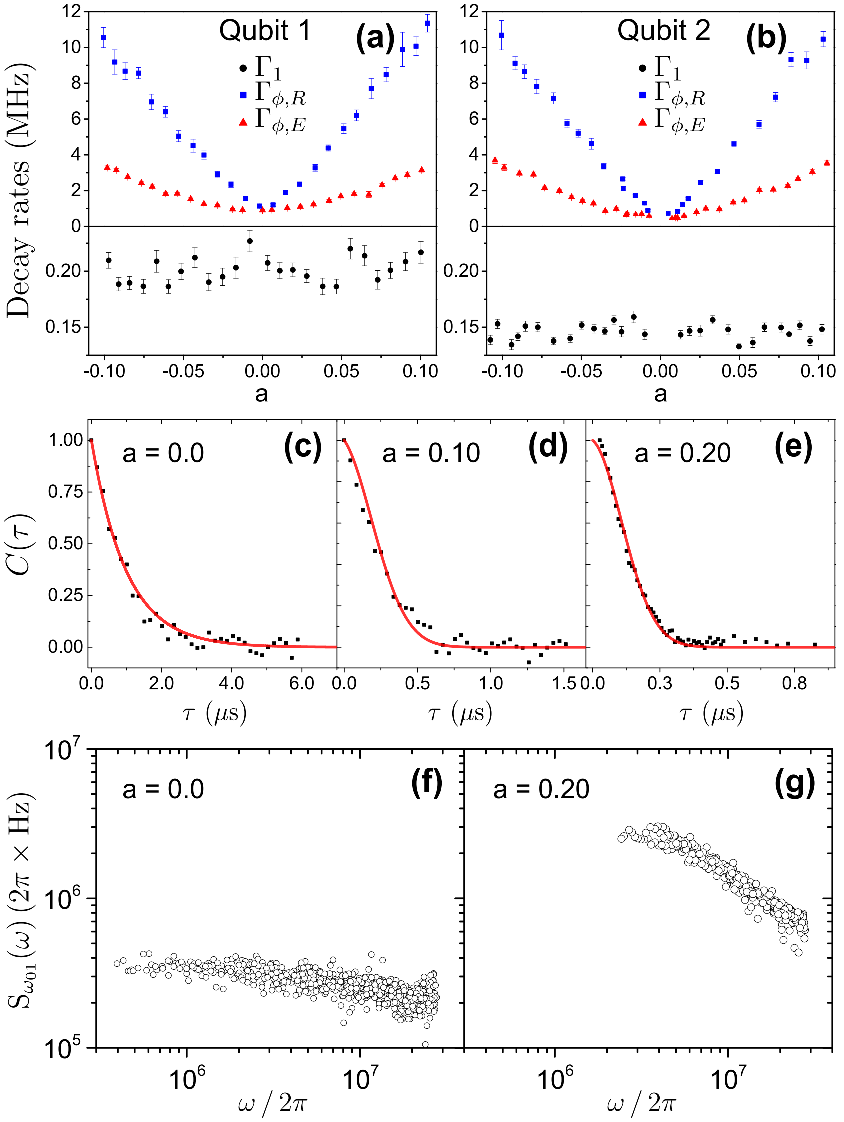

Figure 7.3: Decoherence and frequency noise PSD. (a, b) Energy relaxation (black dots) and dephasing rates performed using Ramsey (blue squares) and spin-echo pulse (red triangles) sequences for qubits 1 (a) and 2 (b). **(c, d, e)** Spin-echo decay for qubit 1 for different coupling angles to flux noise, where the solid lines represent a fit to a coherence function defined in the text. **(f, g)** Qubit 1 frequency noise PSD calculated from measurements based on dynamical decoupling at the symmetry point (f) and at a coupling angle $a = 0.2$ (g).

Josephson junction areas, as measured for a nominally identical device, and using the experimentally measured persistent current and gap. The thus estimated values of E_J and E_c yield $\delta\Delta_\mathrm{c} = 83$ (52) kHz for qubit 1 (2). However we note that this value is strongly dependent on the junction areas; assuming a size of the smallest junction different by only 10 %, a difference that could arise due to lithography or edge effects, we find $\delta\Delta_\mathrm{c} = 4$ (3) MHz for qubit 1 (2). With these larger values, dephasing could arise through a combination of slow offset charge fluctuations and random telegraph noise due to quasiparticles tunneling with a rate larger than the charge modulation.

7.4 Qubit-qubit interaction

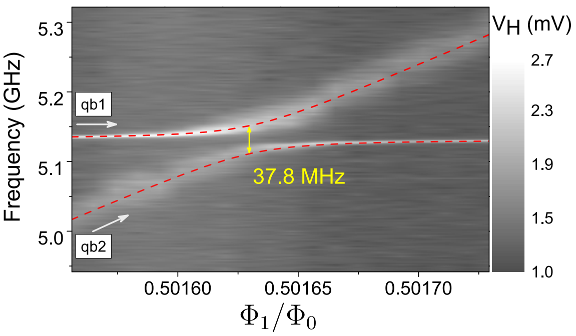

Figure 7.4: Qubit-qubit anticrossing. Readout homodyne voltage (V_H) versus frequency (vertical axis) and the flux applied to qubit 2. The overlaid dashed lines are a fit of the excited energies for the coupled system, providing a coupling strength 37.8 MHz.

We finally discuss the use of the proposed setup to implement qubit-qubit interactions. In Fig. 7.4 we show spectroscopy measurements where qubit 1 is biased at the symmetry point, whereas the flux bias of qubit 2 is changed. An anticrossing arises due to an effective qubit-qubit interaction, mediated by virtual excitations of the resonator [134]. The large qubit-qubit interaction of 37.8 MHz is made possible by the strong coupling of the flux qubits to the resonator. A two-qubit gate can be implemented using the method proposed in [37], which only requires control of each qubit, a feature already included in our setup. The large anharmonicity of the flux qubits enables fast two-qubit gates, with a time limited by the inverse of the interaction strength [63]. We will present these results in a follow-up paper. The ability to perform high-fidelity gates between distant qubits will be important for experiments using flux qubits in hybrid architectures [132, 133].

7.5 Chapter summary

We presented experiments on flux qubits coupled to a superconducting on-chip resonator. The measured qubits have long energy relaxation times and low levels of flux noise. Readout contrast is high, exceeding 70 %. We also demonstrated the strong, resonator mediated, interaction between the two qubits. Further improvements of coherence will have to address the role of quasiparticles and loss due to surfaces and interfaces in energy relaxation and the origin of pure dephasing at the flux-insensitive point. The experiments presented here demonstrate the potential that this platform has for systematic studies of coherence and dynamics of flux qubits.

Note. A recent paper [153] reports on related experiments on measurements of decoherence of persistent current qubits coupled to a three-dimensional resonator.

Chapter 8

Implementation of a Controlled-NOT gate using the Selective Darkening technique

Quantum computers require a universal set of gates operating on interconnected qubits, including several single-qubit gates and one type of two-qubit gate. The quantum controlled-NOT (C-NOT) gate, is a two-qubit (or more) that fulfills the requirements for an entangling gate of a universal set. All other operations on a quantum computer can be reduced to a sequence of gates from the universal set. The CNOT operation is represented by the unitary matrix:

$$U_{\mathrm{CNOT}} = \begin{pmatrix} 1 & 0 & 0 & 0 \\ 0 & 1 & 0 & 0 \\ 0 & 0 & 0 & 1 \\ 0 & 0 & 1 & 0 \end{pmatrix} \tag{8.1}$$

Controlled gates act on two or more qubits. For the case of a two-qubits CNOT gate, one qubit acts as the control and the other qubit as the target on which the NOT (Pauli X gate) operation is performed only if the control qubit is in the $|1\rangle$ sate. The state of the target qubit is otherwise left unchanged. The CNOT gate is typically represented by the following circuit representation

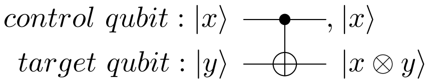

in which the control qubit in the $|1\rangle$ state changes the target qubit from the $|0\rangle$ to $|1\rangle$ state.

The main requirements for the implementation of a CNOT gates are that the gate has a high fidelity, be fast in comparison with the qubits decoherence time, and that it doesn't not affect the qubits intrinsic coherence. In this chapter, results on the implementation of a CNOT gate realized using two distant flux qubits coupled through a microwave resonator and the selective darkening technique are reported.

8.1 Theory overview of the selective darkening technique

The selective darkening (SD) technique, presented and demonstrated by de Groot et al. using two inductively coupled flux qubits [37, 63], is a method that applies to transversely coupled qubits (xx-coupling in comparison to longitudinal or zz-coupling). In this section, we summarize the principles of this method from [63] for completeness.

Two transversely coupled qubits can lead to quantum levels with degenerate energy differences which prevent frequency-selective quantum operations on the qubit pair. In the SD method, the transition of a degenerate pair is selectively suppressed (darkened) while the other one is coherently excited thus creating an artificial selection rule. This method only requires driving the two qubits at the same time with the same frequency with a specific amplitude and phase on each qubit control line.

Figure 8.1 shows the energy-level diagram of the coupled qubits where the arrows of the same color represent transitions that are degenerate in frequency. Without any loss of generality and matching the device for which the CNOT gate results are presented in this chapter, we assume $\Delta_2 < \Delta_1$.

Let's consider the following Hamiltonian for our two transversely coupled flux qubits:

$$H = -\frac{1}{2}(\Delta_1\sigma_z^{(1)} + \Delta_2\sigma_z^{(2)}) + J\sigma_x^{(1)}\sigma_x^{(2)} \tag{8.2}$$

with Δ_i the respective qubit energy splitting, J the qubit-qubit coupling energy and $\sigma_{x,z}^{(i)}$ are the Pauli spin matrices with $\sigma_{x,z}^{(1)} = \sigma_{x,z} \otimes \mathbb{1}$ and $\sigma_{x,z}^{(2)} = \mathbb{1} \otimes \sigma_{x,z}$.

The transverse Hamiltonian (8.2) can be diagonalized analytically and we obtain the following

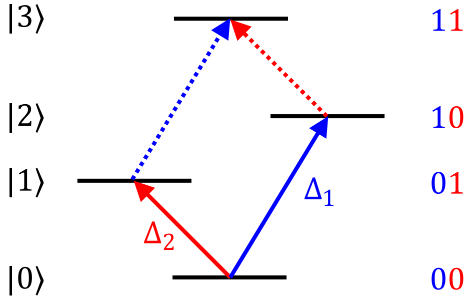

Figure 8.1: Energy-level diagram of the two coupled qubits. Qubit 2 energy splitting Δ_2 is smaller than Δ_1 of qubit 1. Arrows of the same color are degenerate in frequency.

eigenenergies:

$$E_0 = -\frac{1}{2}\sqrt{4J^2 + (\Delta_1 - \Delta_2)^2} \tag{8.3}$$

$$E_1 = -\frac{1}{2}\sqrt{4J^2 + (\Delta_1 + \Delta_2)^2} \tag{8.4}$$

$$E_2 = \frac{1}{2}\sqrt{4J^2 + (\Delta_1 + \Delta_2)^2} \tag{8.5}$$

$$E_3 = \frac{1}{2}\sqrt{4J^2 + (\Delta_1 - \Delta_2)^2} \tag{8.6}$$

and the resonance frequencies are expressed as:

$$E_1 - E_0 = E_3 - E_2 = \frac{1}{2}\left(\sqrt{4J^2 + (\Delta_1 + \Delta_2)^2} - \sqrt{4J^2 + (\Delta_1 - \Delta_2)^2}\right) \tag{8.7}$$

$$E_2 - E_0 = E_3 - E_1 = \frac{1}{2}\left(\sqrt{4J^2 + (\Delta_1 + \Delta_2)^2} + \sqrt{4J^2 + (\Delta_1 - \Delta_2)^2}\right) \tag{8.8}$$

For the two qubits device used in this work, with $\Delta_1/h = 5.1317$ GHz and $\Delta_2/h = 3.664$ GHz, with a coupling $J/h = 18.895\,\text{MHz}$ when both qubits are operated at their respective symmetry point, we find that the effective degenerate frequency pairs are only modified by less than 300 kHz from their respective Δ (see Fig. 8.2 with J indicated by the black dashed line). Since $J \ll |\Delta_1 - \Delta_2|$ and since this relative change is even less than the spectroscopy peak width of each qubits the resonance frequencies simplifies to $E_2 - E_0 = E_3 - E_1 = \Delta_1$ and $E_1 - E_0 = E_3 - E_2 = \Delta_2$.

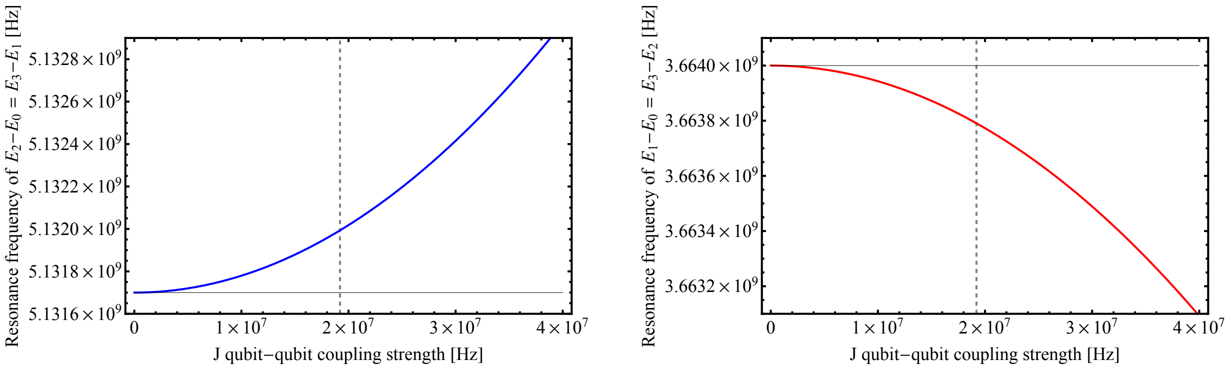

(a) Resonance frequency of $E_2 - E_0 = E_3 - E_1$ as a function of J/h.

(b) Resonance frequency of $E_2 - E_0 = E_3 - E_1$ as a function of J/h.

Figure 8.2: Dressed qubit frequencies due to qubit-qubit coupling. Resonance frequencies of the transversely coupled qubits as a function of J/h. In both a) and b), the grey dashed line indicates the experimentally extracted J/h parameter, and the thin horizontal black line the uncoupled qubit Δ/h frequency.

The reduced energy eigenstates are expressed in first order as:

$$|0\rangle = |00\rangle \tag{8.9}$$

$$|1\rangle = |01\rangle - \frac{J}{\Delta_1 - \Delta_2}|10\rangle \tag{8.10}$$

$$|2\rangle = |10\rangle + \frac{J}{\Delta_1 - \Delta_2}|01\rangle \tag{8.11}$$

$$|3\rangle = |11\rangle. \tag{8.12}$$

Let's as well consider the following driving Hamiltonian for our system:

$$\begin{aligned} H_{\text{drive}} &= a_1 \cos(\omega t + \varphi_1)\sigma_x^{(1)} + a_2 \cos(\omega t + \varphi_2)\sigma_x^{(2)} && (8.13) \\ &= H^+_{\text{drive}} e^{i\omega t} + H^-_{\text{drive}} e^{-i\omega t}, && (8.14) \end{aligned}$$

with

$$H^{\pm}_{\text{drive}} = \frac{a_1}{2} e^{\pm i\varphi_1}\sigma_x^{(1)} + \frac{a_2}{2} e^{\pm i\varphi_2}\sigma_x^{(2)}, \tag{8.15}$$

where ω is the frequency resonant with one of the degenerate transitions which couples to qubit i with real and positive amplitude a_i and phase φ_i. If ω is chosen to be equal to $\Delta_1/\hbar$, we can flip the state of qubit 1. The transition strengths $T_{k\leftrightarrow l} = \langle l|H_{drive}|k\rangle$ between transitions $|0\rangle \leftrightarrow |2\rangle$

and $|1\rangle \leftrightarrow |3\rangle$ (blue arrows in 8.1) can be calculated, assuming the rotating wave approximation. The required ratio of driving amplitudes to drive only one transition can be deduced, fixing the phase difference $\varphi_2 - \varphi_1 = \pi$ for a CNOT gate:

$$\frac{a_1}{a_2} = \frac{J}{\Delta_1 - \Delta_2} \tag{8.16}$$

and for a darkened transition of qubit 2, the ratio of driving amplitudes is inverted:

$$\frac{a_2}{a_1} = \frac{J}{\Delta_1 - \Delta_2} \tag{8.17}$$

Figure 8.3 shows the energy-level diagram for a CNOT gate either performed with qubit 1 or 2 as the target. The control qubit is first prepared in the excited state with a π pulse quickly followed by a CNOT pulse applied to both qubit control lines with the appropriate amplitude and phase to match the above darkened transition conditions.

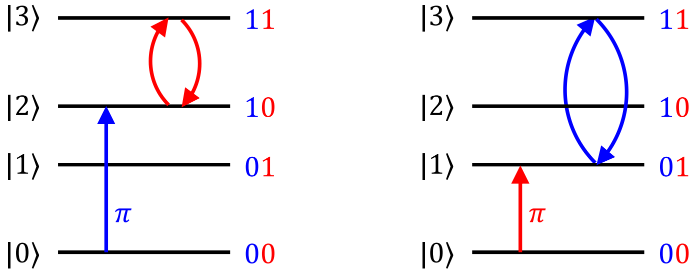

Figure 8.3: Energy-level diagram for a CNOT gate and preparation pulse. Energy-level diagram for a CNOT gate using either qubit 1 (blue) as the control and qubit 2 (red) as the target **(left)** or the reverse **(right)**.

We present in the following sections the microwave setup for qubit control to implement the SD CNOT gate and the experimental results obtained.

8.2 Microwave setup for a CNOT gate implementation

In order to implement the SD technique for our two flux qubits driven through their respective control line, the qubit control microwave setup was modified so as to allow the same frequency to be sent through both lines simultaneously with independently controlled amplitude and phase to fulfill the darkened transition conditions for the CNOT gate on a given target qubit. Direct modulation was not possible since we could not fit the needed frequencies in the bandwidth of the mixers with the AWGs we used.

Since only one frequency is sent at any given time, the signal coming from two microwave signal generators were fed into a microwave switch controlled by a frequency toggle digital signal coming from an arbitrary waveform generator allowing to feed the selected frequency down the microwave path of the board controlling the amplitude and phase sent to each qubits. Each qubit control channel consists of a fast microwave switch, an amplifier, an IQ mixer which I and Q inputs are controlled by two analog channels of an AWG, and a variable attenuator.

Figure 8.5 is a photo of the two-qubit control board laid out so as to easily expand it to a four-qubit control board by duplicating the first two channels. A custom DC power supply with multiple channels was also designed and assembled to support four channels with multiple active devices.

Thanks to the work of my teammate Chunqing Deng, the qubit pulse generation software and driver layers were modified to support the hardware modifications and the automatic frequency toggling for a given vector of pulse definitions each at a given frequency, duration, amplitude and phase.

8.3 Experimental protocol

8.3.1 Finding compensation conditions

In order to find the compensation conditions for a given darkened transition, we first obtained the linear dependence of the Rabi frequencies of each qubit when excited through their dedicated control line and through the other qubit control line for a given variable attenuators setting on the lines. Indeed, there is a finite transmission of microwave signal which propagates through the cavity from the control line antenna of one qubit to the other qubit. Figure 8.6 shows the four linear dependences of the Rabi frequencies of both qubits with respect to the voltage of the I quadrature of the IQ mixers of control line 1 and 2.

In order to account for the path length difference of the microwave signals at a given qubit frequency from the room temperature setup, through the coaxial cables inside the dilution

Figure 8.4: CNOT gate Experimental setup schematic. Experimental setup for one an two flux qubits devices.

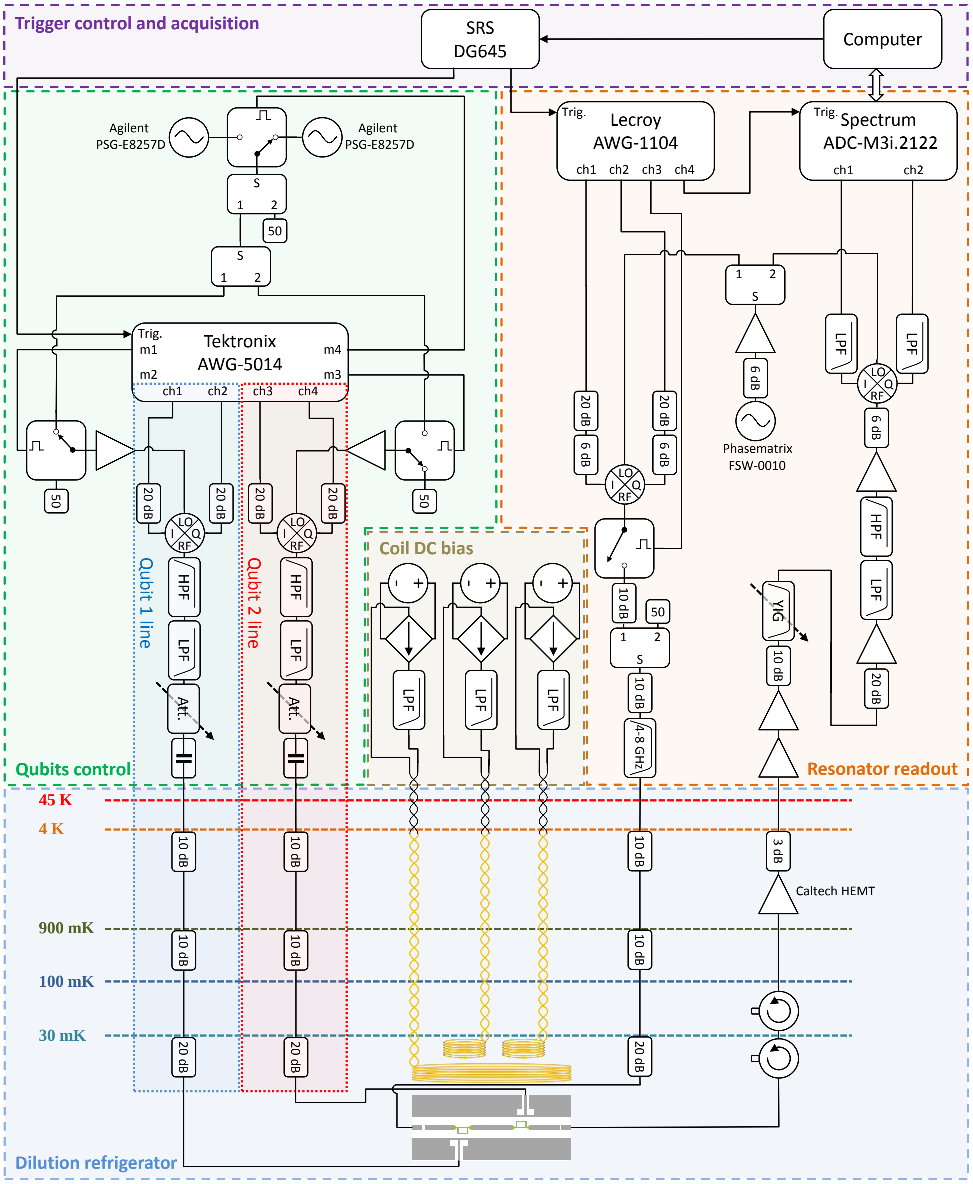
Trigger control and acquisition
SRS DG645
Computer
Agilent PSG-E8257D
Agilent PSG-E8257D
S
1
2
50
S
1
2
Trig.
m1
m2
Tektronix AWG-5014
m4
m3
ch1
ch2
ch3
ch4
50
50
20 dB
20 dB
20 dB
20 dB
LO
I
Q
RF
HPF
LPF
Att.
Qubit 1 line
Qubit 2 line
Qubits control
Trig.
Lecroy AWG-1104
ch1
ch2
ch3
ch4
Trig.
Spectrum ADC-M3i.2122
ch1
ch2
1
2
S
6 dB
Phasematrix FSW-0010
LPF
LPF
6 dB
HPF
LPF
20 dB
20 dB
6 dB
20 dB
6 dB
10 dB
50
1
2
S
10 dB
4-8 GHz
YIG
10 dB
Coil DC bias
-
+
LPF
Resonator readout
45 K
4 K
900 mK
100 mK
30 mK
10 dB
10 dB
20 dB
3 dB
Caltech HEMT
Dilution refrigerator

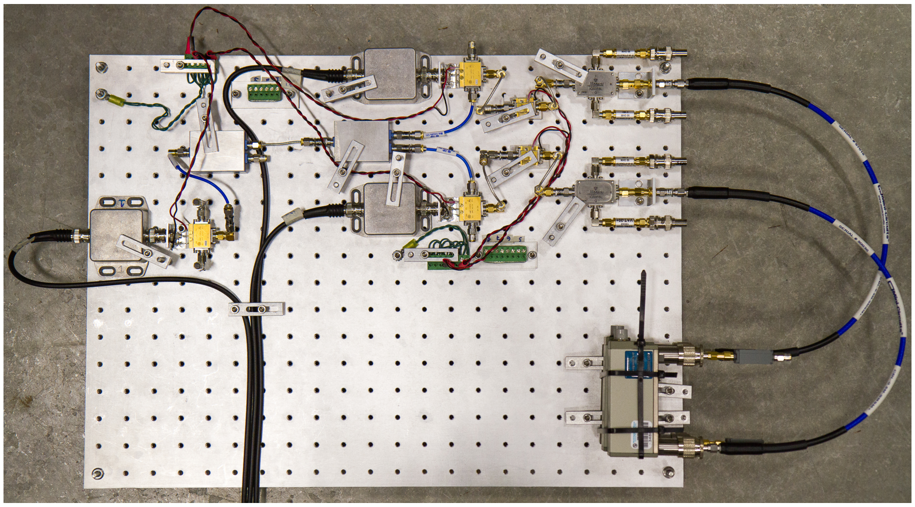

Figure 8.5: CNOT gate microwave experimental setup board.

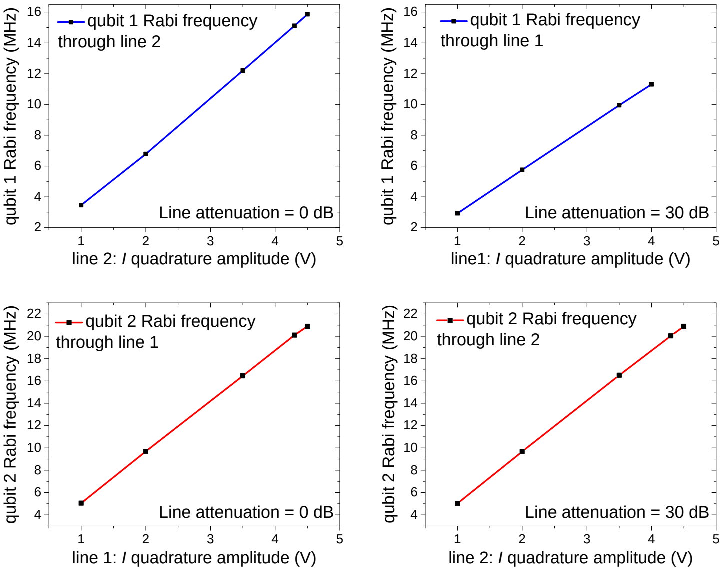

Figure 8.6: Rabi frequencies of both qubits controlled through each qubit lines. Rabi frequencies for both qubits obtained by either exciting a qubit through its local control line or through the control line of the other qubit with a different attenuation.

refrigerator and the signal path on the microwave device itself, we then need to sweep the relative phase between the two-qubit control channels to fulfill the SD transition conditions (destructive interference of counterpropagating microwave signals at the location of the target qubit). For a given Rabi frequency of the target qubit, we program the microwave pulses for a fixed duration τ, and with amplitudes obtained from the graph of Fig. 8.6 for a given target qubit, and sweep the phase of one line. Figure 8.7 shows the pulses scheme to find the compensation conditions to selectively darken the transition of qubit 1.

The optimal phase is the one that minimizes the measured qubit 1 population. The relative amplitude of the target qubit line is then swept over a narrow range to further minimize qubit 1 population. The relative phase of the target line if swept again with a finer step and the above sequence is iterated until qubit 1 population is negligible.

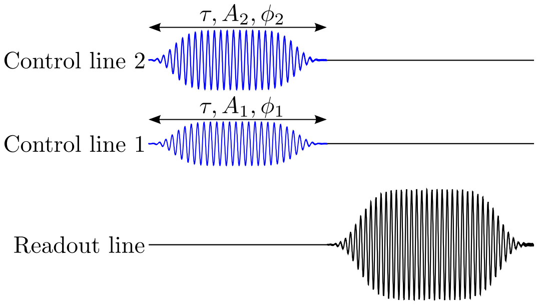

Figure 8.7: Microwave pulse sequence to find the compensation conditions for the SD technique. Microwave pulses sequence to find the compensation conditions for darkening the transition of qubit 1. A pulse resonant with Δ_1 (blue) is sent through both control lines with different amplitudes and phases. The state of the system is then probed with a readout pulse (black) through the resonator.

It was found that the optimum phase was reached simply by adjusting the I and Q quadratures of the mixer and it was not necessary to use the adjustable path delay functionality of the AWG used to generate the fast pulses on the mixers since all BNC and SMA cables used outside the fridge were all of matching lengths across the two channels. Inside the dilution unit and down to the sample holder the cable lengths only vary by a couple centimeters, resulting in relative delays of tens of picoseconds at most.

8.3.2 CNOT pulse scheme

Once the compensation conditions have been found and we have verified that they hold for various pulse durations τ, we can proceed with the following pulse scheme (Fig. 8.8) to characterize the CNOT gate with qubit 2 as the control qubit. A π pulse resonant with Δ_2 is sent through the control line 2 to initialize qubit 2 in the excited state. A digital frequency toggle pulse then reconfigures the microwave path on the microwave board in less than 10 ns to allow for the CNOT pulse resonant with Δ_1 to be sent through both lines with a duration τ that is swept in order to measure multiple CNOT rotations.

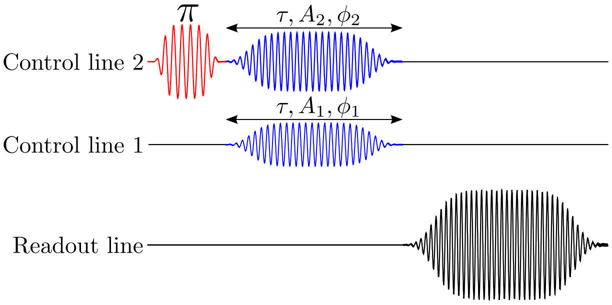

Figure 8.8: CNOT gate microwave pulses sequence with qubit 2 as the control qubit. Qubit 2 is prepared in the excited state with a pi pulse resonant with Δ_2 (red), followed by a pulse sent from both qubit control lines with different amplitude and phase, resonant with Δ_1 (blue). The state of the system is then probed with a readout pulse (black) through the resonator.

8.4 Results

8.4.1 CNOT gate at various speeds

Following the experimental protocol described in the previous section, we proceeded with characterizing a two-qubit CNOT gate by measuring multiple CNOT rotations on the target qubit 1 for various line compensation conditions leading to different gate speed. We obtained the cancellation conditions for the $|00\rangle \leftrightarrow |10\rangle$ transition and performed a CNOT rotations on the $|01\rangle \leftrightarrow |11\rangle$ transition by preparing the control qubit (qubit 2) with a π pulse of 50 ns duration. The results are summarized in Table 8.9. For the slowest speed, we did not observe oscillations between the $|11\rangle$ and $|01\rangle$ state.This is possibly due to the fact that the voltage amplitudes sent to the

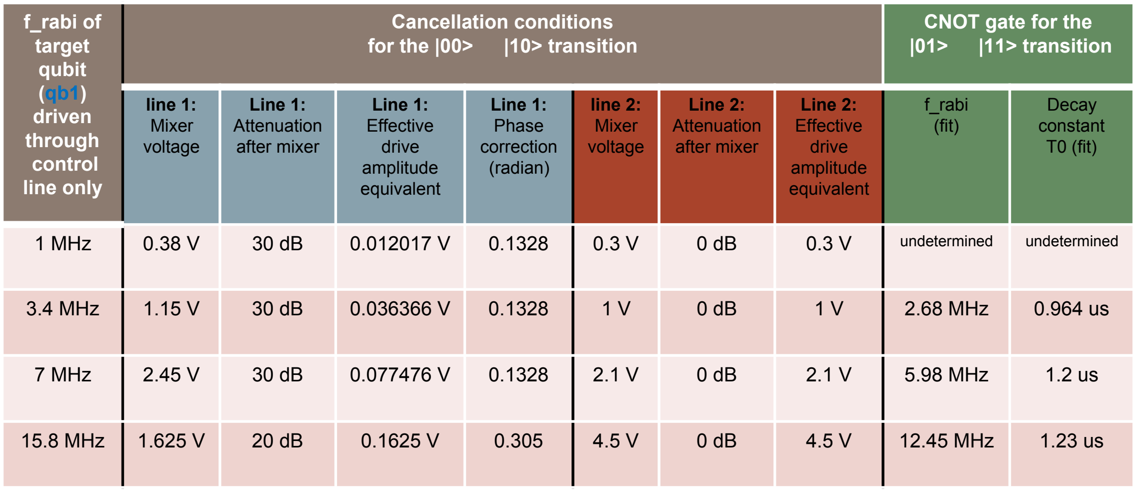

f_rabi of target qubit (qb1) driven through control line only	Cancellation conditions for the |00> |10> transition							CNOT gate for the |01> |11> transition	
	line 1: Mixer voltage	**Line 1:** Attenuation after mixer	**Line 1:** Effective drive amplitude equivalent	**Line 1:** Phase correction (radian)	**line 2:** Mixer voltage	**Line 2:** Attenuation after mixer	**Line 2:** Effective drive amplitude equivalent	f_rabi (fit)	Decay constant T0 (fit)
1 MHz	0.38 V	30 dB	0.012017 V	0.1328	0.3 V	0 dB	0.3 V	undetermined	undetermined
3.4 MHz	1.15 V	30 dB	0.036366 V	0.1328	1 V	0 dB	1 V	2.68 MHz	0.964 us
7 MHz	2.45 V	30 dB	0.077476 V	0.1328	2.1 V	0 dB	2.1 V	5.98 MHz	1.2 us
15.8 MHz	1.625 V	20 dB	0.1625 V	0.305	4.5 V	0 dB	4.5 V	12.45 MHz	1.23 us

Figure 8.9: Table of parameters for cancellation condition of the $|00\rangle \leftrightarrow |10\rangle$ and CNOT rotations on the $|01\rangle \leftrightarrow |11\rangle$ transition, with obtained CNOT Rabi speeds and envelope decay constant.

quadrature of the mixers of both channels were relatively low and closer to the DC offsets than for the other cases. Possible noise fluctuations on the quadratures would lead to microwave amplitude fluctuations sent to both qubit control line, thus affecting the cancellation condition over time and multiple repeated acquisitions. For the three remaining cases, the CNOT rotations are fitted with an exponential decay function in order to extract the decay constant of the signal's envelope. For the fastest case (insert d) of Fig. 8.10) we also observed a shift in the levels of the acquired quadrature which is not related to the speed at which the gate was performed but most slow drifts of the calibrated state levels.

The maximum decay constant measured was 1.23 µs, allowing multiple CNOT gates to be performed on the qubit pairs before decoherence destroys the quantum state. Since for the fastest case, a maximum allowable quadrature voltage of 4.5 V was already used for the correct compensation conditions, it was not possible to characterize the gate at a faster rate using qubit 1 as the target.

CNOT gates on qubit 1 were equally tested with control qubit π pulses of durations as short as 6 ns at various speeds, where similar decay constant were measured.

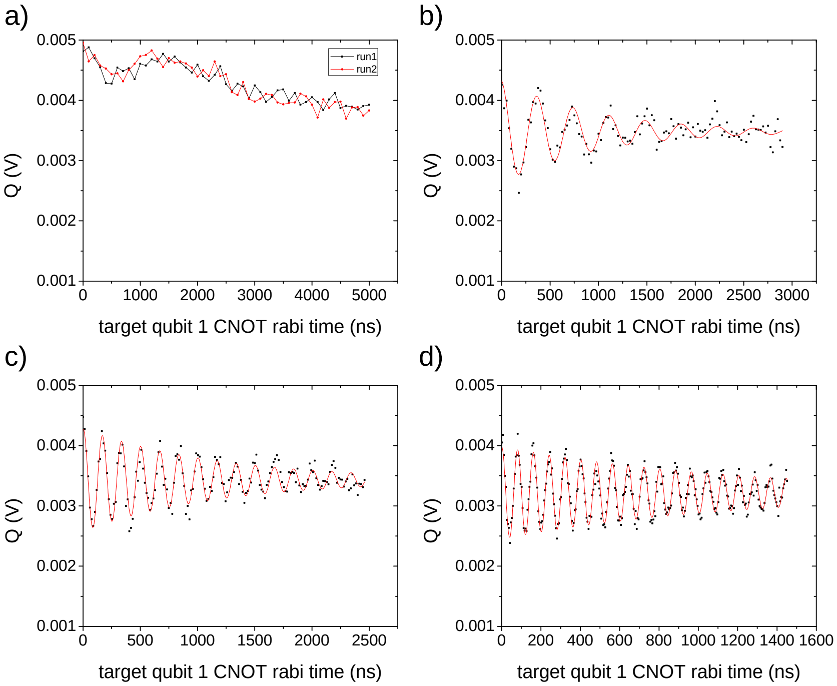

Figure 8.10: CNOT Rabi oscillations measured at various speeds. **a)** 1 MHz. **b)** 3.4 MHz. **c)** 7 MHz. **d)** 15.8 MHz.

8.4.2 2D scans

The SD-CNOT implementation was also characterized with 2D scans where both the control qubit pulse and the SD-CNOT gate pulse durations were swept. For every pulse duration of the control qubit, a CNOT pulse on both qubit control lines is sent to the device while sweeping its duration. We observe in Fig. 8.11 CNOT rotations along the vertical axis when qubit 2 is prepared in the excited state (π pulse).

We observed unwanted qubit excitation during this pulse scheme. Indeed, we observe in the top plot of Fig. 8.12, for a control qubit pulse duration of 0 ns, small oscillations above the Q quadrature level of the ground state. The readout levels were independently calibrated just before and after the 2D scan acquisition, to make sure that there were only negligible drifts of the state levels during the sweeps. The frequency of the oscillations is the same as the CNOT rotations

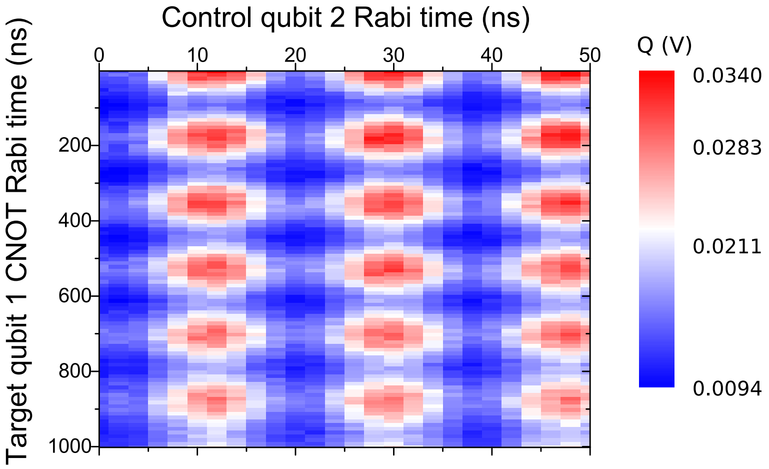

Figure 8.11: CNOT oscillations 2D map. 2D scan corresponding to a control qubit Rabi frequency of 55.5 MHz (horizontal axis). CNOT rotations on target qubit 1 ($|01\rangle \leftrightarrow |11\rangle$ transitions) are observed along the vertical axis when the control qubit (qubit 2) is in the excited state, at around 11, 29 and 47 ns, as read on the horizontal axis.

when qubit 2 is prepared with a π pulse (11 ns). They are the signature of CNOT rotation on target qubit 1 due to spurious population of qubit 2 which is imperfectly prepared in the ground state due to either thermal activation, of setup induced population (higher power readout or noise coming through the qubit control line 2 configured with 30 dB less attenuation that qubit 1 line).

Since the four states calibration levels are acquired with the same microwave setup configuration and pulse durations as for the CNOT characterization scripts, the unwanted qubit population is hidden from the measured quadrature levels which are then a mixture of a complex combination of effective states populations. We are still investigating this issue and have attempted to improve our readout calibration procedure by considering non-trivial states mixtures to better reconstruct the measured quantum states.

8.4.3 Improving the CNOT gate fidelity

Given the issues observed with unwanted qubit population induced by the setup configuration, the readout power or thermal activation, the calibration of the quantum states and their reconstructions were affected, and the quantum state tomography experiments and state reconstructions were not deemed conclusive. The fidelity of the CNOT gate was therefore only extracted from CNOT Rabi

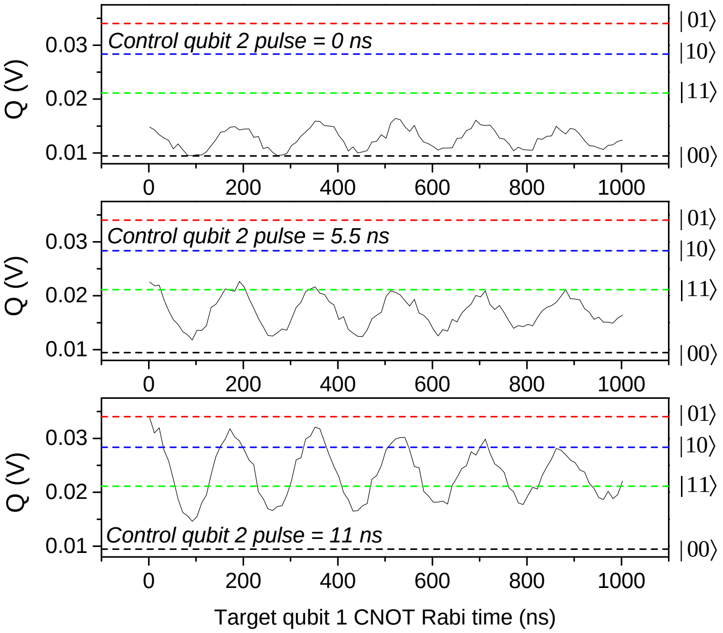

Figure 8.12: CNOT gate with control qubit preparation in ground, superposition or excited state. 3 vertical slices taken from 2d scan (Fig. 8.11) at different control qubit 2 pulse durations: 0 ns, 5.5 ns ($\frac{\pi}{2}$) and 11 ns (π). Horizontal dashed lines are the measured calibration level acquired just after the measurement.

curves similar to Fig. 8.13 by exponentiating the ratio of the duration of the first CNOT π pulse with the decay constant obtained by fitting the oscillations. This estimated fidelity, assuming no unwanted qubit population, was found to be around 95 %. Further study of this implementation of a CNOT gate is needed. One way which fridge availability did not allow at this time would be to perform the CNOT gate characterization using qubit 2 as the target, which would allow adding more attenuation on the line and limit its spurious excitation due to the setup. Better filtering and thermal anchoring of cables at the cryogenic level could improve the ground state preparation of qubit 2 which has the lowest Δ.

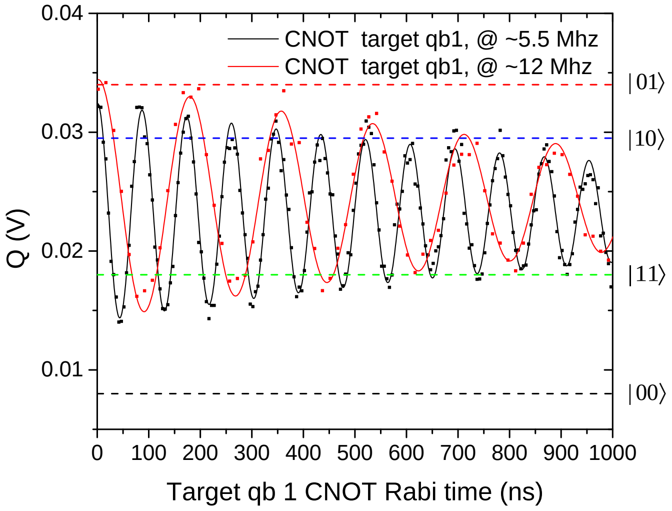

Figure 8.13: CNOT rotations on qubit 1 obtained at two different speeds. Horizontal dashed lines are the measured calibration level acquired just after the measurement.

8.5 Chapter summary

In this chapter, our implementation of a CNOT gate using the SD technique with two flux qubits transversely coupled through a microwave resonator was presented. The CNOT gate was operated at various speeds and we presented some of the current limitations observed with the particular device that was tested. Despite some unwanted qubit population affecting the measured quantum states of the system, we measured multiple CNOT rotations on a target qubit for a single control qubit excitation.

This technique has the advantage of requiring a relatively simple microwave pulse scheme and permits fast CNOT gates (measured to be as short as 50 ns with the presented device) even with relatively low qubit-qubit $J/h = 18.895\,\text{MHz}$ coupling strength.

Chapter 9

Conclusions and outlook

Summary and contributions

I have presented in this thesis the theoretical and experimental framework used for the design and characterization of superconducting flux qubits in cQED. We considered how such circuit quantum electrodynamics architecture enables multiple flux qubits to interact with each other strongly through a superconducting resonator, and permits single and entangling quantum gates operations using microwave pulses. Numerical simulations of all the parameters of a multi-qubit chip guided the design of the experiment setup, cryogenic apparatus, control electronics, wiring and signal conditioning. The laboratory and clean room fabrication processes were built from the ground up at the beginning of this work, for the purpose of this project and our group projects that followed, which inherited from the expertise acquired in designing, fabrication and characterizing superconducting flux qubits. We successfully measured decoherence properties of flux qubits which were strongly coupled to the modes of the resonators. The results obtained establish a solid baseline from which variations of coupling regimes, filtering, fabrication material and process improvements, can all contribute to making useful practical quantum devices for quantum computing or quantum sensing.

This project established a flexible platform to study the decoherence of flux tunable qubits [143, 2] as well as the strong interaction between artificial atoms and electromagnetic radiation [154, 155, 156, 157]. We introduce briefly below two published works that derive from this project's experimental achievements in the domain of ultra fast driving of a flux qubit and ultra strong coupling:

Observation of Floquet states in a strongly driven artificial atom

In the work by Chunqing Deng *et al.* titled *Observation of Floquet states in a strongly driven artificial atom* [154], we presented experiments on the driven dynamics of a flux qubit driven at a strength of 4.78 GHz which exceeds greatly the qubit's energy gap Δ frequency of 2.288 GHz. The measured qubit dynamics is in good agreements with the simulated quasienergies described by Floquet theory (see also [155] for a more in depth modelization that followed this work). Instead of using our regular approach to generate control pulses to drive the qubits, where I and Q quadratures shape a continuous wave from a stable microwave synthesizer, we used instead a high-speed AWG with rise and fall times shorter than 22 ps. This initial study of flux qubit dynamics under strong driving regime opens to door of sub nanosecond quantum gates with fidelities exceeding 0.9996.

Ultrastrong coupling of a single artificial atom to an electromagnetic continuum

In another work led by Pol Forn-Díaz titled *Ultrastrong coupling of a single artificial atom to an electromagnetic continuum in the nonperturbative regime* [158], a flux qubit is coupled to a transmission line. This superconducting one-dimensional waveguide supports a continuum of modes. The qubit can be tuned to be strongly coupled to this waveguide and the regime of ultrastrong coupling (USC) can be reached. This large (controllable) light-matter interaction strength leads to the high spontaneous emission rate of this artificial atom. The advantages of using a higher coupling are the obvious speedup of gate time, especially the qubit-resonator gate time [159]. In addition, the system of qubit+resonator in the ultrastrong coupling regime [160] leads to being able to study physics beyond the standard Jaynes-Cummings model [161]. This is useful for quantum simulation as some real physical systems can be described using models equivalent to the Rabi model (Rabi model is the full Hamiltonian of a two-level system and a harmonic oscillator with dipole coupling between them): Jahn-Teller phase transitions [162] or some variation of the Ising model [163] are just a couple of examples. For the case of one qubit coupled to free space with ultrastrong coupling we can emulate the spin-boson model [164]. This

---

is used in many condensed matter settings where a two-level system is surrounded by a bath of harmonic oscillators. Depending on the parameters one can reach the Kondo regime where the *magnetization* of the two-level system becomes entangled with its surroundings. Such a system based on flux qubit in cQED was studied in another co-authored work led by L. Magazzú titled *Probing the strongly driven spin-boson model in a superconducting quantum circuit* [157].

References

[1] Florian R. Ong, Jean-Luc Orgiazzi, Arlette de Waard, Giorgio Frossati, and Adrian Lupaşcu. Insertable system for fast turnaround time microwave experiments in a dilution refrigerator. *Rev. Sci. Instrum.*, 83(9):093904, sep 2012. doi: 10.1063/1.4754634. URL `https://aip.scitation.org/doi/10.1063/1.4754634`.

[2] J.-L. Orgiazzi, C. Deng, D. Layden, R. Marchildon, F. Kitapli, F. Shen, M. Bal, F. R. Ong, and A. Lupaşcu. Flux qubits in a planar circuit quantum electrodynamics architecture: Quantum control and decoherence. *Phys. Rev. B*, 93(10):104518, March 2016. doi: 10.1103/PhysRevB.93.104518. URL `https://link.aps.org/doi/10.1103/PhysRevB.93.104518`.

[3] Richard Feynman. Simulating physics with computers. *Int. J. Theor. Phys.*, 21(6):467–488, jun 1982. ISSN 0020-7748. doi: 10.1007/BF02650179. URL `https://link.springer.com/article/10.1007/BF02650179`.

[4] D. Deutsch. Quantum theory, the chuch-turing principle and the universal quantum computer. *Proc.R.Soc.Lond.A*, 400:97–117, 1985. doi: 10.1098/rspa.1985.0070. URL `https://doi.org/10.1098/rspa.1985.0070`.

[5] P.W. Shor. Algorithms for quantum computation: discrete logarithms and factoring. *Foundations of Computer Science, Annual IEEE Symposium on*, 0:124–134, 1994. doi: 10.1109/SFCS.1994.365700. URL `http://ieeexplore.ieee.org/stamp/stamp.jsp?tp=&arnumber=365700&isnumber=8384`.

[6] Lov K. Grover. A fast quantum mechanical algorithm for database search. In *STOC '96: Proceedings of the twenty-eighth annual ACM symposium on Theory of computing*, pages

212–219, New York, NY, USA, 1996. ACM. ISBN 0-89791-785-5. doi: 10.1145/237814.237866. URL `https://dl.acm.org/citation.cfm?doid=237814.237866`.

[7] M.A. Nielsen and I.L. Chuang. *Quantum Computation and Quantum Information*. Cambridge University Press, 2000. doi: 10.1017/cbo9780511976667. URL `https://www.cambridge.org/core/books/quantum-computation-and-quantum-information/01E10196D0A682A6AEFFEA52D53BE9AE`.

[8] D.P.DiVincenzo. The physical implementation of quantum computation. *Fortschr. Phys.*, 48(9-11):771–783, jan 2000. doi: 10.1002/3527603182.ch1. URL `https://doi.org/10.1002/3527603182.ch1`.

[9] John Clarke and Frank K. Wilhelm. Superconducting quantum bits. *Nature*, 453(7198): 1031–1042, June 2008. ISSN 0028-0836. doi: 10.1038/nature07128. URL `https://www.nature.com/articles/nature07128`.

[10] Erik Lucero, M. Hofheinz, M. Ansmann, Radoslaw C. Bialczak, N. Katz, Matthew Neeley, A. D. O'Connell, H. Wang, A. N. Cleland, and John M. Martinis. High-fidelity gates in a single josephson qubit. *Phys. Rev. Lett.*, 100(24):247001–, June 2008. doi: 10.1103/PhysRevLett.100.247001. URL `https://link.aps.org/doi/10.1103/PhysRevLett.100.247001`.

[11] Jay Gambetta and Sarah Sheldon. Cramming more power into a quantum device, March 2019. URL `https://www.ibm.com/blogs/research/2019/03/power-quantum-device/`.

[12] J. H. Plantenberg, P. C. de Groot, C. J. P. M. Harmans, and J. E. Mooij. Demonstration of controlled-not quantum gates on a pair of superconducting quantum bits. *Nature*, 447 (7146):836–839, June 2007. ISSN 0028-0836. doi: 10.1038/nature05896. URL `https://www.nature.com/articles/nature05896`.

[13] Matthias Steffen, M. Ansmann, Radoslaw C. Bialczak, N. Katz, Erik Lucero, R. McDermott, Matthew Neeley, E. M. Weig, A. N. Cleland, and John M. Martinis. Measurement of the entanglement of two superconducting qubits via state tomography. *Science*, 313(5792): 1423–1425, 2006. doi: 10.1126/science.1130886. URL `http://www.sciencemag.org/cgi/content/abstract/313/5792/1423`.

[14] Austin G. Fowler, William F. Thompson, Zhizhong Yan, Ashley M. Stephens, B. L. T. Plourde, and Frank K. Wilhelm. Long-range coupling and scalable architecture for superconducting flux qubits. *Phys. Rev. B*, 76(17):174507–, November 2007. doi: 10.1103/PhysRevB.76.174507. URL https://link.aps.org/doi/10.1103/PhysRevB.76.174507.

[15] A. A. Houck, J. A. Schreier, B. R. Johnson, J. M. Chow, Jens Koch, J. M. Gambetta, D. I. Schuster, L. Frunzio, M. H. Devoret, S. M. Girvin, and R. J. Schoelkopf. Controlling the spontaneous emission of a superconducting transmon qubit. *Phys. Rev. Lett.*, 101(8):080502–, August 2008. doi: 10.1103/PhysRevLett.101.080502. URL https://link.aps.org/doi/10.1103/PhysRevLett.101.080502.

[16] M. H. Devoret and R. J. Schoelkopf. Superconducting circuits for quantum information: An outlook. *Science*, 339(6124):1169–1174, March 2013. doi: 10.1126/science.1231930. URL https://science.sciencemag.org/content/339/6124/1169.

[17] J. M. Raimond, M. Brune, and S. Haroche. Manipulating quantum entanglement with atoms and photons in a cavity. *Rev. Mod. Phys.*, 73(3):565–, August 2001. doi: 10.1103/RevModPhys.73.565. URL https://link.aps.org/doi/10.1103/RevModPhys.73.565.

[18] H. Mabuchi and A. C. Doherty. Cavity quantum electrodynamics: Coherence in context. *Science*, 298(5597):1372–1377, 2002. doi: 10.1126/science.1078446. URL http://www.sciencemag.org/cgi/content/abstract/298/5597/1372.

[19] Samuel Deleglise, Igor Dotsenko, Clement Sayrin, Julien Bernu, Michel Brune, Jean-Michel Raimond, and Serge Haroche. Reconstruction of non-classical cavity field states with snapshots of their decoherence. *Nature*, 455(7212):510–514, September 2008. ISSN 0028-0836. doi: 10.1038/nature07288. URL https://doi.org/10.1038/nature07288.

[20] Herbert Walther. Cavity quantum electrodynamics. *Rep. Prog. Phys.*, 69(5):1325–, apr 2006. ISSN 0034-4885. doi: 10.1088/0034-4885/69/5/R02. URL http://stacks.iop.org/0034-4885/69/i=5/a=R02.

[21] C. J. Hood, T. W. Lynn, A. C. Doherty, A. S. Parkins, and H. J. Kimble. The atom-cavity microscope: Single atoms bound in orbit by single photons. *Science*, 287(5457):1447–1453, 2000. doi: 10.1126/science.287.5457.1447. URL http://www.sciencemag.org/cgi/content/abstract/287/5457/1447.

[22] Alexandre Blais, Ren-Shou Huang, Andreas Wallraff, S. M. Girvin, and R. J. Schoelkopf. Cavity quantum electrodynamics for superconducting electrical circuits: An architecture for quantum computation. *Phys. Rev. A*, 69(6):062320–, June 2004. doi: 10.1103/PhysRevA.69.062320. URL https://link.aps.org/doi/10.1103/PhysRevA.69.062320.

[23] E.T. Jaynes and F.W. Cummings. Comparison of quantum and semiclassical radiation theories with application to the beam maser. *Proceedings of the IEEE DOI - 10.1109/PROC.1963.1664*, 51(1):89–109, 1963. ISSN 0018-9219. doi: 10.1109/proc.1963.1664. URL http://ieeexplore.ieee.org/stamp/stamp.jsp?tp=&arnumber=1443594&isnumber=31044.

[24] A. Wallraff, D. I. Schuster, A. Blais, L. Frunzio, R.-S. Huang, J. Majer, S. Kumar, S. M. Girvin, and R. J. Schoelkopf. Strong coupling of a single photon to a superconducting qubit using circuit quantum electrodynamics. *Nature*, 431(7005):162–167, September 2004. ISSN 0028-0836. doi: 10.1038/nature02851. URL https://www.nature.com/articles/nature02851.

[25] A. A. Houck, D. I. Schuster, J. M. Gambetta, J. A. Schreier, B. R. Johnson, J. M. Chow, L. Frunzio, J. Majer, M. H. Devoret, S. M. Girvin, and R. J. Schoelkopf. Generating single microwave photons in a circuit. *Nature*, 449(7160):328–331, September 2007. ISSN 0028-0836. doi: 10.1038/nature06126. URL https://doi.org/10.1038/nature06126.

[26] Max Hofheinz, E. M. Weig, M. Ansmann, Radoslaw C. Bialczak, Erik Lucero, M. Neeley, A. D. O'Connell, H. Wang, John M. Martinis, and A. N. Cleland. Generation of fock states in a superconducting quantum circuit. *Nature*, 454(7202):310–314, July 2008. ISSN 0028-0836. doi: 10.1038/nature07136. URL https://doi.org/10.1038/nature07136.

[27] Max Hofheinz, H. Wang, M. Ansmann, Radoslaw C. Bialczak, Erik Lucero, M. Neeley, A. D. O'Connell, D. Sank, J. Wenner, John M. Martinis, and A. N. Cleland. Synthesizing arbitrary quantum states in a superconducting resonator. *Nature*, 459(7246):546–549, May 2009. ISSN 0028-0836. doi: 10.1038/nature08005. URL https://doi.org/10.1038/nature08005.

[28] Agustin Palacios-Laloy, Francois Mallet, Francois Nguyen, Patrice Bertet, Denis Vion, Daniel Esteve, and Alexander N. Korotkov. Experimental violation of a bell/'s inequality in

time with weak measurement. *Nat. Phys.*, 6(6):442–447, June 2010. ISSN 1745-2473. doi: 10.1038/nphys1641. URL https://doi.org/10.1038/nphys1641.

[29] I. Chiorescu, P. Bertet, K. Semba, Y. Nakamura, C. J. P. M. Harmans, and J. E. Mooij. Coherent dynamics of a flux qubit coupled to a harmonic oscillator. *Nature*, 431(7005): 159–162, September 2004. ISSN 0028-0836. doi: 10.1038/nature02831. URL https://www.nature.com/articles/nature02831.

[30] J. Johansson, S. Saito, T. Meno, H. Nakano, M. Ueda, K. Semba, and H. Takayanagi. Vacuum rabi oscillations in a macroscopic superconducting qubit lc oscillator system. *Phys. Rev. Lett.*, 96(12):127006–, March 2006. doi: 10.1103/PhysRevLett.96.127006. URL https://link.aps.org/doi/10.1103/PhysRevLett.96.127006.

[31] D. I. Schuster, A. A. Houck, J. A. Schreier, A. Wallraff, J. M. Gambetta, A. Blais, L. Frunzio, J. Majer, B. Johnson, M. H. Devoret, S. M. Girvin, and R. J. Schoelkopf. Resolving photon number states in a superconducting circuit. *Nature*, 445(7127):515–518, February 2007. ISSN 0028-0836. doi: 10.1038/nature05461. URL https://www.nature.com/articles/nature05461.

[32] O. Astafiev, K. Inomata, A. O. Niskanen, T. Yamamoto, Yu. A. Pashkin, Y. Nakamura, and J. S. Tsai. Single artificial-atom lasing. *Nature*, 449(7162):588–590, October 2007. ISSN 0028-0836. doi: 10.1038/nature06141. URL https://www.nature.com/articles/nature06141.

[33] F. Deppe, M. Mariantoni, E. P. Menzel, A. Marx, S. Saito, K. Kakuyanagi, H. Tanaka, T. Meno, K. Semba, H. Takayanagi, E. Solano, and R. Gross. Two-photon probe of the jaynes-cummings model and controlled symmetry breaking in circuit qed. *Nat. Phys.*, 4 (9):686–691, September 2008. ISSN 1745-2473. doi: 10.1038/nphys1016. URL https://www.nature.com/articles/nphys1016.

[34] J. M. Fink, M. Goppl, M. Baur, R. Bianchetti, P. J. Leek, A. Blais, and A. Wallraff. Climbing the jaynes-cummings ladder and observing its nonlinearity in a cavity qed system. *Nature*, 454(7202):315–318, July 2008. ISSN 0028-0836. doi: 10.1038/nature07112. URL https://www.nature.com/articles/nature07112.

[35] Abdufarrukh A. Abdumalikov, Oleg Astafiev, Yasunobu Nakamura, Yuri A. Pashkin, and JawShen Tsai. Vacuum rabi splitting due to strong coupling of a flux qubit and a coplanar-

waveguide resonator. *Phys. Rev. B*, 78(18):180502–, November 2008. doi: 10.1103/PhysRevB.78.180502. URL https://link.aps.org/doi/10.1103/PhysRevB.78.180502.

[36] R. Barends, J. Kelly, A. Megrant, A. Veitia, D. Sank, E. Jeffrey, T. C. White, J. Mutus, A. G. Fowler, B. Campbell, Y. Chen, Z. Chen, B. Chiaro, A. Dunsworth, C. Neill, P. O/'Malley, P. Roushan, A. Vainsencher, J. Wenner, A. N. Korotkov, A. N. Cleland, and John M. Martinis. Superconducting quantum circuits at the surface code threshold for fault tolerance. *Nature*, 508(7497):500–503, April 2014. ISSN 0028-0836. doi: 10.1038/nature13171. URL https://www.nature.com/articles/nature13171.

[37] P. C. de Groot, J. Lisenfeld, R. N. Schouten, S. Ashhab, A. Lupaşcu, C. J. P. M. Harmans, and J. E. Mooij. Selective darkening of degenerate transitions demonstrated with two superconducting quantum bits. *Nat. Phys.*, 6(10):763–766, October 2010. ISSN 1745-2473. doi: 10.1038/nphys1733. URL https://doi.org/10.1038/nphys1733.

[38] B.D. Josephson. Possible new effects in superconducting tunnelling. *Phys. Lett.*, 1:251, 1962. doi: 10.1016/0031-9163(62)91369-0. URL http://www.sciencedirect.com/science/article/pii/0031916362913690.

[39] V. Ambegaokar and A. Baratoff. Tunneling between superconductors. *Phys. Rev. Lett.*, 11 (2):104–, July 1963. doi: 10.1103/PhysRevLett.10.486. URL https://link.aps.org/doi/10.1103/PhysRevLett.10.486.

[40] John M. Martinis, S. Nam, J. Aumentado, and C. Urbina. Rabi oscillations in a large josephson-junction qubit. *Phys. Rev. Lett.*, 89(11):117901–, August 2002. doi: 10.1103/PhysRevLett.89.117901. URL https://link.aps.org/doi/10.1103/PhysRevLett.89.117901.

[41] Matthias Steffen, M. Ansmann, R. McDermott, N. Katz, Radoslaw C. Bialczak, Erik Lucero, Matthew Neeley, E. M. Weig, A. N. Cleland, and John M. Martinis. State tomography of capacitively shunted phase qubits with high fidelity. *Phys. Rev. Lett.*, 97(5):050502–, August 2006. doi: 10.1103/PhysRevLett.97.050502. URL https://link.aps.org/doi/10.1103/PhysRevLett.97.050502.

[42] Jens Koch, Terri M. Yu, Jay Gambetta, A. A. Houck, D. I. Schuster, J. Majer, Alexandre Blais, M. H. Devoret, S. M. Girvin, and R. J. Schoelkopf. Charge-insensitive qubit design

derived from the cooper pair box. *Phys. Rev. A*, 76(4):042319–, October 2007. doi: 10.1103/PhysRevA.76.042319. URL https://link.aps.org/doi/10.1103/PhysRevA.76.042319.

[43] J. A. Schreier, A. A. Houck, Jens Koch, D. I. Schuster, B. R. Johnson, J. M. Chow, J. M. Gambetta, J. Majer, L. Frunzio, M. H. Devoret, S. M. Girvin, and R. J. Schoelkopf. Suppressing charge noise decoherence in superconducting charge qubits. *Phys. Rev. B*, 77(18):180502–, May 2008. doi: 10.1103/PhysRevB.77.180502. URL https://link.aps.org/doi/10.1103/PhysRevB.77.180502.

[44] Y. Nakamura, Yu. A. Pashkin, and J. S. Tsai. Coherent control of macroscopic quantum states in a single-cooper-pair box. *Nature*, 398(6730):786–788, April 1999. ISSN 0028-0836. doi: 10.1038/19718. URL https://www.nature.com/articles/19718.

[45] J. E. Mooij, T. P. Orlando, L. Levitov, Lin Tian, Caspar H. van der Wal, and Seth Lloyd. Josephson persistent-current qubit. *Science*, 285(5430):1036–1039, 1999. doi: 10.1126/science.285.5430.1036. URL http://www.sciencemag.org/cgi/content/abstract/285/5430/1036.

[46] D. Vion, A. Aassime, A. Cottet, P. Joyez, H. Pothier, C. Urbina, D. Esteve, and M. H. Devoret. Manipulating the quantum state of an electrical circuit. *Science*, 296(5569):886–889, May 2002. doi: 10.1126/science.1069372. URL http://www.sciencemag.org/cgi/content/abstract/296/5569/886.

[47] T. P. Orlando, J. E. Mooij, Lin Tian, Caspar H. van der Wal, L. S. Levitov, Seth Lloyd, and J. J. Mazo. Superconducting persistent-current qubit. *Phys. Rev. B*, 60(22):15398–, December 1999. doi: 10.1103/PhysRevB.60.15398. URL https://link.aps.org/doi/10.1103/PhysRevB.60.15398.

[48] Guido Burkard, David P. DiVincenzo, P. Bertet, I. Chiorescu, and J. E. Mooij. Asymmetry and decoherence in a double-layer persistent-current qubit. *Phys. Rev. B*, 71(13):134504–8, April 2005. doi: 10.1103/physrevb.71.134504. URL http://link.aps.org/abstract/PRB/v71/e134504.

[49] Diego Ristè, Josephine G van Leeuwen, H-S Ku, Konrad W Lehnert, and Leonardo DiCarlo. Initialization by measurement of a superconducting quantum bit circuit. *Physi-*

cal review letters, 109(5):050507, 2012. URL https://link.aps.org/doi/10.1103/PhysRevLett.109.050507.

[50] M. C. Goorden and F. K. Wilhelm. Theoretical analysis of continuously driven dissipative solid-state qubits. *PRB*, 68(1):012508, July 2003. doi: 10.1103/PhysRevB.68.012508. URL https://link.aps.org/doi/10.1103/PhysRevB.68.012508.

[51] Milena Grifoni and Peter Hänggi. Driven quantum tunneling. *Phys. Rep.*, 304(5):229–354, October 1998. ISSN 0370-1573. doi: 10.1016/S0370-1573(98)00022-2. URL http://www.sciencedirect.com/science/article/pii/S0370157398000222.

[52] Michel Devoret. Quantum signals and circuits, lesson 1. College de France lectures, 2008. URL http://www.college-de-france.fr/media/michel-devoret/UPL3351655385606172215_Lecture_08_I_0513_110514_w_.pdf.

[53] C. W. Gardiner and M. J. Collett. Input and output in damped quantum systems: Quantum stochastic differential equations and the master equation. *Phys. Rev. A*, 31:3761–3774, Jun 1985. doi: 10.1103/PhysRevA.31.3761. URL https://link.aps.org/doi/10.1103/PhysRevA.31.3761.

[54] C. W. Gardiner and P. Zoller. *Quantum noise*. Springer, 2004. ISBN 978-3-540-22301-6.

[55] Aaron D. O'Connell, M. Ansmann, R. C. Bialczak, M. Hofheinz, N. Katz, Erik Lucero, C. McKenney, M. Neeley, H. Wang, E. M. Weig, A. N. Cleland, and J. M. Martinis. Microwave dielectric loss at single photon energies and millikelvin temperatures. *Appl. Phys. Lett.*, 92(11):112903, 2008. doi: 10.1063/1.2898887. URL http://link.aip.org/link/?APL/92/112903/1.

[56] C. Song, M. P. DeFeo, K. Yu, and B. L. T. Plourde. Reducing microwave loss in superconducting resonators due to trapped vortices. *Appl. Phys. Lett.*, 95(23):232501, November 2009. ISSN 0003-6951. doi: 10.1063/1.3271523. URL https://aip.scitation.org/doi/10.1063/1.3271523.

[57] Jeremy M. Sage, Vladimir Bolkhovsky, William D. Oliver, Benjamin Turek, and Paul B. Welander. Study of loss in superconducting coplanar waveguide resonators. *J. Appl. Phys.*, 109(6):063915, 2011. doi: 10.1063/1.3552890. URL http://link.aip.org/link/?JAP/109/063915/1.

[58] David M. Pozar. *Microwave Engineering, Third Edition.* John Wiley & Sons, Inc., 2005. ISBN 978-8126510498.

[59] T Lindström, C H Webster, J E Healey, M S Colclough, C M Muirhead, and A Ya Tzalenchuk. Circuit qed with a flux qubit strongly coupled to a coplanar transmission line resonator. *Supercond. Sci. Technol.*, 20(8):814, jun 2007. doi: 10.1088/0953-2048/20/8/016. URL http://stacks.iop.org/0953-2048/20/i=8/a=016.

[60] J. Bourassa, J. M. Gambetta, A. A. Abdumalikov, O. Astafiev, Y. Nakamura, and A. Blais. Ultrastrong coupling regime of cavity qed with phase-biased flux qubits. *Phys. Rev. A*, 80 (3):032109–, September 2009. doi: 10.1103/PhysRevA.80.032109. URL https://link.aps.org/doi/10.1103/PhysRevA.80.032109.

[61] Daniel F Walls and Gerard J Milburn. *Quantum optics.* Springer Science & Business Media, 2007. doi: 10.1007/978-0-387-30420-5_14. URL https://doi.org/10.1007/978-0-387-30420-5_14.

[62] L. DiCarlo, M. D. Reed, L. Sun, B. R. Johnson, J. M. Chow, J. M. Gambetta, L. Frunzio, S. M. Girvin, M. H. Devoret, and R. J. Schoelkopf. Preparation and measurement of three-qubit entanglement in a superconducting circuit. *Nature*, 467(7315):574–578, September 2010. ISSN 0028-0836. doi: 10.1038/nature09416. URL https://www.nature.com/articles/nature09416.

[63] P C de Groot, S Ashhab, A Lupaşcu, L DiCarlo, Franco Nori, C J P M Harmans, and J E Mooij. Selective darkening of degenerate transitions for implementing quantum controlled-not gates. *New J. Phys.*, 14(7):073038, jul 2012. doi: https://doi.org/10.1088/1367-2630/14/7/073038. URL http://stacks.iop.org/1367-2630/14/i=7/a=073038.

[64] Howard Carmichael. *An Open Systems Approach to Quantum Optics.* Number 18 in Lecture Notes in Physics Monographs. Springer-Verlag Berlin Heidelberg, 1993. ISBN 978-3-540-56634-2. doi: 10.1007/978-3-540-47620-7. URL https://doi.org/10.1007/978-3-540-47620-7.

[65] Félix Beaudoin, Jay M Gambetta, and A Blais. Dissipation and ultrastrong coupling in circuit qed. *Physical Review A*, 84(4):043832, 2011. doi: 10.1103/PhysRevA.84.043832. URL https://link.aps.org/doi/10.1103/PhysRevA.84.043832.

[66] A. Wallraff, D. I. Schuster, A. Blais, L. Frunzio, J. Majer, M. H. Devoret, S. M. Girvin, and R. J. Schoelkopf. Approaching unit visibility for control of a superconducting qubit with dispersive readout. *Phys. Rev. Lett.*, 95(6):060501–, August 2005. doi: 10.1103/PhysRevLett.95.060501. URL `https://link.aps.org/doi/10.1103/PhysRevLett.95.060501`.

[67] Jack Ekin. *Experimental Techniques for Low-Temperature Measurements: Cryostat Design, Material Properties and Superconductor Critical-Current Testing.* Oxford University Press, 2006. ISBN 978-0198570547.

[68] Frank Pobell. *Matter and methods at low temperatures.* Springer Science & Business Media, 2007. ISBN 978-3-540-46356-6. doi: 10.1007/978-3-540-46360-3. URL `http://dx.doi.org/10.1007/978-3-540-46360-3`.

[69] Iulia Buluta, Sahel Ashhab, and Franco Nori. Natural and artificial atoms for quantum computation. *Rep. Prog. Phys.*, 74(10):104401, sep 2011. doi: 10.1088/0034-4885/74/10/104401. URL `http://stacks.iop.org/0034-4885/74/i=10/a=104401`.

[70] J. Q. You and Franco Nori. Atomic physics and quantum optics using superconducting circuits. *Nature*, 474(7353):589–597, June 2011. ISSN 0028-0836. doi: 10.1038/nature10122. URL `https://doi.org/10.1038/nature10122`.

[71] A. A. Clerk, M. H. Devoret, S. M. Girvin, Florian Marquardt, and R. J. Schoelkopf. Introduction to quantum noise, measurement, and amplification. *Rev. Mod. Phys.*, 82:1155–1208, Apr 2010. doi: 10.1103/RevModPhys.82.1155. URL `https://link.aps.org/doi/10.1103/RevModPhys.82.1155`.

[72] Michael Mück, JB Kycia, and John Clarke. Superconducting quantum interference device as a near-quantum-limited amplifier at 0.5 ghz. *Appl. Phys. Lett.*, 78(7):967–969, 2001. doi: 10.1063/1.1347384. URL `https://doi.org/10.1063/1.1347384`.

[73] M. A. Castellanos-Beltran, K. D. Irwin, G. C. Hilton, L. R. Vale, and K. W. Lehnert. Amplification and squeezing of quantum noise with a tunable josephson metamaterial. *Nat. Phys.*, 4(12):929–931, December 2008. ISSN 1745-2473. doi: 10.1038/nphys1090. URL `https://doi.org/10.1038/nphys1090`.

[74] N. Bergeal, R. Vijay, V. E. Manucharyan, I. Siddiqi, R. J. Schoelkopf, S. M. Girvin, and M. H. Devoret. Analog information processing at the quantum limit with a josephson ring modulator. *Nat. Phys.*, 6(4):296–302, April 2010. ISSN 1745-2473. doi: 10.1038/nphys1516. URL `https://doi.org/10.1038/nphys1516`.

[75] G. A. Steele, A. K. Hüttel, B. Witkamp, M. Poot, H. B. Meerwaldt, L. P. Kouwenhoven, and H. S. J. van der Zant. Strong coupling between single-electron tunneling and nanomechanical motion. *Science*, 325(5944):1103–1107, 2009. doi: 10.1126/science.1176076. URL `http://www.sciencemag.org/content/325/5944/1103.abstract`.

[76] A. D. O'Connell, M. Hofheinz, M. Ansmann, Radoslaw C. Bialczak, M. Lenander, Erik Lucero, M. Neeley, D. Sank, H. Wang, M. Weides, J. Wenner, John M. Martinis, and A. N. Cleland. Quantum ground state and single-phonon control of a mechanical resonator. *Nature*, 464(7289):697–703, April 2010. ISSN 0028-0836. doi: 10.1038/nature08967. URL `https://www.nature.com/articles/nature08967`.

[77] J. D. Teufel, T. Donner, Dale Li, J. W. Harlow, M. S. Allman, K. Cicak, A. J. Sirois, J. D. Whittaker, K. W. Lehnert, and R. W. Simmonds. Sideband cooling of micromechanical motion to the quantum ground state. *Nature*, 475(7356):359–363, July 2011. ISSN 0028-0836. doi: 10.1038/nature10261. URL `https://doi.org/10.1038/nature10261`.

[78] Y.V. Nazarov and Y.M. Blanter. *Quantum Transport: Introduction to Nanoscience*. Cambridge University Press, 2009. ISBN 9781139478175. doi: 10.1017/cbo9780511626906. URL `http://books.google.ca/books?id=bjmXJOFmqZIC`.

[79] R. J. Schoelkopf, P. J. Burke, A. A. Kozhevnikov, D. E. Prober, and M. J. Rooks. Frequency dependence of shot noise in a diffusive mesoscopic conductor. *Phys. Rev. Lett.*, 78:3370–3373, Apr 1997. doi: 10.1103/PhysRevLett.78.3370. URL `https://link.aps.org/doi/10.1103/PhysRevLett.78.3370`.

[80] J. Gabelli, L.-H. Reydellet, G. Fève, J.-M. Berroir, B. Plaçais, P. Roche, and D. C. Glattli. Hanbury brown–twiss correlations to probe the population statistics of ghz photons emitted by conductors. *Phys. Rev. Lett.*, 93:056801, Jul 2004. doi: 10.1103/PhysRevLett.93.056801. URL `https://link.aps.org/doi/10.1103/PhysRevLett.93.056801`.

[81] Katrin Steinberg, Marc Scheffler, and Martin Dressel. Broadband microwave spectroscopy

in corbino geometry at 3he temperatures. *Rev. Sci. Instrum.*, 83(2):024704, feb 2012. doi: 10.1063/1.3680576. URL https://doi.org/10.1063/1.3680576.

[82] Michael Tinkham. *Introduction to Superconductivity : Second Edition*. Dover Books on Physics, 2004. ISBN 978-0486435039.

[83] Yoseph Imry. *Introduction to Mesoscopic Physics : Second Edition*. Oxford University Press, 2009. ISBN 9780198507383.

[84] S. Nadj-Perge, S. M. Frolov, E. P. A. M. Bakkers, and L. P. Kouwenhoven. Spin-orbit qubit in a semiconductor nanowire. *Nature*, 468(7327):1084–1087, December 2010. ISSN 0028-0836. doi: 10.1038/nature09682. URL 10.1038/nature09682.

[85] URL www.leidencryogenics.com. Leiden Cryogenics B.V. is a manufacturer of dilution refrigerators and low temperature accessories.

[86] All the SMP connectors used in this work are available either from Rosenberger or Fairview Microwave.

[87] An upgraded version of the thermalization system now yields a differential of 2 mK.

[88] Peter K. Day, Henry G. LeDuc, Benjamin A. Mazin, Anastasios Vayonakis, and Jonas Zmuidzinas. A broadband superconducting detector suitable for use in large arrays. *Nature*, 425(6960):817–821, October 2003. ISSN 0028-0836. doi: 10.1038/nature02037. URL https://www.nature.com/articles/nature02037.

[89] Serge Haroche and Jean-Michel Raimond. *Exploring the Quantum : Atom, Cavities and Photons*. Oxford University Press, 2006. ISBN 9780198509141. doi: 10.1093/acprof:oso/9780198509141.001.0001. URL https://www.oxfordscholarship.com/view/10.1093/acprof:oso/9780198509141.001.0001/acprof-9780198509141.

[90] The coherence is expected to be optimal at $\Phi/\Phi_0 = 0.5$ (symmetry point). However at that working point the detuning between the flux qubit and the resonator is not large enough compared to g so their dynamics are hybridized. To be sensitive to the coherence of the qubit only we chose to work away from the symmetry point.

[91] G. J. Dolan. Offset masks for lift-off photoprocessing. *Appl. Phys. Lett.*, 31(5):337–339, September 1977. doi: https://doi.org/10.1063/1.89690. URL http://link.aip.org/link/?APL/31/337/1.

[92] T. A. Fulton and G. J. Dolan. Observation of single-electron charging effects in small tunnel junctions. *Phys. Rev. Lett.*, 59(1):109–, July 1987. doi: 10.1103/PhysRevLett.59.109. URL `https://link.aps.org/doi/10.1103/PhysRevLett.59.109`.

[93] URL `https://www.nfcorp.co.jp/english/pro/mi/lcr/zm/dl/zm_spec.pdf`.

[94] Johannes Schindelin, Ignacio Arganda-Carreras, Erwin Frise, Verena Kaynig, Mark Longair, Tobias Pietzsch, Stephan Preibisch, Curtis Rueden, Stephan Saalfeld, Benjamin Schmid, Jean-Yves Tinevez, Daniel James White, Volker Hartenstein, Kevin Eliceiri, Pavel Tomancak, and Albert Cardona. Fiji: an open-source platform for biological-image analysis. *Nat. Methods*, 9:676, June 2012. doi: 10.1038/nmeth.2019. URL `https://doi.org/10.1038/nmeth.2019`.

[95] Curtis T. Rueden, Johannes Schindelin, Mark C. Hiner, Barry E. DeZonia, Alison E. Walter, Ellen T. Arena, and Kevin W. Eliceiri. Imagej2: Imagej for the next generation of scientific image data. *BMC Bioinf.*, 18(1):529, Nov 2017. ISSN 1471-2105. doi: 10.1186/s12859-017-1934-z. URL `https://doi.org/10.1186/s12859-017-1934-z`.

[96] D. I. Schuster. *Circuit quantum electrodynamics*. PhD thesis, Yale University, 2007.

[97] M. Goppl, A. Fragner, M. Baur, R. Bianchetti, S. Filipp, J. M. Fink, P. J. Leek, G. Puebla, L. Steffen, and A. Wallraff. Coplanar waveguide resonators for circuit quantum electrodynamics. *J. Appl. Phys.*, 104(11):113904, 2008. doi: 10.1063/1.3010859. URL `http://link.aip.org/link/?JAP/104/113904/1`.

[98] Kunihiro Inomata, Tsuyoshi Yamamoto, Michio Watanabe, Kazuaki Matsuba, and Jaw-Shen Tsai. Film-thickness dependence of 10 ghz nb coplanar-waveguide resonators. *Journal of Vacuum Science & Technology B: Microelectronics and Nanometer Structures*, 27(5):2286–2291, 2009. doi: 10.1116/1.3232301. URL `http://link.aip.org/link/?JVB/27/2286/1`.

[99] Gheorghe Stan, Stuart B. Field, and John M. Martinis. Critical field for complete vortex expulsion from narrow superconducting strips. *Phys. Rev. Lett.*, 92(9):097003–, March 2004. doi: 10.1103/PhysRevLett.92.097003. URL `https://link.aps.org/doi/10.1103/PhysRevLett.92.097003`.

[100] C. Song, T. W. Heitmann, M. P. DeFeo, K. Yu, R. McDermott, M. Neeley, John M. Martinis, and B. L. T. Plourde. Microwave response of vortices in superconducting thin films of re and al. *PRB*, 79(17):174512, May 2009. doi: 10.1103/PhysRevB.79.174512. URL https://link.aps.org/doi/10.1103/PhysRevB.74.174512.

[101] K.H. Kuit, John R. Kirtley, John R. Clem, Horst Rogalla, and J. Flokstra. Vortex trapping and expulsion in thin-film type-ii superconducting strips. *Applied Superconductivity, IEEE Transactions on*, 19(3):3537–3540, 2009. ISSN 1051-8223. doi: 10.1109/TASC.2009.2018080. URL https://link.aps.org/doi/10.1109/TASC.2009.2018080.

[102] H. Wang, M. Hofheinz, J. Wenner, M. Ansmann, R. C. Bialczak, M. Lenander, Erik Lucero, M. Neeley, A. D. O'Connell, D. Sank, M. Weides, A. N. Cleland, and John M. Martinis. Improving the coherence time of superconducting coplanar resonators. *Appl. Phys. Lett.*, 95 (23):233508, 2009. doi: 10.1063/1.3273372. URL http://link.aip.org/link/?APL/95/233508/1.

[103] D. Bothner, T. Gaber, M. Kemmler, D. Koelle, and R. Kleiner. Improving the performance of superconducting microwave resonators in magnetic fields. *Appl. Phys. Lett.*, 98(10): 102504, November 2011. ISSN 0003-6951. doi: 10.1063/1.3560480. URL https://aip.scitation.org/doi/10.1063/1.3560480.

[104] A. Fragner, M. Göppl, J. M. Fink, M. Baur, R. Bianchetti, P. J. Leek, A. Blais, and A. Wallraff. Resolving vacuum fluctuations in an electrical circuit by measuring the lamb shift. *Science*, 322(5906):1357–1360, 2008. doi: 10.1126/science.1164482. URL http://www.sciencemag.org/content/322/5906/1357.abstract.

[105] D. I. Schuster, A. Wallraff, A. Blais, L. Frunzio, R.-S. Huang, J. Majer, S. M. Girvin, and R. J. Schoelkopf. ac stark shift and dephasing of a superconducting qubit strongly coupled to a cavity field. *Phys. Rev. Lett.*, 94(12):123602–, March 2005. doi: 10.1103/PhysRevLett.94.123602. URL https://link.aps.org/doi/10.1103/PhysRevLett.94.123602.

[106] Jay Gambetta, Alexandre Blais, D. I. Schuster, A. Wallraff, L. Frunzio, J. Majer, M. H. Devoret, S. M. Girvin, and R. J. Schoelkopf. Qubit-photon interactions in a cavity: Measurement-induced dephasing and number splitting. *Phys. Rev. A*, 74(4):042318–, October 2006. doi: 10.1103/PhysRevA.74.042318. URL https://link.aps.org/doi/10.1103/PhysRevA.74.042318.

[107] Maxime Boissonneault, J. M. Gambetta, and Alexandre Blais. Improved superconducting qubit readout by qubit-induced nonlinearities. *Phys. Rev. Lett.*, 105(10):100504, Sep 2010. doi: 10.1103/PhysRevLett.105.100504. URL https://link.aps.org/doi/10.1103/PhysRevLett.105.100504.

[108] Lev S. Bishop, Eran Ginossar, and S. M. Girvin. Response of the strongly driven jaynes-cummings oscillator. *Phys. Rev. Lett.*, 105(10):100505, Sep 2010. doi: 10.1103/PhysRevLett.105.100505. URL https://link.aps.org/doi/10.1103/PhysRevLett.105.100505.

[109] M. D. Reed, L. DiCarlo, B. R. Johnson, L. Sun, D. I. Schuster, L. Frunzio, and R. J. Schoelkopf. High-fidelity readout in circuit quantum electrodynamics using the jaynes-cummings nonlinearity. *Phys. Rev. Lett.*, 105(17):173601, Oct 2010. doi: 10.1103/PhysRevLett.105.173601. URL https://link.aps.org/doi/10.1103/PhysRevLett.105.173601.

[110] C. Deng. *Fast control and decoherence in superconducting quantum circuits*. PhD thesis, University of Waterloo, 2015. URL http://hdl.handle.net/10012/9575.

[111] Sergio O. Valenzuela, William D. Oliver, David M. Berns, Karl K. Berggren, Leonid S. Levitov, and Terry P. Orlando. Microwave-induced cooling of a superconducting qubit. *Science*, 314(5805):1589, December 2006. doi: 10.1126/science.1134008. URL http://science.sciencemag.org/content/314/5805/1589.abstract.

[112] K. Geerlings, Z. Leghtas, I. M. Pop, S. Shankar, L. Frunzio, R. J. Schoelkopf, M. Mirrahimi, and M. H. Devoret. Demonstrating a driven reset protocol for a superconducting qubit. *PRL*, 110(12):120501, March 2013. doi: 10.1103/PhysRevLett.110.120501. URL https://link.aps.org/doi/10.1103/PhysRevLett.110.120501.

[113] Norman F. Ramsey. A molecular beam resonance method with separated oscillating fields. *Phys. Rev.*, 78:695–699, Jun 1950. doi: 10.1103/PhysRev.78.695. URL https://link.aps.org/doi/10.1103/PhysRev.78.695.

[114] E. L. Hahn. Spin echoes. *PR*, 80(4):580–594, November 1950. doi: 10.1103/PhysRev.80.580. URL https://link.aps.org/doi/10.1103/PhysRev.80.580.

[115] C. P. Slichter. *Principles of Magnetic Resonance*. Series in Solid-State Sciences. Springer, 1990. ISBN 978-3-662-09441-9. doi: 10.1007/978-3-662-09441-9. URL https://doi.org/10.1007/978-3-662-09441-9.

[116] Michael J. Biercuk, Hermann Uys, Aaron P. VanDevender, Nobuyasu Shiga, Wayne M. Itano, and John J. Bollinger. Experimental uhrig dynamical decoupling using trapped ions. *Phys. Rev. A*, 79(6):062324–, June 2009. doi: 10.1103/PhysRevA.79.062324. URL https://link.aps.org/doi/10.1103/PhysRevA.65.062324.

[117] Herman Y Carr and Edward M Purcell. Effects of diffusion on free precession in nuclear magnetic resonance experiments. *Phys. Rev.*, 94(3):630, 1954. doi: 10.1103/physrev.94.630. URL https://link.aps.org/doi/10.1103/PhysRev.94.630.

[118] Saul Meiboom and David Gill. Modified spin-echo method for measuring nuclear relaxation times. *Rev. Sci. Instrum.*, 29(8):688–691, 1958. doi: 10.1063/1.1716296. URL https://doi.org/10.1063/1.1716296.

[119] Gonzalo A. Álvarez and Dieter Suter. Measuring the spectrum of colored noise by dynamical decoupling. 107(23):230501, November 2011. doi: 10.1103/PhysRevLett.107.230501. URL https://link.aps.org/doi/10.1103/PhysRevLett.107.230501.

[120] Michael J. Biercuk. Quantum measurement: A quantum spectrum analyser. *Nat. Phys.*, 7(7):525–526, July 2011. ISSN 1745-2473. doi: 10.1038/nphys2005. URL https://www.nature.com/articles/nphys2005.

[121] Jonas Bylander, Simon Gustavsson, Fei Yan, Fumiki Yoshihara, Khalil Harrabi, George Fitch, David G. Cory, Yasunobu Nakamura, Jaw-Shen Tsai, and William D. Oliver. Noise spectroscopy through dynamical decoupling with a superconducting flux qubit. *Nat. Phys.*, 7 (7):565–570, July 2011. ISSN 1745-2473. doi: 10.1038/nphys1994. URL https://nature.com/articles/nphys1994.

[122] Peter Grünberg Institut. *Quantum Information Processing: Lecture Notes of the 44th IFF Spring School 2013*. Forschungszentrum, 2013. URL https://www.tib.eu/en/search/id/TIBKAT%3A751635839/Quantum-information-processing-lecture-notes-of/.

[123] M J Biercuk, A C Doherty, and H Uys. Dynamical decoupling sequence construction as a filter-design problem. *J. Phys. B: At., Mol. Opt. Phys.*, 44(15):154002, jul 2011. doi: 10.1088/0953-4075/44/15/154002. URL http://stacks.iop.org/0953-4075/44/i=15/a=154002.

[124] Götz S. Uhrig. Keeping a quantum bit alive by optimized π-pulse sequences. *PRL*, 98(10): 100504, March 2007. doi: 10.1103/PhysRevLett.98.100504. URL https://link.aps.org/doi/10.1103/PhysRevLett.98.100504.

[125] J. Majer, J. M. Chow, J. M. Gambetta, Jens Koch, B. R. Johnson, J. A. Schreier, L. Frunzio, D. I. Schuster, A. A. Houck, A. Wallraff, A. Blais, M. H. Devoret, S. M. Girvin, and R. J. Schoelkopf. Coupling superconducting qubits via a cavity bus. *Nature*, 449(7161): 443–447, September 2007. ISSN 0028-0836. doi: 10.1038/nature06184. URL https://www.nature.com/articles/nature06184.

[126] M.H. Devoret and R.J. Schoelkopf. Superconducting circuits for quantum information: An outlook. *Science*, 339(6124):1169–1174, 2013. doi: 10.1126/science.1231930. URL https://science.sciencemag.org/content/339/6124/1169.

[127] J. Q. You and Franco Nori. Atomic physics and quantum optics using superconducting circuits. *Nature*, 474(7353):589–597, June 2011. ISSN 0028-0836. URL http://dx.doi.org/10.1038/nature10122.

[128] T. Niemczyk, F. Deppe, H. Huebl, E. P. Menzel, F. Hocke, M. J. Schwarz, J. J. García-Ripoll, D. Zueco, T. Hummer, E. Solano, A. Marx, and R. Gross. Circuit quantum electrodynamics in the ultrastrong-coupling regime. *Nature Phys.*, 6(10):772–776, October 2010. ISSN 1745-2473. doi: 10.1038/nphys1730. URL https://doi.org/10.1038/nphys1730.

[129] B. Peropadre, D. Zueco, D. Porras, and J. J. García-Ripoll. Nonequilibrium and nonperturbative dynamics of ultrastrong coupling in open lines. *Phys. Rev. Lett.*, 111:243602, Dec 2013. doi: 10.1103/PhysRevLett.111.243602. URL http://link.aps.org/doi/10.1103/PhysRevLett.111.243602.

[130] Carlos Sabin, Borja Peropadre, Marco del Rey, and Eduardo Martin-Martinez. Extracting past-future vacuum correlations using circuit qed. *Phys. Rev. Lett.*, 109:033602, Jul 2012. doi: 10.1103/PhysRevLett.109.033602. URL http://link.aps.org/doi/10.1103/PhysRevLett.109.033602.

[131] M. Bal, C. Deng, J-L. Orgiazzi, F.R. Ong, and A. Lupaşcu. Ultrasensitive magnetic field detection using a single artificial atom. *Nat. Commun.*, 3(1):1324–, December 2012. doi: 10.1038/ncomms2332. URL `https://nature.com/articles/ncomms2332`.

[132] X. Zhu, S. Saito, A. Kemp, K. Kakuyanagi, S. Karimoto, H. Nakano, W. J. Munro, Y. Tokura, M. S. Everitt, K. Nemoto, M. Kasu, N. Mizuochi, and K. Semba. Coherent coupling of a superconducting flux qubit to an electron spin ensemble in diamond. *Nature*, 478:221, 2011. doi: 10.1038/nature10462. URL `https://doi.org/10.1038/nature10462`.

[133] K. Harrabi. Fabrication of flux qubit with a mechanical degree of freedom. *J. Supercond. Novel Magn.*, 26(11):3231–3234, 2013. ISSN 1557-1939. doi: 10.1007/s10948-013-2191-7. URL `http://dx.doi.org/10.1007/s10948-013-2191-7`.

[134] Alexandre Blais, Jay Gambetta, A. Wallraff, D. I. Schuster, S. M. Girvin, M. H. Devoret, and R. J. Schoelkopf. Quantum-information processing with circuit quantum electrodynamics. *Phys. Rev. A*, 75(3):032329–, March 2007. doi: 10.1103/PhysRevA.75.032329. URL `https://link.aps.org/doi/10.1103/PhysRevA.75.032329`.

[135] A. Wallraff, D. I. Schuster, A. Blais, L. Frunzio, R. S. Huang, J. Majer, S. Kumar, S. M. Girvin, and R. J. Schoelkopf. Strong coupling of a single photon to a superconducting qubit using circuit quantum electrodynamics. *Nature*, 431(7005):162, July 2004. doi: 10.1038/nature02851. URL `https://www.nature.com/articles/nature02851`.

[136] A. Wallraff, D.I. Schuster, A. Blais, L. Frunzio, J. Majer, M.H. Devoret, S.M. Girvin, and R.J. Schoelkopf. Approaching unit visibility for control of a superconducting qubit with dispersive readout. *Phys. Rev. Lett.*, 95(6):060501, August 2005. doi: 10.1103/PhysRevLett.95.060501. URL `https://link.aps.org/doi/10.1103/PhysRevLett.95.060501`.

[137] G. Oelsner, S. H. W. van der Ploeg, P. Macha, U. Hübner, D. Born, S. Anders, E. Il'ichev, H.-G. Meyer, M. Grajcar, S. Wünsch, M. Siegel, A. N. Omelyanchouk, and O. Astafiev. Weak continuous monitoring of a flux qubit using coplanar waveguide resonator. *Phys. Rev. B*, 81(17):172505–, May 2010. doi: 10.1103/PhysRevB.81.172505. URL `http://link.aps.org/doi/10.1103/PhysRevB.81.172505`.

[138] M. Jerger, S. Poletto, P. Macha, U. Hübner, A. Lukashenko, E. Il'ichev, and A. V. Ustinov. Readout of a qubit array via a single transmission line. *EPL (Europhysics Letters)*, 96

(4):40012, nov 2011. doi: https://doi.org/10.1209/0295-5075/96/40012. URL http://stacks.iop.org/0295-5075/96/i=4/a=40012.

[139] M. Jerger, S. Poletto, P. Macha, U. Hubner, E. Il'ichev, and A. V. Ustinov. Frequency division multiplexing readout and simultaneous manipulation of an array of flux qubits. *Appl. Phys. Lett.*, 101(4):042604–4, July 2012. doi: 10.1063/1.4739454. URL https://doi.org/10.1063/1.4739454.

[140] K. Inomata, T. Yamamoto, P.-M. Billangeon, Y. Nakamura, and J. S. Tsai. Large dispersive shift of cavity resonance induced by a superconducting flux qubit in the straddling regime. *Phys. Rev. B*, 86(14):140508–, October 2012. doi: 10.1103/PhysRevB.86.140508. URL https://link.aps.org/doi/10.1103/PhysRevB.86.140508.

[141] P. Bertet, I. Chiorescu, G. Burkard, K. Semba, C. J. P. M. Harmans, D. P. DiVincenzo, and J. E. Mooij. Dephasing of a superconducting qubit induced by photon noise. *Phys. Rev. Lett.*, 95:257002, Dec 2005. doi: 10.1103/PhysRevLett.95.257002. URL https://link.aps.org/doi/10.1103/PhysRevLett.95.257002.

[142] T. P. Orlando, J. E. Mooij, L. Tian, C. H. van der Wal, L. S. Levitov, S. Lloyd, and J. J. Mazo. Superconducting persistent-current qubit. *Phys. Rev. B*, 60:15398, 1999. doi: 10.1103/PhysRevB.60.15398. URL https://link.aps.org/doi/10.1103/PhysRevB.60.15398.

[143] M. Bal, M. H. Ansari, J.-L. Orgiazzi, R. M. Lutchyn, and A. Lupaşcu. Dynamics of parametric fluctuations induced by quasiparticle tunneling in superconducting flux qubits. *Physical Review B*, 91(19), June 2014. doi: 10.1103/PhysRevB.91.195434. URL https://link.aps.org/doi/10.1103/PhysRevB.91.195434.

[144] R. Barends, J. Kelly, A. Megrant, D. Sank, E. Jeffrey, Y. Chen, Y. Yin, B. Chiaro, J. Mutus, C. Neill, P. O'Malley, P. Roushan, J. Wenner, T. C. White, A. N. Cleland, and John M. Martinis. Coherent josephson qubit suitable for scalable quantum integrated circuits. *Phys. Rev. Lett.*, 111:080502, Aug 2013. doi: 10.1103/PhysRevLett.111.080502. URL http://link.aps.org/doi/10.1103/PhysRevLett.111.080502.

[145] G. Ithier, E. Collin, P. Joyez, P. J. Meeson, D. Vion, D. Esteve, F. Chiarello, A. Shnirman, Y. Makhlin, J. Schriefl, and G. Schön. Decoherence in a superconducting quantum bit

circuit. *Phys. Rev. B*, 72(13):134519, Oct 2005. doi: 10.1103/PhysRevB.72.134519. URL https://link.aps.org/doi/10.1103/PhysRevB.72.134519.

[146] K. Kakuyanagi, T. Meno, S. Saito, H. Nakano, K. Semba, H. Takayanagi, F. Deppe, and A. Shnirman. Dephasing of a superconducting flux qubit. *Phys. Rev. Lett.*, 98(4):047004–, January 2007. doi: 10.1103/PhysRevLett.98.047004. URL https://link.aps.org/doi/10.1103/PhysRevLett.98.047004.

[147] F. Yoshihara, K. Harrabi, A. O. Niskanen, Y. Nakamura, and J. S. Tsai. Decoherence of flux qubits due to 1/f flux noise. *Phys. Rev. Lett.*, 97(16):167001–, October 2006. doi: 10.1103/PhysRevLett.97.167001. URL https://link.aps.org/doi/10.1103/PhysRevLett.97.167001.

[148] S. M. Anton, J. S. Birenbaum, S. R. O'Kelley, V. Bolkhovsky, D. A. Braje, G. Fitch, M. Neeley, G. C. Hilton, H.-M. Cho, K. D. Irwin, F. C. Wellstood, W. D. Oliver, A. Shnirman, and John Clarke. Magnetic flux noise in dc squids: Temperature and geometry dependence. *Phys. Rev. Lett.*, 110:147002, Apr 2013. doi: 10.1103/PhysRevLett.110.147002. URL http://link.aps.org/doi/10.1103/PhysRevLett.110.147002.

[149] Y. Makhlin and A. Shnirman. Dephasing of solid-state qubits at optimal points. *Phys. Rev. Lett.*, 92:178301, April 2004. doi: 10.1103/PhysRevLett.92.178301. URL https://link.aps.org/doi/10.1103/PhysRevLett.92.178301.

[150] P. Bertet, I. Chiorescu, G. Burkard, K. Semba, C. J P M Harmans, D. P. DiVincenzo, and J. E. Mooij. Dephasing of a superconducting qubit induced by photon noise. *Phys. Rev. Lett.*, 95(25):257002, Dec 2005. doi: 10.1103/PhysRevLett.95.257002. URL http://link.aps.org/doi/10.1103/PhysRevLett.95.257002.

[151] Chad Rigetti, Jay M. Gambetta, Stefano Poletto, B. L. T. Plourde, Jerry M. Chow, A. D. Córcoles, John A. Smolin, Seth T. Merkel, J. R. Rozen, George A. Keefe, Mary B. Rothwell, Mark B. Ketchen, and M. Steffen. Superconducting qubit in a waveguide cavity with a coherence time approaching 0.1 ms. *Phys. Rev. B*, 86:100506, Sep 2012. doi: 10.1103/PhysRevB.86.100506. URL http://link.aps.org/doi/10.1103/PhysRevB.86.100506.

[152] A. P. Sears, A. Petrenko, G. Catelani, L. Sun, Hanhee Paik, G. Kirchmair, L. Frunzio, L. I. Glazman, S. M. Girvin, and R. J. Schoelkopf. Photon shot noise dephasing in the strong-

dispersive limit of circuit qed. *Phys. Rev. B*, 86:180504, Nov 2012. doi: 10.1103/PhysRevB.86.180504. URL http://link.aps.org/doi/10.1103/PhysRevB.86.180504.

[153] M. Stern, Y. Kubo, C. Grezes, A. Bienfait, D. Vion, D. Esteve, and P. Bertet. Flux Qubits in Three-Dimensional Circuit-QED Architecture. *Physical Review Letters*, 113(12), March 2014. doi: 10.1103/PhysRevLett.113.123601. URL https://link.aps.org/doi/10.1103/PhysRevLett.113.123601.

[154] Chunqing Deng, Jean-Luc Orgiazzi, Feiruo Shen, Sahel Ashhab, and Adrian Lupaşcu. Observation of floquet states in a strongly driven artificial atom. *Phys. Rev. Lett.*, 115(13):133601, sep 2015. doi: 10.1103/PhysRevLett.115.133601. URL https://link.aps.org/doi/10.1103/PhysRevLett.115.133601.

[155] Chunqing Deng, Feiruo Shen, Sahel Ashhab, and Adrian Lupaşcu. Dynamics of a two-level system under strong driving: Quantum-gate optimization based on floquet theory. *Phys. Rev. A*, 94(3):032323, sep 2016. doi: 10.1103/PhysRevA.94.032323. URL https://link.aps.org/doi/10.1103/PhysRevA.94.032323.

[156] Eyal Buks, Chunqing Deng, Jean-Luc F. X. Orgazzi, Martin Otto, and Adrian Lupaşcu. Superharmonic resonances in a strongly coupled cavity-atom system. *Phys. Rev. A*, 94(3):033807, September 2016. doi: 10.1103/PhysRevA.94.033807. URL https://link.aps.org/doi/10.1103/PhysRevA.94.033807.

[157] L. Magazzú, P. Forn-Díaz, R. Belyansky, J.-L. Orgiazzi, M. A. Yurtalan, M. R. Otto, A. Lupaşcu, C. M. Wilson, and M. Grifoni. Probing the strongly driven spin-boson model in a superconducting quantum circuit. *Nat. Commun.*, 9(1):1403, April 2018. ISSN 2041-1723. doi: 10.1038/s41467-018-03626-w. URL https://www.nature.com/articles/s41467-018-04348-9.

[158] P. Forn-Díaz, J. J. García-Ripoll, B. Peropadre, J.-L. Orgiazzi, M. A. Yurtalan, R. Belyansky, C. M. Wilson, and A. Lupaşcu. Ultrastrong coupling of a single artificial atom to an electromagnetic continuum in the nonperturbative regime. *Nat. Phys.*, 13(1):39, October 2016. doi: 10.1038/nphys3905. URL https://doi.org/10.1038/nphys2035.

[159] G. Romero, D. Ballester, Y. M. Wang, V. Scarani, and E. Solano. Ultrafast quantum gates in circuit qed. *Phys. Rev. Lett.*, 108:120501, Mar 2012. doi: 10.1103/PhysRevLett.108.120501. URL https://link.aps.org/doi/10.1103/PhysRevLett.108.120501.

[160] Fumiki Yoshihara, Tomoko Fuse, Sahel Ashhab, Kosuke Kakuyanagi, Shiro Saito, and Kouichi Semba. Superconducting qubit–oscillator circuit beyond the ultrastrong-coupling regime. *Nature Physics*, 13(1):44, October 2016. doi: 10.1038/nphys3906. URL `https://doi.org/10.1038/nphys3906`.

[161] D. Braak. Integrability of the rabi model. *Phys. Rev. Lett.*, 107(10):100401, Aug 2011. doi: 10.1103/PhysRevLett.107.100401. URL `https://link.aps.org/doi/10.1103/PhysRevLett.107.100401`.

[162] Charles P. Meaney, Tim Duty, Ross H. McKenzie, and G. J. Milburn. Jahn-teller instability in dissipative quantum systems. *Phys. Rev. A*, 81(4):043805, Apr 2010. doi: 10.1103/PhysRevA.81.043805. URL `https://link.aps.org/doi/10.1103/PhysRevA.81.043805`.

[163] M. Schiró, M. Bordyuh, B. Öztop, and H. E. Türeci. Phase transition of light in cavity qed lattices. *Phys. Rev. Lett.*, 109:053601, Aug 2012. doi: 10.1103/PhysRevLett.109.053601. URL `https://link.aps.org/doi/10.1103/PhysRevLett.109.053601`.

[164] B. Peropadre, D. Zueco, D. Porras, and J. J. García-Ripoll. Nonequilibrium and nonperturbative dynamics of ultrastrong coupling in open lines. *Phys. Rev. Lett.*, 111(24):243602, Dec 2013. doi: 10.1103/PhysRevLett.111.243602. URL `https://link.aps.org/doi/10.1103/PhysRevLett.111.243602`.

APPENDICES

Appendix A

Fabrication recipe cards

A.1 Pd/Au markers on Si fabrication using PMGI SF7 / Shipley 1811

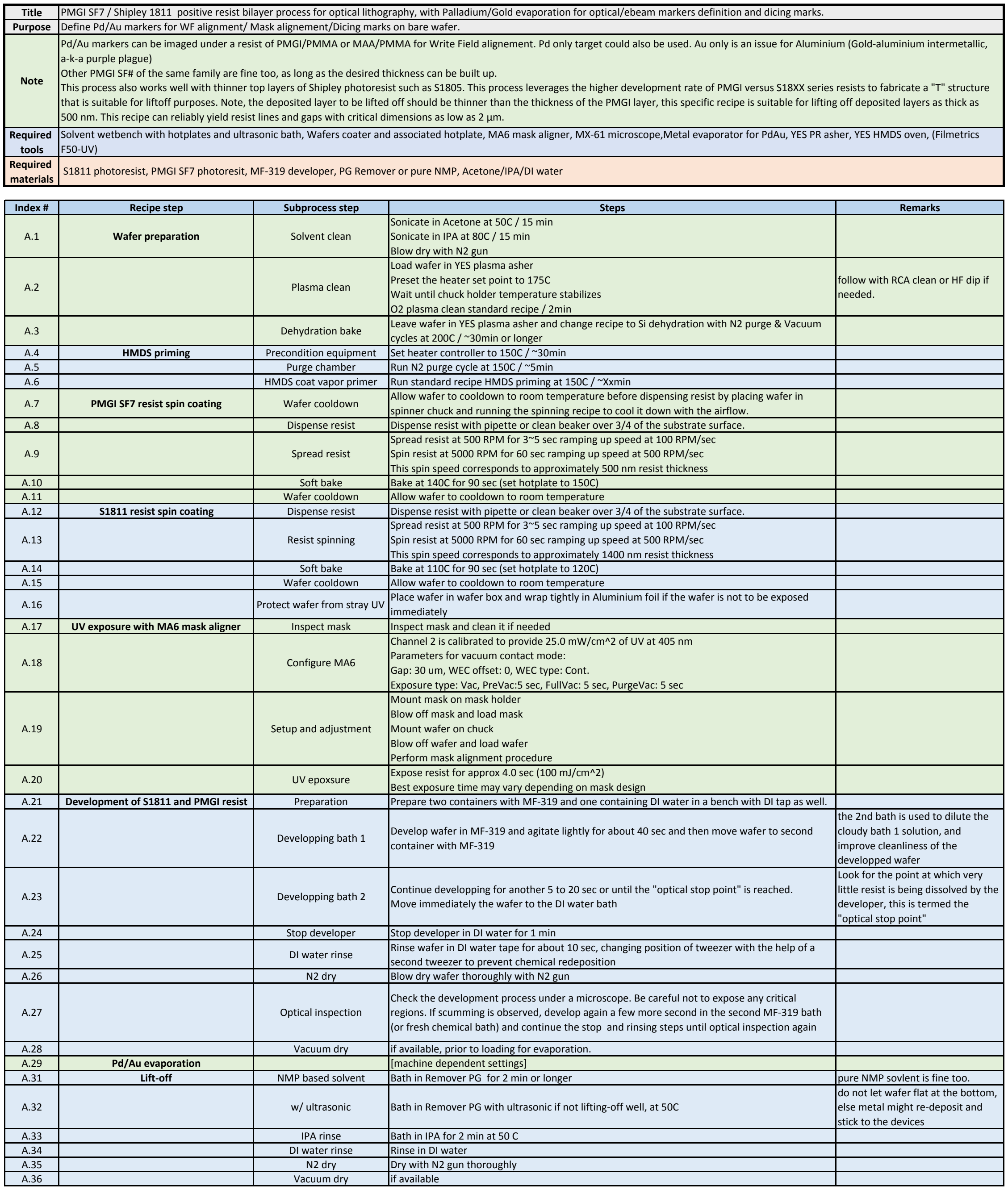

Title	PMGI SF7 / Shipley 1811 positive resist bilayer process for optical lithography, with Palladium/Gold evaporation for optical/ebeam markers definition and dicing marks.
Purpose	Define Pd/Au markers for WF alignment/ Mask alignement/Dicing marks on bare wafer.
Note	Pd/Au markers can be imaged under a resist of PMGI/PMMA or MAA/PMMA for Write Field alignement. Pd only target could also be used. Au only is an issue for Aluminium (Gold-aluminium intermetallic, a-k-a purple plague) Other PMGI SF# of the same family are fine too, as long as the desired thickness can be built up. This process also works well with thinner top layers of Shipley photoresist such as S1805. This process leverages the higher development rate of PMGI versus S18XX series resists to fabricate a "T" structure that is suitable for liftoff purposes. Note, the deposited layer to be lifted off should be thinner than the thickness of the PMGI layer, this specific recipe is suitable for lifting off deposited layers as thick as 500 nm. This recipe can reliably yield resist lines and gaps with critical dimensions as low as 2 µm.
Required tools	Solvent wetbench with hotplates and ultrasonic bath, Wafers coater and associated hotplate, MA6 mask aligner, MX-61 microscope,Metal evaporator for PdAu, YES PR asher, YES HMDS oven, (Filmetrics F50-UV)
Required materials	S1811 photoresist, PMGI SF7 photoresit, MF-319 developer, PG Remover or pure NMP, Acetone/IPA/DI water

Index #	Recipe step	Subprocess step	Steps	Remarks
A.1	**Wafer preparation**	Solvent clean	Sonicate in Acetone at 50C / 15 min Sonicate in IPA at 80C / 15 min Blow dry with N2 gun	
A.2		Plasma clean	Load wafer in YES plasma asher Preset the heater set point to 175C Wait until chuck holder temperature stabilizes O2 plasma clean standard recipe / 2min	follow with RCA clean or HF dip if needed.
A.3		Dehydration bake	Leave wafer in YES plasma asher and change recipe to Si dehydration with N2 purge & Vacuum cycles at 200C / ~30min or longer	
A.4	**HMDS priming**	Precondition equipment	Set heater controller to 150C / ~30min	
A.5		Purge chamber	Run N2 purge cycle at 150C / ~5min	
A.6		HMDS coat vapor primer	Run standard recipe HMDS priming at 150C / ~Xxmin	
A.7	**PMGI SF7 resist spin coating**	Wafer cooldown	Allow wafer to cooldown to room temperature before dispensing resist by placing wafer in spinner chuck and running the spinning recipe to cool it down with the airflow.	
A.8		Dispense resist	Dispense resist with pipette or clean beaker over 3/4 of the substrate surface.	
A.9		Spread resist	Spread resist at 500 RPM for 3~5 sec ramping up speed at 100 RPM/sec Spin resist at 5000 RPM for 60 sec ramping up speed at 500 RPM/sec This spin speed corresponds to approximately 500 nm resist thickness	
A.10		Soft bake	Bake at 140C for 90 sec (set hotplate to 150C)	
A.11		Wafer cooldown	Allow wafer to cooldown to room temperature	
A.12	**S1811 resist spin coating**	Dispense resist	Dispense resist with pipette or clean beaker over 3/4 of the substrate surface.	
A.13		Resist spinning	Spread resist at 500 RPM for 3~5 sec ramping up speed at 100 RPM/sec Spin resist at 5000 RPM for 60 sec ramping up speed at 500 RPM/sec This spin speed corresponds to approximately 1400 nm resist thickness	
A.14		Soft bake	Bake at 110C for 90 sec (set hotplate to 120C)	
A.15		Wafer cooldown	Allow wafer to cooldown to room temperature	
A.16		Protect wafer from stray UV	Place wafer in wafer box and wrap tightly in Aluminium foil if the wafer is not to be exposed immediately	
A.17	**UV exposure with MA6 mask aligner**	Inspect mask	Inspect mask and clean it if needed	
A.18		Configure MA6	Channel 2 is calibrated to provide 25.0 mW/cm^2 of UV at 405 nm Parameters for vacuum contact mode: Gap: 30 um, WEC offset: 0, WEC type: Cont. Exposure type: Vac, PreVac:5 sec, FullVac: 5 sec, PurgeVac: 5 sec	
A.19		Setup and adjustment	Mount mask on mask holder Blow off mask and load mask Mount wafer on chuck Blow off wafer and load wafer Perform mask alignment procedure	
A.20		UV epoxsure	Expose resist for approx 4.0 sec (100 mJ/cm^2) Best exposure time may vary depending on mask design	
A.21	**Development of S1811 and PMGI resist**	Preparation	Prepare two containers with MF-319 and one containing DI water in a bench with DI tap as well.	
A.22		Developping bath 1	Develop wafer in MF-319 and agitate lightly for about 40 sec and then move wafer to second container with MF-319	the 2nd bath is used to dilute the cloudy bath 1 solution, and improve cleanliness of the developped wafer
A.23		Developping bath 2	Continue developping for another 5 to 20 sec or until the "optical stop point" is reached. Move immediately the wafer to the DI water bath	Look for the point at which very little resist is being dissolved by the developer, this is termed the "optical stop point"
A.24		Stop developer	Stop developer in DI water for 1 min	
A.25		DI water rinse	Rinse wafer in DI water tape for about 10 sec, changing position of tweezer with the help of a second tweezer to prevent chemical redeposition	
A.26		N2 dry	Blow dry wafer thoroughly with N2 gun	
A.27		Optical inspection	Check the development process under a microscope. Be careful not to expose any critical regions. If scumming is observed, develop again a few more second in the second MF-319 bath (or fresh chemical bath) and continue the stop and rinsing steps until optical inspection again	
A.28		Vacuum dry	if available, prior to loading for evaporation.	
A.29	**Pd/Au evaporation**		[machine dependent settings]	
A.31	**Lift-off**	NMP based solvent	Bath in Remover PG for 2 min or longer	pure NMP sovlent is fine too.
A.32		w/ ultrasonic	Bath in Remover PG with ultrasonic if not lifting-off well, at 50C	do not let wafer flat at the bottom, else metal might re-deposit and stick to the devices
A.33		IPA rinse	Bath in IPA for 2 min at 50 C	
A.34		DI water rinse	Rinse in DI water	
A.35		N2 dry	Dry with N2 gun thoroughly	
A.36		Vacuum dry	if available	

A.2 Aluminium resonator fabrication using negative photoresist ma-N 1410

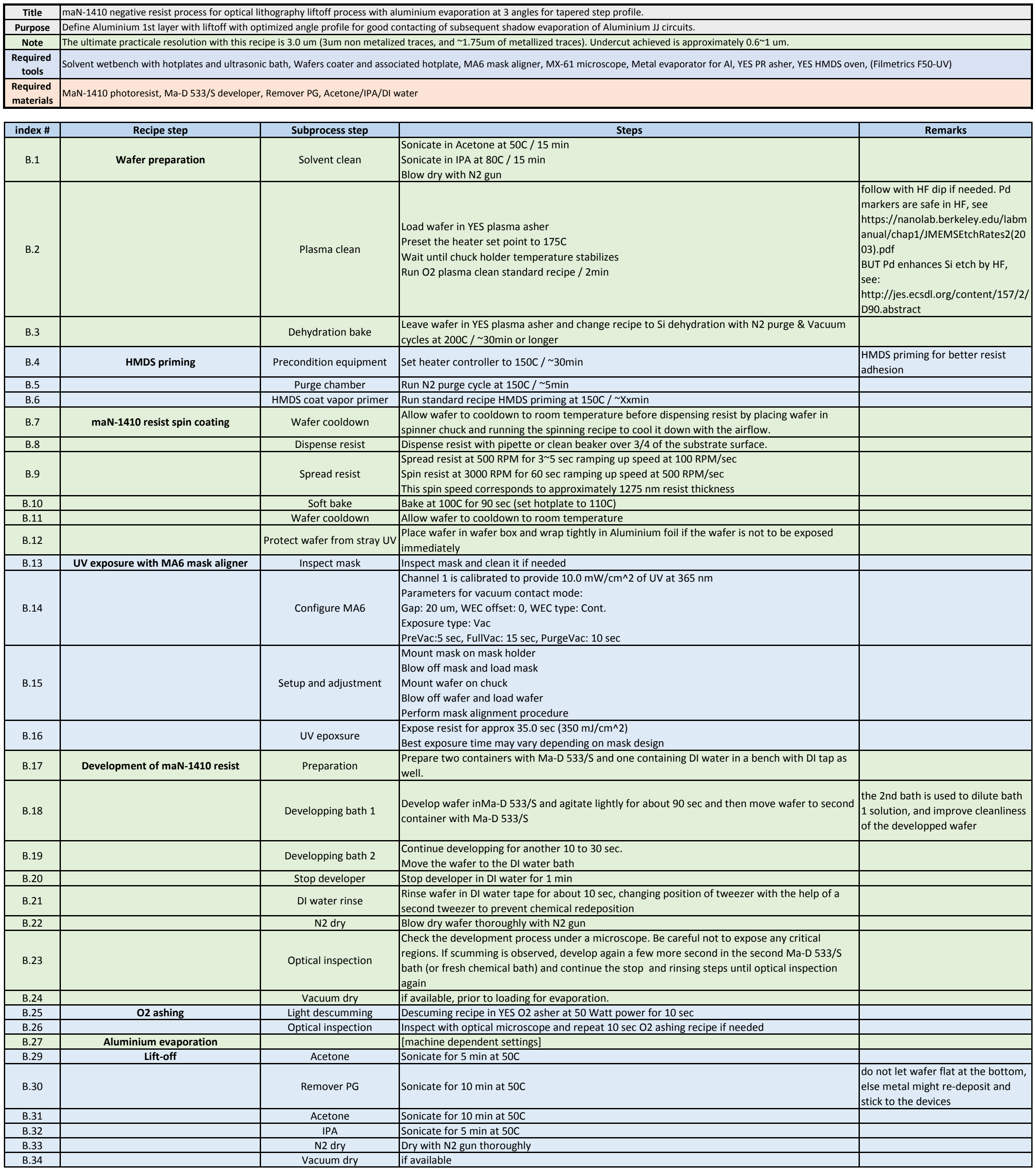

Title	maN-1410 negative resist process for optical lithography liftoff process with aluminium evaporation at 3 angles for tapered step profile.
Purpose	Define Aluminium 1st layer with liftoff with optimized angle profile for good contacting of subsequent shadow evaporation of Aluminium JJ circuits.
Note	The ultimate practicale resolution with this recipe is 3.0 um (3um non metalized traces, and ~1.75um of metallized traces). Undercut achieved is approximately 0.6~1 um.
Required tools	Solvent wetbench with hotplates and ultrasonic bath, Wafers coater and associated hotplate, MA6 mask aligner, MX-61 microscope, Metal evaporator for Al, YES PR asher, YES HMDS oven, (Filmetrics F50-UV)
Required materials	MaN-1410 photoresist, Ma-D 533/S developer, Remover PG, Acetone/IPA/DI water

index #	Recipe step	Subprocess step	Steps	Remarks
B.1	**Wafer preparation**	Solvent clean	Sonicate in Acetone at 50C / 15 min Sonicate in IPA at 80C / 15 min Blow dry with N2 gun	
B.2		Plasma clean	Load wafer in YES plasma asher Preset the heater set point to 175C Wait until chuck holder temperature stabilizes Run O2 plasma clean standard recipe / 2min	follow with HF dip if needed. Pd markers are safe in HF, see https://nanolab.berkeley.edu/labmanual/chap1/JMEMSEtchRates2(2003).pdf BUT Pd enhances Si etch by HF, see: http://jes.ecsdl.org/content/157/2/D90.abstract
B.3		Dehydration bake	Leave wafer in YES plasma asher and change recipe to Si dehydration with N2 purge & Vacuum cycles at 200C / ~30min or longer	
B.4	**HMDS priming**	Precondition equipment	Set heater controller to 150C / ~30min	HMDS priming for better resist adhesion
B.5		Purge chamber	Run N2 purge cycle at 150C / ~5min	
B.6		HMDS coat vapor primer	Run standard recipe HMDS priming at 150C / ~Xxmin	
B.7	**maN-1410 resist spin coating**	Wafer cooldown	Allow wafer to cooldown to room temperature before dispensing resist by placing wafer in spinner chuck and running the spinning recipe to cool it down with the airflow.	
B.8		Dispense resist	Dispense resist with pipette or clean beaker over 3/4 of the substrate surface.	
B.9		Spread resist	Spread resist at 500 RPM for 3~5 sec ramping up speed at 100 RPM/sec Spin resist at 3000 RPM for 60 sec ramping up speed at 500 RPM/sec This spin speed corresponds to approximately 1275 nm resist thickness	
B.10		Soft bake	Bake at 100C for 90 sec (set hotplate to 110C)	
B.11		Wafer cooldown	Allow wafer to cooldown to room temperature	
B.12		Protect wafer from stray UV	Place wafer in wafer box and wrap tightly in Aluminium foil if the wafer is not to be exposed immediately	
B.13	**UV exposure with MA6 mask aligner**	Inspect mask	Inspect mask and clean it if needed	
B.14		Configure MA6	Channel 1 is calibrated to provide 10.0 mW/cm^2 of UV at 365 nm Parameters for vacuum contact mode: Gap: 20 um, WEC offset: 0, WEC type: Cont. Exposure type: Vac PreVac:5 sec, FullVac: 15 sec, PurgeVac: 10 sec	
B.15		Setup and adjustment	Mount mask on mask holder Blow off mask and load mask Mount wafer on chuck Blow off wafer and load wafer Perform mask alignment procedure	
B.16		UV epoxsure	Expose resist for approx 35.0 sec (350 mJ/cm^2) Best exposure time may vary depending on mask design	
B.17	**Development of maN-1410 resist**	Preparation	Prepare two containers with Ma-D 533/S and one containing DI water in a bench with DI tap as well.	
B.18		Developping bath 1	Develop wafer inMa-D 533/S and agitate lightly for about 90 sec and then move wafer to second container with Ma-D 533/S	the 2nd bath is used to dilute bath 1 solution, and improve cleanliness of the developped wafer
B.19		Developping bath 2	Continue developping for another 10 to 30 sec. Move the wafer to the DI water bath	
B.20		Stop developer	Stop developer in DI water for 1 min	
B.21		DI water rinse	Rinse wafer in DI water tape for about 10 sec, changing position of tweezer with the help of a second tweezer to prevent chemical redeposition	
B.22		N2 dry	Blow dry wafer thoroughly with N2 gun	
B.23		Optical inspection	Check the development process under a microscope. Be careful not to expose any critical regions. If scumming is observed, develop again a few more second in the second Ma-D 533/S bath (or fresh chemical bath) and continue the stop and rinsing steps until optical inspection again	
B.24		Vacuum dry	if available, prior to loading for evaporation.	
B.25	**O2 ashing**	Light descumming	Descuming recipe in YES O2 asher at 50 Watt power for 10 sec	
B.26		Optical inspection	Inspect with optical microscope and repeat 10 sec O2 ashing recipe if needed	
B.27	**Aluminium evaporation**		[machine dependent settings]	
B.29	**Lift-off**	Acetone	Sonicate for 5 min at 50C	
B.30		Remover PG	Sonicate for 10 min at 50C	do not let wafer flat at the bottom, else metal might re-deposit and stick to the devices
B.31		Acetone	Sonicate for 10 min at 50C	
B.32		IPA	Sonicate for 5 min at 50C	
B.33		N2 dry	Dry with N2 gun thoroughly	
B.34		Vacuum dry	if available	

A.3 Josephson junctions and Flux qubits fabrication using PMGI SF7 / PMMA 950K A3

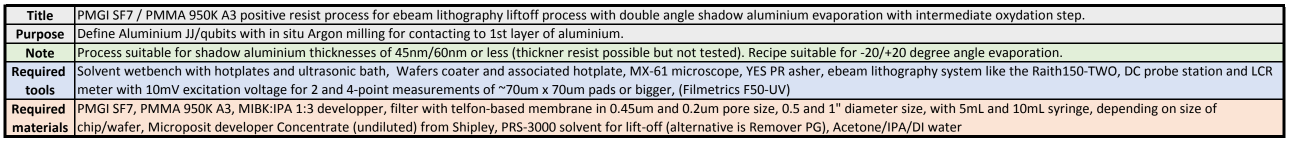

Title	PMGI SF7 / PMMA 950K A3 positive resist process for ebeam lithography liftoff process with double angle shadow aluminium evaporation with intermediate oxydation step.
Purpose	Define Aluminium JJ/qubits with in situ Argon milling for contacting to 1st layer of aluminium.
Note	Process suitable for shadow aluminium thicknesses of 45nm/60nm or less (thickner resist possible but not tested). Recipe suitable for -20/+20 degree angle evaporation.
Required tools	Solvent wetbench with hotplates and ultrasonic bath, Wafers coater and associated hotplate, MX-61 microscope, YES PR asher, ebeam lithography system like the Raith150-TWO, DC probe station and LCR meter with 10mV excitation voltage for 2 and 4-point measurements of ~70um x 70um pads or bigger, (Filmetrics F50-UV)
Required materials	PMGI SF7, PMMA 950K A3, MIBK:IPA 1:3 developper, filter with telfon-based membrane in 0.45um and 0.2um pore size, 0.5 and 1" diameter size, with 5mL and 10mL syringe, depending on size of chip/wafer, Microposit developer Concentrate (undiluted) from Shipley, PRS-3000 solvent for lift-off (alternative is Remover PG), Acetone/IPA/DI water

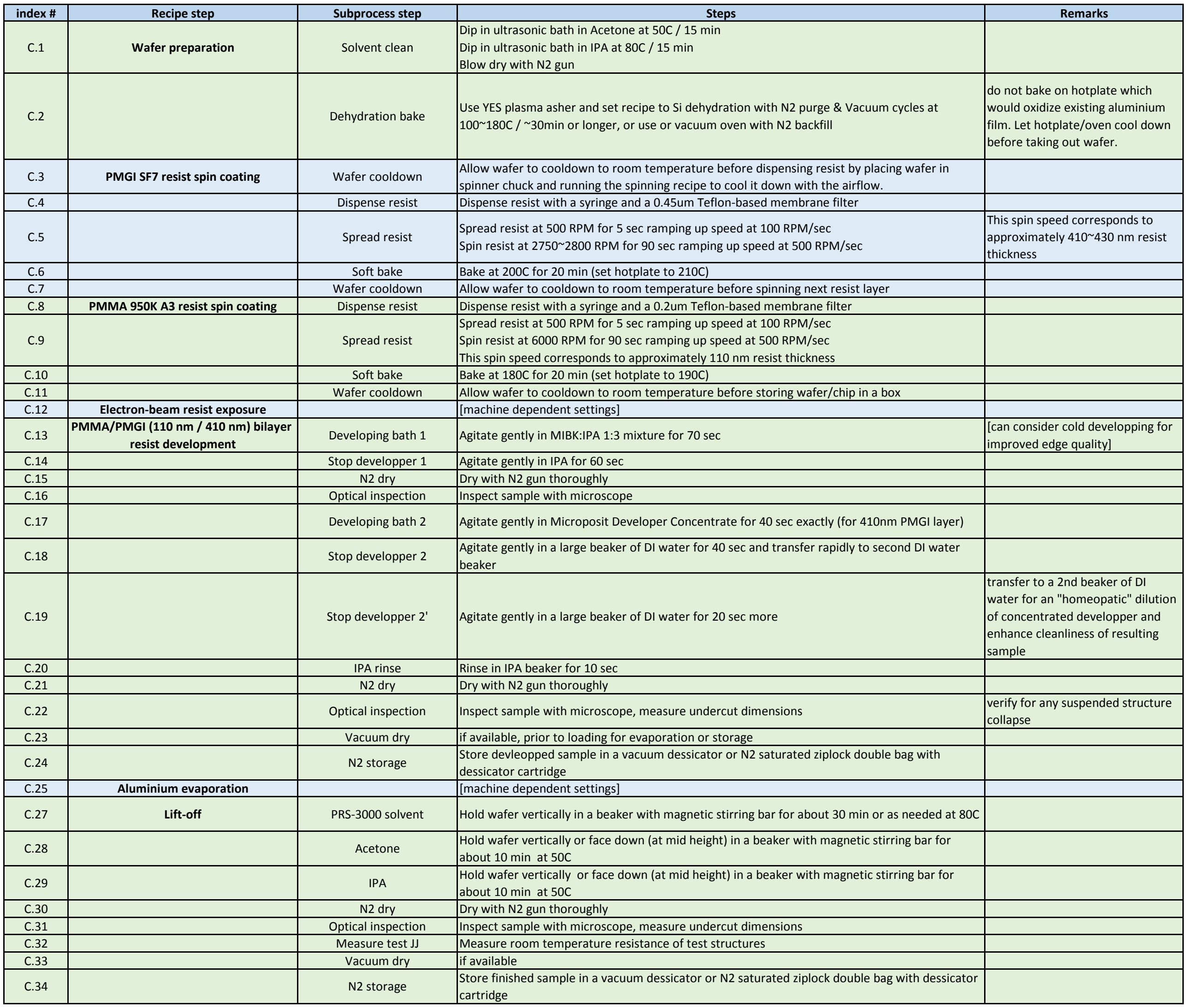

index #	Recipe step	Subprocess step	Steps	Remarks
C.1	**Wafer preparation**	Solvent clean	Dip in ultrasonic bath in Acetone at 50C / 15 min Dip in ultrasonic bath in IPA at 80C / 15 min Blow dry with N2 gun	
C.2		Dehydration bake	Use YES plasma asher and set recipe to Si dehydration with N2 purge & Vacuum cycles at 100~180C / ~30min or longer, or use or vacuum oven with N2 backfill	do not bake on hotplate which would oxidize existing aluminium film. Let hotplate/oven cool down before taking out wafer.
C.3	**PMGI SF7 resist spin coating**	Wafer cooldown	Allow wafer to cooldown to room temperature before dispensing resist by placing wafer in spinner chuck and running the spinning recipe to cool it down with the airflow.	
C.4		Dispense resist	Dispense resist with a syringe and a 0.45um Teflon-based membrane filter	
C.5		Spread resist	Spread resist at 500 RPM for 5 sec ramping up speed at 100 RPM/sec Spin resist at 2750~2800 RPM for 90 sec ramping up speed at 500 RPM/sec	This spin speed corresponds to approximately 410~430 nm resist thickness
C.6		Soft bake	Bake at 200C for 20 min (set hotplate to 210C)	
C.7		Wafer cooldown	Allow wafer to cooldown to room temperature before spinning next resist layer	
C.8	**PMMA 950K A3 resist spin coating**	Dispense resist	Dispense resist with a syringe and a 0.2um Teflon-based membrane filter	
C.9		Spread resist	Spread resist at 500 RPM for 5 sec ramping up speed at 100 RPM/sec Spin resist at 6000 RPM for 90 sec ramping up speed at 500 RPM/sec This spin speed corresponds to approximately 110 nm resist thickness	
C.10		Soft bake	Bake at 180C for 20 min (set hotplate to 190C)	
C.11		Wafer cooldown	Allow wafer to cooldown to room temperature before storing wafer/chip in a box	
C.12	**Electron-beam resist exposure**		[machine dependent settings]	
C.13	**PMMA/PMGI (110 nm / 410 nm) bilayer resist development**	Developing bath 1	Agitate gently in MIBK:IPA 1:3 mixture for 70 sec	[can consider cold developping for improved edge quality]
C.14		Stop developper 1	Agitate gently in IPA for 60 sec	
C.15		N2 dry	Dry with N2 gun thoroughly	
C.16		Optical inspection	Inspect sample with microscope	
C.17		Developing bath 2	Agitate gently in Microposit Developer Concentrate for 40 sec exactly (for 410nm PMGI layer)	
C.18		Stop developper 2	Agitate gently in a large beaker of DI water for 40 sec and transfer rapidly to second DI water beaker	
C.19		Stop developper 2'	Agitate gently in a large beaker of DI water for 20 sec more	transfer to a 2nd beaker of DI water for an "homeopatic" dilution of concentrated developper and enhance cleanliness of resulting sample
C.20		IPA rinse	Rinse in IPA beaker for 10 sec	
C.21		N2 dry	Dry with N2 gun thoroughly	
C.22		Optical inspection	Inspect sample with microscope, measure undercut dimensions	verify for any suspended structure collapse
C.23		Vacuum dry	if available, prior to loading for evaporation or storage	
C.24		N2 storage	Store devleopped sample in a vacuum dessicator or N2 saturated ziplock double bag with dessicator cartridge	
C.25	**Aluminium evaporation**		[machine dependent settings]	
C.27	**Lift-off**	PRS-3000 solvent	Hold wafer vertically in a beaker with magnetic stirring bar for about 30 min or as needed at 80C	
C.28		Acetone	Hold wafer vertically or face down (at mid height) in a beaker with magnetic stirring bar for about 10 min at 50C	
C.29		IPA	Hold wafer vertically or face down (at mid height) in a beaker with magnetic stirring bar for about 10 min at 50C	
C.30		N2 dry	Dry with N2 gun thoroughly	
C.31		Optical inspection	Inspect sample with microscope, measure undercut dimensions	
C.32		Measure test JJ	Measure room temperature resistance of test structures	
C.33		Vacuum dry	if available	
C.34		N2 storage	Store finished sample in a vacuum dessicator or N2 saturated ziplock double bag with dessicator cartridge	